

Arbeitsbericht NAB 13-78

**Extent and shape of the EDZ around
underground structures of a geological
repository for radioactive waste –
A sensitivity study for the Opalinus
Clay formation in the proposed siting
regions in Northern Switzerland**

November 2013

Geomechanica Inc.

Nationale Genossenschaft
für die Lagerung
radioaktiver Abfälle

Hardstrasse 73
CH-5430 Wettingen
Telefon 056-437 11 11

www.nagra.ch

Arbeitsbericht NAB 13-78

**Extent and shape of the EDZ around
underground structures of a geological
repository for radioactive waste –
A sensitivity study for the Opalinus
Clay formation in the proposed siting
regions in Northern Switzerland**

November 2013

Geomechanica Inc.

KEYWORDS

Opalinus Clay, SF/HLW, L/ILW, shaft, seal section,
numerical simulation; EDZ; fracture network

**Nationale Genossenschaft
für die Lagerung
radioaktiver Abfälle**

Hardstrasse 73
CH-5430 Wettingen
Telefon 056-437 11 11

www.nagra.ch

Nagra Working Reports concern work in progress that may have had limited review. They are intended to provide rapid dissemination of information. The viewpoints presented and conclusions reached are those of the author(s) and do not necessarily represent those of Nagra.

"Copyright © 2013 by Nagra, Wettingen (Switzerland) / All rights reserved.

All parts of this work are protected by copyright. Any utilisation outwith the remit of the copyright law is unlawful and liable to prosecution. This applies in particular to translations, storage and processing in electronic systems and programs, microfilms, reproductions, etc."

Zusammenfassung

Beim Bau und Betrieb eines geologischen Tiefenlagers entwickelt sich im Umfeld der Untertagebauwerke eine Auflockerungszone, die nach Lagerverschluss einen möglichen Freisetzungspfad für Radionuklide darstellt und somit im Rahmen der Langzeit-Sicherheitsanalysen zu berücksichtigen ist. Die Wirksamkeit dieses Freisetzungspfads hängt nicht nur von der Form und der räumlichen Erstreckung der Auflockerungszone ab, sondern auch von der Art der Gebirgsauflockerung. In überkonsolidierten Tonformationen zeigen sowohl empirische Befunde als auch experimentelle Untersuchungen ausnahmslos, dass Spröddeformation des Gebirges der vorherrschende Mechanismus ist, d.h. die Auflockerungszone wird durch diskrete, exkavationsbedingte Trennflächensysteme gebildet.

Zu diesem Zweck wurden mit einem sogenannten FEMDEM Modell (Methode der hybriden finiten Elemente) rissmechanische Sensitivitätsstudien zur Abschätzung der Auflockerungszone im Umfeld eines geologischen Tiefenlagers durchgeführt. Konkret wurden 3 verschiedene Lagerkomponenten modelliert, nämlich ein BE/HAA-Lagerstollen, eine SMA-Lagerkaverne (Typ K09) und ein Schachtquerschnitt. Die durchgeführten Sensitivitätsstudien beziehen sich auf ein geologisches Tiefenlager im Opalinuston in den potenziellen Standortgebieten in der Nordschweiz. Der Schwerpunkt der rissmechanischen Modellierungen lag auf der Erstellung eines Katalogs von charakteristischen Rissbildern in der Umgebung der Untertagebauwerke unter Berücksichtigung der konzeptionellen und parametrischen Ungewissheiten in den vorgeschlagenen Standortregionen. Es sind dies:

- der Einfluss der Lagertiefe und der Gebirgsspannungs-Anisotropie
- der Einfluss der geomechanischen Eigenschaften des Wirtgesteins;
- der Einfluss der notwendigen Ausbaumassnahmen
- der Einfluss der Rückbildung der Auflockerungszone nach der Verfüllung der BE/HAA Lagerstollen mit quellfähigem Bentonit

Als maximale Tunnelkonvergenz wurden Werte bis zu 4% angenommen¹, so dass die in diesem Bericht ermittelten Rissbilder eine konservative Abschätzung der zu erwartenden Ausdehnung der Auflockerungszone darstellen. Die berechneten Rissbilder in Form eines digitalen Rissinventars (Risstyp, Risslänge, Rissorientierung, Rissbreite, vergl. Anhang) liefern die Grundlage für die quantitative Abschätzung der effektiven hydraulischen Durchlässigkeit der Auflockerungszone im Rahmen weiterführender hydraulischer Modellierungen (Alcolea et al. 2014).

¹ Die in den Sensitivitätsrechnungen festgelegte maximale Tunnelkonvergenz überschreitet die aus bautechnischer Sicht als „bedingt günstig“ eingestufteten Verformungen von 2.5%.

Table of Contents

Zusammenfassung.....	I
Table of Contents	II
List of Tables	IV
List of Figures.....	V
1 Introduction	1
1.1 Background and motivation.....	1
1.2 Scope and objectives.....	1
1.3 Report organisation.....	2
2 Modelling software: FEMDEM.....	3
2.1 Contact detection and interaction	3
2.2 Elastic behaviour and anisotropy of stiffness	4
2.3 Material failure and anisotropy of strength.....	5
2.4 Mesh sensitivity.....	8
3 Modelling methodology: laboratory-scale simulations	9
3.1 Geometry and boundary conditions.....	9
3.2 Model calibration and input parameters	9
4 Results: laboratory-scale simulations	11
4.1 Brazilian disc test.....	11
4.2 Uniaxial compression test.....	12
5 Modelling methodology: EDZ simulations	17
5.1 Geometries, mesh generation and input parameters	17
5.2 In situ stress and boundary conditions.....	21
5.3 Modelling procedure for excavation advance.....	22
5.4 Modelling procedure for support installation	23
5.5 Estimation of excavation-induced fracture aperture.....	24
5.6 Modelling procedure for the EDZ reconsolidation.....	24
6 Results: EDZ simulations for SF/HLW emplacement tunnel.....	25
6.1 Analysis of sensitivity to <i>in situ</i> stress conditions	27
6.2 Analysis of sensitivity to strength values	42
6.3 Analysis of sensitivity to the presence of faults	47
6.4 Analysis of sensitivity to shotcrete stiffness.....	52
7 Results: EDZ simulations for L/ILW emplacement cavern.....	59
7.1 Analysis of sensitivity to <i>in situ</i> stress conditions	60
7.2 Analysis of sensitivity to the presence faults.....	73

7.3	Analysis of sensitivity to strength parameters	80
8	Results: EDZ simulations for shaft section.....	85
8.1	Analysis of sensitivity to <i>in situ</i> stress conditions	86
8.2	Analysis of sensitivity to strength parameters	94
9	Results: simulation of EDZ reconsolidation.....	109
9.1	SF/HLW emplacement tunnel	110
9.2	Shaft model.....	121
10	Discussion on the EDZ modeling results.....	129
10.1	SF/HLW emplacement tunnel simulations	129
10.2	L/ILW emplacement cavern simulations	130
10.3	Shaft seal section simulations	130
10.4	EDZ reconsolidation simulations	130
11	Summary and conclusions	131
12	References.....	133
Appendix: File Identification Tables		A-135

List of Tables

Tab. 1:	Input parameters of the FEM/DEM model calibrated based on laboratory-scale rock mechanics tests on Opalinus Clay (Nagra 2002).....	10
Tab. 2:	Comparison between the mechanical properties of the Opalinus Clay and the emergent macroscopic properties of the FEM/DEM model.....	15
Tab.3:	Input parameters for the sensitivity analysis to the geomechanical properties of the HAA and K09 models.	20
Tab. 4:	Input parameters for the sensitivity analysis to the geomechanical properties of the shaft model.	20
Tab. 5:	Summary of <i>in situ</i> stress conditions applied to the numerical models. Vertical and horizontal stresses coincide with the principal stresses. The stress ratio to the vertical stress, K_0 , is reported in brackets.....	22
Tab. 6:	Summary of HAA model simulations.	26
Tab. 7:	Summary of K09 model simulations.	59
Tab. 8:	Summary of shaft simulations.	85
Tab. 9:	Summary of EDZ reconsolidation simulations.....	109
Tab. A1:	List of directories containing the output files of the simulation cases reported in Table 6, 7 and 8 (Sensitivity analysis).....	A-136
Tab. A2:	List of directories containing the output files of the simulation cases reported in Table 9 (Reconsolidation study).....	A-137

List of Figures

Fig. 2-1:	Transversely isotropic material. (a) Associated elastic constants. (b) Adopted naming convention for standard rock mechanics tests (i.e., compression and Brazilian tests) on transversely isotropic rocks. Source: Lisjak et al. (2013).....	4
Fig. 2-2:	Cohesive-zone approach for material failure modelling in FEM/DEM. (a) Conceptual model of a tensile crack in a heterogeneous rock material (after Labuz et al. (1987), modified). (b) Theoretical FPZ model of Hillerborg (Hillerborg et al. 1976). (c) FEM/DEM implementation of the FPZ using triangular elastic elements and four-noded crack elements to represent the bulk material and the fracture, respectively. Triangular elements are shrunk for illustration purposes.....	5
Fig. 2-3:	Simulation of fracturing with the Y-Geo FEM/DEM code. (a) Representation of a continuum using cohesive crack elements interspersed throughout a mesh of triangular elastic elements. Triangles are shrunk for illustration purposes. (b) Constitutive behaviour of the crack elements defined in terms of normal and tangential bonding stress, σ and τ , vs. crack relative displacement, o and s (i.e., opening and sliding). (c) Elliptical coupling relationship between crack opening, o , and sliding, s , for mixed-mode fracturing.....	7
Fig. 2-4:	FEM/DEM modelling of strength anisotropy. (a) Linear variation of cohesive strength parameters with the angle, γ , between crack element and bedding. (b) Example of mesh combining a Delaunay triangulation for the intra-layer material with edges preferentially aligned along the bedding plane direction.....	8
Fig. 3-1:	Zoomed-in view of the flat contact zone between the triangular loading platen and the Brazilian disc specimen.....	9
Fig. 4-1:	Curves of tensile stress versus platen vertical displacement for the Brazilian disc simulation. (b) Axial stress vs. axial strain for the UCS simulation (Jahns 2010).....	11
Fig. 4-2:	Evolution of fracture pattern of the calibrated laboratory-scale Brazilian disc models at increasing axial displacement values. (a) P sample. (b) S sample.	12
Fig. 4-3:	Typical fracture patterns observed during Brazilian tests (disc diameter = 30 mm, after Jahns (2010)) on Opalinus Clay.	12
Fig. 4-4:	Curves of axial stress versus axial strain for the UCS simulation.	13
Fig. 4-5:	Typical fracture patterns observed during UCS tests (sample height = 120 mm, sample diameter = 60 mm, after Popp et al. (2008)) on Opalinus Clay.	13
Fig. 4-6:	Evolution of fracture patterns of the calibrated laboratory-scale uniaxial compression models at increasing axial strain values. (a) P sample. (b) Z-45° sample. (c) S sample.	14
Fig. 5-1:	HAA model. Geometry and boundary conditions of the FEM/DEM model of the SF-HLW emplacement tunnels.....	18
Fig. 5-2:	K09 model. Geometry and boundary conditions of the FEM/DEM model of the L-ILW emplacement caverns.....	18

Fig. 5-3: Shaft model. Geometry and boundary conditions of the FEM/DEM model of the repository shaft. 19

Fig. 5-4: Geometries of the SF-HLW emplacement tunnel (left) and K09 (right) model containing three stylised fault zones..... 19

Fig. 5-5: Modelling procedure for excavation advance and support installation using the core replacement technique. (a) Replacement of core with reduced elastic modulus material. (b) Installation of tunnel lining. (c) Qualitative example of ground reaction curve simulated via stepwise modulus reduction and support characteristic curve for a linear elastic lining 23

Fig. 5-6: Modelling procedure for the EDZ reconsolidation..... 24

Fig. 6-1: Ground reactions curves of the HAA model under different *in situ* stress conditions. For each case, the *in situ* vertical stress, σ_v , is reported together with the stress ratio, K_0 , in brackets. Strength parameters are "Opa x 2". The exact location of points P1-P4 is reported in Fig. 5-1. 27

Fig. 6-2: Evolution of displacement, δ , around the excavation boundary of the HAA model under different *in situ* stress conditions. For each case, the stress ratio, K_0 , to the *in situ* vertical stress, $\sigma_v = 19.6$ MPa, is reported in brackets, together with the core softening ratio, α_s , at the time of support installation. Strength parameters are "Opa x 2" (the reference points P1 to P4 are defined in Fig. 5-1). 28

Fig. 6-3: Contours of displacement, δ , of the HAA model under different *in situ* stress conditions. For each case, the stress ratio, K_0 , to the *in situ* vertical stress, $\sigma_v = 19.6$ MPa, is reported in brackets, together with the core softening ratio, α_s , at the time of support installation. Strength parameters are "Opa x 2". 29

Fig. 6-4: Final fracture patterns of the HAA model under different *in situ* stress conditions. Tensile and shear failure are indicated in blue and orange, respectively. For each case, the stress ratio, K_0 , to the *in situ* vertical stress, $\sigma_v = 19.6$ MPa, is reported in brackets, together with the core softening ratio, α_s , at the time of support installation. Strength parameters are "Opa x 2". 30

Fig. 6-5: Contours of maximum principal stress, σ_1 , of the HAA model under different *in situ* stress conditions. For each case, the stress ratio, K_0 , to the *in situ* vertical stress, $\sigma_v = 19.6$ MPa, is reported in brackets, together with the core softening ratio, α_s , at the time of support installation. Strength parameters are "Opa x 2". 31

Fig. 6-6: Contours of minimum principal stress, σ_3 , of the HAA model under different *in situ* stress conditions. For each case, the stress ratio, K_0 , to the *in situ* vertical stress, $\sigma_v = 19.6$ MPa, is reported in brackets, together with the core softening ratio, α_s , at the time of support installation. Strength parameters are "Opa x 2". 32

Fig. 6-7: Contours of maximum principal stress, σ_1 , in the support layer of the HAA model under different *in situ* stress conditions. For each case, the stress ratio, K_0 , to the *in situ* vertical stress, $\sigma_v = 19.6$ MPa, is reported in brackets, together with the core softening ratio, α_s , at the time of support installation. Strength parameters are "Opa x 2". 33

- Fig. 6-8: Contour of minimum principal stress, σ_3 , in the support layer of the HAA model under different *in situ* stress conditions. For each case, the stress ratio, K_0 , to the *in situ* vertical stress, $\sigma_v = 19.6$ MPa, is reported in brackets, together with the core softening ratio, α_s , at the time of support installation. Strength parameters are "Opa x 2". 34
- Fig. 6-9: Evolution of displacement, δ , around the excavation boundary of the HAA model under different *in situ* stress conditions. For each case, the *in situ* vertical stress, σ_v , is reported together with the stress ratio, K_0 , in brackets, and with the core softening ratio, α_s , at the time of support installation. Strength parameters are "Opa x 2". The exact location of points P1-P4 is reported in Fig. 5-1. 35
- Fig. 6-10: Contours of displacement, δ , of the HAA model under different *in situ* stress conditions. For each case, the *in situ* vertical stress, σ_v , is reported together with the stress ratio, K_0 , in brackets, and with the core softening ratio, α_s , at the time of support installation. Strength parameters are "Opa x 2". 36
- Fig. 6-11: Final fracture patterns of the HAA model under different *in situ* stress conditions. Tensile and shear failure are indicated in blue and orange, respectively. For each case, the *in situ* vertical stress, σ_v , is reported together with the stress ratio, K_0 , in brackets, and with the core softening ratio, α_s , at the time of support installation. Strength parameters are "Opa x 2". 37
- Fig. 6-12: Contours of maximum principal stress, σ_1 , of the HAA model under different *in situ* stress conditions. For each case, the *in situ* vertical stress, σ_v , is reported together with the stress ratio, K_0 , in brackets, and with the core softening ratio, α_s , at the time of support installation. Strength parameters are "Opa x 2". 38
- Fig. 6-13: Contours of minimum principal stress, σ_3 , of the HAA model under different *in situ* stress conditions. For each case, the *in situ* vertical stress, σ_v , is reported together with the stress ratio, K_0 , in brackets, and with the core softening ratio, α_s , at the time of support installation. Strength parameters are "Opa x 2". 39
- Fig. 6-14: Contours of maximum principal stress, σ_1 , in the support layer of the HAA model under different *in situ* stress conditions. For each case, the *in situ* vertical stress, σ_v , is reported together with the stress ratio, K_0 , in brackets, and with the core softening ratio, α_s , at the time of support installation. Strength parameters are "Opa x 2". 40
- Fig. 6-15: Contours of minimum principal stress, σ_3 , in the support layer of the HAA model under different *in situ* stress conditions. For each case, the *in situ* vertical stress, σ_v , is reported together with the stress ratio, K_0 , in brackets, and with the core softening ratio, α_s , at the time of support installation. Strength parameters are "Opa x 2". 41
- Fig. 6-16: Ground reactions curves of the HAA model for different rock strength levels. The vertical *in situ* stress is equal to 15.9 MPa with a stress ratio $K_0 = 1.3$, while the core softening ratio at the time of support installation is equal to 0.008. The exact location of points P1-P4 is reported in Fig. 5-1. 42
- Fig. 6-17: Evolution of displacement, δ , around the excavation boundary of the HAA model for different rock strength levels. The vertical *in situ* stress is equal to

15.9 MPa with a stress ratio $K_0 = 1.3$, while the core softening ratio at the time of support installation is equal to 0.008. The exact location of points P1-P4 is reported in Fig. 5-1..... 43

Fig. 6-18: Contours of displacement, δ , of the HAA model for different rock strength levels. The vertical *in situ* stress is equal to 15.9 MPa with a stress ratio $K_0 = 1.3$, while the core softening ratio at the time of support installation is equal to 0.008..... 44

Fig. 6-19: Final fracture patterns of the HAA model for different rock strength levels. Tensile and shear failure are indicated in blue and orange, respectively. The vertical *in situ* stress is equal to 15.9 MPa with a stress ratio $K_0 = 1.3$, while the core softening ratio at the time of support installation is equal to 0.008..... 44

Fig. 6-20: Contours of maximum principal stress, σ_1 , of the HAA model for different rock strength levels. The vertical *in situ* stress is equal to 15.9 MPa with a stress ratio $K_0 = 1.3$, while the core softening ratio at the time of support installation is equal to 0.008..... 45

Fig. 6-21: Contours of minimum principal stress, σ_3 , of the HAA model for different rock strength levels. The vertical *in situ* stress is equal to 15.9 MPa with a stress ratio $K_0 = 1.3$, while the core softening ratio at the time of support installation is equal to 0.008..... 45

Fig. 6-22: Contours of maximum principal stress, σ_1 , in the support layer of the HAA model for different rock strength levels. The vertical *in situ* stress is equal to 15.9 MPa with a stress ratio $K_0 = 1.3$, while the core softening ratio at the time of support installation is equal to 0.008..... 46

Fig. 6-23: Contours of minimum principal stress, σ_3 , in the support layer of the HAA model for different rock strength levels. The vertical *in situ* stress is equal to 15.9 MPa with a stress ratio $K_0 = 1.3$, while the core softening ratio at the time of support installation is equal to 0.008..... 46

Fig. 6-24: Ground reactions curves of the HAA with faults model for different rock strength levels. The vertical *in situ* stress is equal to 15.9 MPa with a stress ratio $K_0 = 1.3$, while the core softening ratio at the time of support installation is equal to 0.008. The exact location of points P1-P4 is reported in Fig. 5-1. 47

Fig. 6-25: Evolution of displacement, δ , around the excavation boundary of the HAA model with faults for different rock strength levels. The vertical *in situ* stress is equal to 15.9 MPa with a stress ratio $K_0 = 1.3$, while the core softening ratio at the time of support installation is equal to 0.008. The exact location of points P1-P4 is reported in Fig.5-1..... 48

Fig. 6-26: Contours of displacement, δ , of the HAA model with faults for different rock strength levels. The vertical *in situ* stress is equal to 15.9 MPa with a stress ratio $K_0 = 1.3$, while the core softening ratio at the time of support installation is equal to 0.008..... 49

Fig. 6-27: Final fracture patterns of the HAA model with faults for different rock strength levels. Tensile and shear failure are indicated in blue and orange, respectively. The vertical *in situ* stress is equal to 15.9 MPa with a stress ratio $K_0 = 1.3$, while the core softening ratio at the time of support installation is equal to 0.008..... 49

- Fig. 6-28: Contours of maximum principal stress, σ_1 , of the HAA model with faults for different rock strength levels. The vertical *in situ* stress is equal to 15.9 MPa with a stress ratio $K_0 = 1.3$, while the core softening ratio at the time of support installation is equal to 0.008. 50
- Fig. 6-29: Contours of minimum principal stress, σ_3 , of the HAA model with faults for different rock strength levels. The vertical *in situ* stress is equal to 15.9 MPa with a stress ratio $K_0 = 1.3$, while the core softening ratio at the time of support installation is equal to 0.008. 50
- Fig. 6-30: Contours of maximum principal stress, σ_1 , in the support layer of the HAA model with faults for different rock strength levels. The vertical *in situ* stress is equal to 15.9 MPa with a stress ratio $K_0 = 1.3$, while the core softening ratio at the time of support installation is equal to 0.008. 51
- Fig. 6-31: Contours of minimum principal stress, σ_3 , in the support layer of the HAA model with faults for different rock strength levels. The vertical *in situ* stress is equal to 15.9 MPa with a stress ratio $K_0 = 1.3$, while the core softening ratio at the time of support installation is equal to 0.008. 51
- Fig. 6-32: Evolution of displacement, δ , around the excavation boundary of the HAA model for different rock strength levels and values of the shotcrete elastic modulus, E_c . The vertical *in situ* stress is equal to 15.9 MPa with a stress ratio $K_0 = 1.3$, while the core softening ratio at the time of support installation is equal to 0.008. The exact location of points P1-P4 is reported in Fig. 5-1. 52
- Fig. 6-33: Contour of displacement, δ , of the HAA model for different rock strength levels and values of the shotcrete elastic modulus, E_c . The vertical *in situ* stress is equal to 15.9 MPa with a stress ratio $K_0 = 1.3$, while the core softening ratio at the time of support installation is equal to 0.008. 53
- Fig. 6-34: Final fracture patterns of the HAA model for different rock strength levels and values of the shotcrete elastic modulus, E_c . Tensile and shear failure are indicated in blue and orange, respectively. The vertical *in situ* stress is equal to 15.9 MPa with a stress ratio $K_0 = 1.3$, while the core softening ratio at the time of support installation is equal to 0.008. 54
- Fig. 6-35: Contours of maximum principal stress, σ_1 , of the HAA model for different rock strength levels and values of the shotcrete elastic modulus, E_c . The vertical *in situ* stress is equal to 15.9 MPa with a stress ratio $K_0 = 1.3$, while the core softening ratio at the time of support installation is equal to 0.008. 55
- Fig. 6-36: Contours of minimum principal stress, σ_3 , of the HAA model for different rock strength levels and values of the shotcrete elastic modulus, E_c . The vertical *in situ* stress is equal to 15.9 MPa with a stress ratio $K_0 = 1.3$, while the core softening ratio at the time of support installation is equal to 0.008. 56
- Fig. 6-37: Contours of maximum principal stress, σ_1 , in the support layer of the HAA model for different rock strength levels and values of the shotcrete elastic modulus, E_c . The vertical *in situ* stress is equal to 15.9 MPa with a stress ratio $K_0 = 1.3$, while the core softening ratio at the time of support installation is equal to 0.008. 57
- Fig. 6-38: Contours of minimum principal stress, σ_3 , in the support layer of the HAA model for different rock strength levels and values of the shotcrete elastic modulus, E_c . The vertical *in situ* stress is equal to 15.9 MPa with a stress

ratio $K_0 = 1.3$, while the core softening ratio at the time of support installation is equal to 0.008. 58

Fig. 7-1: Ground reactions curves of the K09 model under different *in situ* stress conditions. For each case, the *in situ* vertical stress, σ_v , is reported together with the stress ratio, K_0 , in brackets. The exact location of points P1-P4 is reported in Fig. 5-2. 60

Fig. 7-2: Evolution of displacement, δ , around the excavation boundary of the K09 model under different *in situ* stress conditions. The core softening ratio at the time of support installation is equal to 0.01. Rock strength parameters are "Opa x 2". The exact location of points P1-P4 is reported in Fig. 5-2. 61

Fig. 7-3: Contour of displacement, δ , of the K09 model under different *in situ* stress conditions. The core softening ratio at the time of support installation is equal to 0.01. Rock strength parameters are "Opa x 2". 62

Fig. 7-4: Fracture patterns around the excavation of the K09 model under different *in situ* stress conditions. Tensile and shear failure are indicated in blue and orange, respectively. The core softening ratio at the time of support installation is equal to 0.01. Rock strength parameters are "Opa x 2" 63

Fig. 7-5: Contours of maximum principal stress, σ_1 , of the K09 model under different *in situ* stress conditions. The core softening ratio at the time of support installation is equal to 0.01. Rock strength parameters are "Opa x 2" 64

Fig. 7-6: Contours of minimum principal stress, σ_3 , of the K09 model under different *in situ* stress conditions. The core softening ratio at the time of support installation is equal to 0.01. Rock strength parameters are "Opa x 2" 65

Fig. 7-7: Contours of maximum principal stress, σ_1 , in the support layer of the K09 model under different *in situ* stress conditions. The core softening ratio at the time of support installation is equal to 0.01. Rock strength parameters are "Opa x 2". 66

Fig. 7-8: Contours of minimum principal stress, σ_3 , inside the support layer of the K09 model under different *in situ* stress conditions. The core softening ratio at the time of support installation is equal to 0.01. Rock strength parameters are "Opa x 2". 67

Fig. 7-9: Ground reactions curves of the K09 model under different *in situ* stress conditions. For each case, the *in situ* vertical stress, σ_v , is reported together with the stress ratio, K_0 , in brackets. Rock strength parameters are "Opa x 2". The exact location of points P1-P4 is reported in Fig. 5-2. 68

Fig. 7-10: Evolution of displacement, δ , around the excavation boundary of the K09 model under different *in situ* stress conditions. The core softening ratio at the time of support installation is equal to 0.01. Rock strength parameters are "Opa x 2". The exact location of points P1-P4 is reported in Fig. 5-2. 69

Fig. 7-11: Contours of displacement, δ , of the K09 model under different *in situ* stress conditions. The core softening ratio at the time of support installation is equal to 0.01. Rock strength parameters are "Opa x 2". 70

Fig. 7-12: Final fracture patterns around the excavation of the K09 model under different *in situ* stress conditions. Tensile and shear failure are indicated in blue and orange, respectively. The core softening ratio at the time of support installation is equal to 0.01. Rock strength parameters are "Opa x 2" 70

Fig. 7-13: Contours of maximum principal stress, σ_1 , of the K09 model under different *in situ* stress conditions. The core softening ratio at the time of support installation is equal to 0.01. Rock strength parameters are "Opa x 2"..... 71

Fig. 7-14: Contour of minimum principal stress, σ_3 , of the K09 model under different *in situ* stress conditions. The core softening ratio at the time of support installation is equal to 0.01. Rock strength parameters are "Opa x 2"..... 71

Fig. 7-15: Contours of maximum principal stress, σ_1 , in the support layer of the K09 model under different *in situ* stress conditions. The core softening ratio at the time of support installation is equal to 0.01. Rock strength parameters are "Opa x 2". 72

Fig. 7-16: Contours of minimum principal stress, σ_3 , in the support layer of the K09 model under different *in situ* stress conditions. The core softening ratio at the time of support installation is equal to 0.01. Rock strength parameters are "Opa x 2". 72

Fig. 7-17: Ground reactions of the K09 model with faults for different rock strength levels. The vertical *in situ* stress is equal to 18.4 MPa with a stress ratio $K_0 = 1.0$. The exact location of points P1-P4 is reported in Fig. 5-2. 73

Fig. 7-18: Evolution of displacement, δ , around the excavation boundary of the K09 model with faults for different rock strength levels. The vertical *in situ* stress is equal to 18.4 MPa with a stress ratio $K_0 = 1.0$, while the core softening ratio at the time of support installation is equal to 0.01. The exact location of points P1-P4 is reported in Fig. 5-2. 74

Fig. 7-19: Contour of displacement, δ , around the excavation of the K09 model with faults for different rock strength levels. The vertical *in situ* stress is equal to 18.4 MPa with a stress ratio $K_0 = 1.0$, while the core softening ratio at the time of support installation is equal to 0.01..... 75

Fig. 7-20: Fracture patterns around the excavation of the K09 model with faults for different rock strength levels. Tensile and shear failure are indicated in blue and orange, respectively. The vertical *in situ* stress is equal to 18.4 MPa with a stress ratio $K_0 = 1.0$, while the core softening ratio at the time of support installation is equal to 0.01..... 76

Fig. 7-21: Contour of maximum principal stress, σ_1 , around the excavation of the K09 model with faults for different rock strength levels. The vertical *in situ* stress is equal to 18.4 MPa with a stress ratio $K_0 = 1.0$, while the core softening ratio at the time of support installation is equal to 0.01..... 77

Fig. 7-22: Contour of minimum principal stress, σ_3 , around the excavation of the K09 model with faults for different rock strength levels. The vertical *in situ* stress is equal to 18.4 MPa with a stress ratio $K_0 = 1.0$, while the core softening ratio at the time of support installation is equal to 0.01..... 78

Fig. 7-23: Contour of maximum principal stress, σ_1 , inside the support layer of the K09 model with faults for different rock strength levels. The vertical *in situ* stress is equal to 18.4 MPa with a stress ratio $K_0 = 1.0$, while the core softening ratio at the time of support installation is equal to 0.01..... 79

Fig. 7-24: Contour of minimum principal stress, σ_3 , inside the support layer of the K09 model with faults for different rock strength levels. The vertical *in situ* stress

is equal to 18.4 MPa with a stress ratio $K_0 = 1.0$, while the core softening ratio at the time of support installation is equal to 0.01..... 80

Fig. 7-25: Ground reactions of the K09 model for different rock strength levels. The vertical *in situ* stress is equal to 18.4 MPa with a stress ratio $K_0 = 1.0$. The exact location of points P1-P4 is reported in Fig. 5-2. 80

Fig. 7-26: Evolution of displacement, δ , around the excavation boundary of the K09 model for different rock strength levels. The vertical *in situ* stress is equal to 18.4 MPa with a stress ratio $K_0 = 1.0$, while the core softening ratio at the time of support installation is equal to 0.01. The exact location of points P1-P4 is reported in Fig. 5-2. 81

Fig. 7-27: Contours of displacement, δ , of the K09 model for different rock strength levels. The vertical *in situ* stress is equal to 18.4 MPa with a stress ratio $K_0 = 1.0$, while the core softening ratio at the time of support installation is equal to 0.01. 81

Fig. 7-28: Fracture patterns around the excavation of the K09 model for different rock strength levels. Tensile and shear failure are indicated in blue and orange, respectively. The vertical *in situ* stress is equal to 18.4 MPa with a stress ratio $K_0 = 1.0$, while the core softening ratio at the time of support installation is equal to 0.01. 82

Fig. 7-29: Contours of maximum principal stress, σ_1 , of the K09 model for different rock strength levels. The vertical *in situ* stress is equal to 18.4 MPa with a stress ratio $K_0 = 1.0$, while the core softening ratio at the time of support installation is equal to 0.01. 82

Fig. 7-30: Contours of minimum principal stress, σ_3 , of the K09 model for different rock strength levels. The vertical *in situ* stress is equal to 18.4 MPa with a stress ratio $K_0 = 1.0$, while the core softening ratio at the time of support installation is equal to 0.01. 82

Fig. 7-31: Contours of maximum principal stress, σ_1 , in the support layer of the K09 model for different rock strength levels. The vertical *in situ* stress is equal to 18.4 MPa with a stress ratio $K_0 = 1.0$, while the core softening ratio at the time of support installation is equal to 0.01..... 83

Fig. 7-32: Contours of minimum principal stress, σ_3 , in the support layer of the K09 model for different rock strength levels. The vertical *in situ* stress is equal to 18.4 MPa with a stress ratio $K_0 = 1.0$, while the core softening ratio at the time of support installation is equal to 0.01..... 83

Fig. 8-1: Ground reactions of the shaft model under different *in situ* stress conditions. For each case, the *in situ* vertical stress, σ_v , is reported together with the stress ratio, K_0 , in brackets. Strength parameters are "OpaMax". The exact location of points P1-P4 is reported in Fig. 5-3..... 86

Fig. 8-2: Evolution of displacement, δ , around the excavation boundary of the shaft model under different *in situ* stress conditions. For each case, the *in situ* vertical stress, σ_v , is reported together with the stress ratio, K_0 , in brackets. Strength parameters are "OpaMax", while the core softening ratio at the time of support installation is equal to 0.01. The exact location of points P1-P4 is reported in Fig. 5-3. 87

Fig. 8-3:	Contours of displacement, δ , of the shaft model under different <i>in situ</i> stress conditions. For each case, the <i>in situ</i> vertical stress, σ_v , is reported together with the stress ratio, K_0 , in brackets. Strength parameters are "OpaMax", while the core softening ratio at the time of support installation is equal to 0.01.	88
Fig. 8-4:	Fracture patterns around the excavation of the shaft model under different <i>in situ</i> stress conditions. Tensile and shear failure are indicated in blue and orange, respectively. For each case, the <i>in situ</i> vertical stress, σ_v , is reported together with the stress ratio, K_0 , in brackets. Strength parameters are "OpaMax", while the core softening ratio at the time of support installation is equal to 0.01.	89
Fig. 8-5:	Contours of maximum principal stress, σ_1 , of the shaft model under different <i>in situ</i> stress conditions. For each case, the <i>in situ</i> vertical stress, σ_v , is reported together with the stress ratio, K_0 , in brackets. Strength parameters are "OpaMax", while the core softening ratio at the time of support installation is equal to 0.01.	90
Fig. 8-6:	Contours of minimum principal stress, σ_3 , of the shaft model under different <i>in situ</i> stress conditions. For each case, the <i>in situ</i> vertical stress, σ_v , is reported together with the stress ratio, K_0 , in brackets. Strength parameters are "OpaMax", while the core softening ratio at the time of support installation is equal to 0.01.	91
Fig. 8-7:	Contours of maximum principal stress, σ_1 , in the support layer of the shaft model under different <i>in situ</i> stress conditions. For each case, the <i>in situ</i> vertical stress, σ_v , is reported together with the stress ratio, K_0 , in brackets. Strength parameters are "OpaMax", while the core softening ratio at the time of support installation is equal to 0.01.	92
Fig. 8-8:	Contours of minimum principal stress, σ_3 , in the support layer of the shaft model under different <i>in situ</i> stress conditions. For each case, the <i>in situ</i> vertical stress, σ_v , is reported together with the stress ratio, K_0 , in brackets. Strength parameters are "OpaMax", while the core softening ratio at the time of support installation is equal to 0.01.	93
Fig. 8-9:	Ground reactions of the shaft model under different <i>in situ</i> stress conditions. For each case, the <i>in situ</i> vertical stress, σ_v , is reported together with the stress ratio, K_0 , in brackets. Strength parameters are "OpaMax x 0.75". The exact location of points P1-P4 is reported in Fig. 5-3.	94
Fig. 8-10:	Evolution of displacement, δ , around the excavation boundary of the shaft model under different <i>in situ</i> stress conditions. For each case, the <i>in situ</i> vertical stress, σ_v , is reported together with the stress ratio, K_0 , in brackets. Strength parameters are "OpaMax x 0.75", while the core softening ratio at the time of support installation is equal to 0.01. The exact location of points P1-P4 is reported in Fig. 5-3.	95
Fig. 8-11:	Contours of displacement, δ , of the shaft model under different <i>in situ</i> stress conditions. For each case, the <i>in situ</i> vertical stress, σ_v , is reported together with the stress ratio, K_0 , in brackets. Strength parameters are "OpaMax x 0.75", while the core softening ratio at the time of support installation is equal to 0.01.	96

Fig. 8-12: Fracture patterns around the excavation of the shaft model under different *in situ* stress conditions. Tensile and shear failure are indicated in blue and orange, respectively. For each case, the *in situ* vertical stress, σ_v , is reported together with the stress ratio, K_0 , in brackets. Strength parameters are "OpaMax x 0.75", while the core softening ratio at the time of support installation is equal to 0.01. 97

Fig. 8-13: Contours of maximum principal stress, σ_1 , of the shaft model under different *in situ* stress conditions. For each case, the *in situ* vertical stress, σ_v , is reported together with the stress ratio, K_0 , in brackets. Strength parameters are "OpaMax x 0.75", while the core softening ratio at the time of support installation is equal to 0.01. 98

Fig. 8-14: Contours of minimum principal stress, σ_3 , of the shaft model under different *in situ* stress conditions. For each case, the *in situ* vertical stress, σ_v , is reported together with the stress ratio, K_0 , in brackets. Strength parameters are "OpaMax x 0.75", while the core softening ratio at the time of support installation is equal to 0.01. 98

Fig. 8-15: Contours of maximum principal stress, σ_1 , in the support layer of the shaft model under different *in situ* stress conditions. For each case, the *in situ* vertical stress, σ_v , is reported together with the stress ratio, K_0 , in brackets. Strength parameters are "OpaMax x 0.75", while the core softening ratio at the time of support installation is equal to 0.01. 99

Fig. 8-16: Contours of minimum principal stress, σ_3 , in the support layer of the shaft model under different *in situ* stress conditions. For each case, the *in situ* vertical stress, σ_v , is reported together with the stress ratio, K_0 , in brackets. Strength parameters are "OpaMax x 0.75", while the core softening ratio at the time of support installation is equal to 0.01. 100

Fig. 8-17: Ground reactions of the shaft model under different *in situ* stress conditions. For each case, the *in situ* vertical stress, σ_v , is reported together with the stress ratio, K_0 , in brackets. Strength parameters are "OpaMax x 0.50". The exact location of points P1-P4 is reported in Fig. 5-3. 101

Fig. 8-18: Evolution of displacement, δ , around the excavation boundary of the shaft model under different *in situ* stress conditions. For each case, the *in situ* vertical stress, σ_v , is reported together with the stress ratio, K_0 , in brackets. Strength parameters are "OpaMax x 0.50", while the core softening ratio at the time of support installation is equal to 0.01. The exact location of points P1-P4 is reported in Fig. 5-3. 102

Fig. 8-19: Contours of displacement, δ , of the shaft model under different *in situ* stress conditions. For each case, the *in situ* vertical stress, σ_v , is reported together with the stress ratio, K_0 , in brackets. Strength parameters are "OpaMax x 0.50", while the core softening ratio at the time of support installation is equal to 0.01. 103

Fig. 8-20: Fracture patterns around the excavation of the shaft model under different *in situ* stress conditions. Tensile and shear failure are indicated in blue and orange, respectively. For each case, the *in situ* vertical stress, σ_v , is reported together with the stress ratio, K_0 , in brackets. Strength parameters are "OpaMax x 0.50", while the core softening ratio at the time of support installation is equal to 0.01. 104

- Fig. 8-21: Contours of maximum principal stress, σ_1 , of the shaft model under different *in situ* stress conditions. For each case, the *in situ* vertical stress, σ_v , is reported together with the stress ratio, K_0 , in brackets. Strength parameters are "OpaMax x 0.50", while the core softening ratio at the time of support installation is equal to 0.01. 105
- Fig. 8-22: Contours of minimum principal stress, σ_3 , of the shaft model under different *in situ* stress conditions. For each case, the *in situ* vertical stress, σ_v , is reported together with the stress ratio, K_0 , in brackets. Strength parameters are "OpaMax x 0.50", while the core softening ratio at the time of support installation is equal to 0.01. 105
- Fig. 8-23: Contours of maximum principal stress, σ_1 , in the support layer of the shaft model under different *in situ* stress conditions. For each case, the *in situ* vertical stress, σ_v , is reported together with the stress ratio, K_0 , in brackets. Strength parameters are "OpaMax x 0.50", while the core softening ratio at the time of support installation is equal to 0.01. 106
- Fig. 8-24: Contours of minimum principal stress, σ_3 , in the support layer of the shaft model under different *in situ* stress conditions. For each case, the *in situ* vertical stress, σ_v , is reported together with the stress ratio, K_0 , in brackets. Strength parameters are "OpaMax x 0.50", while the core softening ratio at the time of support installation is equal to 0.01. 107
- Fig. 9-1: Evolution of total fracture area and displacement, δ , around the excavation boundary of the HAA reconsolidation model under different *in situ* stress conditions and for varying strength parameters. For each case, the *in situ* vertical stress, σ_v , is reported together with the stress ratio, K_0 , and the strength parameters in brackets. The core softening ratio at the time of support installation is equal to 0.008. The exact location of points P1-P4 is reported in Fig. 5-1. 110
- Fig. 9-2: Contours of displacement, δ , of the HAA reconsolidation model under different *in situ* stress conditions and for varying strength parameters. For each case, the *in situ* vertical stress, σ_v , is reported together with the stress ratio, K_0 , and the strength parameters in brackets. The core softening ratio at the time of support installation is equal to 0.008. 111
- Fig. 9-3: Fracture patterns around the excavation of the HAA reconsolidation model under different *in situ* stress conditions and for varying strength parameters. Tensile and shear failure are indicated in blue and orange, respectively. For each case, the *in situ* vertical stress, σ_v , is reported together with the stress ratio, K_0 , and the strength parameters in brackets. The core softening ratio at the time of support installation is equal to 0.008. 112
- Fig. 9-4: Contours of maximum principal stress, σ_1 , of the HAA reconsolidation model under different *in situ* stress conditions and for varying strength parameters. For each case, the *in situ* vertical stress, σ_v , is reported together with the stress ratio, K_0 , and the strength parameters in brackets. The core softening ratio at the time of support installation is equal to 0.008. 113
- Fig. 9-5: Contours of minimum principal stress, σ_3 , of the HAA reconsolidation model under different *in situ* stress conditions and for varying strength parameters. For each case, the *in situ* vertical stress, σ_v , is reported together

with the stress ratio, K_0 , and the strength parameters in brackets. The core softening ratio at the time of support installation is equal to 0.008. 114

Fig. 9-6: Contours of maximum principal stress, σ_1 , in the support layer of the HAA reconsolidation model under different *in situ* stress conditions and for varying strength parameters. For each case, the *in situ* vertical stress, σ_v , is reported together with the stress ratio, K_0 , and the strength parameters in brackets. The core softening ratio at the time of support installation is equal to 0.008. 115

Fig. 9-7: Contours of minimum principal stress, σ_3 , in the support layer of the HAA reconsolidation model under different *in situ* stress conditions and for varying strength parameters. For each case, the *in situ* vertical stress, σ_v , is reported together with the stress ratio, K_0 , and the strength parameters in brackets. The core softening ratio at the time of support installation is equal to 0.008. 116

Fig. 9-8: Evolution of total fracture area and displacement, δ , around the excavation boundary of the HAA reconsolidation model for varying strength parameters. The vertical *in situ* stress is equal to 15.9 MPa with a stress ratio $K_0 = 1.3$, while the core softening ratio at the time of support installation is equal to 0.01. The initial Young's modulus of the support layer is equal to 3.2 GPa. The exact location of points P1-P4 is reported in Fig. 5-1. 117

Fig. 9-9: Contours of displacement, δ , of the HAA reconsolidation model for varying strength parameters. The vertical *in situ* stress is equal to 15.9 MPa with a stress ratio $K_0 = 1.3$, while the core softening ratio at the time of support installation is equal to 0.01. The initial Young's modulus of the support layer is equal to 3.2 GPa. 118

Fig. 9-10: Fracture patterns around the HAA reconsolidation model for varying strength parameters. Tensile and shear failure are indicated in blue and orange, respectively. The vertical *in situ* stress is equal to 15.9 MPa with a stress ratio $K_0 = 1.3$, while the core softening ratio at the time of support installation is equal to 0.01. The initial Young's modulus of the support layer is equal to 3.2 GPa. 118

Fig. 9-11: Contours of maximum principal stress, σ_1 , of the HAA reconsolidation model for varying strength parameters. The vertical *in situ* stress is equal to 15.9 MPa with a stress ratio $K_0 = 1.3$, while the core softening ratio at the time of support installation is equal to 0.01. The initial Young's modulus of the support layer is equal to 3.2 GPa. 119

Fig. 9-12: Contours of minimum principal stress, σ_3 , of the HAA reconsolidation model for varying strength parameters. The vertical *in situ* stress is equal to 15.9 MPa with a stress ratio $K_0 = 1.3$, while the core softening ratio at the time of support installation is equal to 0.01. The initial Young's modulus of the support layer is equal to 3.2 GPa. 119

Fig. 9-13: Contours of maximum principal stress, σ_1 , in the support layer of the HAA reconsolidation model for varying strength parameters. The vertical *in situ* stress is equal to 15.9 MPa with a stress ratio $K_0 = 1.3$, while the core softening ratio at the time of support installation is equal to 0.01. The initial Young's modulus of the support layer is equal to 3.2 GPa. 120

- Fig. 9-14: Contours of minimum principal stress, σ_3 , in the support layer the HAA reconsolidation model for varying strength parameters. The vertical *in situ* stress is equal to 15.9 MPa with a stress ratio $K_0 = 1.3$, while the core softening ratio at the time of support installation is equal to 0.01. The initial Young's modulus of the support layer is equal to 3.2 GPa. 120
- Fig. 9-15: Evolution of total fracture area and displacement, δ , around the excavation boundary of the shaft reconsolidation model under different *in situ* stress conditions and for varying strength parameters. For each case, the *in situ* vertical stress, σ_v , is reported together with the stress ratio, K_0 , and the strength parameters in brackets. The core softening ratio at the time of support installation is equal to 0.01. The exact location of points P1-P4 is reported in Fig.5-3. 121
- Fig. 9-16: Contours of displacement, δ , around the excavation boundary of the shaft reconsolidation model under different *in situ* stress conditions and for varying strength parameters. For each case, the *in situ* vertical stress, σ_v , is reported together with the stress ratio, K_0 , and the strength parameters in brackets. The core softening ratio at the time of support installation is equal to 0.01. 122
- Fig. 9-17: Fracture patterns around the excavation of the shaft reconsolidation model under different *in situ* stress conditions and for varying strength parameters. Tensile and shear failure are indicated in blue and orange, respectively. For each case, the *in situ* vertical stress, σ_v , is reported together with the stress ratio, K_0 , and the strength parameters in brackets. The core softening ratio at the time of support installation is equal to 0.01. 123
- Fig. 9-18: Contours of maximum principal stress, σ_1 , of the shaft reconsolidation model under different *in situ* stress conditions and for varying strength parameters. For each case, the *in situ* vertical stress, σ_v , is reported together with the stress ratio, K_0 , and the strength parameters in brackets. The core softening ratio at the time of support installation is equal to 0.01. 124
- Fig. 9-19: Contours of minimum principal stress, σ_3 , of the shaft reconsolidation model under different *in situ* stress conditions and for varying strength parameters. For each case, the *in situ* vertical stress, σ_v , is reported together with the stress ratio, K_0 , and the strength parameters in brackets. The core softening ratio at the time of support installation is equal to 0.01. 125
- Fig. 9-20: Contours of maximum principal stress, σ_1 , in the support layer of the shaft reconsolidation model under different *in situ* stress conditions and for varying strength parameters. For each case, the *in situ* vertical stress, σ_v , is reported together with the stress ratio, K_0 , and the strength parameters in brackets. The core softening ratio at the time of support installation is equal to 0.01. 126
- Fig. 9-21: Contours of minimum principal stress, σ_3 , in the support layer of the shaft reconsolidation model under different *in situ* stress conditions and for varying strength parameters. For each case, the *in situ* vertical stress, σ_v , is reported together with the stress ratio, K_0 , and the strength parameters in brackets. The core softening ratio at the time of support installation is equal to 0.01. 127

1 Introduction

1.1 Background and motivation

The selection of sites for repositories for the disposal of radioactive waste in Switzerland is defined in the Sectoral Plan for Deep Geological Repositories ("SGT", SFOE 2008). The Swiss disposal concept foresees separate repositories for low- and intermediate-level waste (L/ILW) and for high-level waste (HLW) – or, as a possibility, both of them together in a so-called combined repository. In stage 1 of the Sectoral Plan several potential geological siting areas for the disposal of L/ILW and several potential geological siting areas for the disposal of HLW were selected. It is the objective of Stage 2 to select at least two sites for each repository type, followed by the selection of a single site for each repository type and the preparation of the application for the general licence in Stage 3. As a decision basis for the second stage of the site-selection process, so-called provisional safety analyses are to be elaborated. Together with further documents on the geological basis and studies on construction feasibility, the provisional safety analyses provide input for the qualitative and quantitative comparison of long-term safety of the proposed repository configurations in the candidate siting regions.

As part of the provisional safety analyses, the influence of repository-induced effects specifically on the host rock properties is evaluated. The key repository-induced effects addressed by Nagra in SGT stage 2 are the pH-plume associated with the cementitious backfill of the L/ILW caverns, the accumulation and release of repository gases, the heat emission of the HLW canisters and the excavation damaged zone (EDZ) around the backfilled underground structures. The present study provides a part of the input for the evaluation of the repository-induced effects in that it evaluates the creation of the EDZ during repository construction and its temporal evolution after backfilling of the underground structures for the considered geological boundary conditions and repository configurations. For this, a hybrid finite/discrete element method (FEMDEM) is used to simulate the discrete fracture network which develops in response to the excavation process in the rock mass around the underground structures of a radioactive waste repository. The fracture network simulations presented in this report will feed in a hydraulic model, aimed at providing abstracted representations of the EDZ as input for safety analyses (Alcolea et al. 2014).

1.2 Scope and objectives

This study is composed as a sensitivity analysis, aimed at assessing the spectrum of expectations with regard to the creation and evolution of the EDZ around SF/HLW tunnels, L/ILW caverns and seal sections of a geological repository. Fracture mechanics simulations are conducted in 2-D cross sections for representative repository configurations in the candidate siting regions, drawing on the geomechanical characteristics of the Opalinus Clay as a possible host rock formation. The scope of the study comprises:

- A review of the relevant geomechanical characteristics of the Opalinus Clay. Consistency of the FEMDEM formulations of the constitutive laws and the conventional continuum formulations is perused. Experience on failure mechanisms and constitutive laws from previous calibration exercises on Opalinus Clay (Mont Terri TN 2012-06) is considered in the data review. Laboratory tests on Opalinus Clay are used to model the deformation behavior of the rock in response to compressive and tensile stresses.
- Simulation of discrete fracture network patterns in the host rock around the excavations. The fractures are characterized by fracture mode, orientation, length and width. The sensitivity of the shape and extent of the fracture network is analysed with regard to the

following aspects: (i) parameter variations concerning the geomechanical properties of the Opalinus Clay (including the impact of pre-existing tectonic features); (ii) variations of the geomechanical boundary conditions in the host rock (outer boundaries); (iii) parameter variants with regard to tunnel lining (inner boundary).

- Derivation of principal stress components and displacements in the host rock around the excavations for all fracture network simulations. Extraction of ground reaction curves from the calculated displacements.
- Simulation of the EDZ re-compaction process after repository closure. For selected system components (SF/HLW emplacement tunnels, seal sections) the partial closure of the EDZ fracture network is simulated by applying a radial stress on the liner. This prescribed stress boundary condition mimics the swelling pressure of bentonite, which acts on the tunnel walls after re-saturation of the SF/HLW emplacement tunnels and the seal sections respectively.

The fracture mechanics simulations are performed for 2-D cross-sections, representing the following components of the repository system: (i) an SF/HLW emplacement tunnel (circular shape), (ii) a L/ILW emplacement cavern K9 (horse-shoe), (iii) a repository seal section (circular shape) and (iv) a shaft seal section. The sensitivity studies on the impact of the in situ stress conditions are formulated in terms of vertical stress and stress ratio. The key deliverable of this study is a catalogue of EDZ fracture patterns for a wide range of repository settings, feeding in the abstracted representations of hydraulic conductance of the EDZ as input for safety analyses (Alcolea et al. 2014).

1.3 Report organisation

Chapter 1 presents the background and motivation for the present study. The objectives are specified and the report organization is discussed.

Fundamentals of FEMDEM modeling are summarized in chapter 2. This includes a brief synopsis of the software developments and basic formulations of the implemented deformation behavior.

Chapters 3 and 4 are dedicated to the analysis of laboratory data (uniaxial compression tests, Brazilian tests) needed for the calibration of a suitable constitutive law for the Opalinus Clay.

Chapter 5 describes the methodology and the basic work flow applied for the simulation of the EDZ fracture networks.

Chapters 6 to 8 display the simulation results obtained for the investigated repository components, namely the SF/HLW tunnel, the L/ILW cavern, and the shaft section. Results of the base case simulations and parameter variants are presented.

The results of re-compaction of the SF/HLW tunnel near-field and of the repository seal section are presented in chapter 9.

Chapter 10 provides discussion on the modeling results presented in Chapters 6 to 9.

Chapter 11 summarizes the achievements and provides the main conclusions of the study.

Appendix 1 provides a list of directories containing the files of all simulation cases provided in the digital appendix.

2 Modelling software: FEMDEM

The hybrid finite/discrete element method (FEM/DEM) is a numerical method which combines continuum mechanics principles with DEM algorithms to simulate multiple interacting deformable bodies (Munjiza et al., 1995; Munjiza, 2004). In FEM/DEM, each solid is discretized as a mesh consisting of nodes and triangular elements. An explicit time integration scheme is applied to solve the equations of motion for the discretized system and to update the nodal coordinates at each simulation time step. In general, the governing equations can be expressed as (Munjiza et al. 1995):

$$\mathbf{M}\ddot{\mathbf{x}} + \mathbf{C}\dot{\mathbf{x}} + \mathbf{F}_{\text{int}} - \mathbf{F}_{\text{ext}} - \mathbf{F}_c = 0 \quad (1)$$

Where \mathbf{M} and \mathbf{C} are the system mass and damping diagonal matrices, respectively; \mathbf{x} is the vector of nodal displacements; \mathbf{F}_{int} , \mathbf{F}_{ext} , and \mathbf{F}_c are the vectors of internal resisting forces, of applied external loads and of contact forces, respectively. Contact forces, \mathbf{F}_c , are calculated either between contacting discrete bodies or along internal discontinuities (i.e., pre-existing or newly created fractures) (Section 0). Internal resisting forces, \mathbf{F}_{int} , include the contribution from the elastic forces, \mathbf{F}_e , and the crack element bonding forces, \mathbf{F}_b , which are used to simulate material elastic deformation and progressive failure, respectively, as further explained in sections 2.2 and 2.3.

Numerical damping is introduced in the governing equation to account for energy dissipation due to non-linear material behaviour or to model quasi-static phenomena by dynamic relaxation (Munjiza 2004). The matrix \mathbf{C} is equal to:

$$\mathbf{C} = \mu \mathbf{I}$$

where μ is a constant damping coefficient and \mathbf{I} is the identity matrix.

2.1 Contact detection and interaction

A FEM/DEM simulation can comprise a very large number of potentially interacting distinct elements. To correctly capture this behaviour, contacting couples (i.e., pairs of contacting discrete elements) must first be detected. Subsequently, the interaction forces, \mathbf{F}_c , resulting from such contacts can be defined. Contact interaction forces are calculated between all pairs of elements that overlap in space. Two types of forces are applied to the elements of each contacting pair: repulsive forces and frictional forces. The repulsive forces between the elements of each contacting pair (i.e., couples) are calculated using a penalty function method (Munjiza and Andrews 2000). Contacting couples tend to penetrate into each other, generating distributed contact forces, which depend on the shape and size of the overlap between the two bodies and the value of the penalty term, p_n . As penalty values tend to infinity, a body impenetrability condition is approached. The frictional forces between contacting couples are calculated using a Coulomb-type friction law. These frictional forces are used to simulate the shear strength of intact material and of pre-existing and newly created fractures (Mahabadi et al. 2012a).

2.2 Elastic behaviour and anisotropy of stiffness

Since the material strain is expected to be localized in the crack elements (see Section 2.3), the bulk material is treated as linear-elastic using constant-strain triangular elements. To capture the stiffness anisotropy of the Opalinus Clay, a stress-strain constitutive law for a linearly elastic, transversely isotropic medium is typically adopted. With this model, the elastic deformation is fully characterized by five independent elastic constants (Jaeger and Cook 1976) (Fig. 2-1):

- E and E' are the Young's moduli in the direction parallel and perpendicular to the plane of transverse isotropy, respectively;
- ν and ν' are the Poisson's ratios that characterize the transverse strain in the plane of isotropy due to a stress applied in the direction parallel and perpendicular to it, respectively;
- G' is the shear modulus for planes normal to the plane of transverse isotropy.

In general, the elastic response of a FEM/DEM model depends not only on the constitutive relationship of the triangular elements but also on the properties of the crack elements. Since the elastic deformation before the onset of fracturing takes place in the bulk material, no deformation should in theory occur in the crack elements before the intrinsic strength is exceeded. However, a finite stiffness is required for the crack elements by the time-explicit formulation of FEM/DEM. Such an artificial compliance is represented by the normal, tangential and fracture penalty values, p_n , p_t , and p_f , for compressive, shear and tensile loading conditions, respectively. For practical purposes, the contribution of crack elements to the overall model compliance can be largely limited by adopting very high (i.e., dummy) penalty values (Mahabadi et al. 2012; Munjiza 2004). Consequently, no anisotropy in deformation is introduced in the penalty formulation at the crack element level and the elastic response is effectively controlled by the choice of the stress-strain relationship of the continuum triangular elements.

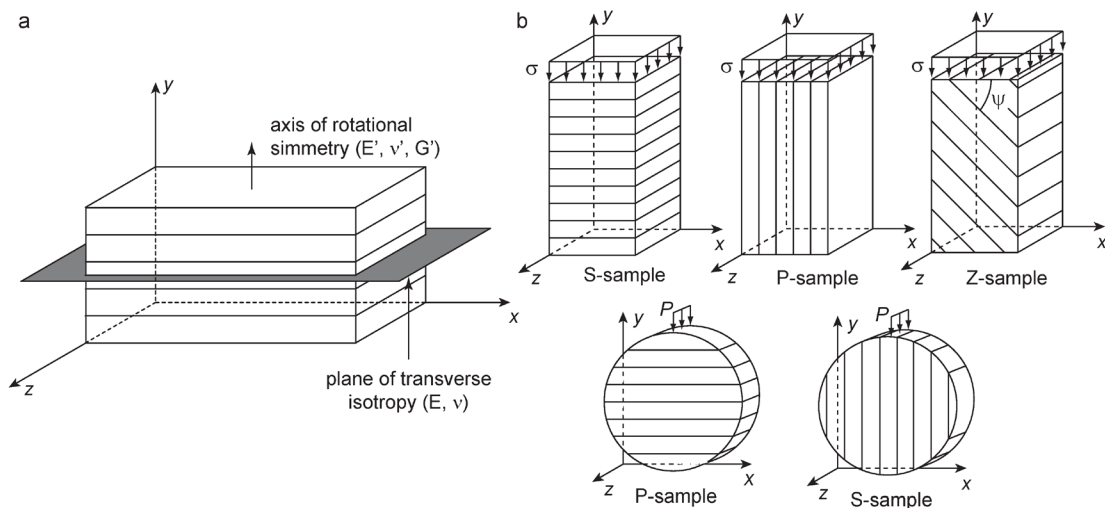


Fig. 2-1: Transversely isotropic material. (a) Associated elastic constants. (b) Adopted naming convention for standard rock mechanics tests (i.e., compression and Brazilian tests) on transversely isotropic rocks. Source: Lisjak et al. (2013).

2.3 Material failure and anisotropy of strength

The progressive failure of rock material is modelled using a cohesive-zone approach, a technique first introduced in the context of the elasto-plastic fracturing of ductile metals (Barenblatt 1962; Dugdale 1960). This approach aims at capturing the non-linear interdependence between stresses and strain that characterizes the zone ahead of a macro-crack tip known as the Fracture Process Zone (FPZ). As depicted in Figure 2-2, the FPZ in brittle rocks manifests itself in the form of micro-cracking and interlocking related to the presence of micro-scale inhomogeneities (e.g., mineral grains and pre-existing defects or voids) (Labuz et al. 1987). When using cohesive-zone models, the failure of the material progresses based solely on the strength degradation of dedicated interface elements (referred herein to as crack elements) and therefore emerges as a natural outcome of the deformation process without employing any additional macroscopic failure criterion.

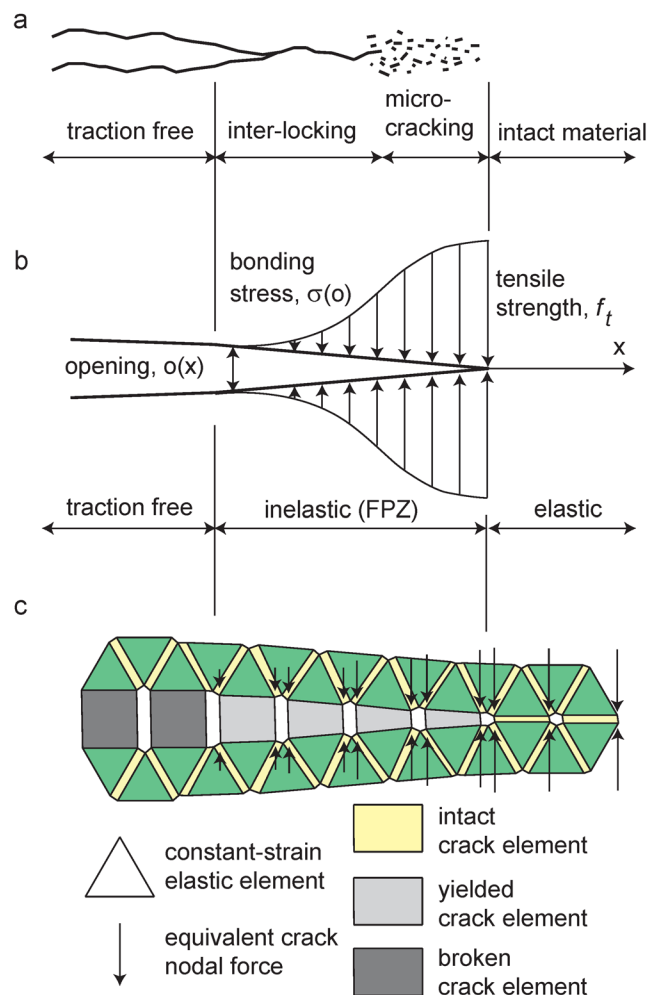


Fig. 2-2: Cohesive-zone approach for material failure modelling in FEM/DEM. (a) Conceptual model of a tensile crack in a heterogeneous rock material (after Labuz et al. (1987), modified). (b) Theoretical FPZ model of Hillerborg (Hillerborg et al. 1976). (c) FEM/DEM implementation of the FPZ using triangular elastic elements and four-noded crack elements to represent the bulk material and the fracture, respectively. Triangular elements are shrunk for illustration purposes.

In the Y-Geo FEM/DEM code, the bonding stresses transferred by the material are decreasing functions of the displacement discontinuity across the crack elements according to the cohesive laws illustrated in Figure 2-3b. These constitutive relationships represent a modified version of the crack model response proposed by Munjiza et al. (1999). Mode I (i.e., opening) fracturing is simulated by a cohesive model based on the FPZ model originally developed for concrete by Hillerborg under the name of fictitious crack model (Hillerborg et al. 1976). A fracture is assumed to initiate when the crack tip opening, o , reaches a critical value, o_p , related to the intrinsic tensile strength of the material, f_t . When the crack opens, the normal bonding stress, σ , is not assumed to fall to zero at once but to decrease with increasing crack opening until a residual opening value, o_r , is reached and a stress-free surface is created (i.e., $\sigma = 0$). Mode II (i.e., shear) fracturing is simulated by a slip-weakening model conceptually similar to that of Ida (1972). For shear loading conditions, a tangential bonding stress, τ , exists between the two fracture walls, which is a function of the amount of slip, s , and the normal stress on the fracture, σ_n . The critical slip, s_p , corresponds to the intrinsic shear strength of the rock, f_s , defined as:

$$f_s = c + \sigma_n \tan \varphi_i$$

where c is the internal cohesion, φ_i is the material internal friction angle, and σ_n is the normal stress acting across the crack element. Upon undergoing the critical slip, s_p , the tangential bonding stress is gradually reduced to a residual value, f_r , which corresponds to a purely frictional resistance:

$$f_s = \sigma_n \tan \varphi_f$$

where φ_f is the fracture friction angle and σ_n is the normal stress acting across the fracture surfaces. In the current crack element implementation, the unloading path in the softening branch coincides with the loading path. Therefore, the model is strictly only valid for monotonic loading conditions.

For mixed mode fracturing, the rupture of a crack element is defined by the following coupling criterion between crack opening and slip (Figure 2-3c):

$$\left(\frac{o - o_p}{o_r - o_p} \right)^2 - \left(\frac{s - s_p}{s_r - s_p} \right)^2 \geq 1$$

The mode of fracture, m , associated to a broken crack element can be approximated as:

$$m = 1 + \frac{s - s_p}{s_r - s_p}$$

The external energy required to fully break a unit surface area of cohesive crack corresponds to the input specific fracture energy, G_c . G_c is defined in terms of the material properties G_{Ic} and G_{IIc} which correspond to the strain energy release rates for mode I and mode II fracturing, respectively. The crack residual displacement values, o_r and s_r , are such that (Munjiza 2004):

$$G_{Ic} = \int_{o_p}^{o_r} \sigma(o) do$$

$$G_{IIc} = \int_{s_p}^{s_r} (\tau(s) - f_r) ds$$

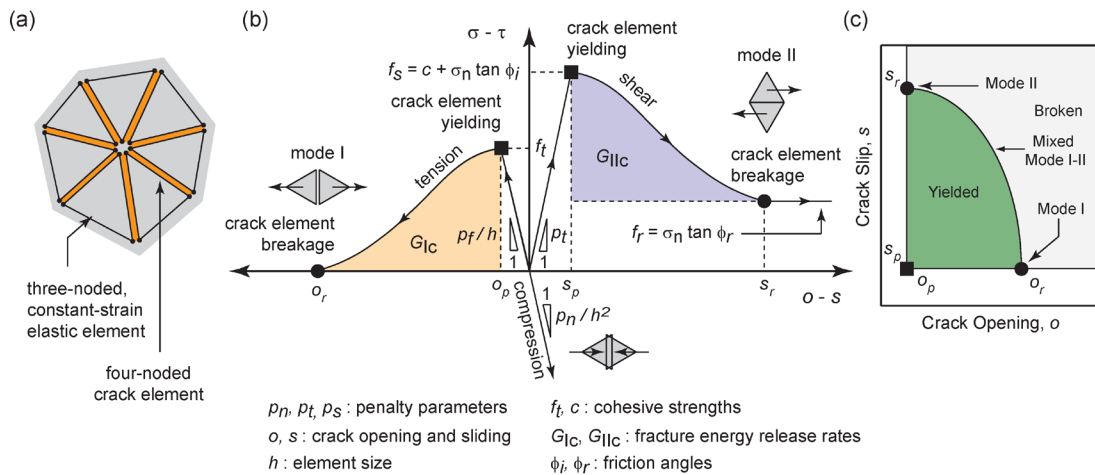


Fig. 2-3: Simulation of fracturing with the Y-Geo FEM/DEM code. (a) Representation of a continuum using cohesive crack elements interspersed throughout a mesh of triangular elastic elements. Triangles are shrunk for illustration purposes. (b) Constitutive behaviour of the crack elements defined in terms of normal and tangential bonding stress, σ and τ , vs. crack relative displacement, o and s (i.e., opening and sliding). (c) Elliptical coupling relationship between crack opening, o , and sliding, s , for mixed-mode fracturing.

Following an approach similar to that pioneered by Xu and Needleman (1994), the crack elements in FEM/DEM are interspersed throughout the material (i.e., across the edges of all triangular element pairs) from the very beginning of the simulation. Thus, cracks are allowed to nucleate and grow without any additional assumption or criterion other than the crack element constitutive response. Upon breakage of the cohesive surface, the crack element is removed from the simulation and therefore the model transition from a continuum to discontinuum is locally completed. The newly created discontinuity is treated by the contact algorithm through the contact forces, \mathbf{F}_c , briefly described in the previous section. As the simulation progresses, finite displacements and rotations of discrete bodies are allowed and new contacts are automatically recognized.

In this study, the simulation of strength anisotropy followed the approach first developed by Lisjak et al. (2013) to model the mechanical response of Opalinus Clay and implemented in the two-dimensional Y-Geo code (Mahabadi et al. 2012a). Specifically, anisotropy of strength is introduced at the crack element level by imposing that the cohesive strength of each crack element is a function of the relative orientation, γ , between the crack element itself and the bedding orientation (Figure 2-4a). The cohesive strength parameters and the fracture energy release rates are assumed to vary linearly between a minimum value for $\gamma = 0^\circ$ (i.e., $f_{t,\min}$, c_{\min} , $G_{Ic,\min}$, $G_{IIc,\min}$) to a maximum value for $\gamma = 90^\circ$ (i.e., $f_{t,\max}$, c_{\max} , $G_{Ic,\max}$, $G_{IIc,\max}$). Note that different power laws with varying exponent values were also preliminary tested; the best fit to the experimental data for Opalinus Clay was however obtained for an exponent value of 1 (i.e., linear relationship). Furthermore, the mesh topology combines a random triangulation for the intra-layer material (i.e., matrix) together with crack elements preferably aligned along the bedding planes (Figure 2-4b).

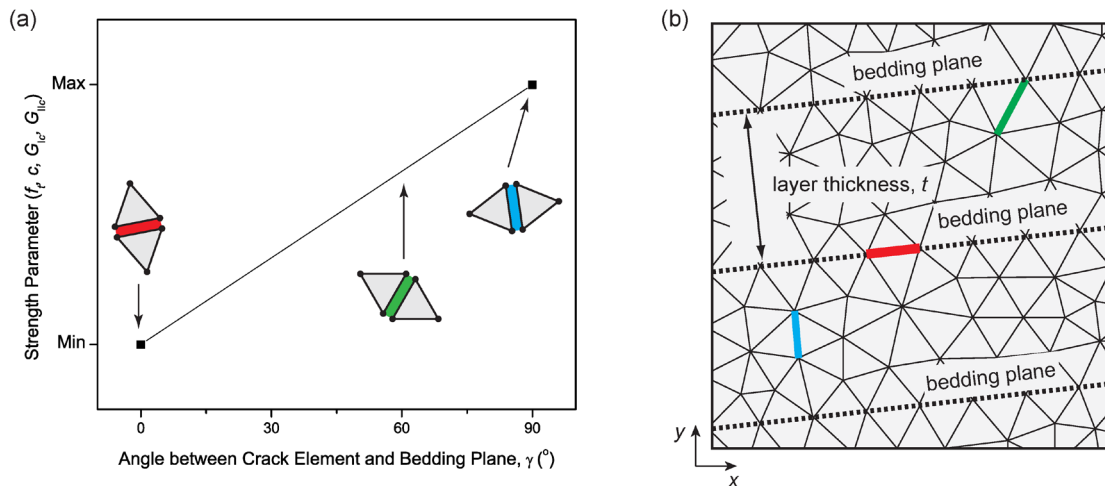


Fig. 2-4: FEM/DEM modelling of strength anisotropy. (a) Linear variation of cohesive strength parameters with the angle, γ , between crack element and bedding. (b) Example of mesh combining a Delaunay triangulation for the intra-layer material with edges preferentially aligned along the bedding plane direction.

2.4 Mesh sensitivity

Owing to the assumptions inherent to the cohesive crack model, the fracturing response of a FEM/DEM model displays two types of mesh sensitivity:

1. sensitivity to the size of the spatial discretization (i.e., element size)
2. sensitivity to the mesh topology (i.e., element orientation)

On the contrary, the emergent elastic properties are independent of the adopted element size and mesh topology, as the model deformability is governed by the continuum formulation of triangular elements.

In general, the element size controls the model spatial resolution, but also the strength of the model and, for the case of bedded materials, the minimum layer thickness, t , that can be employed. The sensitivity of the cohesive element approach to the mesh orientation results from restricting crack growth along the edges of the triangular elements. Although this approach aims at simulating fracturing without any *a priori* assumption regarding the fracture trajectory, a certain mesh bias is induced by the fact that the direction of crack propagation is not entirely free but restricted to a limited number of predefined angles.

Lisjak et al. (2013) investigated the behaviour of unconfined compression test simulations on Opalinus Clay for varying element size and layering thickness. The peak strength appeared to tend to a constant value for decreasing values of h and, in general, to exhibit low element size sensitivity. Similarly, the values of UCS and associated anisotropy ratios appeared to tend to constant values as the number of layers increases. Furthermore, it was noted that to minimize the constraint imposed by the mesh topology on the model behaviour, randomly discretized meshes should be used in place of regularly discretized ones.

In this study, the sensitivity of the model to the adopted numerical discretization was not investigated. Instead, the smallest element size that could be used while keeping the computational demand and, consequently, the total run time within practical limits (i.e., approximately 2 weeks) was used.

3 Modelling methodology: laboratory-scale simulations

3.1 Geometry and boundary conditions

The two-dimensional laboratory-scale models included a 38 mm × 76 mm rectangular specimens for the compression test and 38 mm diameter circular specimens for the Brazilian test. All the specimen cross sections were assumed parallel to the xy plane (Figure 1b) and, therefore, oriented perpendicular to the strike of the bedding planes. Layering orientation within a particular FEM/DEM model was then set by specifying the bedding dip, ψ . The specimens were meshed with a uniform, unstructured grid having $h = 0.6$ mm average element size and embedded layers with thickness $t = 2$ mm (Figure 2-4b). The equation of motion for the discretized system (eq. (1)) was integrated with a time step of 6×10^{-6} ms; this value was the largest time step size that ensured numerical stability for the explicit time integration scheme of the code. Uniaxial loading conditions were obtained by means of two rigid platens moving in opposite directions with a constant velocity $v = 0.1$ m/s. Although this loading rate is significantly greater than that typically used in actual experiments, loading rate sensitivity analyses typically indicate that the simulated strengths tend to approach constant values for loading rates smaller than approximately 0.25 m/s (Lisjak et al. 2013). In the Brazilian test, a finite-sized contact area between the flat platen and the disc was obtained by locally flattening the disc surface at the contact point (Figure 3-1). The FEM/DEM Graphical User Interface Y-GUI (Mahabadi et al. 2010) was used to assign boundary conditions and material properties to the model.

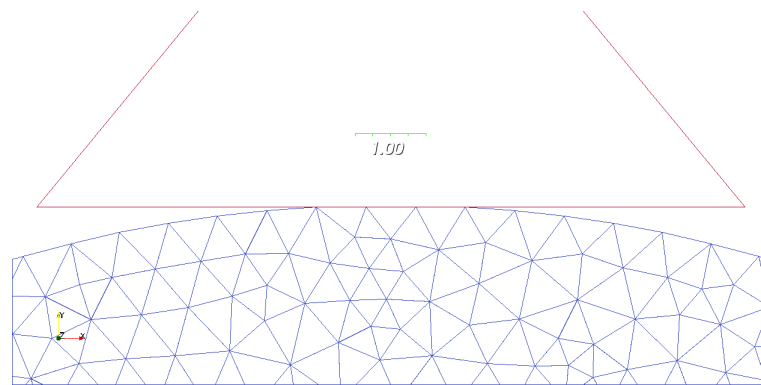


Fig. 3-1: Zoomed-in view of the flat contact zone between the triangular loading platen and the Brazilian disc specimen.

3.2 Model calibration and input parameters

Similarly to other modelling approaches based on DEM (Potyondy and Cundall 2004), the micromechanical input parameters of the FEM/DEM simulations were calibrated by comparing the emergent properties of the model to the relevant response of the tested rock. To this end, an iterative, trial-and-error calibration procedure was adopted. The indirect tensile strength, T , and the uniaxial compressive strength, UCS , were chosen to characterize the short-term, undrained mechanical response of Opalinus Clay and used as calibration targets. Since both macroscopic properties exhibit a strong dependence upon the orientation of bedding, P- and S- values were considered. The UCS value for bedding inclined at 45° (Z-sample) was also considered. The finalized model parameters are reported in Table 1. The values of the strength parameters were obtained as final result of the calibration process, while the provided experimental values of the

elastic constants were directly used as input for the transversely isotropic elastic model. A friction coefficient, k , equal to 0.1 was assumed at the platen-sample interfaces. The effect of the crack element compliance on the overall model stiffness (Sections 2.2 and 2.3) was minimized by selecting appropriate values for the penalty coefficients. Based on the recommendations of Mahabadi (2012), normal penalty, p_n , tangential penalty, p_t , and fracture penalty, p_f , were set equal to 10x, 1x and 5x the largest Young's modulus, E , respectively.

Table 2 compares the emergent properties of the model with the experimental values for Opalinus Clay used as calibration targets. The numerical results are discussed in the following sections.

Tab. 1: Input parameters of the FEM/DEM model calibrated based on laboratory-scale rock mechanics tests on Opalinus Clay (Nagra 2002).

Parameter	Value
Continuum triangular elements	
Bulk density, ρ ($\text{kg}\cdot\text{m}^{-3}$)	2430
Young's modulus parallel to bedding, E (GPa)	11.4
Young's modulus perpendicular to bedding, E' (GPa)	5.5
Poisson's ratio parallel to bedding, ν (-)	0.27
Poisson's ratio perpendicular to bedding, ν' (-)	0.27
Shear modulus, G (GPa)	3.16
Viscous damping coefficient, μ ($\text{kg}\cdot(\text{ms})^{-1}$)	7.4×10^6
Crack elements	
Cohesive strengths	
Tensile strength parallel to bedding, $f_{t,\text{max}}$ (MPa)	2
Tensile strength perpendicular to bedding, $f_{t,\text{min}}$ (MPa)	0.32
Cohesion parallel to bedding, c_{min} (MPa)	0.95
Cohesion perpendicular to bedding, c_{max} (MPa)	17.2
Fracture energy release rates	
Mode I fracture energy parallel to bedding, $G_{\text{Ic,max}}$ (Jm^{-2})	14
Mode I fracture energy perpendicular to bedding, $G_{\text{Ic,min}}$ (Jm^{-2})	5
Mode II fracture energy parallel to bedding, $G_{\text{IIc,min}}$ (Jm^{-2})	40
Mode II fracture energy perpendicular to bedding, $G_{\text{IIc,max}}$ (Jm^{-2})	140
Friction angles	
Friction angle of intact material, ϕ_i ($^\circ$)	24
Friction angle of fractures, ϕ_f ($^\circ$)	24
Cohesive stiffnesses	
Normal contact penalty, p_n (GPa·m)	114
Tangential contact penalty, p_t (GPa/m)	11.4
Fracture penalty, p_f (GPa)	57

4 Results: laboratory-scale simulations

4.1 Brazilian disc test

Fig. 4-1 shows the tensile stress as function of the platen vertical displacement calculated according to the following formula (Bieniawski and Hawkes, 1978):

$$\sigma_t = 2P/\pi Dt$$

where P is the applied load, computed as sum of the nodal reaction forces of the top platen; D is the diameter of the sample (38 mm); and t is the sample thickness (a unit thickness is assumed in 2D). The response of both samples was elastic-brittle with loss of strength after reaching the peak strength values. Peak values of 2.65 MPa and 1.26 MPa were obtained for the P- and S-sample, respectively. These values are considered a good match to the respective experimental values of 2.5 and 1.2 MPa. The fracture pattern evolution of the calibrated Brazilian disc tests are illustrated in Figure 4-2. The simulated failure mechanism is characterized by brittle tensile splitting along the vertical loading path for both samples and, thus, in agreement with typical experimental observations for Opalinus Clay (Fig. 4-3).

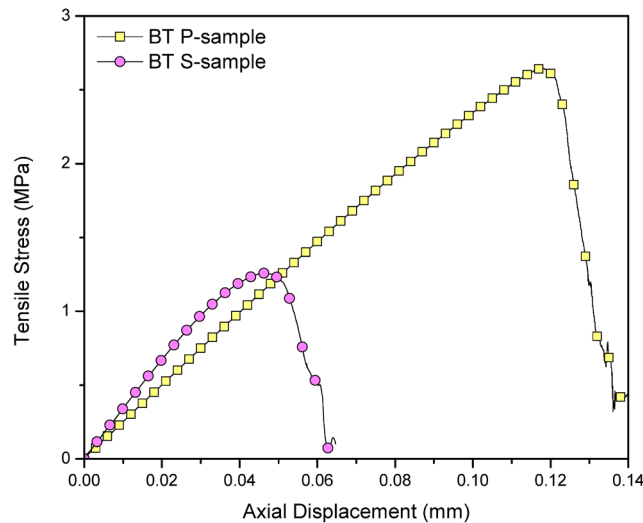


Fig. 4-1: Curves of tensile stress versus platen vertical displacement for the Brazilian disc simulation. (b) Axial stress vs. axial strain for the UCS simulation (Jahns 2010).

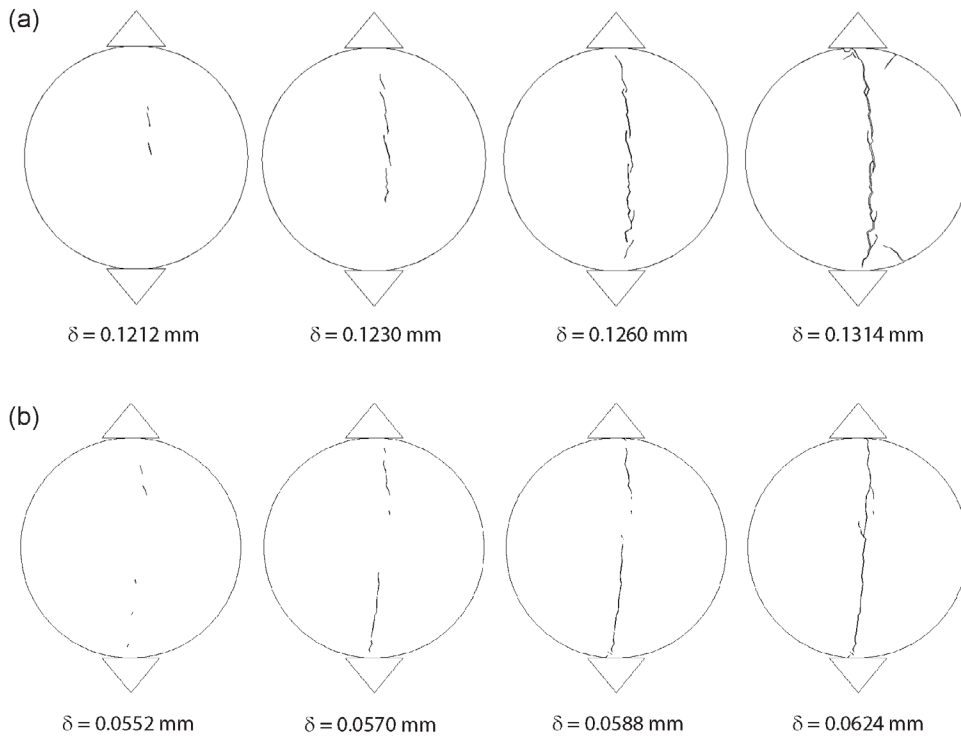


Fig. 4-2: Evolution of fracture pattern of the calibrated laboratory-scale Brazilian disc models at increasing axial displacement values. (a) P sample. (b) S sample.

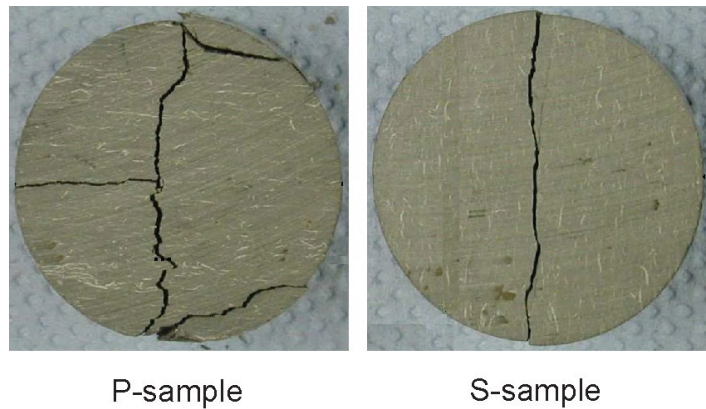


Fig. 4-3: Typical fracture patterns observed during Brazilian tests (disc diameter = 30 mm, after Jahns (2010)) on Opalinus Clay.

4.2 Uniaxial compression test

The simulated curves of applied axial stress versus sample axial strain are displayed in Fig. 4-4 for the UCS P-, S-, and Z- sample. The observed modulus anisotropy is a direct consequence of the adopted transversely isotropic constitutive relationship. The simulated unconfined compressive strength values are equal to 21.5, 8.9 and 34.2 MPa for the P-, Z-, and S-sample, respectively. These values satisfactorily match the respective experimental values of 28.0, 6.1, and 30.3 MPa, used as calibration targets. The brittle post-peak behaviour is characterized by the failure of crack elements with consequent macroscopic fractures propagating throughout the

model, as illustrated in Fig. 4-5. In agreement with typical experimental observations in Opalinus Clay samples (Fig. 4-5), the modelling results highlight a distinct variation of bedding influence on the macroscopic failure response of the sample as a function of the anisotropy direction. For steeply dipping layering (P-sample), the failure of the specimen is induced by the extension of the bedding planes with major cracks developing subparallel to the loading direction and consisting of a combination of tensile split along layers and steeply inclined shear fractures. For mid-dip values (Z-sample), the sample fails due to bedding plane delamination. For loading orientations perpendicular to the bedding orientation (S-sample), the sample rupture occurs as shearing through the rock matrix.

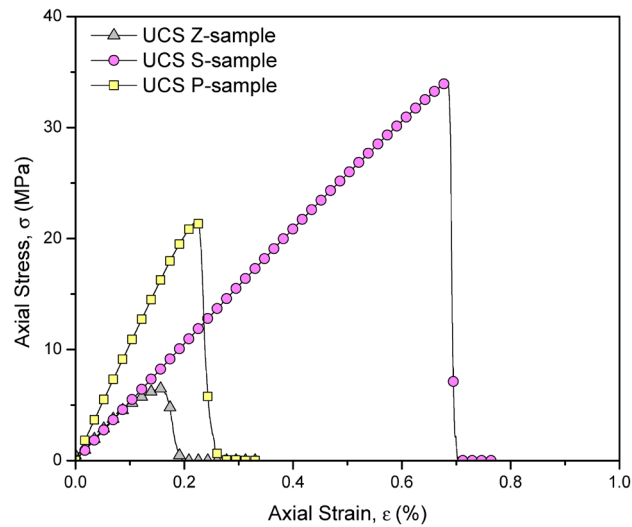


Fig. 4-4: Curves of axial stress versus axial strain for the UCS simulation.

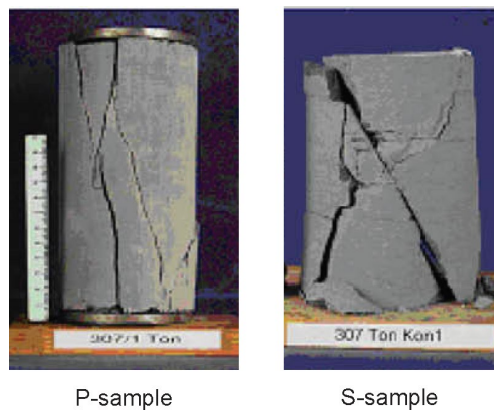


Fig. 4-5: Typical fracture patterns observed during UCS tests (sample height = 120 mm, sample diameter = 60 mm, after Popp et al. (2008)) on Opalinus Clay.

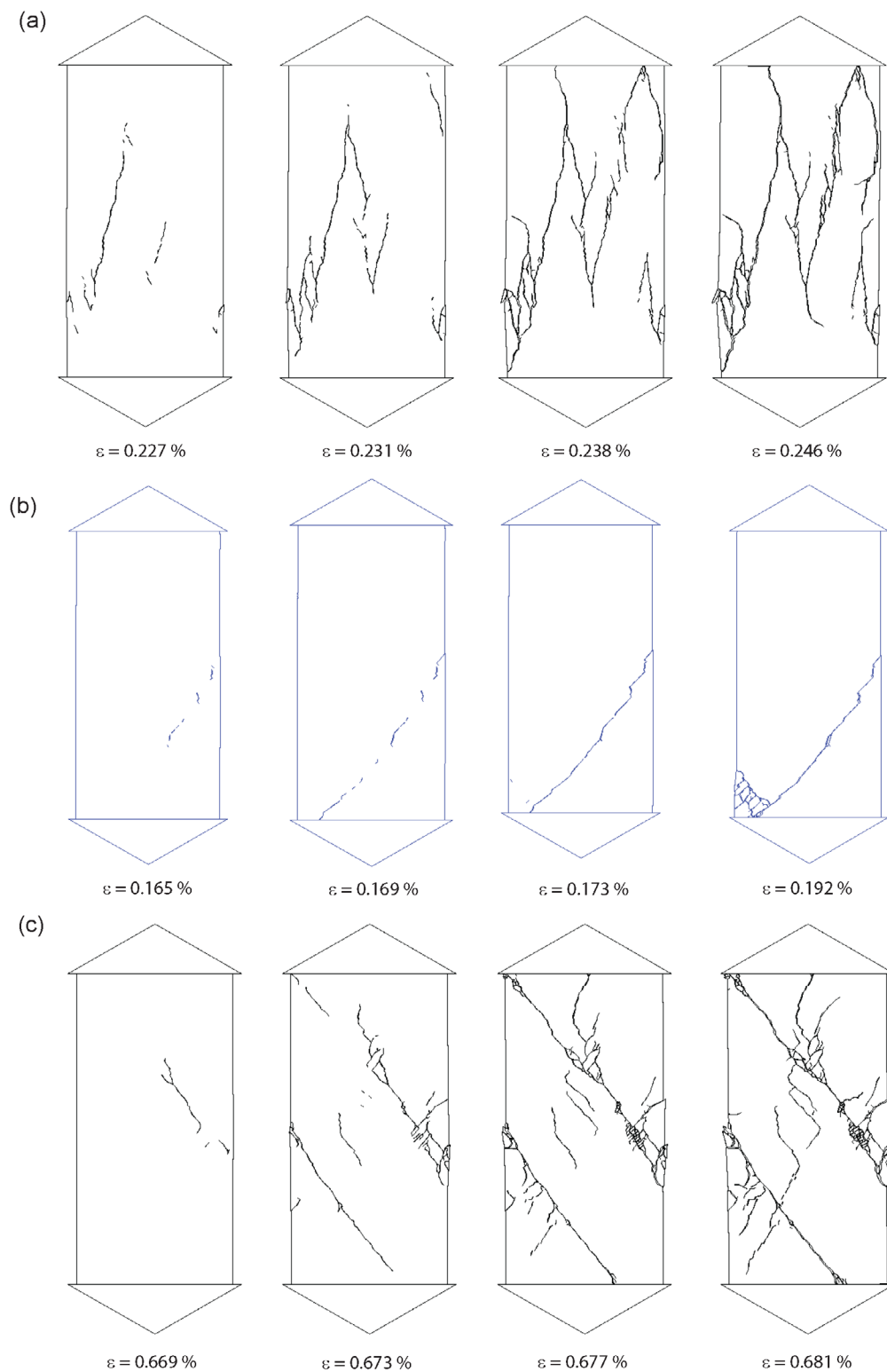


Fig. 4-6: Evolution of fracture patterns of the calibrated laboratory-scale uniaxial compression models at increasing axial strain values. (a) P sample. (b) Z-45° sample. (c) S sample.

Tab. 2: Comparison between the mechanical properties of the Opalinus Clay and the emergent macroscopic properties of the FEM/DEM model.

Property	Experimental Value	FEM/DEM
Elastic modulus parallel to bedding, E_p (GPa)	11.4	10.4
Elastic modulus perpendicular to bedding, E_s (GPa)	5.5	5.1
Poisson's ratio parallel to bedding, ν_p (-)	0.27	0.34
Poisson's ratio perpendicular to bedding, ν_s (-)	0.27	0.30
Uniaxial compressive strength parallel to bedding, UCS_p (MPa)	28	21.5
Uniaxial compressive strength perpendicular to bedding, UCS_s (MPa)	30.3	34.2
Uniaxial compressive strength at 45° to bedding, UCS_z (MPa)	6.1	8.89
Indirect tensile strength parallel to bedding, T_p (MPa)	2.5	2.65
Indirect tensile strength perpendicular to bedding, T_s (MPa)	1.2	1.26

5 Modelling methodology: EDZ simulations

5.1 Geometries, mesh generation and input parameters

Three main model geometries were considered for the EDZ simulations: (i) a 3.0 m diameter circular opening for the SF-HLW emplacement tunnel ("HAA model", Figure 5-1), (ii) a 11.4 m x 13.6 m horseshoe-shaped opening for the L-ILW emplacement cavern ("K09 model", Figure 5-2), and (iii) a 6.0 m diameter circular opening for the vertical shaft ("shaft model", Figure 5-3). The opening was placed at the centre of a square domain with dimensions equal to 50 m x 50 m, 200 m x 200 m, and 100 m x 100 m, for the HAA, K09, and shaft model, respectively. The cross-sections of the HAA and K09 models were assumed perpendicular to the strike of flat-lying bedding planes (i.e., $\psi = 0^\circ$). Thus, the rock mass behaviour was captured using an anisotropic strength and stiffness model. Conversely, the shaft section was assumed to be oriented parallel to the bedding strike and modelled under isotropic material conditions. To maximize the model resolution in the EDZ while keeping the run times within practical limits, a mesh refinement zone was adopted around the excavation boundary, with average element size of 0.03 m, 0.12 m, and 0.06 m, for the HAA, K09, and shaft model, respectively. In this zone, the layering thickness, t , was set to 0.1, 0.4 for the HAA and K09 models, respectively, while no mesh preconditioning was applied to the shaft model. The refinement zone extended radially around the excavation walls for $d_r = 4, 16, \text{ and } 8$ m for the HAA, K09, and shaft model, respectively. From the refinement zone the element size was then graded towards the external boundaries, where an element size equal to 0.6, 2.4 and 1.2 m was used for the HAA, K09, and shaft model, respectively.

The effect of tectonic imprint on the EDZ formation and excavation response was investigated by explicitly introducing a set of faults into the model (Figure 5-4). The stylized fault system was implemented which consisted of three 10 cm thick, 0.5 m spaced fault zones dipping at 80° and intersecting the back and invert of the openings.

The total number of triangular elements employed was approximately 180,000 for all models. Equations of motion for the discretized systems were integrated with a time step of $4e-7$ s; this value was the largest time step size that ensured numerical stability for the explicit solver of the code.

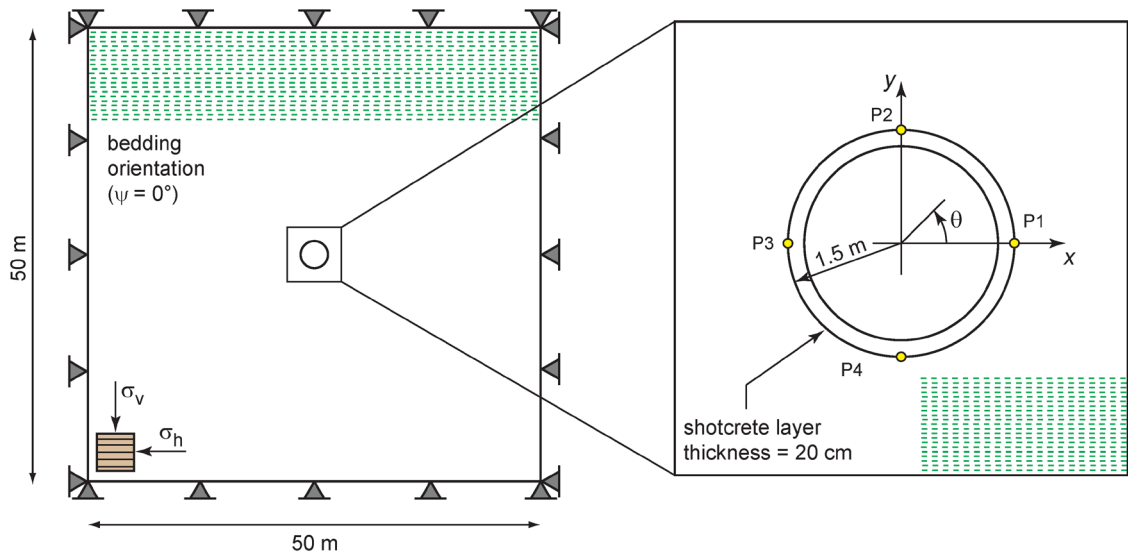


Fig. 5-1: HAA model. Geometry and boundary conditions of the FEM/DEM model of the SF-HLW emplacement tunnels.

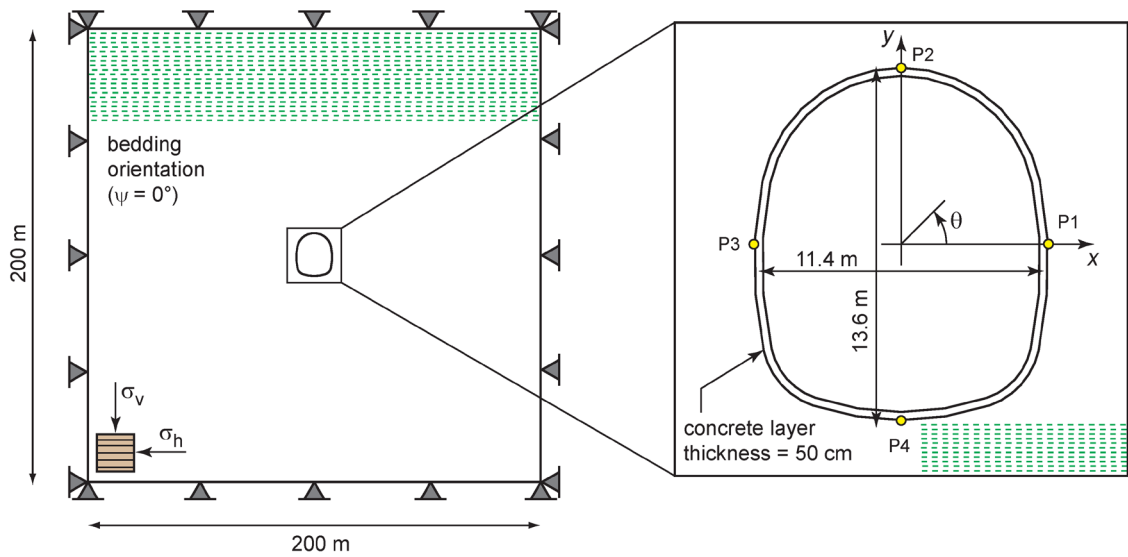


Fig. 5-2: K09 model. Geometry and boundary conditions of the FEM/DEM model of the L-ILW emplacement caverns.

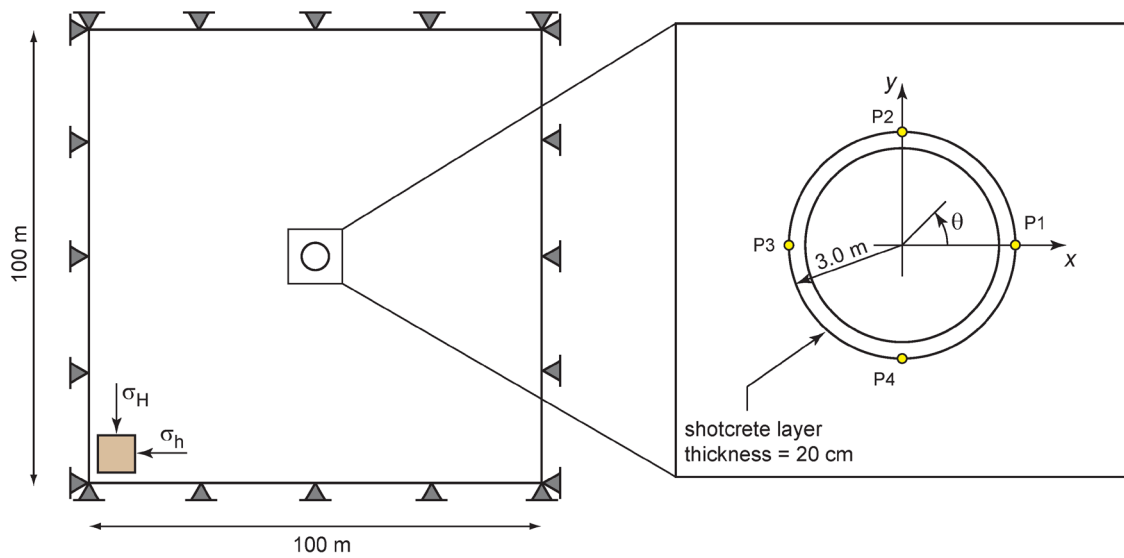


Fig. 5-3: Shaft model. Geometry and boundary conditions of the FEM/DEM model of the repository shaft.

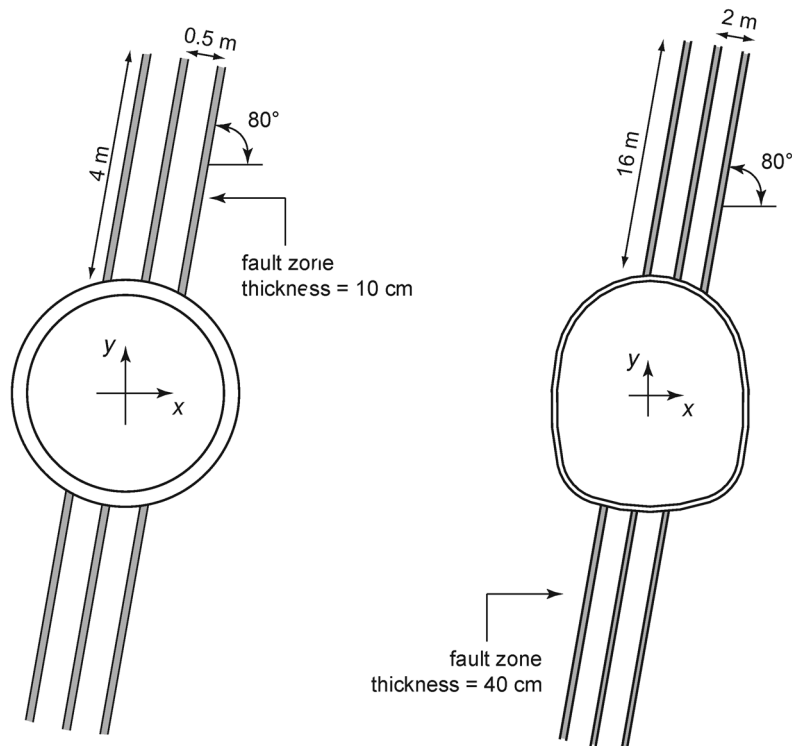


Fig. 5-4: Geometries of the SF-HLW emplacement tunnel (left) and K09 (right) model containing three stylised fault zones.

For the SF-HLW and K09 models, the cohesive strength and fracture energy values determined as a result of the laboratory-scale calibration process (Table 1) were used as a reference values for the sensitivity analysis to the geomechanical properties (Table 3). On the other hand, the experimental values of the elastic constants reported in Table 1 were directly used as input for the transversely isotropic elastic model and were not subjected to any sensitivity analysis.

For the shaft model, an isotropic material model was assumed with Young's modulus and Poisson's ratio equal to 11.4 GPa and 0.27 (i.e., coincident with the values relative to the direction parallel to the bedding planes), respectively, and strength values reported in Table 4. The input parameters for the sensitivity analysis to the geomechanical properties of the shaft model are given therein.

Based on the recommendations of Mahabadi (2012), the penalty values, p_n , p_t and p_f , were set equal to 10x, 1x and 5x the largest Young's modulus, E , respectively, to minimize the effect of the crack element compliance on the overall model stiffness (Mahabadi 2012). Also, a critical viscous damping coefficient, $\mu_c = 3.47 \times 10^3 \text{ kg} \cdot (\text{ms})^{-1}$, was applied to the model to dissipate dynamic oscillations and thus approximate a quasi-static behaviour.

The reduced strength of the material in the fault zones was captured by assuming isotropic strength behaviour with cohesive strength and fracture energy values equal to the minimum values of the Opalinus Clay material:

$$f_t = 0.32 \text{ MPa}, c = 0.95 \text{ MPa}, G_{Ic} = 5 \text{ Jm}^{-2}, \text{ and } G_{IIc} = 40 \text{ Jm}^{-2}.$$

Tab.3: Input parameters for the sensitivity analysis to the geomechanical properties of the HAA and K09 models.

Parameter	OPA	OPA x 2	OPA x 3	OPA x 4	OPA x 5
Tensile strength parallel to bedding, $f_{t,max}$ (MPa)	2	4	6	8	10
Tensile strength perpendicular to bedding, $f_{t,min}$ (MPa)	0.32	0.64	0.96	1.28	1.6
Cohesion parallel to bedding, c_{min} (MPa)	0.95	1.9	2.85	3.8	4.75
Cohesion perpendicular to bedding, c_{max} (MPa)	17.2	34.4	51.6	68.8	86
Mode I fracture energy parallel to bedding, $G_{Ic,max}$ (Jm^{-2})	14	28	42	56	70
Mode I fracture energy perpendicular to bedding, $G_{Ic,min}$ (Jm^{-2})	5	10	15	20	25
Mode II fracture energy parallel to bedding, $G_{IIc,min}$ (Jm^{-2})	40	80	120	160	200
Mode II fracture energy perpendicular to bedding, $G_{IIc,max}$ (Jm^{-2})	140	280	420	560	700

Tab. 4: Input parameters for the sensitivity analysis to the geomechanical properties of the shaft model.

Parameter	OPA-Isotr	OPA-Isotr x 0.5	OPA-Isotr x 0.75
Tensile strength, f_t (MPa)	2	1	1.5
Cohesion, c (MPa)	17.2	8.6	12.9
Mode I fracture energy, G_{Ic} (Jm^{-2})	14	7	10.5
Mode II fracture energy, G_{IIc} (Jm^{-2})	140	70	105

5.2 In situ stress and boundary conditions

The *in situ* stress field reported in Table 5 was used for the calibration of the FEM/DEM model. Since the adopted crack elements do not account for the influence of an out-of-plane stress during the simulation of fracture nucleation and growth, only the in-plane stresses were effectively used in the analysis. Also, gravity-induced stress gradients were neglected in all models. The effect of varying the orientation and magnitude of the in-plane *in situ* stress field was investigated and the results reported in Section 6.1. The initialization of each model with the prescribed *in situ* stress field was accomplished by a preliminary elastic run (i.e., without crack elements) which aimed at obtaining the revised nodal coordinates of the non-excavated model subjected to the prescribed far-field stresses. These revised nodal coordinates were subsequently used as the current nodal coordinates (i.e., deformed mesh) of the actual FEM/DEM simulation run in which crack elements were inserted into the model to capture material failure. By changing the far-field boundaries to be fixed in the horizontal and vertical directions, the first order *in situ* stress conditions were maintained while allowing the excavation sequence to be modelled.

Tab. 5: Summary of *in situ* stress conditions applied to the numerical models. Vertical and horizontal stresses coincide with the principal stresses. The stress ratio to the vertical stress, K_0 , is reported in brackets.

Case	Vertical Stress, σ_v (MPa)	Horizontal Stress, σ_h (MPa)	Horizontal Stress, σ_h (MPa)
HAA simulations			
	19.6	15.7 (0.8)	N/A
	19.6	19.6 (1.0)	N/A
	19.6	25.5 (1.3)	N/A
	15.9	15.9 (1.0)	N/A
	15.9	20.7 (1.3)	N/A
K09 simulations			
	18.4	14.7 (0.8)	N/A
	18.4	18.4 (1.0)	N/A
	18.4	23.9 (1.3)	N/A
	15.9	12.9 (0.8)	N/A
	15.9	15.9 (1.0)	N/A
	15.9	20.7 (1.3)	N/A
	11.0	14.3 (1.3)	N/A
Shaft simulations			
	11.0	16.5 (1.5)	N/A
	15.9	15.9 (1.0)	N/A
	19.6	15.7 (0.8)	N/A
	19.6	25.5 (1.3)	N/A

5.3 Modelling procedure for excavation advance

To capture the supporting effect of the tunnel face in the two-dimensional FEM/DEM model, a core replacement technique was adopted for this study based on the approach first developed by Curran et al. (2003). With this technique, the three-dimensional face effect, which causes a gradual reduction of radial resistance around the excavation boundary, is captured by a fictitious, softening elastic material in the tunnel core. That is, the deformation modulus of the excavated material is progressively reduced from the original rock mass values, corresponding to an undeformed section far ahead of the face, to a value that results in the wall displacements at the time of support installation. The general procedure for modelling excavation advance and support installation in FEM/DEM consisted of the following two main steps, graphically summarized in Figure 5-5:

3. Using the core replacement technique, the modulus reduction is necessary to obtain the prescribed amount of tunnel wall displacement was determined. For the HAA model, the maximum allowed displacement was set to 0.05m, corresponding to a total closure of 0.1 m. To this end, a FEM/DEM simulation was run whereby the elastic parameters of the fictitious core material (i.e., E , E' , G) were reduced in a stepwise fashion over time by a softening ratio, α_s , and the wall displacements were recorded. The result was the plot of the tunnel wall displacements, δ , as function of the core softening ratio, α_s (i.e., the ground reaction curve).
4. The FEM/DEM simulation was then re-run by allowing the excavation boundary to relax up to the point where the prescribed wall displacements were obtained and by subsequently adding the support.

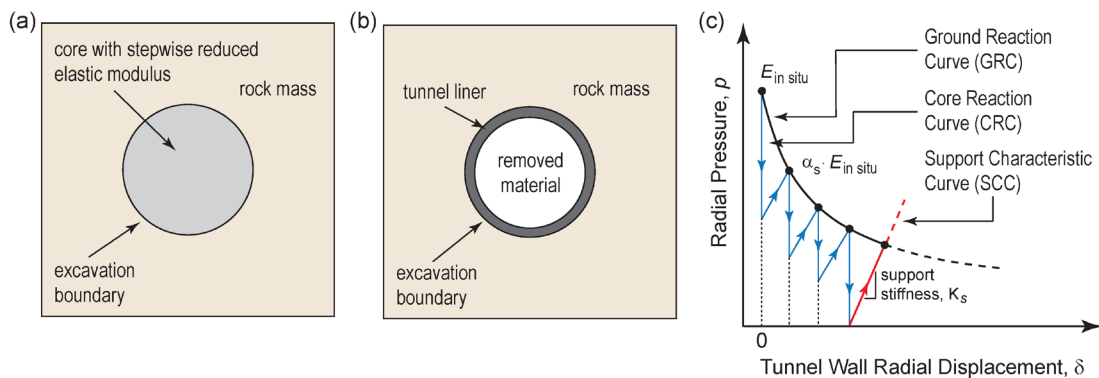


Fig. 5-5: Modelling procedure for excavation advance and support installation using the core replacement technique. (a) Replacement of core with reduced elastic modulus material. (b) Installation of tunnel lining. (c) Qualitative example of ground reaction curve simulated via stepwise modulus reduction and support characteristic curve for a linear elastic lining.

5.4 Modelling procedure for support installation

The application of shotcrete on the walls of the FE tunnel was modelled using the constant-strain, triangular elements implemented in FEM/DEM (Munjiza 2004). Since the constitutive response of the support is at present limited to isotropic, linear elastic conditions (i.e., fracturing is not allowed), the mechanical behaviour of the shotcrete was fully characterized by Young's modulus, $E_c = 32$ GPa, and Poisson's ratio, $\nu_c = 0.20$. Furthermore, the sensitivity of the model to the support stiffness was investigated by considering also the cases of $E_c = 16$ GPa and $E_c = 3.2$ GPa.

The support installation consisted of specifying the liner thickness, t_c , and the installation time from the appropriate core softening ratio, α_s . Since the delayed installation of shotcrete was accomplished by varying the elastic properties of the liner from those of the rock mass to those of the shotcrete (Figure 5-5b), the deformation in the liner had to be zeroed to avoid an artificial build-up of stress in response to an instantaneous increase of material stiffness in a pre-stressed medium. This was accomplished by a dedicated routine which sets the nodal coordinates of the deformed configuration (i.e., at the installation time) as new initial (i.e., undeformed) coordinates for the triangular mesh of the support.

5.5 Estimation of excavation-induced fracture aperture

The fracture network of the models are extracted from the output files of the broken crack elements (joints), and then processed via a python script. Based on the nodal coordinates of the four fracture points, the apparent fracture aperture (defined as the average distance between the two sides of the crack elements), the fracture angle (measured counter clockwise from the horizontal axis), and the exact fracture aperture area are calculated. The failure modes of the fractures are also reported.

5.6 Modelling procedure for the EDZ reconsolidation

The long-term reconsolidation of the EDZ due to the swelling of the bentonite was modelled using an equivalent pressure, p , applied radially from within the excavation boundary (Figure 5-6). With this approach, the short-term (i.e., undrained) excavation process and support installation are first simulated. Upon reaching equilibrium conditions, the internal pressure p is increased in a stepwise fashion over time from 0 to 10 MPa using 1 MPa increments. Subsequently, the mechanical degradation of the shotcrete layer is simulated by gradually reducing the initial value of the Young's modulus, E_c , by 100 times.

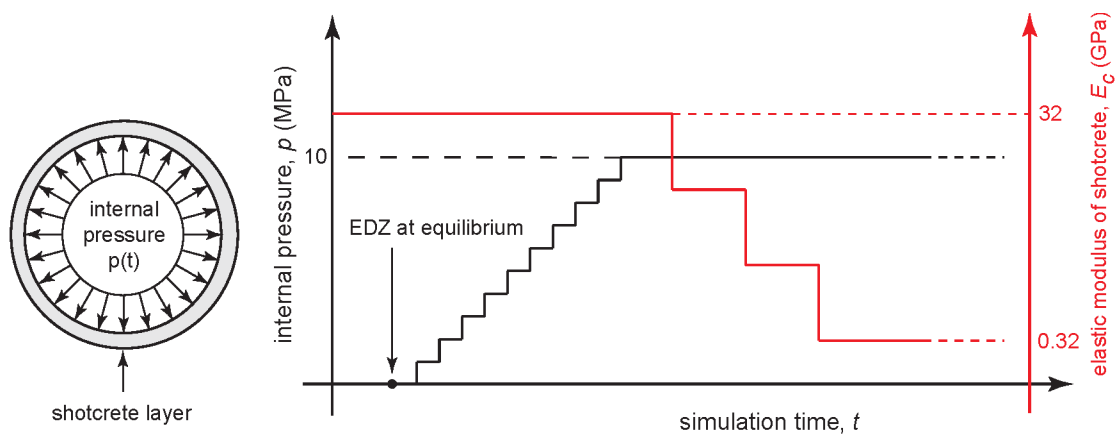


Fig. 5-6: Modelling procedure for the EDZ reconsolidation.

6 Results: EDZ simulations for SF/HLW emplacement tunnel

As summarized in Table 6, four main groups of simulation cases were considered for the HAA model, aiming at investigating the sensitivity to (i) in situ stress conditions and support installation time (Section 6.1), (ii) strength parameters (Section 6.2), (iii) presence of faults (Section 6.3), and (iv) shotcrete stiffness (i.e., E_c) (Section 6.4).

It is noteworthy that the strength properties labelled “Opa x 2” in Table 3 were used as strength parameters of reference for the simulations. A preliminary analysis revealed that if the laboratory-calibrated strength parameters (i.e., “Opa” in Table 3) are used, the excessively large amount of fracturing causes the simulations to stop unexpectedly due to numerical instabilities.

Tab. 6: Summary of HAA model simulations.

Model	Section	In situ stress conditions	Strength properties	Elastic modulus of support	Faults	Core softening ratio at support installation	Reconsolidation pressure
Sensitivity to in situ stress conditions							
HAA-01	HAA	19.6, 0.8	OPA x 2	32	N/A	0.01	N/A
HAA-02	HAA	19.6, 1.0	OPA x 2	32	N/A	0.01	N/A
HAA-03	HAA	19.6, 1.3	OPA x 2	32	N/A	0.01	N/A
HAA-04	HAA	19.6, 0.8	OPA x 2	32	N/A	0.05	N/A
HAA-05	HAA	19.6, 1.0	OPA x 2	32	N/A	0.05	N/A
HAA-06	HAA	19.6, 1.3	OPA x 2	32	N/A	0.05	N/A
HAA-07	HAA	19.6, 1.0	OPA x 2	32	N/A	0.008	N/A
HAA-08	HAA	15.9, 1.3	OPA x 2	32	N/A	0.008	N/A
HAA-09	HAA	15.9, 1.0	OPA x 2	32	N/A	0.003	N/A
Sensitivity to strength parameters							
HAA-10	HAA	15.9, 1.3	OPA x 1.5	32	N/A	0.008	N/A
HAA-11	HAA	15.9, 1.3	OPA x 3	32	N/A	0.008	N/A
HAA-12	HAA	15.9, 1.3	OPA x 4	32	N/A	0.008	N/A
HAA-13	HAA	15.9, 1.3	OPA x 5	32	N/A	0.008	N/A
Sensitivity to the presence of faults							
HAA-14	HAA	19.6, 1.0	OPA x 2	32	yes	0.01	N/A
HAA-15	HAA	15.9, 1.3	OPA x 1.5	32	yes	0.008	N/A
HAA-16	HAA	15.9, 1.3	OPA x 3	32	yes	0.008	N/A
HAA-17	HAA	15.9, 1.3	OPA x 4	32	yes	0.008	N/A
HAA-18	HAA	15.9, 1.3	OPA x 5	32	yes	0.008	N/A
Sensitivity to shotcrete stiffness							
HAA-19	HAA	15.9, 1.3	OPA x 2	16	N/A	0.008	N/A
HAA-20	HAA	15.9, 1.3	OPA x 2	3.2	N/A	0.008	N/A
HAA-21	HAA	15.9, 1.3	OPA x 1.5	3.2	N/A	0.008	N/A
HAA-22	HAA	15.9, 1.3	OPA x 3	3.2	N/A	0.008	N/A
HAA-23	HAA	15.9, 1.3	OPA x 4	3.2	N/A	0.008	N/A
HAA-24	HAA	15.9, 1.3	OPA x 5	3.2	N/A	0.008	N/A

In the following subsections, the simulation results are presented using ground reaction curves, evolution of total displacement, δ , of selected points located along the excavation boundary, contours of total displacements, δ , fracture patterns and contours of maximum and minimum principal stress, σ_1 and σ_3 , in the rock mass and the support layer.

6.1 Analysis of sensitivity to *in situ* stress conditions

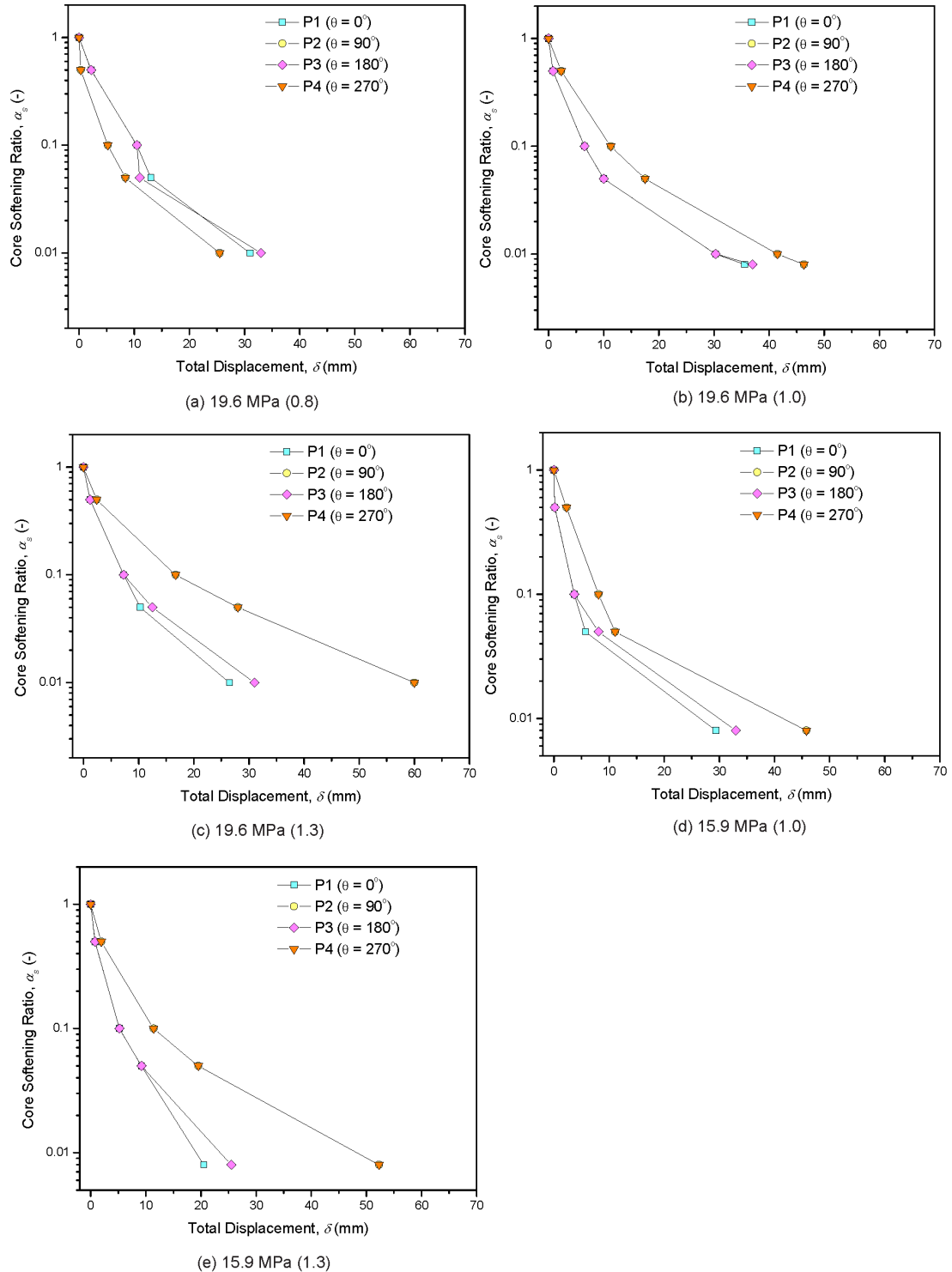


Fig. 6-1: Ground reactions curves of the HAA model under different *in situ* stress conditions. For each case, the *in situ* vertical stress, σ_v , is reported together with the stress ratio, K_0 , in brackets. Strength parameters are "Opa x 2". The exact location of points P1-P4 is reported in Fig. 5-1.

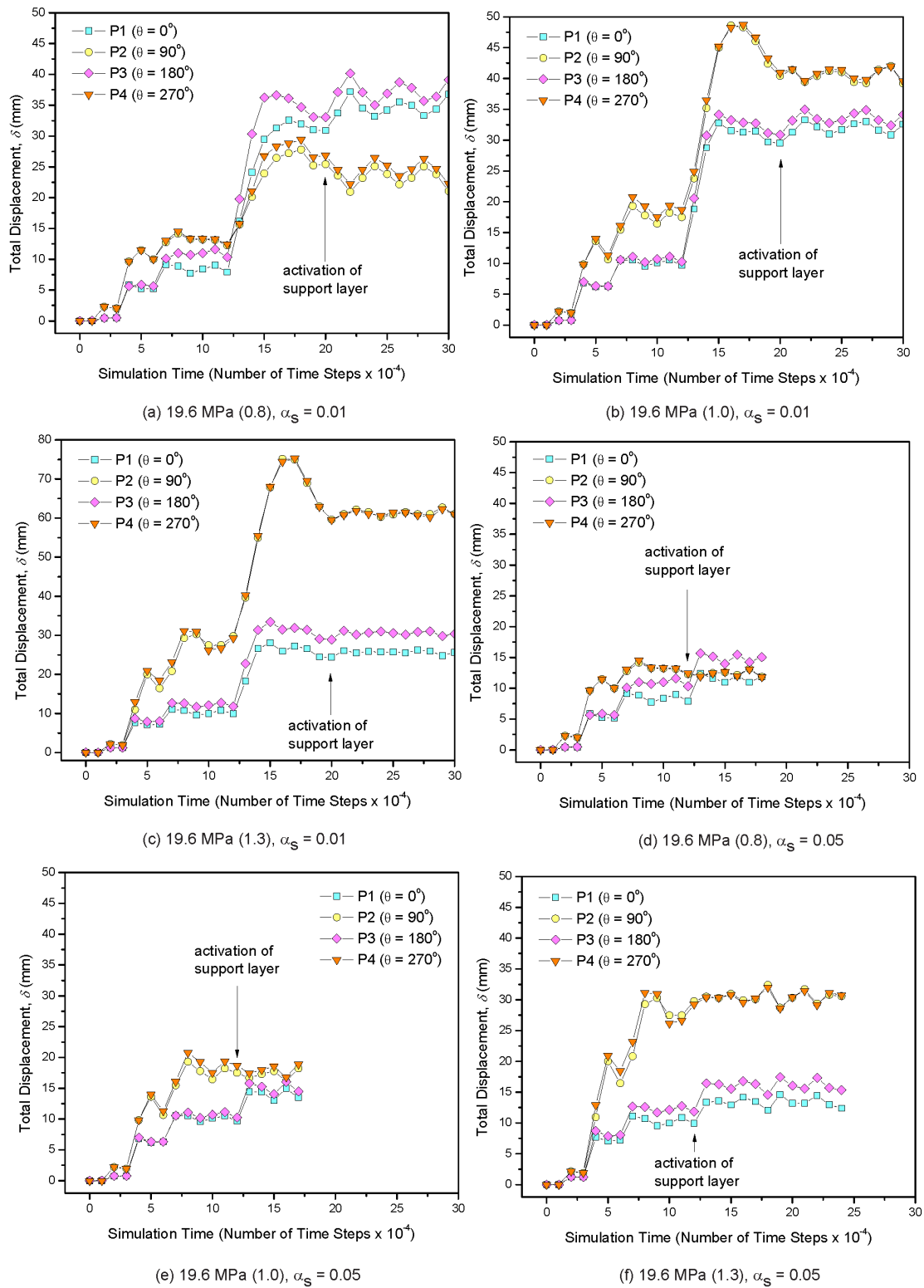


Fig. 6-2: Evolution of displacement, δ , around the excavation boundary of the HAA model under different *in situ* stress conditions. For each case, the stress ratio, K_0 , to the *in situ* vertical stress, $\sigma_v = 19.6$ MPa, is reported in brackets, together with the core softening ratio, α_s , at the time of support installation. Strength parameters are "Opa x 2" (the reference points P1 to P4 are defined in Fig. 5-1).

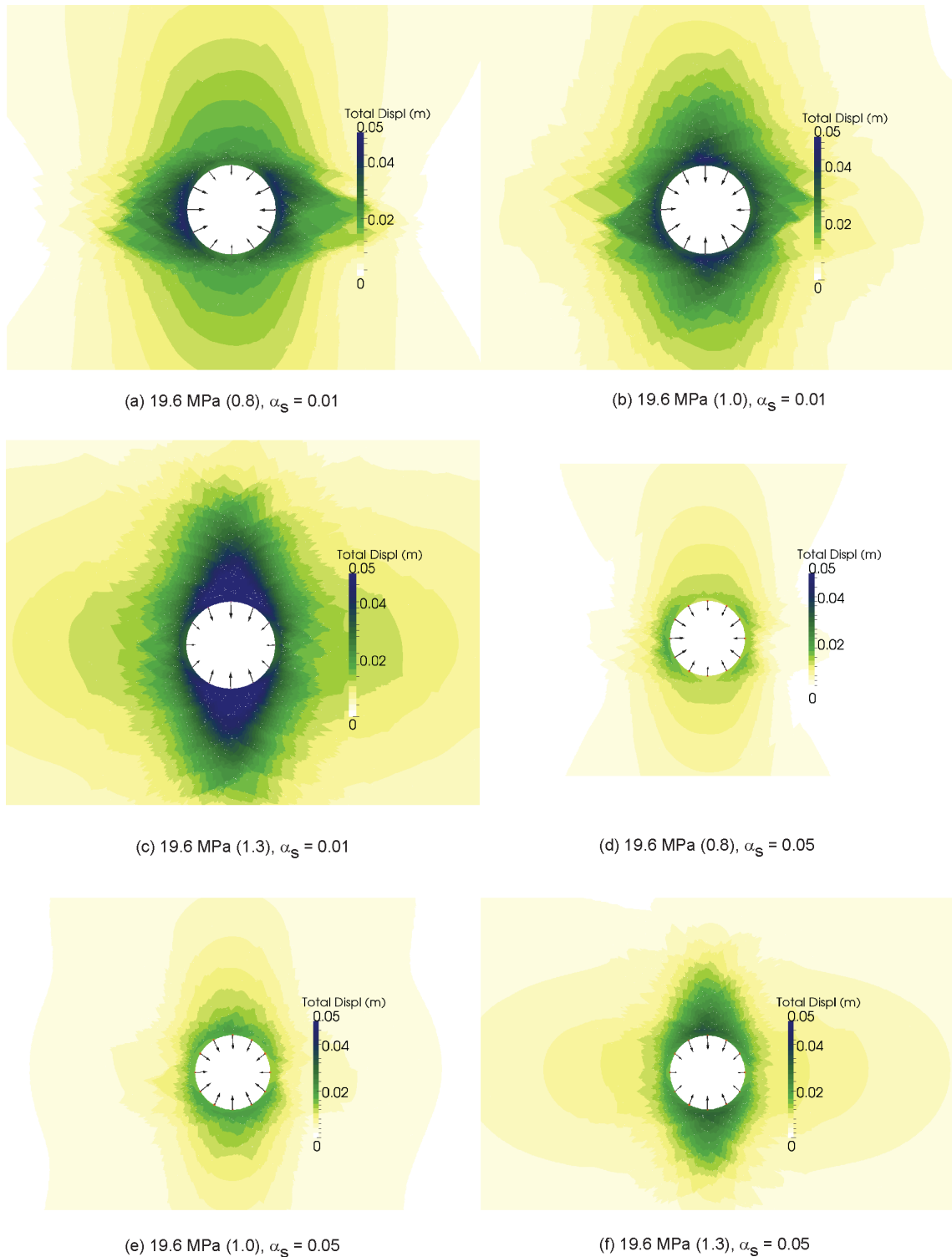


Fig. 6-3: Contours of displacement, δ , of the HAA model under different *in situ* stress conditions. For each case, the stress ratio, K_0 , to the *in situ* vertical stress, $\sigma_v = 19.6$ MPa, is reported in brackets, together with the core softening ratio, α_s , at the time of support installation. Strength parameters are "Opa x 2".

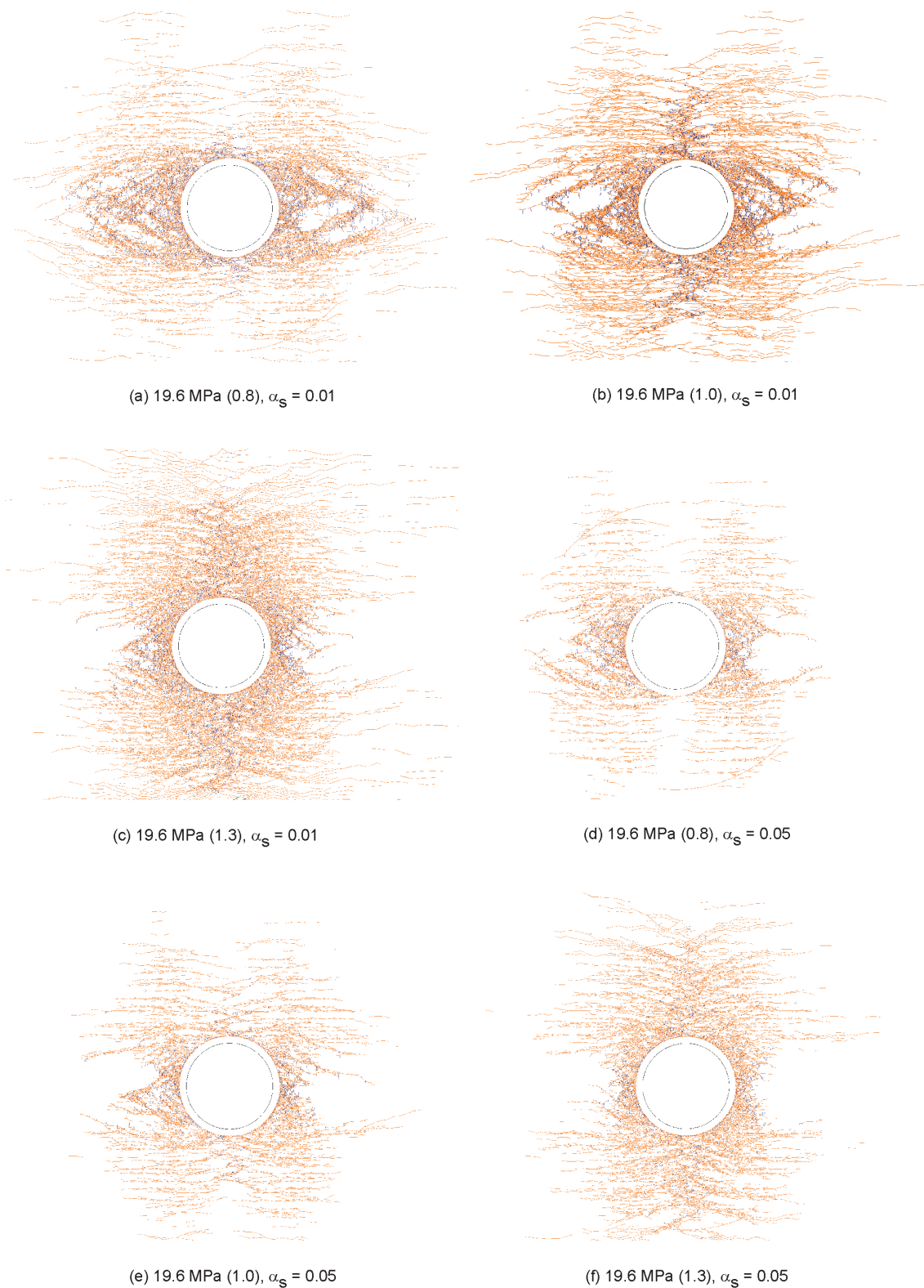


Fig. 6-4: Final fracture patterns of the HAA model under different *in situ* stress conditions. Tensile and shear failure are indicated in blue and orange, respectively. For each case, the stress ratio, K_0 , to the *in situ* vertical stress, $\sigma_v = 19.6$ MPa, is reported in brackets, together with the core softening ratio, α_s , at the time of support installation. Strength parameters are "Opa x 2".

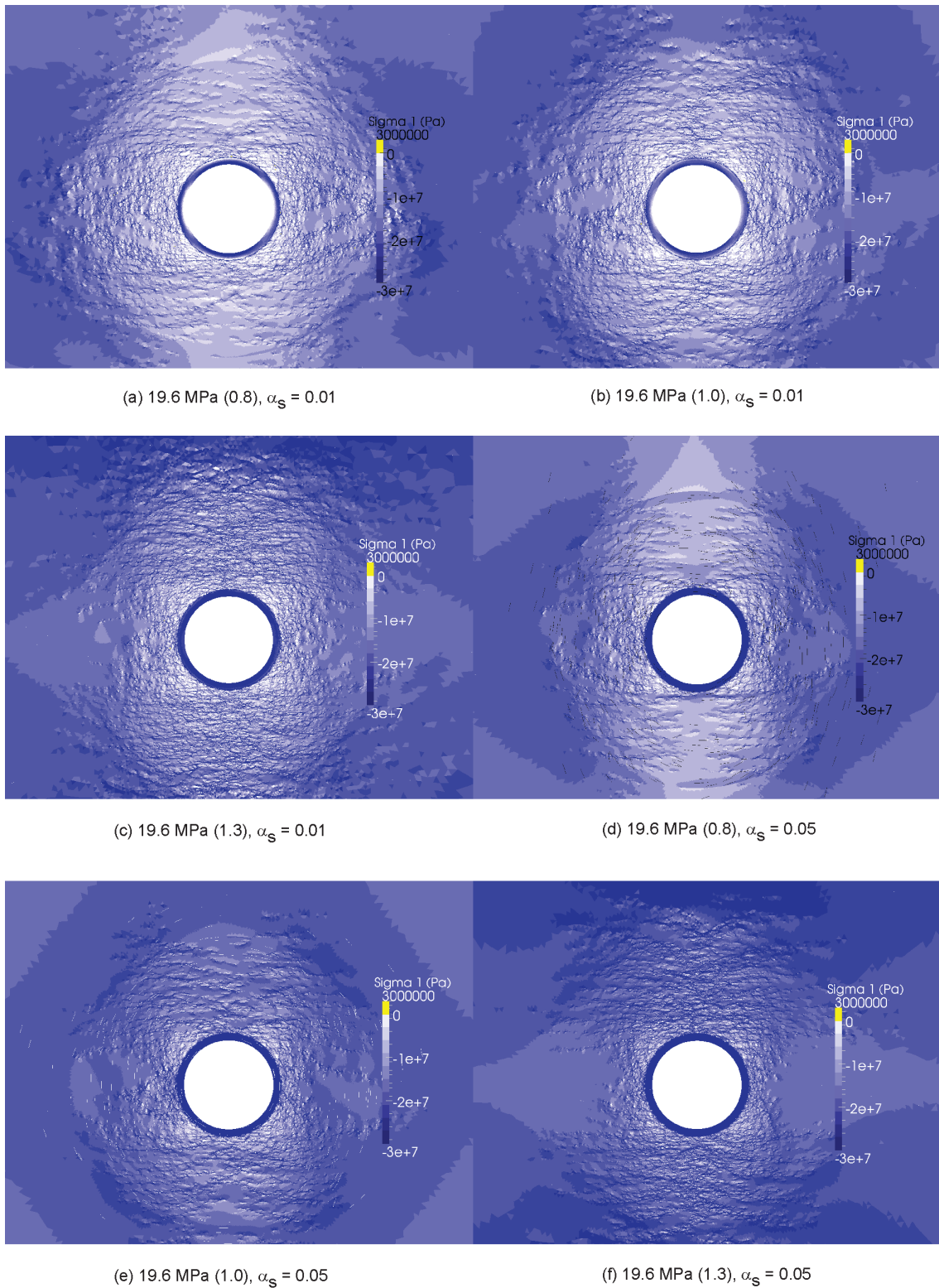


Fig. 6-5: Contours of maximum principal stress, σ_1 , of the HAA model under different *in situ* stress conditions. For each case, the stress ratio, K_0 , to the *in situ* vertical stress, $\sigma_v = 19.6$ MPa, is reported in brackets, together with the core softening ratio, α_s , at the time of support installation. Strength parameters are "Opa x 2".

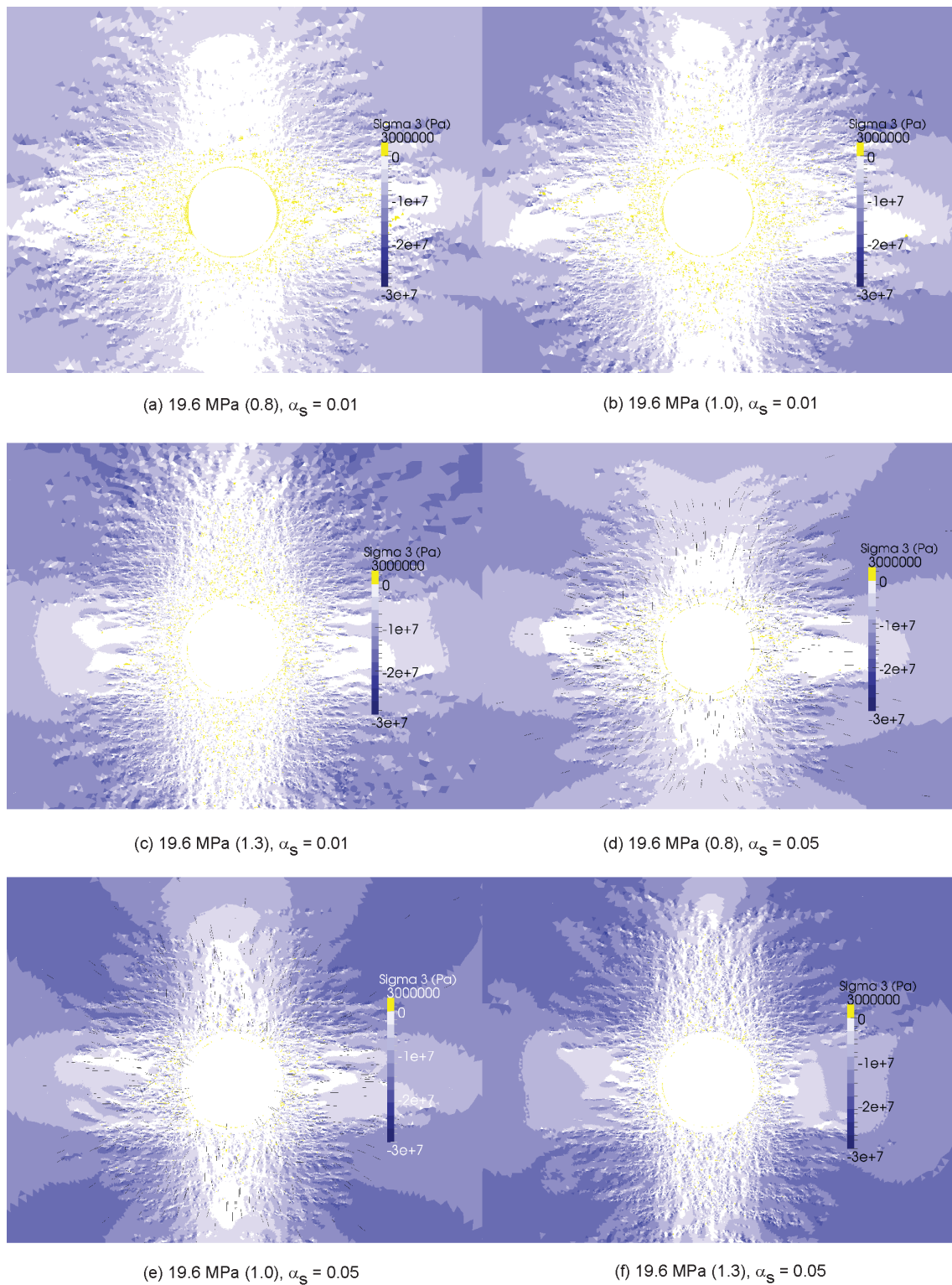


Fig. 6-6: Contours of minimum principal stress, σ_3 , of the HAA model under different *in situ* stress conditions. For each case, the stress ratio, K_0 , to the *in situ* vertical stress, $\sigma_v = 19.6$ MPa, is reported in brackets, together with the core softening ratio, α_s , at the time of support installation. Strength parameters are "Opa x 2".

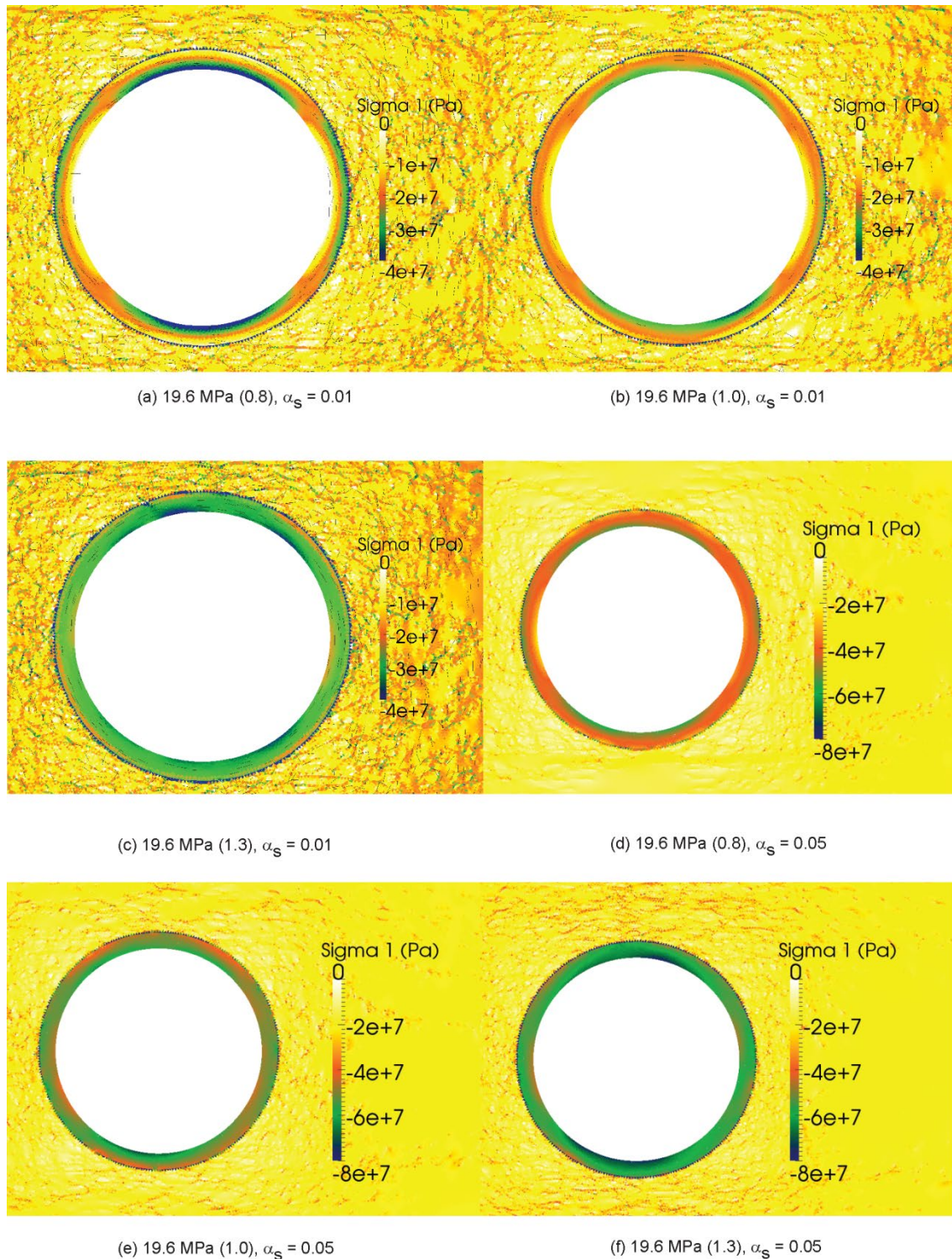
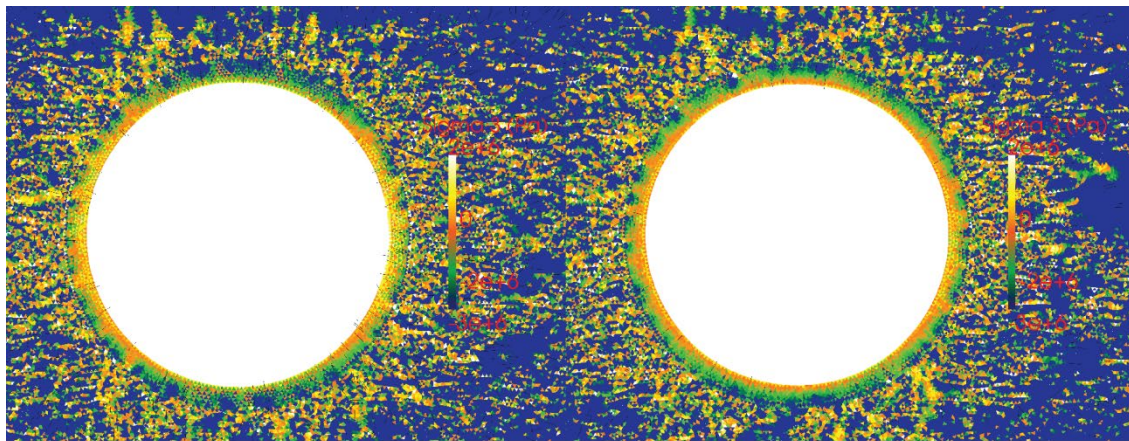
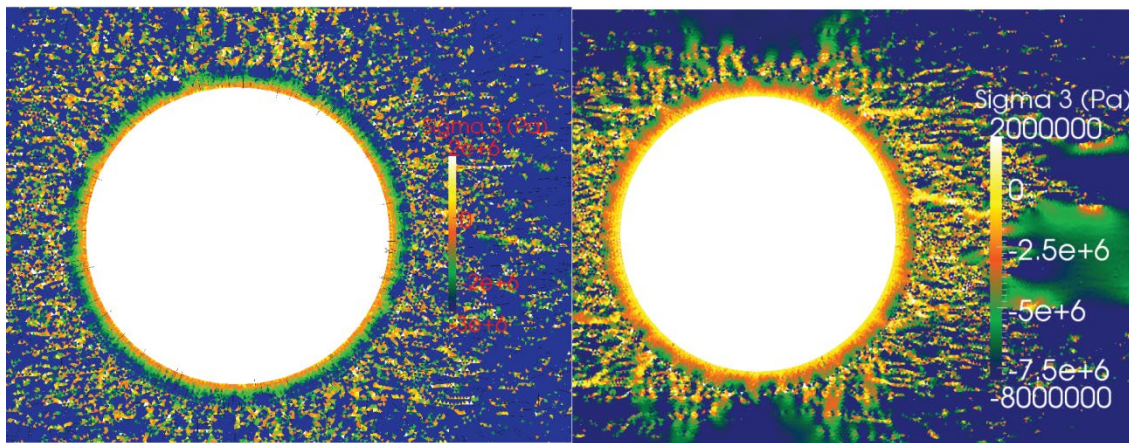


Fig. 6-7: Contours of maximum principal stress, σ_1 , in the support layer of the HAA model under different *in situ* stress conditions. For each case, the stress ratio, K_0 , to the *in situ* vertical stress, $\sigma_v = 19.6$ MPa, is reported in brackets, together with the core softening ratio, α_s , at the time of support installation. Strength parameters are "Opa x 2".



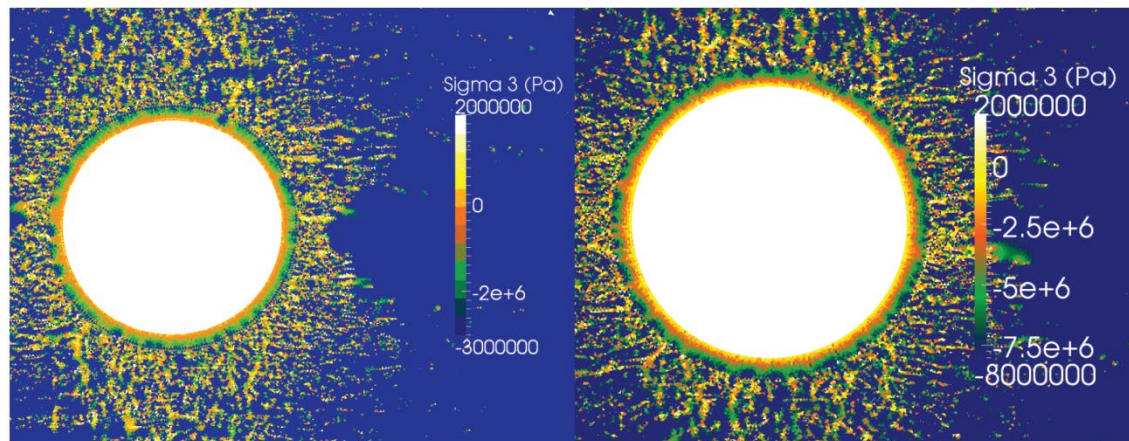
(a) 19.6 MPa (0.8), $\alpha_S = 0.01$

(b) 19.6 MPa (1.0), $\alpha_S = 0.01$



(c) 19.6 MPa (1.3), $\alpha_S = 0.01$

(d) 19.6 MPa (0.8), $\alpha_S = 0.05$



(e) 19.6 MPa (1.0), $\alpha_S = 0.05$

(f) 19.6 MPa (1.3), $\alpha_S = 0.05$

Fig. 6-8: Contour of minimum principal stress, σ_3 , in the support layer of the HAA model under different *in situ* stress conditions. For each case, the stress ratio, K_0 , to the *in situ* vertical stress, $\sigma_v = 19.6$ MPa, is reported in brackets, together with the core softening ratio, α_s , at the time of support installation. Strength parameters are "Opa x 2".

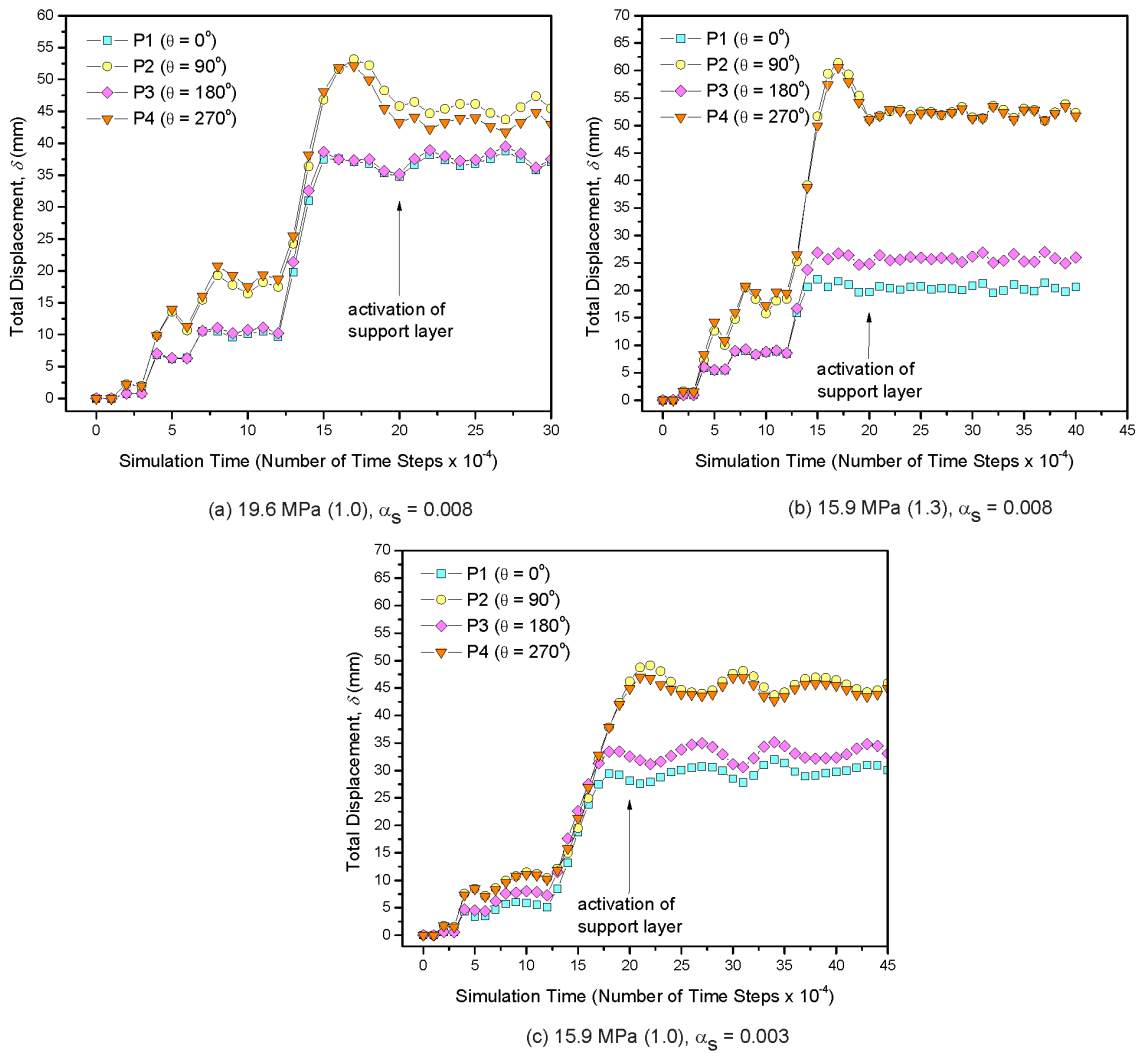


Fig. 6-9: Evolution of displacement, δ , around the excavation boundary of the HAA model under different *in situ* stress conditions. For each case, the *in situ* vertical stress, σ_v , is reported together with the stress ratio, K_0 , in brackets, and with the core softening ratio, α_s , at the time of support installation. Strength parameters are "Opa $\times 2$ ". The exact location of points P1-P4 is reported in Fig. 5-1.

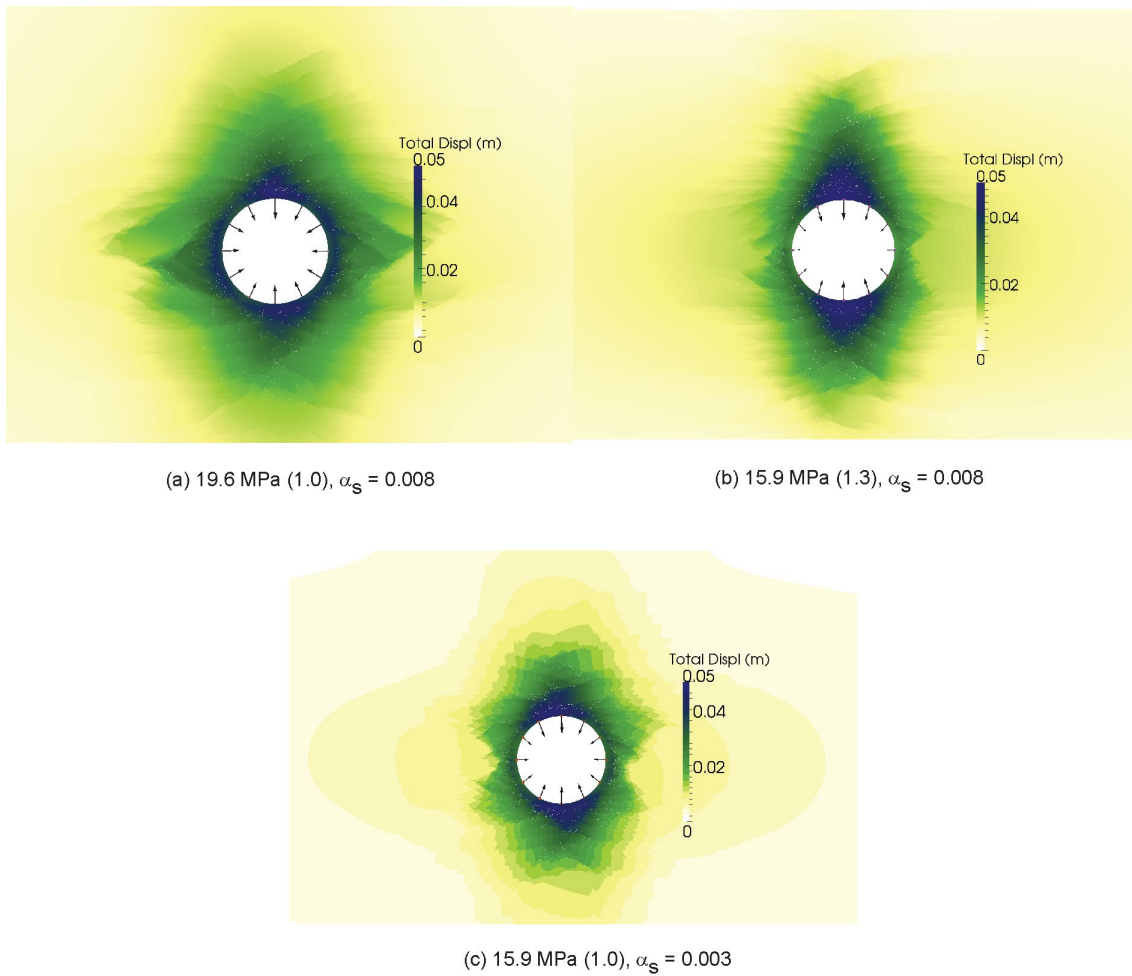


Fig. 6-10: Contours of displacement, δ , of the HAA model under different *in situ* stress conditions. For each case, the *in situ* vertical stress, σ_v , is reported together with the stress ratio, K_0 , in brackets, and with the core softening ratio, α_s , at the time of support installation. Strength parameters are "Opa x 2".

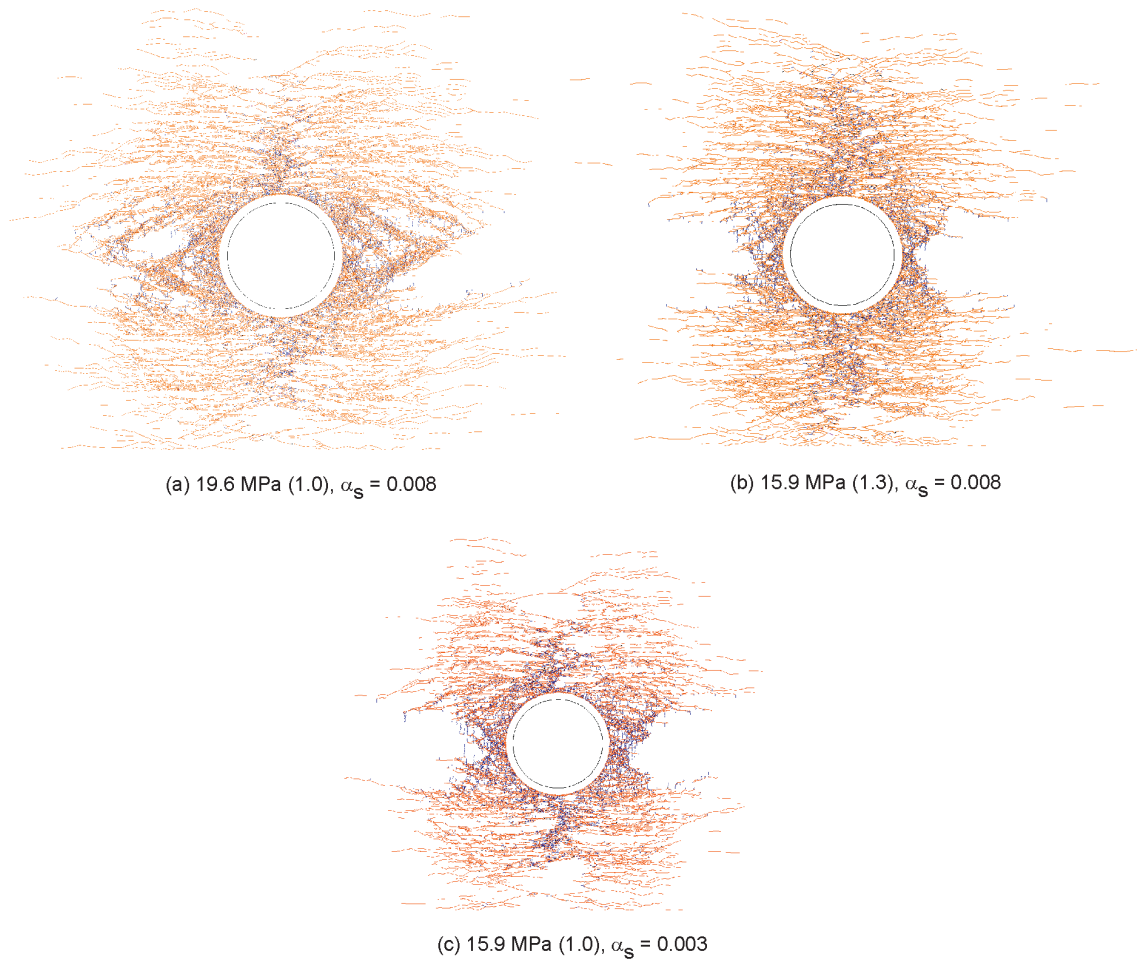


Fig. 6-11: Final fracture patterns of the HAA model under different *in situ* stress conditions. Tensile and shear failure are indicated in blue and orange, respectively. For each case, the *in situ* vertical stress, σ_v , is reported together with the stress ratio, K_0 , in brackets, and with the core softening ratio, α_s , at the time of support installation. Strength parameters are "Opa x 2".

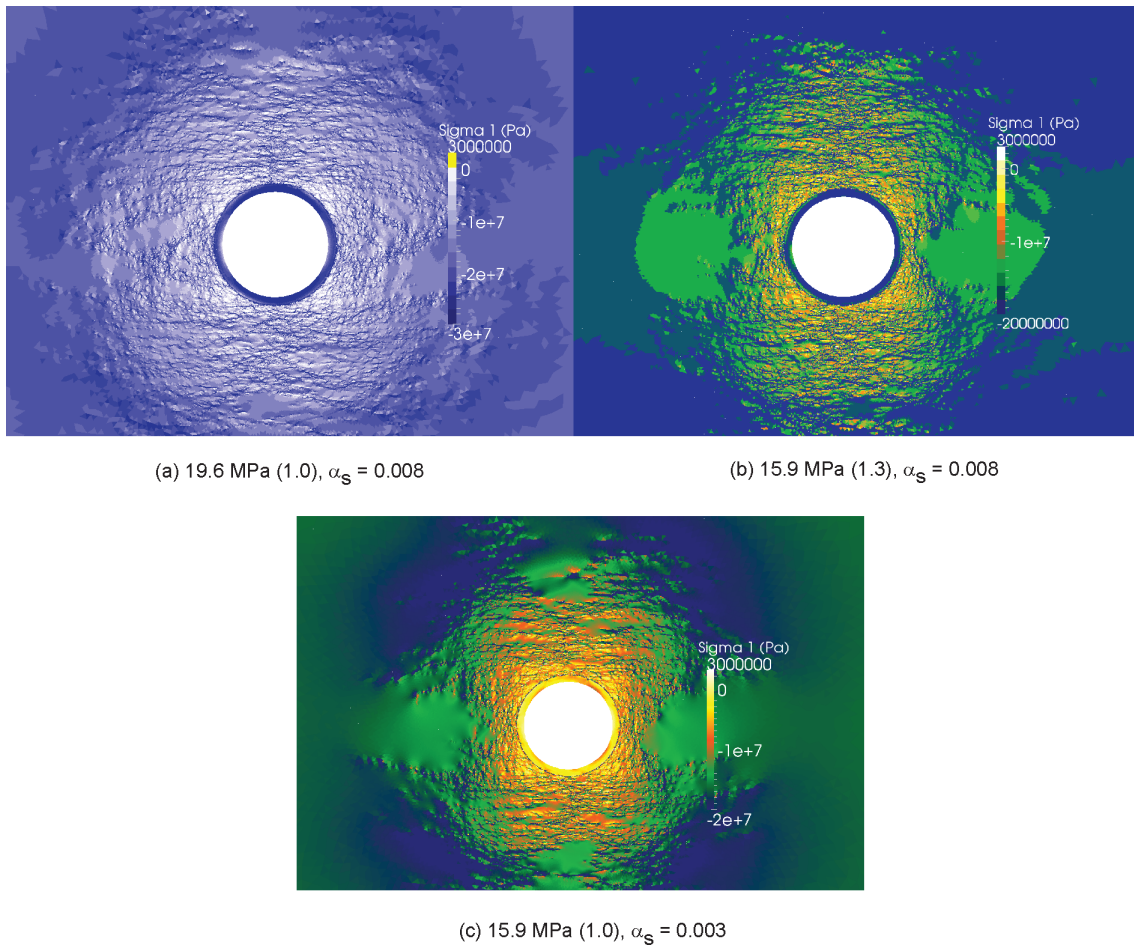


Fig. 6-12: Contours of maximum principal stress, σ_1 , of the HAA model under different *in situ* stress conditions. For each case, the *in situ* vertical stress, σ_v , is reported together with the stress ratio, K_0 , in brackets, and with the core softening ratio, α_s , at the time of support installation. Strength parameters are "Opa x 2".

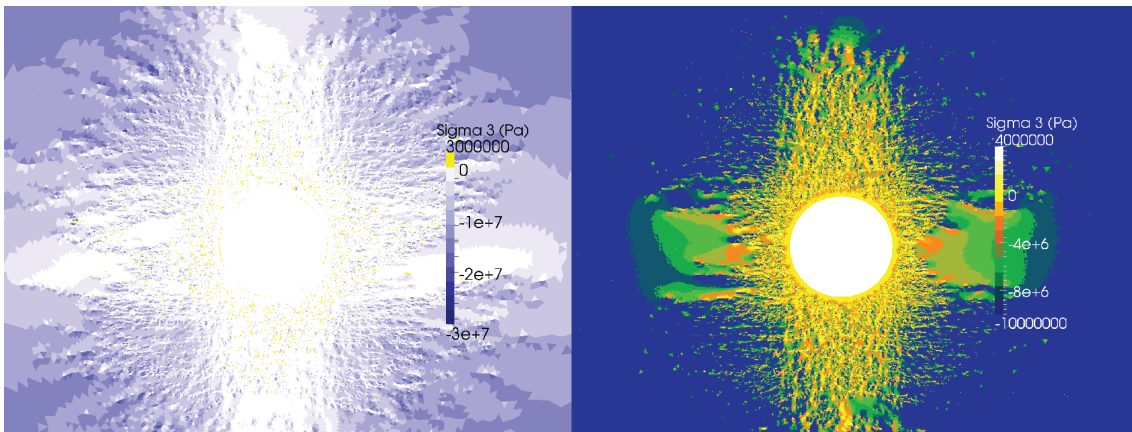
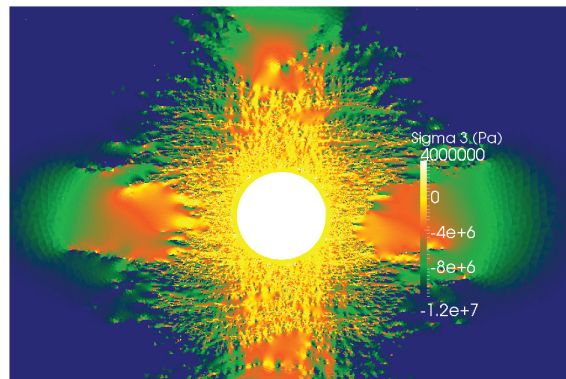
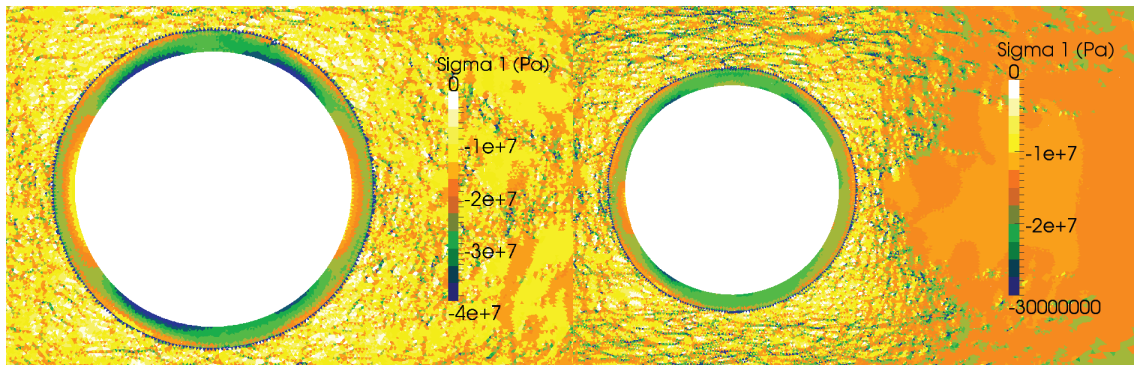
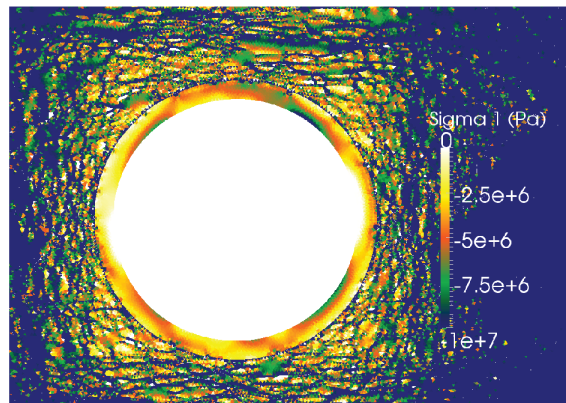
(a) 19.6 MPa (1.0), $\alpha_s = 0.008$ (b) 15.9 MPa (1.3), $\alpha_s = 0.008$ (c) 15.9 MPa (1.0), $\alpha_s = 0.003$

Fig. 6-13: Contours of minimum principal stress, σ_3 , of the HAA model under different *in situ* stress conditions. For each case, the *in situ* vertical stress, σ_v , is reported together with the stress ratio, K_0 , in brackets, and with the core softening ratio, α_s , at the time of support installation. Strength parameters are "Opa x 2".



(a) 19.6 MPa (1.0), $\alpha_s = 0.008$

(b) 15.9 MPa (1.3), $\alpha_s = 0.008$



(c) 15.9 MPa (1.0), $\alpha_s = 0.003$

Fig. 6-14: Contours of maximum principal stress, σ_1 , in the support layer of the HAA model under different *in situ* stress conditions. For each case, the *in situ* vertical stress, σ_v , is reported together with the stress ratio, K_0 , in brackets, and with the core softening ratio, α_s , at the time of support installation. Strength parameters are "Opa x 2".

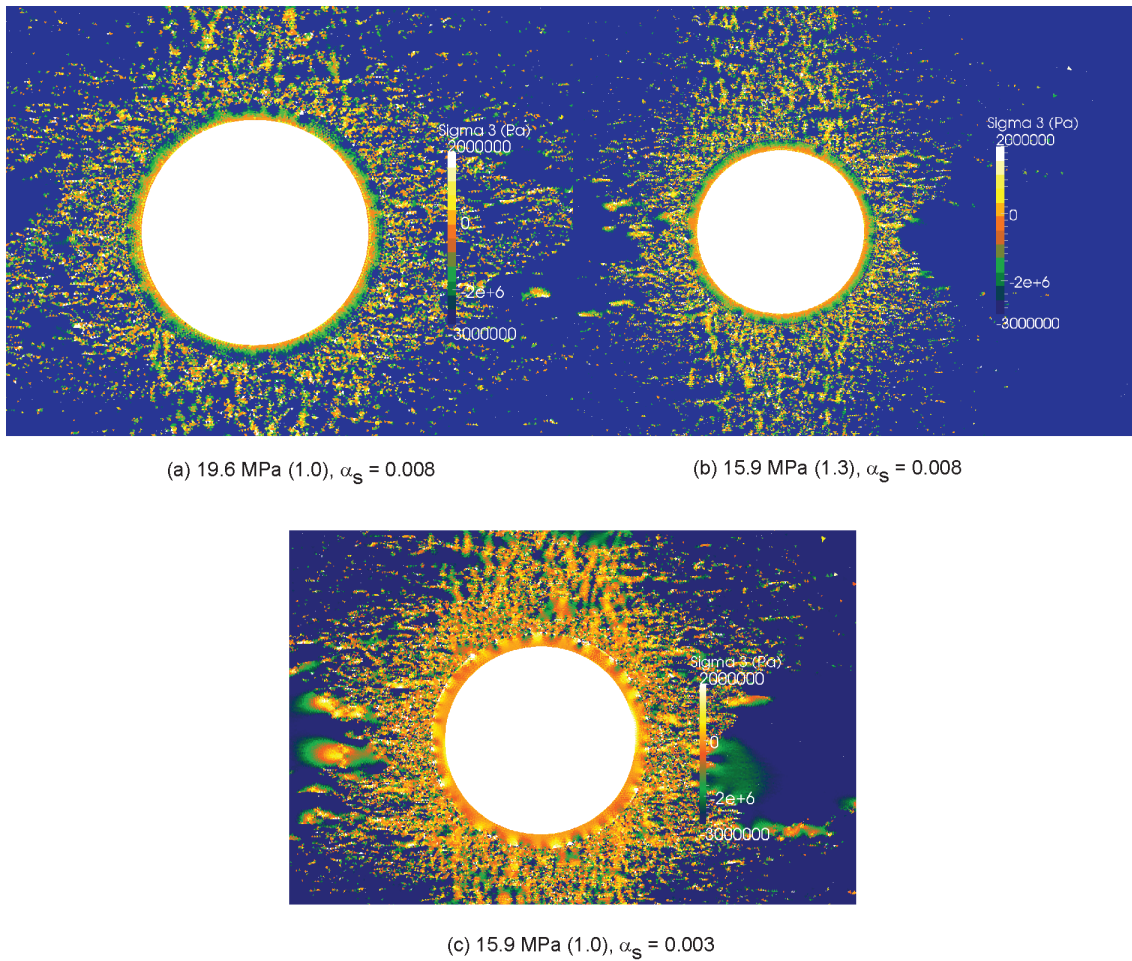


Fig. 6-15: Contours of minimum principal stress, σ_3 , in the support layer of the HAA model under different *in situ* stress conditions. For each case, the *in situ* vertical stress, σ_v , is reported together with the stress ratio, K_0 , in brackets, and with the core softening ratio, α_s , at the time of support installation. Strength parameters are "Opa x 2".

6.2 Analysis of sensitivity to strength values

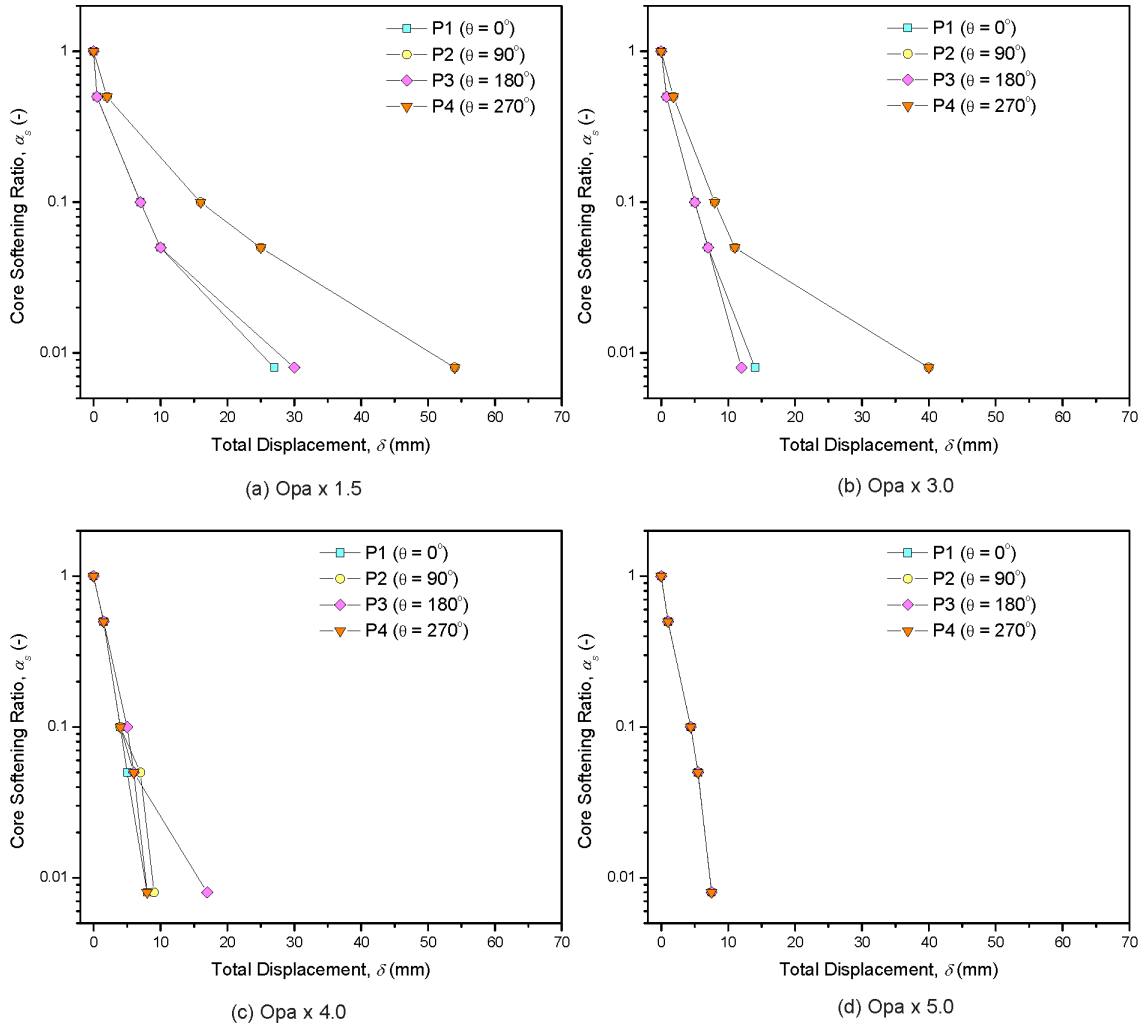


Fig. 6-16: Ground reactions curves of the HAA model for different rock strength levels. The vertical *in situ* stress is equal to 15.9 MPa with a stress ratio $K_0 = 1.3$, while the core softening ratio at the time of support installation is equal to 0.008. The exact location of points P1-P4 is reported in Fig. 5-1.

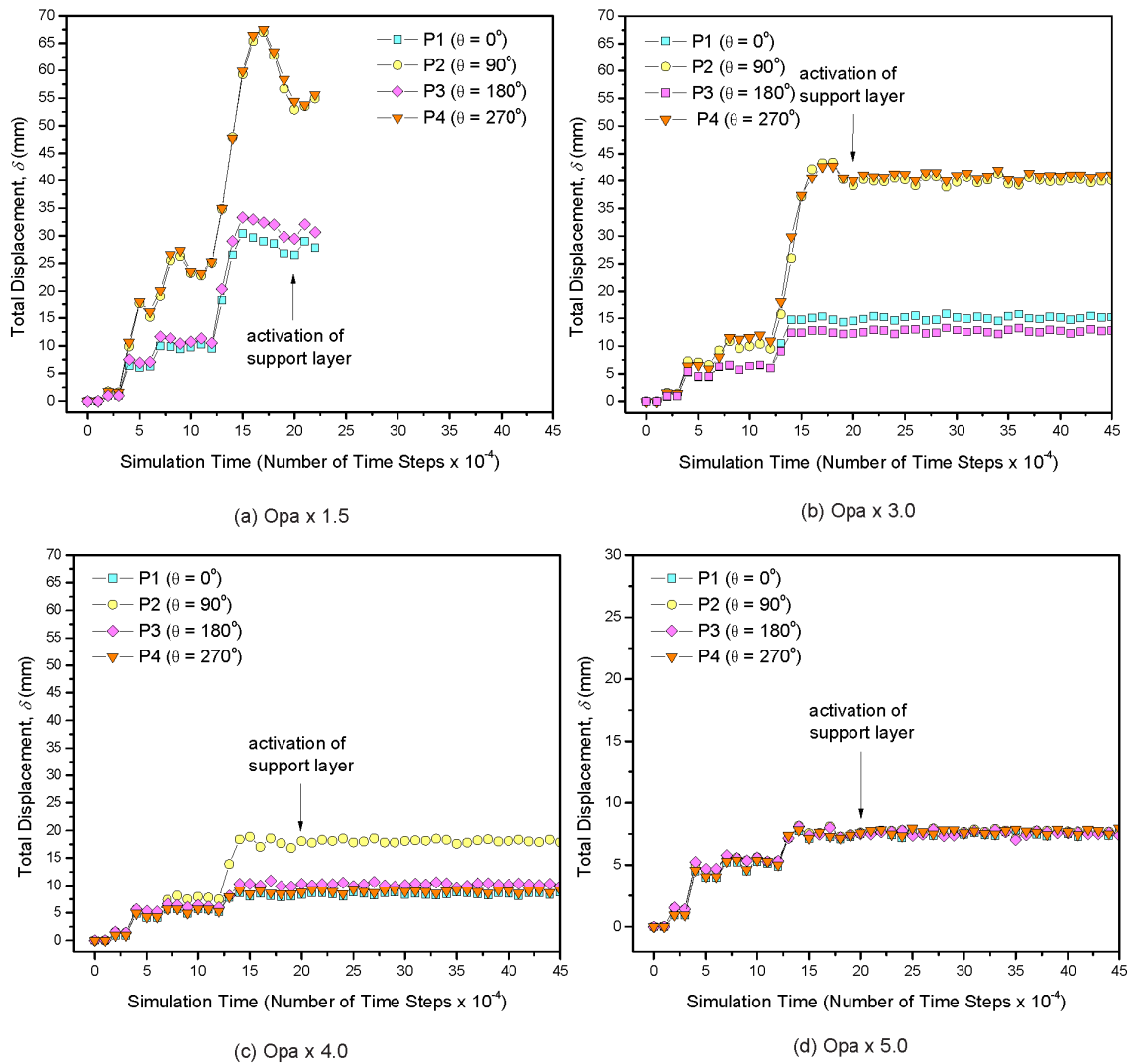


Fig. 6-17: Evolution of displacement, δ , around the excavation boundary of the HAA model for different rock strength levels. The vertical *in situ* stress is equal to 15.9 MPa with a stress ratio $K_0 = 1.3$, while the core softening ratio at the time of support installation is equal to 0.008. The exact location of points P1-P4 is reported in Fig. 5-1.

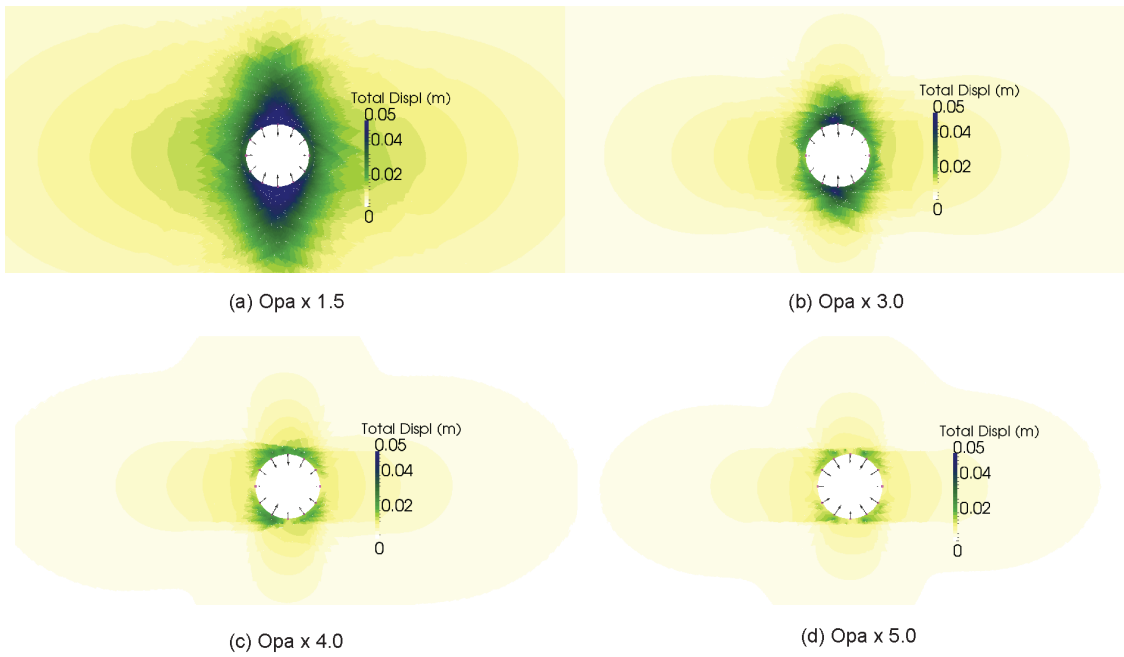


Fig. 6-18: Contours of displacement, δ , of the HAA model for different rock strength levels. The vertical *in situ* stress is equal to 15.9 MPa with a stress ratio $K_0 = 1.3$, while the core softening ratio at the time of support installation is equal to 0.008.

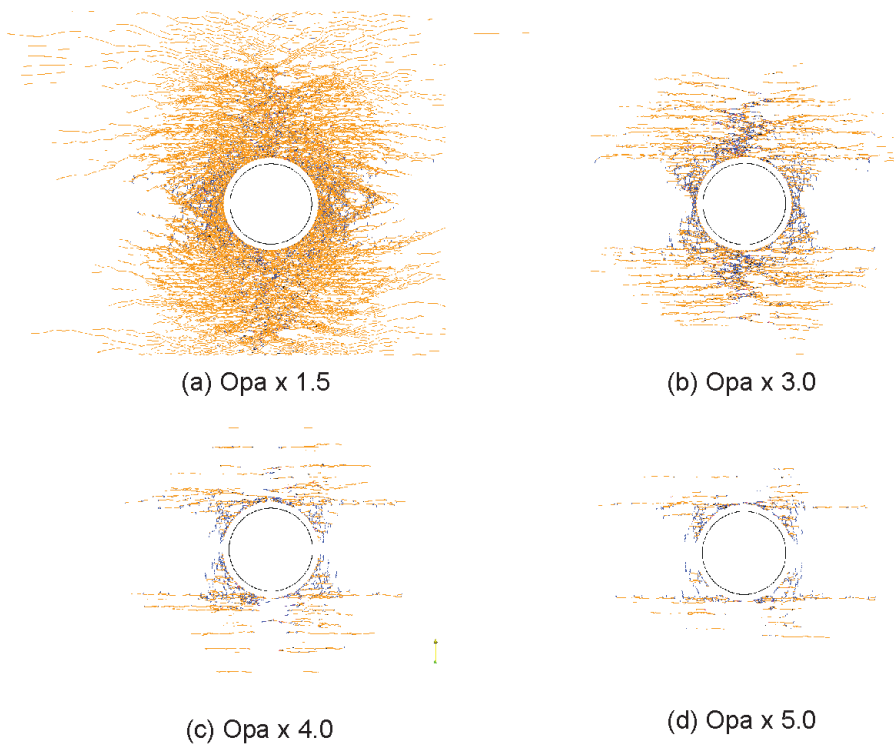


Fig. 6-19: Final fracture patterns of the HAA model for different rock strength levels. Tensile and shear failure are indicated in blue and orange, respectively. The vertical *in situ* stress is equal to 15.9 MPa with a stress ratio $K_0 = 1.3$, while the core softening ratio at the time of support installation is equal to 0.008.

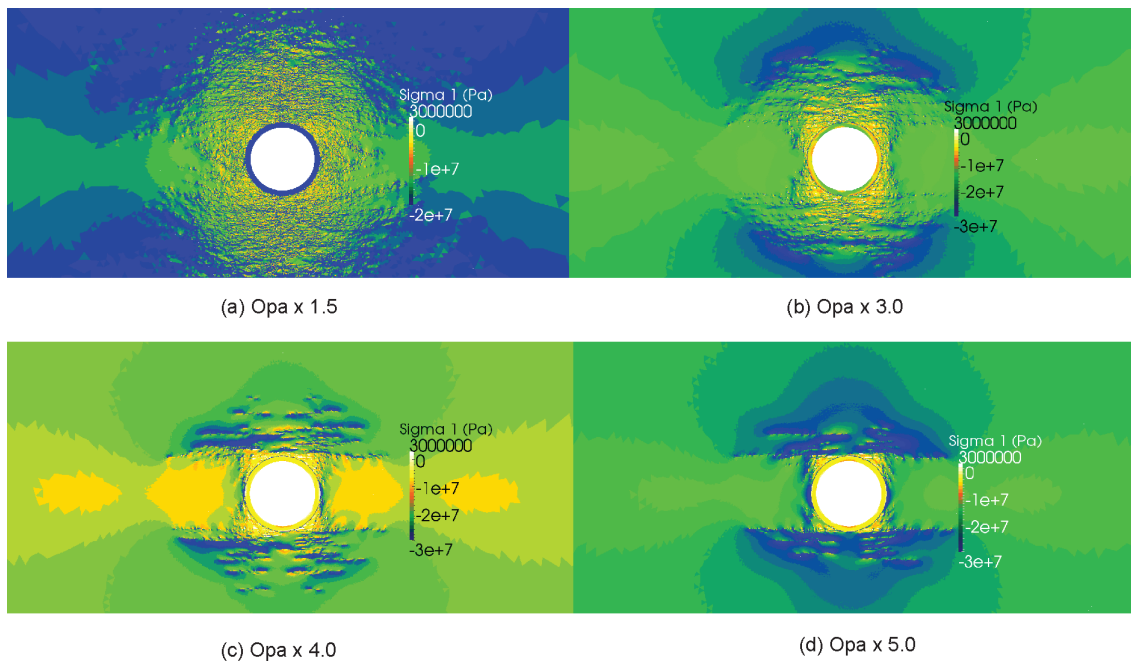


Fig. 6-20: Contours of maximum principal stress, σ_1 , of the HAA model for different rock strength levels. The vertical *in situ* stress is equal to 15.9 MPa with a stress ratio $K_0 = 1.3$, while the core softening ratio at the time of support installation is equal to 0.008.

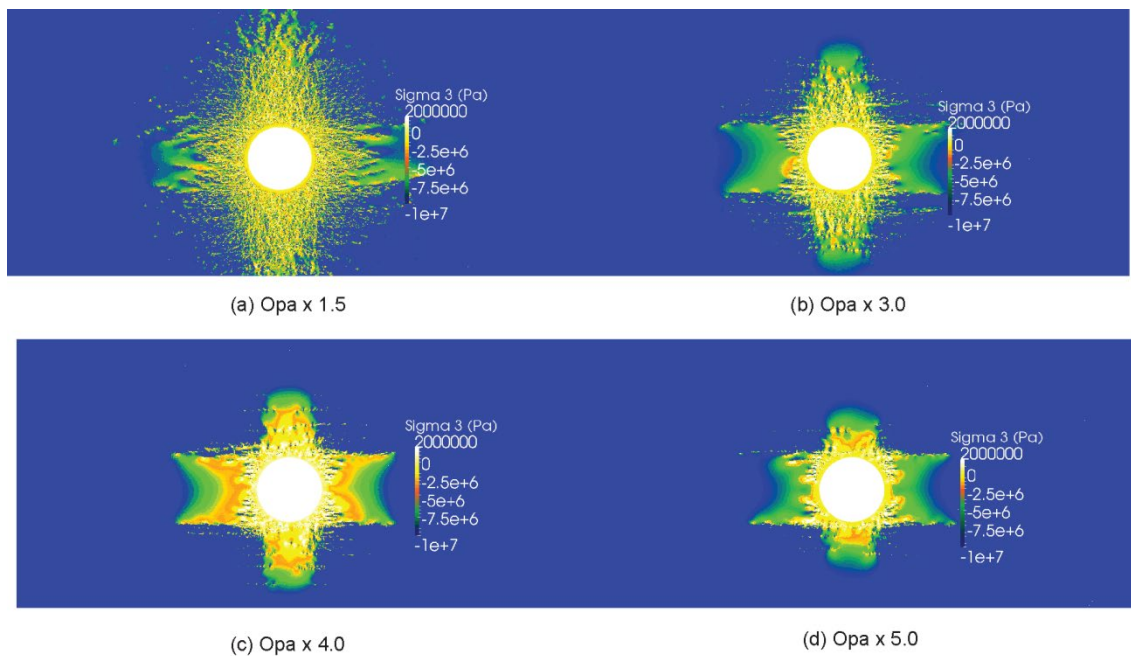


Fig. 6-21: Contours of minimum principal stress, σ_3 , of the HAA model for different rock strength levels. The vertical *in situ* stress is equal to 15.9 MPa with a stress ratio $K_0 = 1.3$, while the core softening ratio at the time of support installation is equal to 0.008.

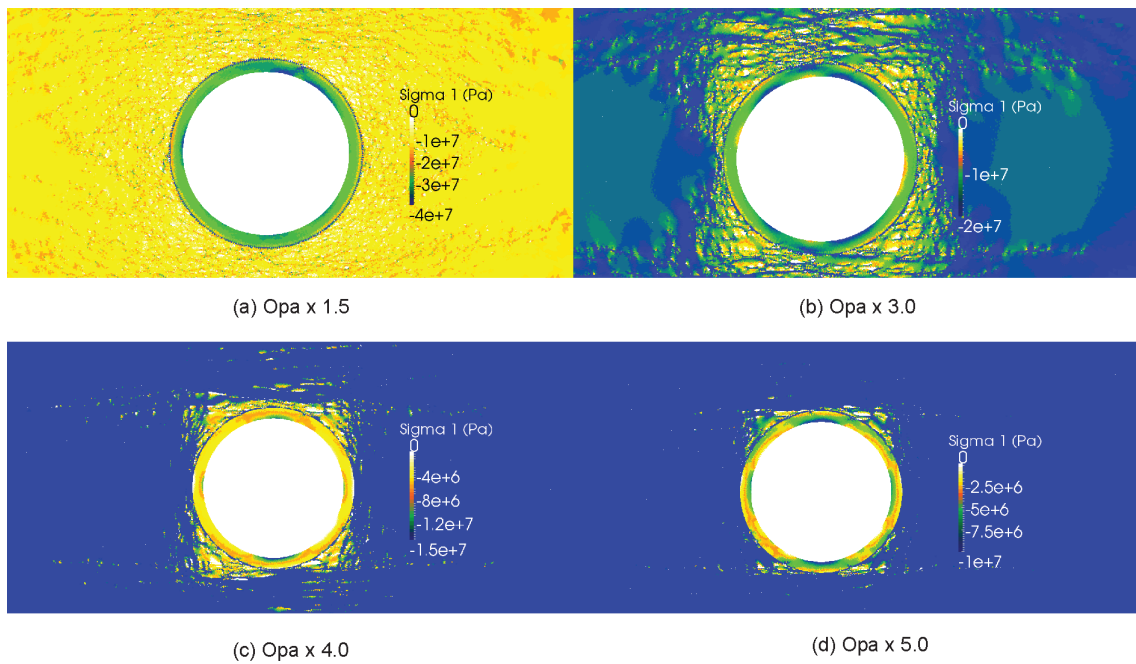


Fig. 6-22: Contours of maximum principal stress, σ_1 , in the support layer of the HAA model for different rock strength levels. The vertical *in situ* stress is equal to 15.9 MPa with a stress ratio $K_0 = 1.3$, while the core softening ratio at the time of support installation is equal to 0.008.

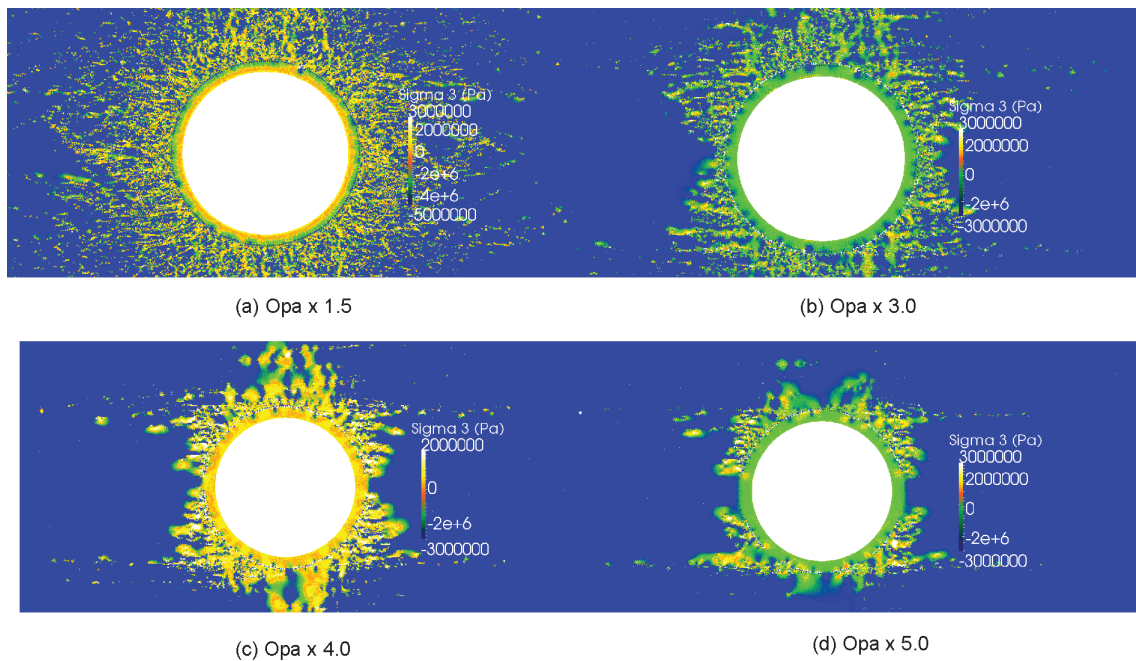


Fig. 6-23: Contours of minimum principal stress, σ_3 , in the support layer of the HAA model for different rock strength levels. The vertical *in situ* stress is equal to 15.9 MPa with a stress ratio $K_0 = 1.3$, while the core softening ratio at the time of support installation is equal to 0.008.

6.3 Analysis of sensitivity to the presence of faults

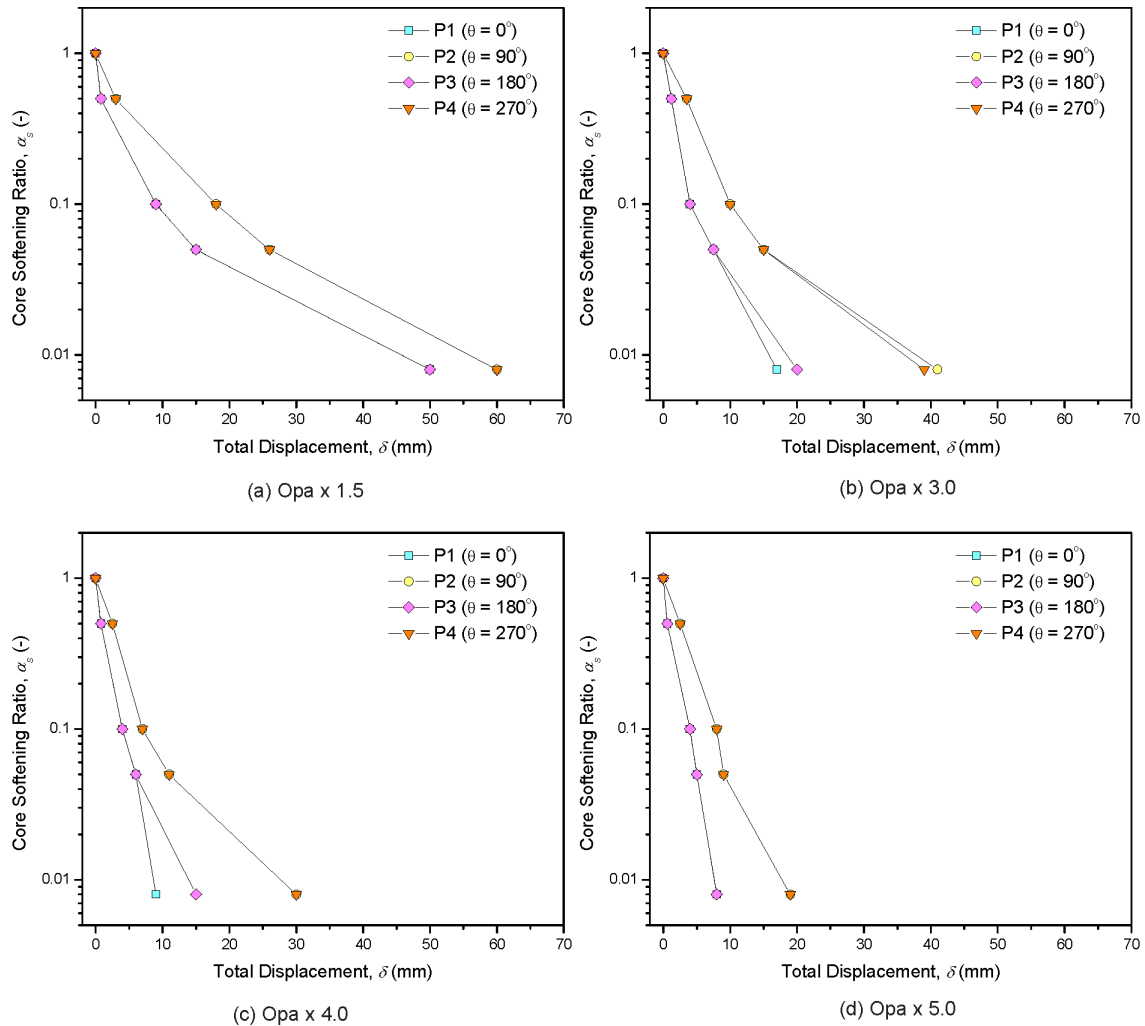


Fig. 6-24: Ground reactions curves of the HAA with faults model for different rock strength levels. The vertical *in situ* stress is equal to 15.9 MPa with a stress ratio $K_0 = 1.3$, while the core softening ratio at the time of support installation is equal to 0.008. The exact location of points P1-P4 is reported in Fig. 5-1.

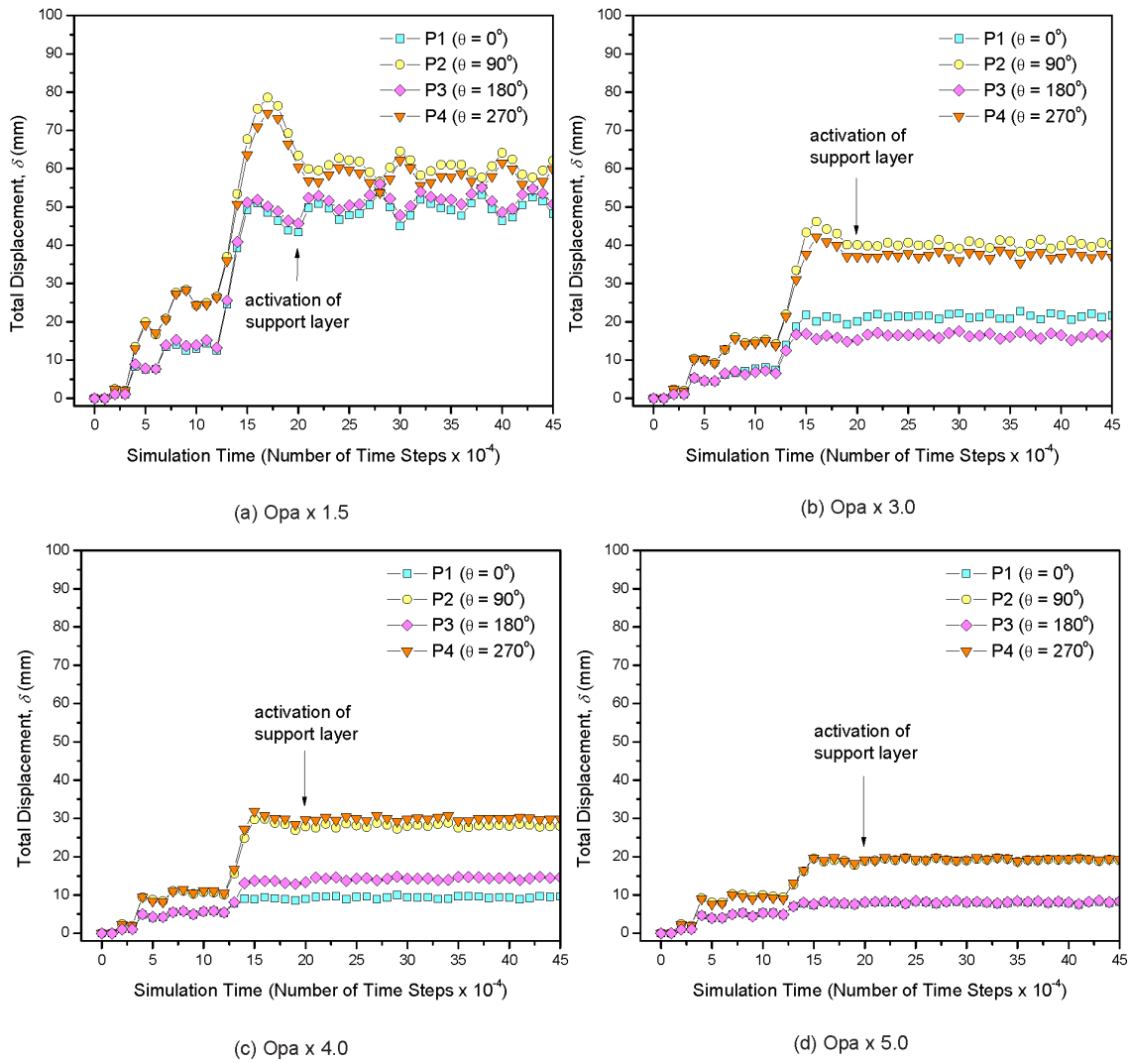


Fig. 6-25: Evolution of displacement, δ , around the excavation boundary of the HAA model with faults for different rock strength levels. The vertical *in situ* stress is equal to 15.9 MPa with a stress ratio $K_0 = 1.3$, while the core softening ratio at the time of support installation is equal to 0.008. The exact location of points P1-P4 is reported in Fig.5-1.

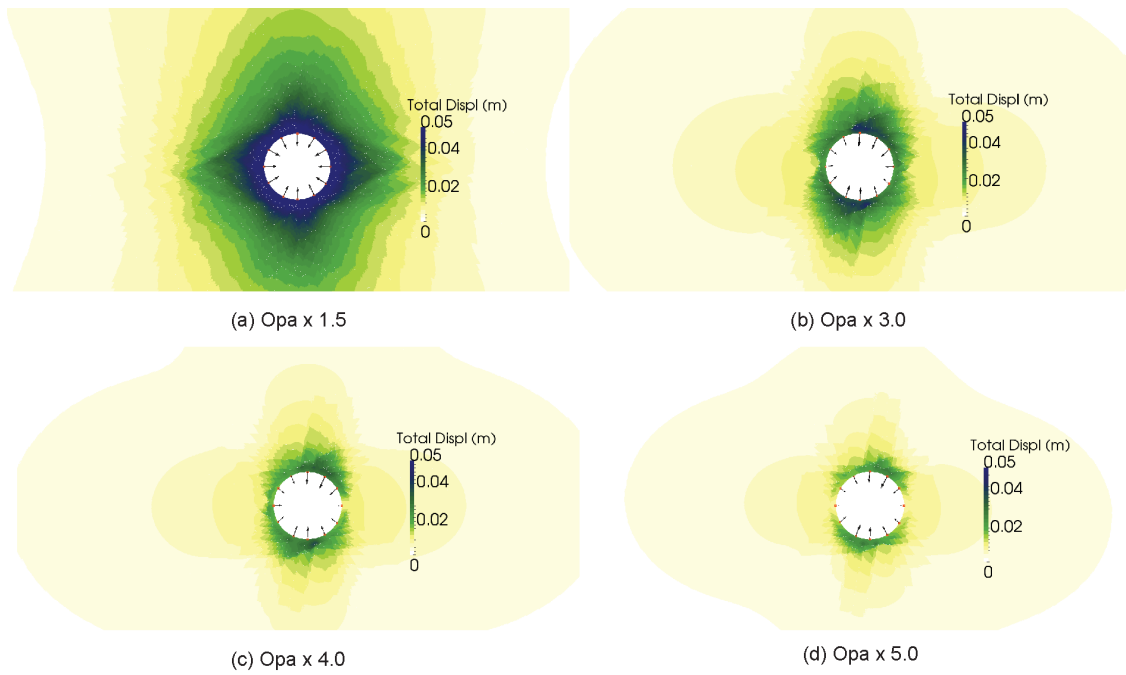


Fig. 6-26: Contours of displacement, δ , of the HAA model with faults for different rock strength levels. The vertical *in situ* stress is equal to 15.9 MPa with a stress ratio $K_0 = 1.3$, while the core softening ratio at the time of support installation is equal to 0.008.

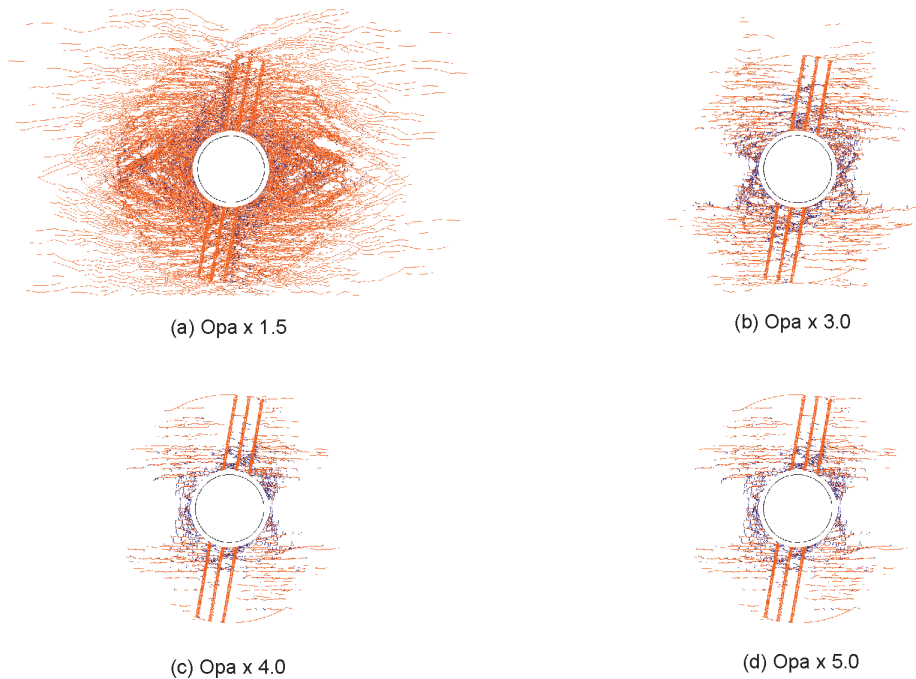


Fig. 6-27: Final fracture patterns of the HAA model with faults for different rock strength levels. Tensile and shear failure are indicated in blue and orange, respectively. The vertical *in situ* stress is equal to 15.9 MPa with a stress ratio $K_0 = 1.3$, while the core softening ratio at the time of support installation is equal to 0.008.

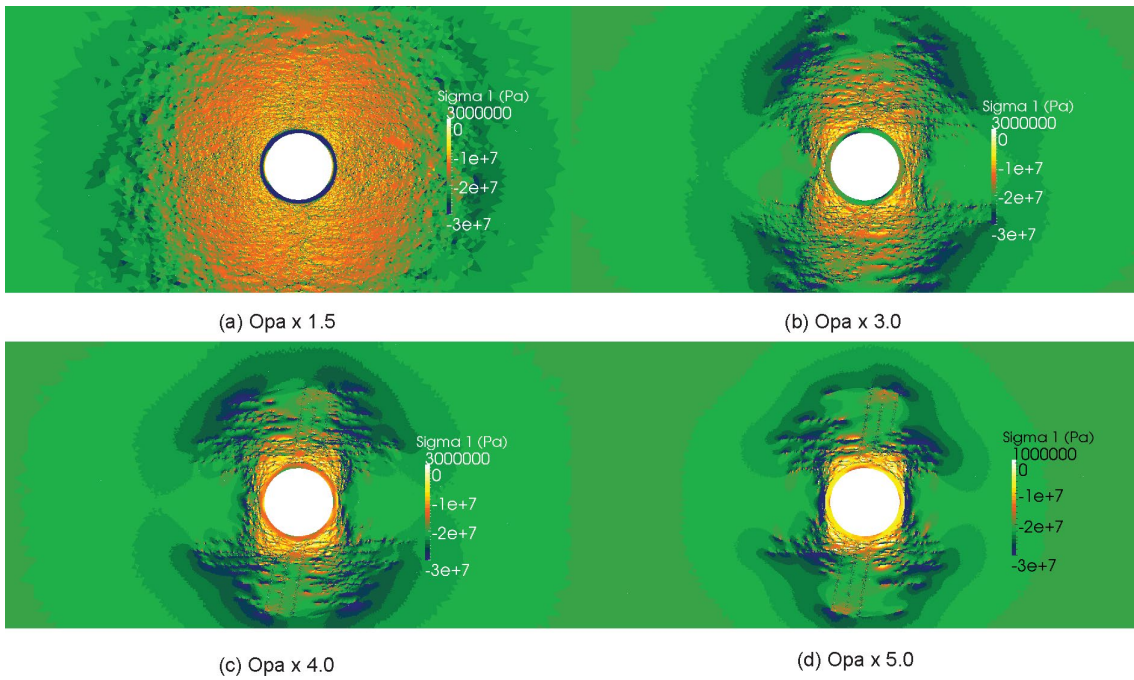


Fig. 6-28: Contours of maximum principal stress, σ_1 , of the HAA model with faults for different rock strength levels. The vertical *in situ* stress is equal to 15.9 MPa with a stress ratio $K_0 = 1.3$, while the core softening ratio at the time of support installation is equal to 0.008.

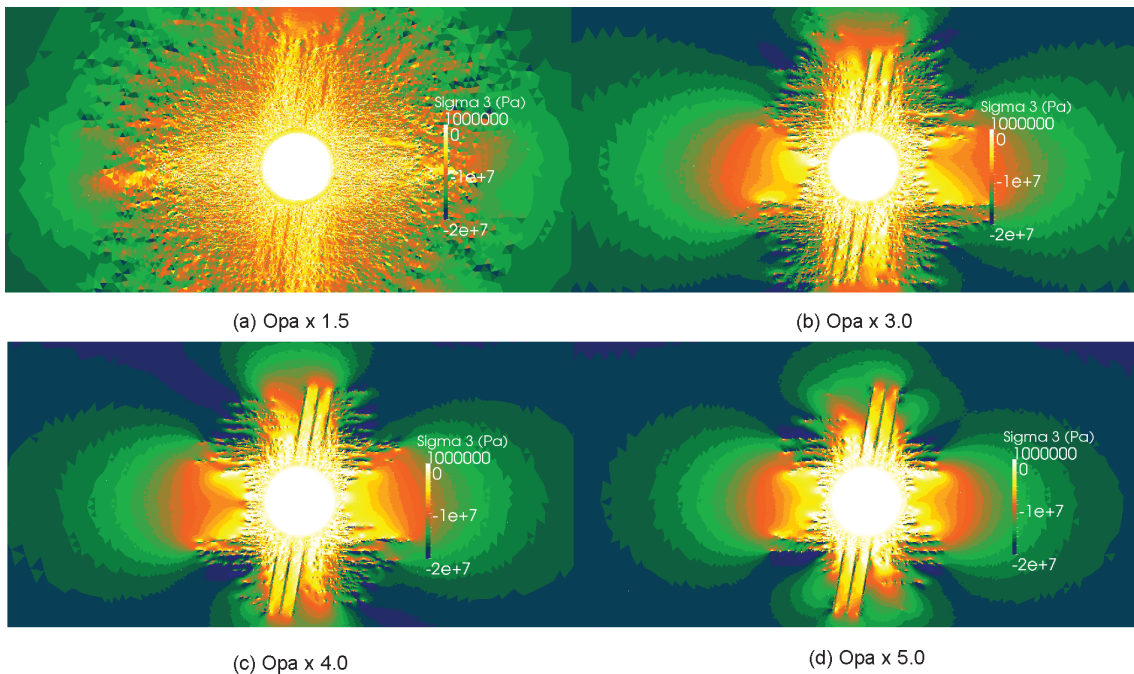


Fig. 6-29: Contours of minimum principal stress, σ_3 , of the HAA model with faults for different rock strength levels. The vertical *in situ* stress is equal to 15.9 MPa with a stress ratio $K_0 = 1.3$, while the core softening ratio at the time of support installation is equal to 0.008.

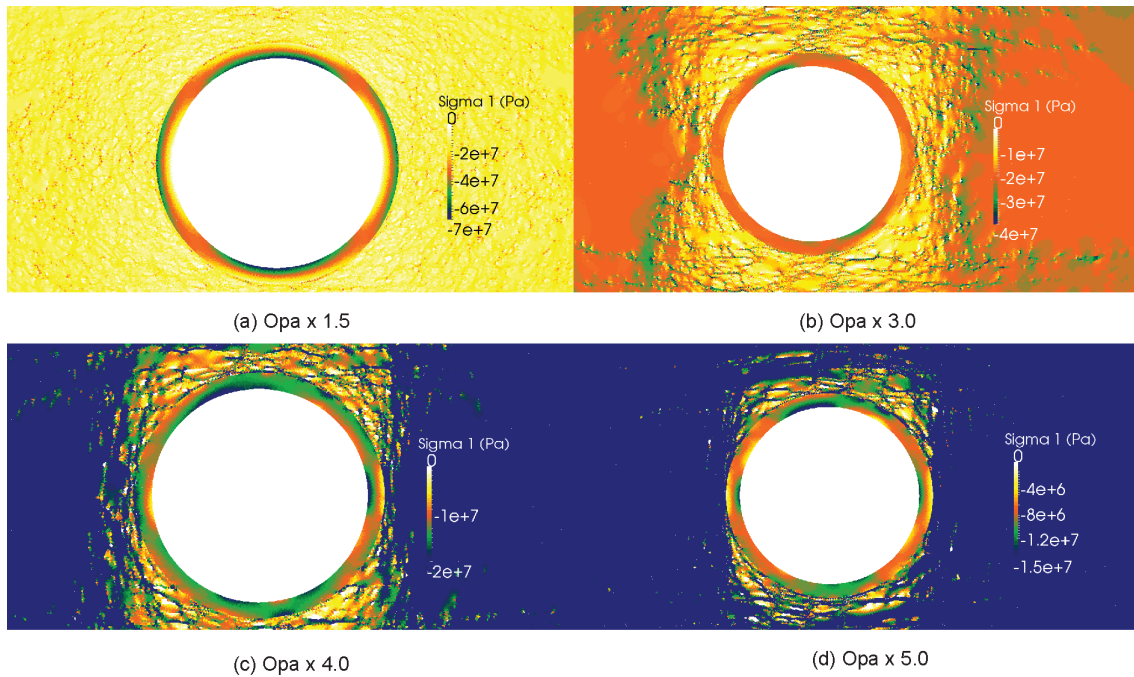


Fig. 6-30: Contours of maximum principal stress, σ_1 , in the support layer of the HAA model with faults for different rock strength levels. The vertical *in situ* stress is equal to 15.9 MPa with a stress ratio $K_0 = 1.3$, while the core softening ratio at the time of support installation is equal to 0.008.

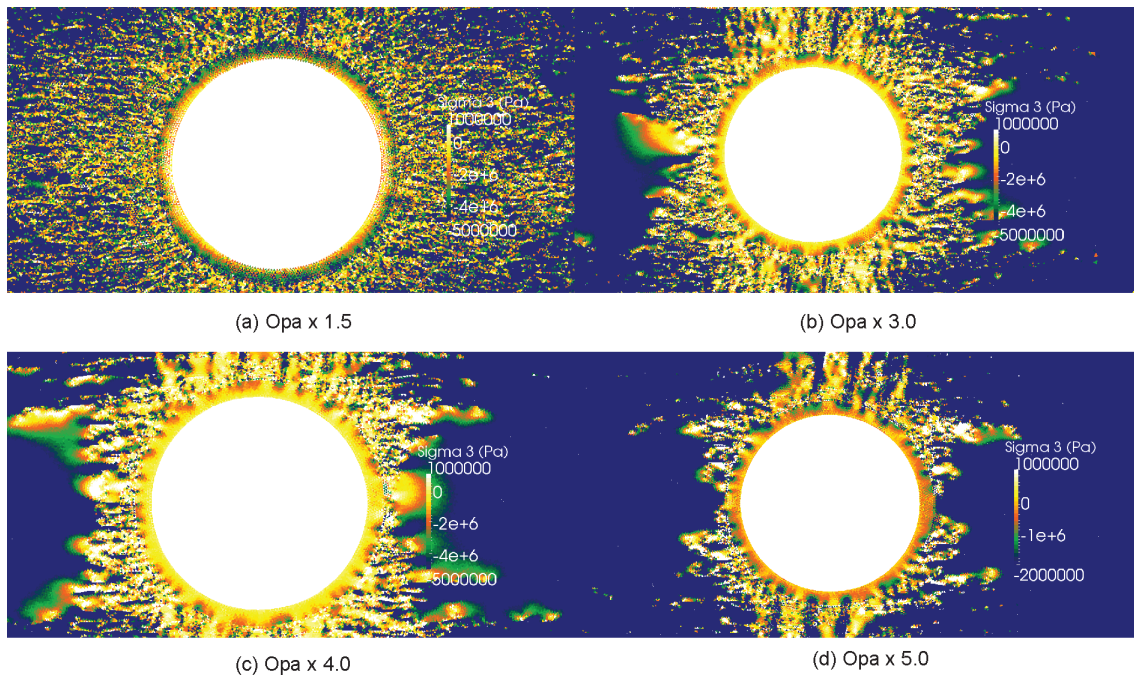


Fig. 6-31: Contours of minimum principal stress, σ_3 , in the support layer of the HAA model with faults for different rock strength levels. The vertical *in situ* stress is equal to 15.9 MPa with a stress ratio $K_0 = 1.3$, while the core softening ratio at the time of support installation is equal to 0.008.

6.4 Analysis of sensitivity to shotcrete stiffness

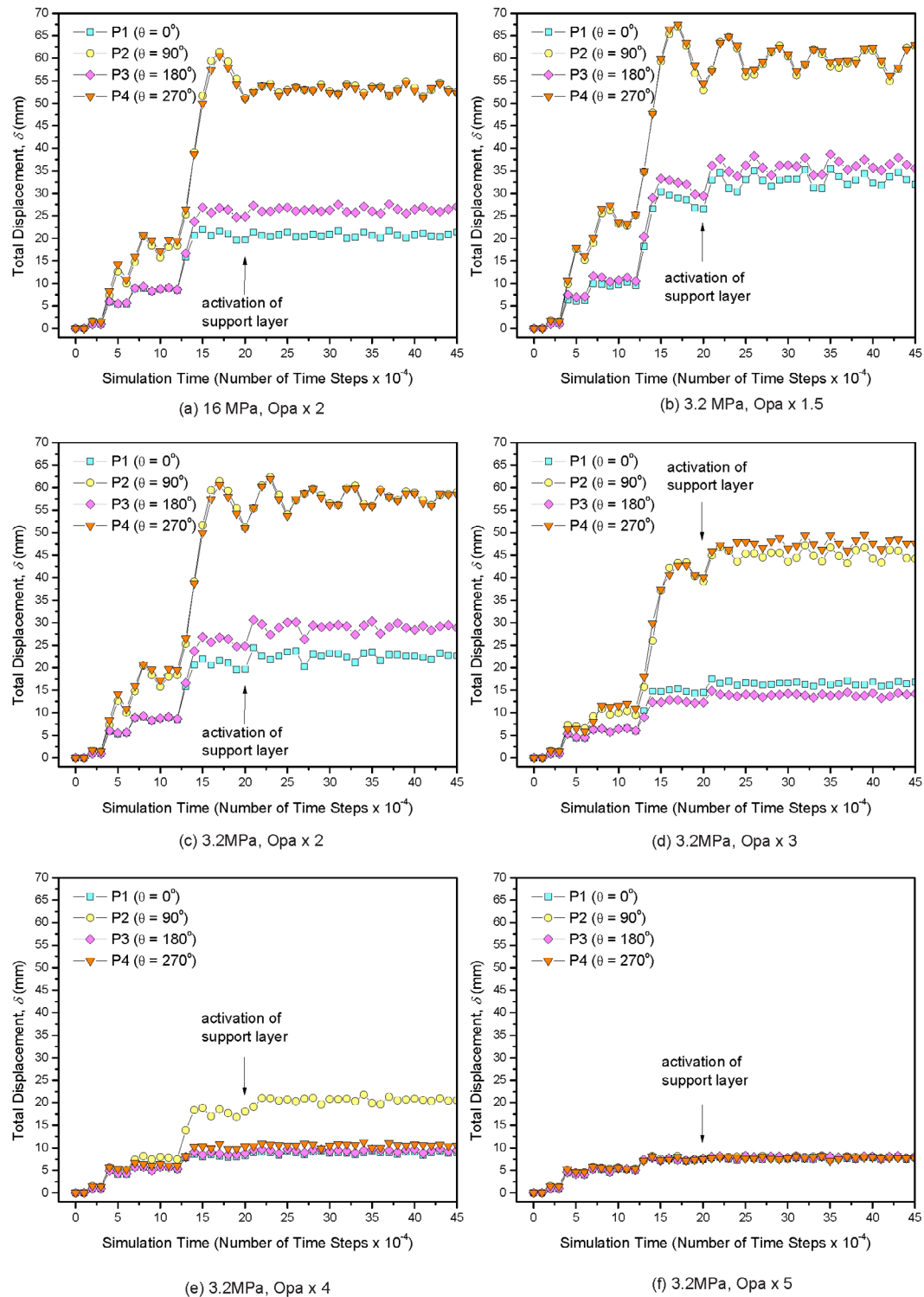


Fig. 6-32: Evolution of displacement, δ , around the excavation boundary of the HAA model for different rock strength levels and values of the shotcrete elastic modulus, E_c . The vertical *in situ* stress is equal to 15.9 MPa with a stress ratio $K_0 = 1.3$, while the core softening ratio at the time of support installation is equal to 0.008. The exact location of points P1-P4 is reported in Fig. 5-1.

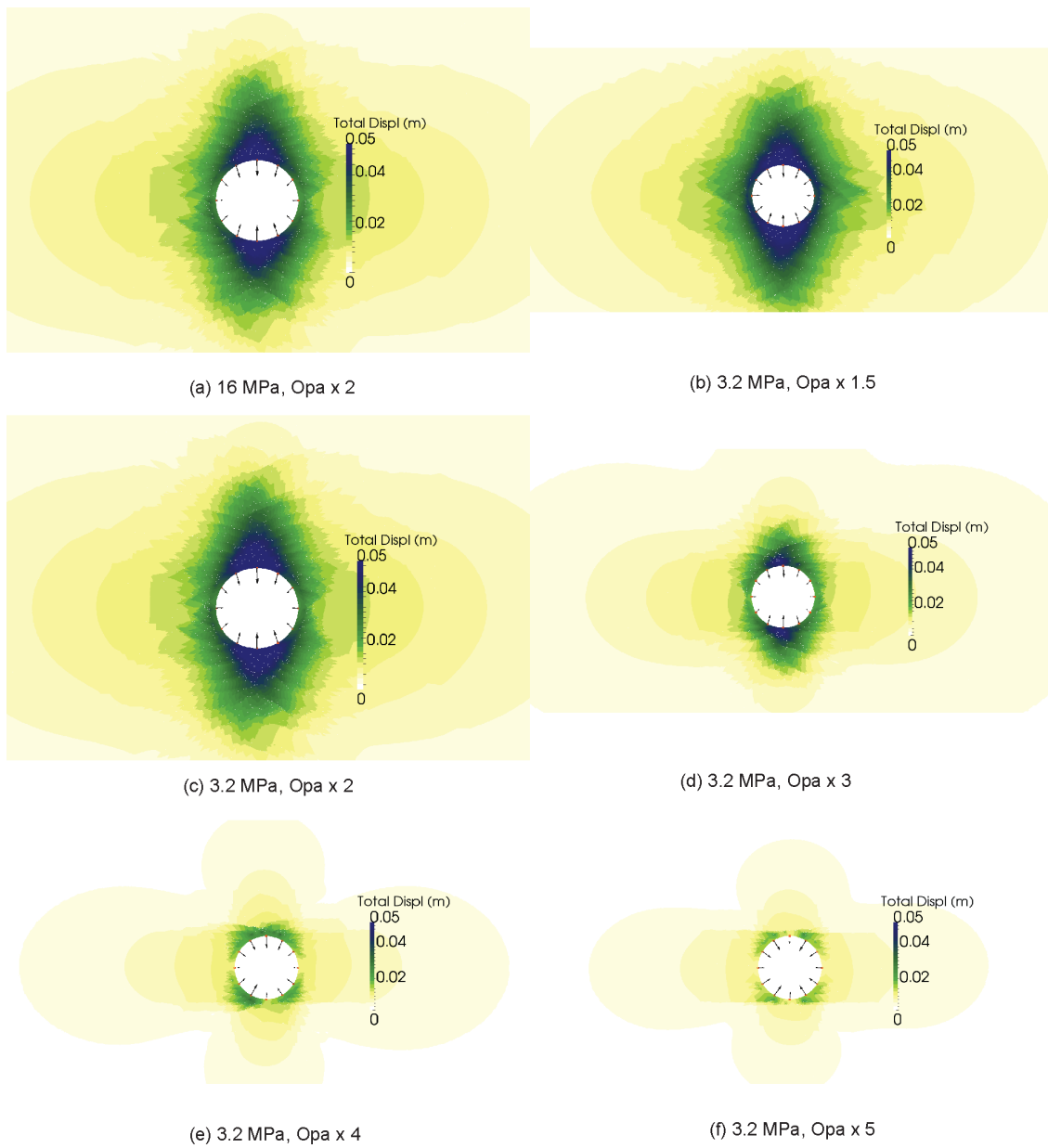


Fig. 6-33: Contour of displacement, δ , of the HAA model for different rock strength levels and values of the shotcrete elastic modulus, E_c . The vertical *in situ* stress is equal to 15.9 MPa with a stress ratio $K_0 = 1.3$, while the core softening ratio at the time of support installation is equal to 0.008.

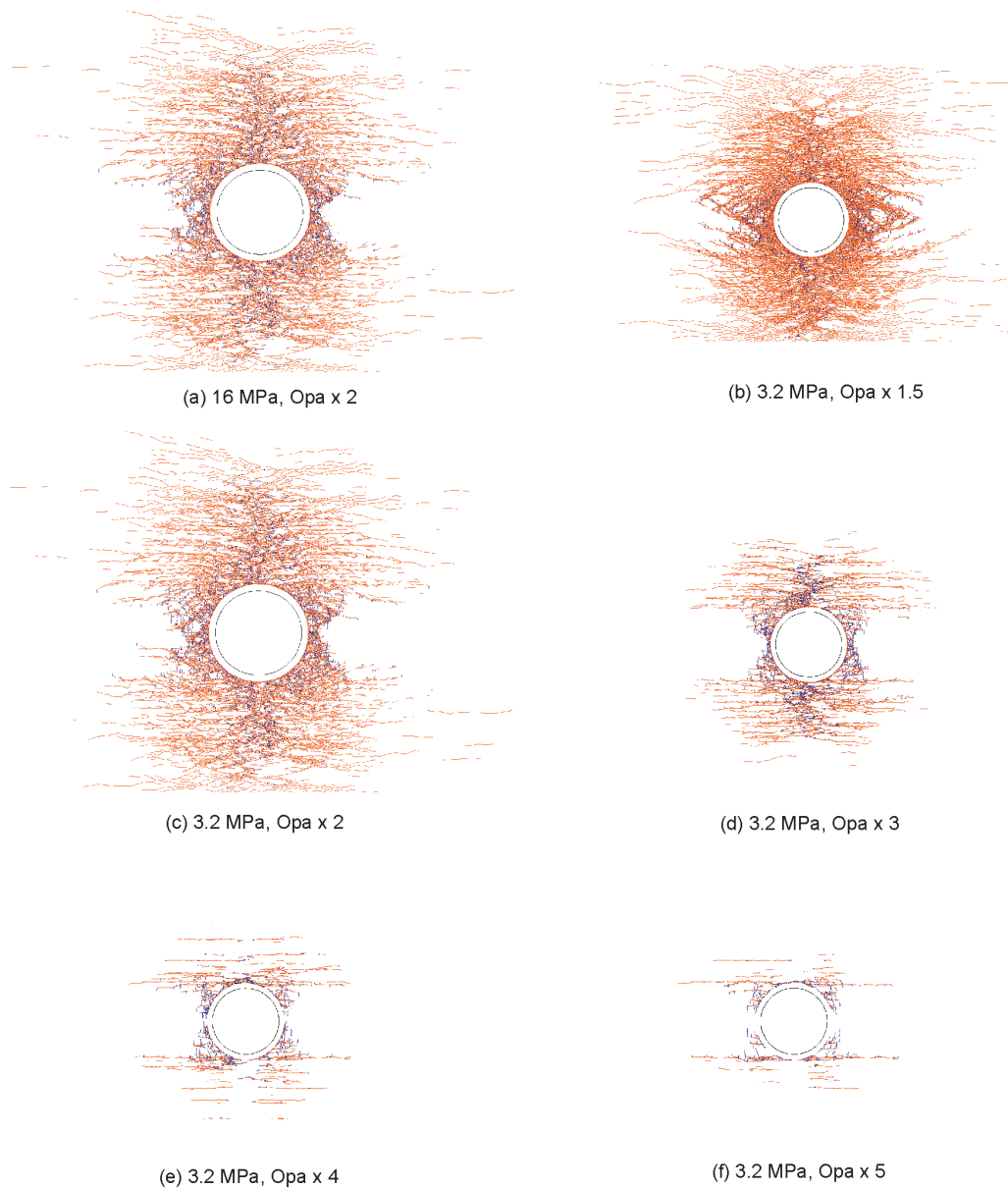


Fig. 6-34: Final fracture patterns of the HAA model for different rock strength levels and values of the shotcrete elastic modulus, E_c . Tensile and shear failure are indicated in blue and orange, respectively. The vertical *in situ* stress is equal to 15.9 MPa with a stress ratio $K_0 = 1.3$, while the core softening ratio at the time of support installation is equal to 0.008.

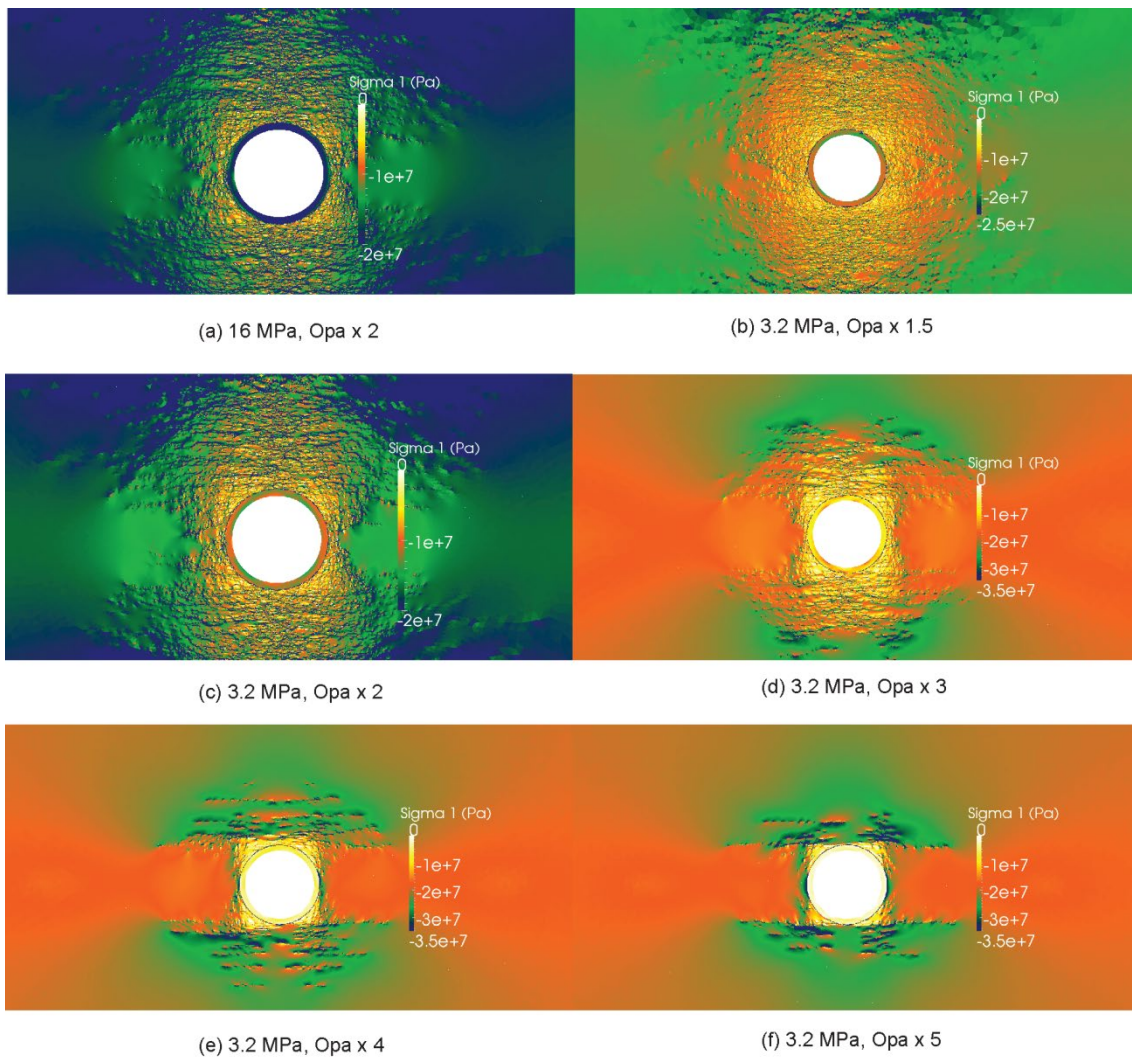


Fig. 6-35: Contours of maximum principal stress, σ_1 , of the HAA model for different rock strength levels and values of the shotcrete elastic modulus, E_c . The vertical *in situ* stress is equal to 15.9 MPa with a stress ratio $K_0 = 1.3$, while the core softening ratio at the time of support installation is equal to 0.008.

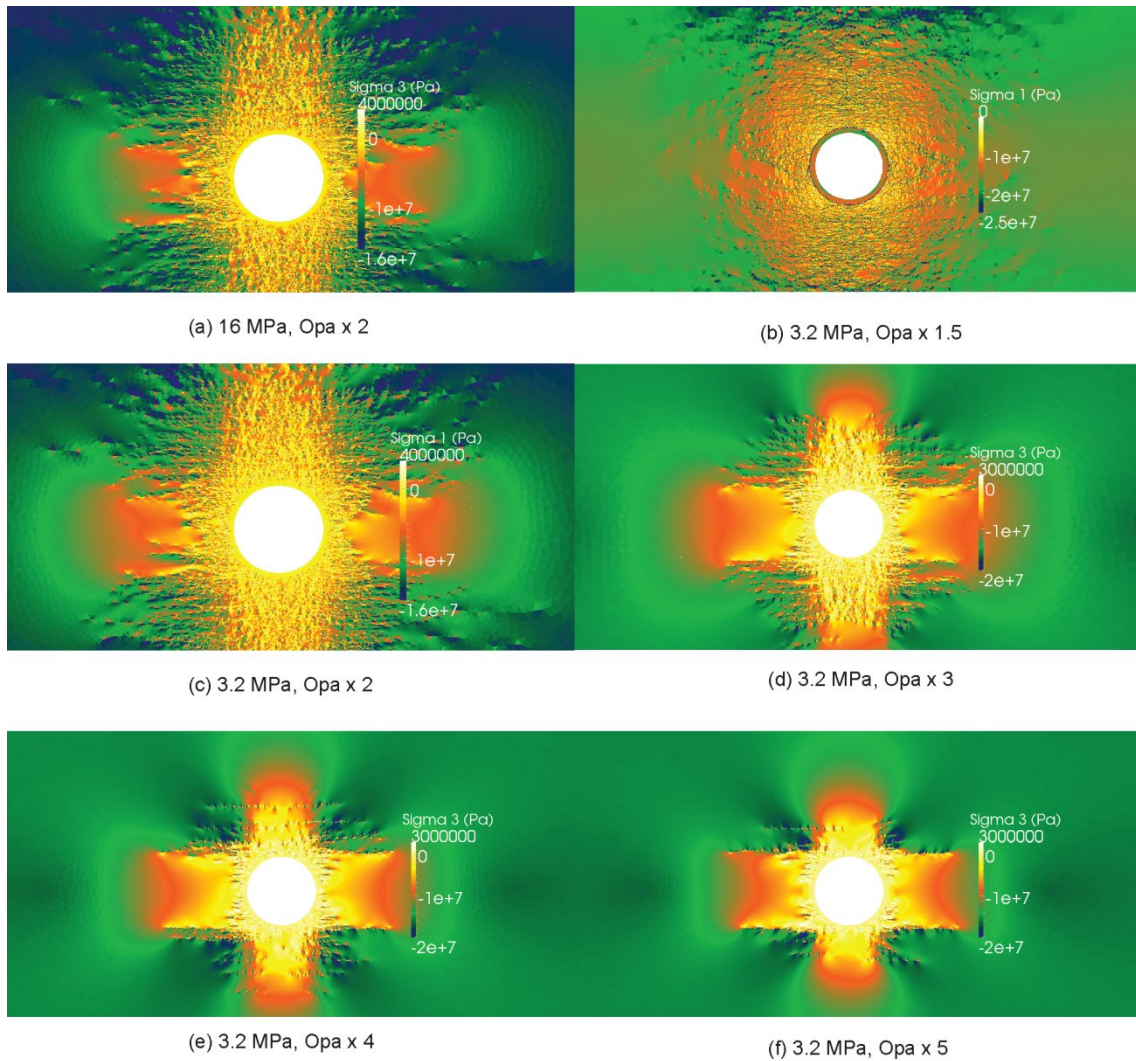


Fig. 6-36: Contours of minimum principal stress, σ_3 , of the HAA model for different rock strength levels and values of the shotcrete elastic modulus, E_c . The vertical *in situ* stress is equal to 15.9 MPa with a stress ratio $K_0 = 1.3$, while the core softening ratio at the time of support installation is equal to 0.008.

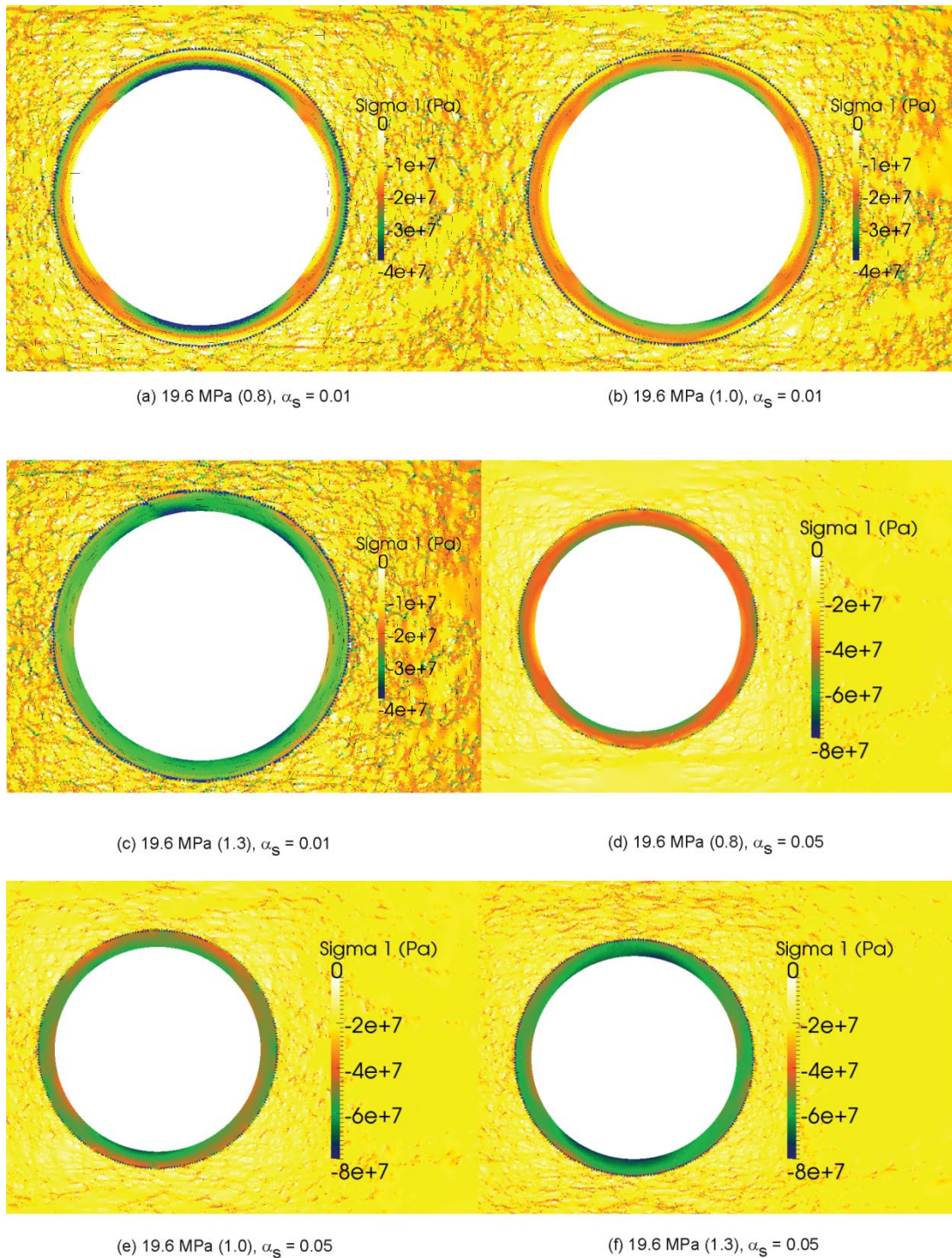


Fig. 6-37: Contours of maximum principal stress, σ_1 , in the support layer of the HAA model for different rock strength levels and values of the shotcrete elastic modulus, E_c . The vertical *in situ* stress is equal to 15.9 MPa with a stress ratio $K_0 = 1.3$, while the core softening ratio at the time of support installation is equal to 0.008.

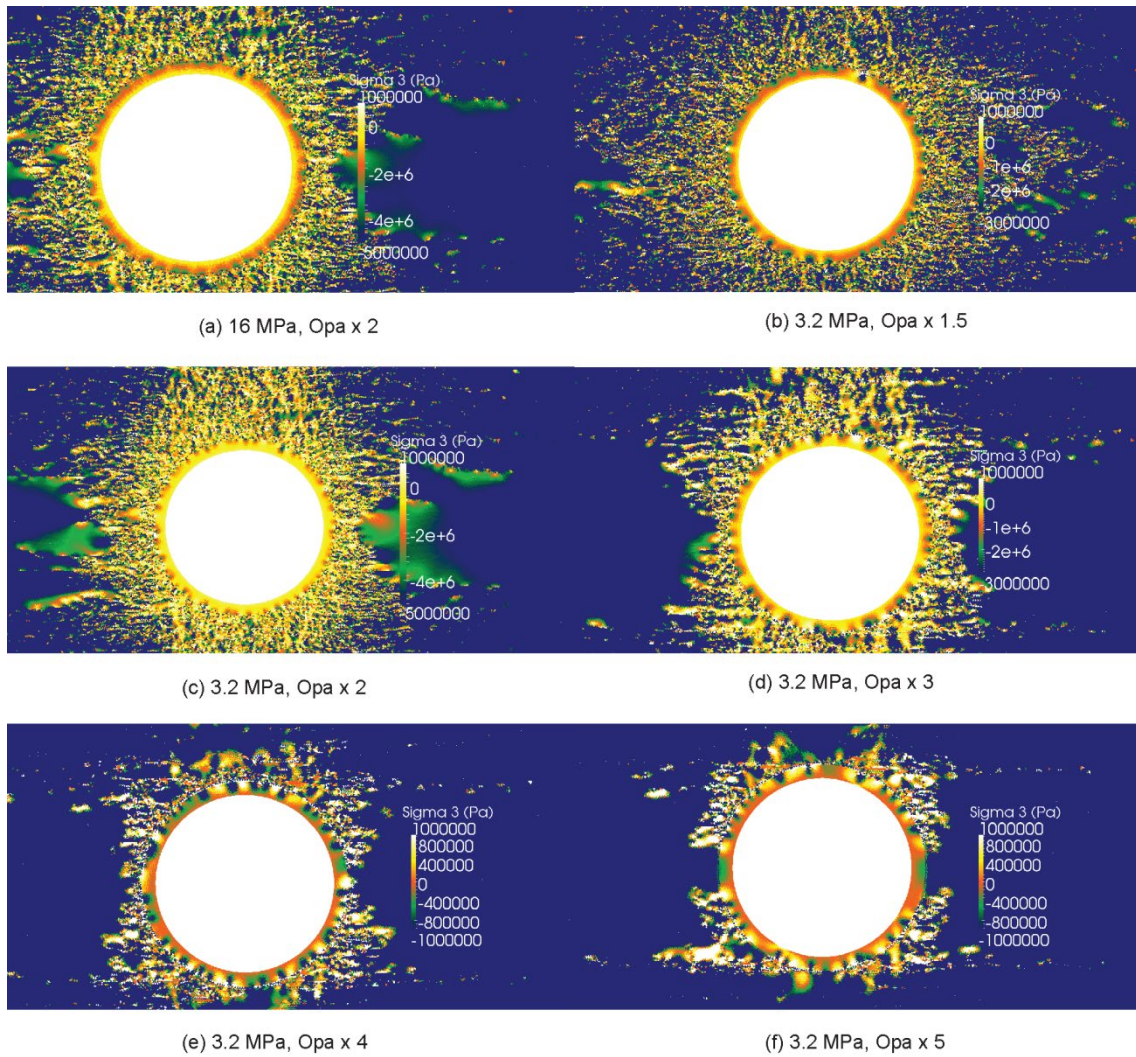


Fig. 6-38: Contours of minimum principal stress, σ_3 , in the support layer of the HAA model for different rock strength levels and values of the shotcrete elastic modulus, E_c . The vertical *in situ* stress is equal to 15.9 MPa with a stress ratio $K_0 = 1.3$, while the core softening ratio at the time of support installation is equal to 0.008.

7 Results: EDZ simulations for L/ILW emplacement cavern

Tab. 7: Summary of K09 model simulations.

Model	Section	In situ stress conditions	Strength properties	Elastic modulus of support	Faults	Core softening ratio at support installation	Reconsolidation pressure
Sensitivity to <i>in situ</i> stress conditions							
SMA-1	K09	18.4, 0.8	OPA x 2	32	N/A	0.01	N/A
SMA-2	K09	18.4, 1.0	OPA x 2	32	N/A	0.01	N/A
SMA-3	K09	18.4, 1.3	OPA x 2	32	N/A	0.01	N/A
SMA-4	K09	15.9, 0.8	OPA x 2	32	N/A	0.01	N/A
SMA-5	K09	15.9, 1.0	OPA x 2	32	N/A	0.01	N/A
SMA-6	K09	15.9, 1.3	OPA x 2	32	N/A	0.01	N/A
SMA-7	K09	11.0, 1.3	OPA x 2	32	N/A	0.05	N/A
Sensitivity to strength parameters							
SMA-8	K09	18.4, 1.0	OPA x 1.5	32	N/A	0.01	N/A
SMA-9	K09	18.4, 1.0	OPA x 3.0	32	N/A	0.01	N/A
Sensitivity to the presence of faults							
SMA-10	K09	18.4, 1.0	OPA x 1.5	32	yes	0.01	N/A
SMA-11	K09	18.4, 1.0	OPA x 2.0	32	yes	0.01	N/A
SMA-12	K09	18.4, 1.0	OPA x 3.0	32	yes	0.01	N/A

7.1 Analysis of sensitivity to *in situ* stress conditions

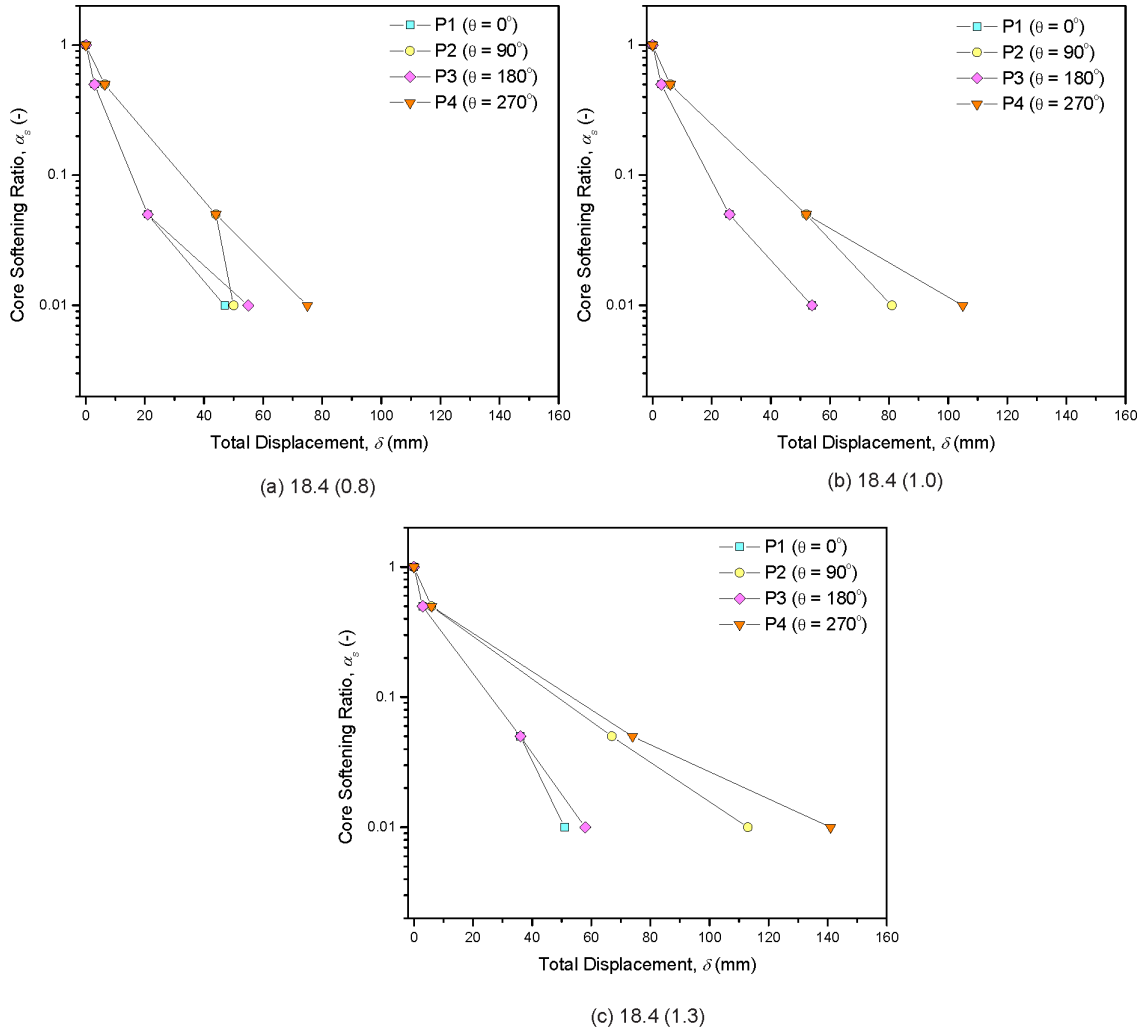


Fig. 7-1: Ground reactions curves of the K09 model under different *in situ* stress conditions. For each case, the *in situ* vertical stress, σ_v , is reported together with the stress ratio, K_0 , in brackets. The exact location of points P1-P4 is reported in Fig. 5-2.

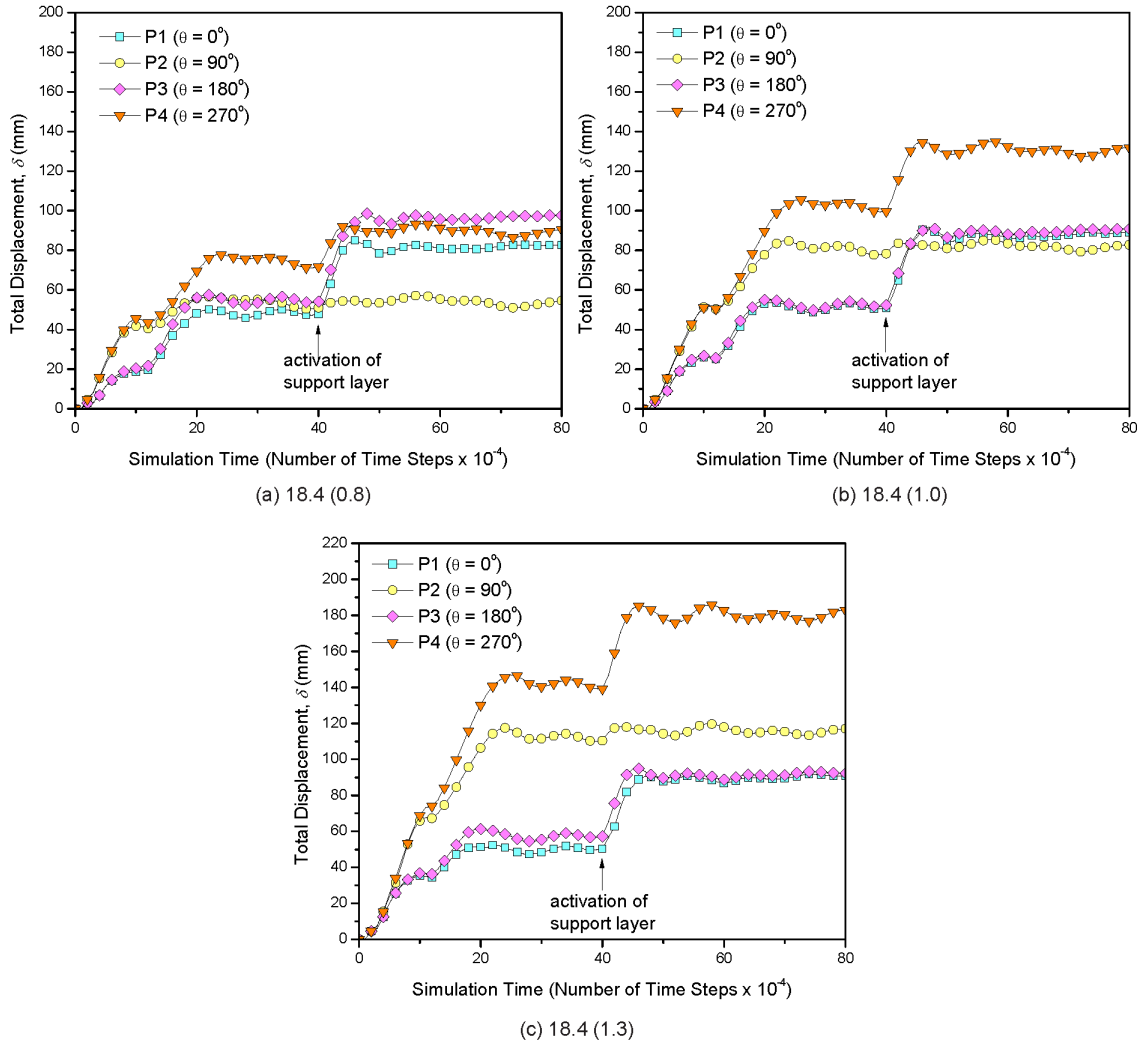


Fig. 7-2: Evolution of displacement, δ , around the excavation boundary of the K09 model under different in situ stress conditions. The core softening ratio at the time of support installation is equal to 0.01. Rock strength parameters are "Opa x 2". The exact location of points P1-P4 is reported in Fig. 5-2.

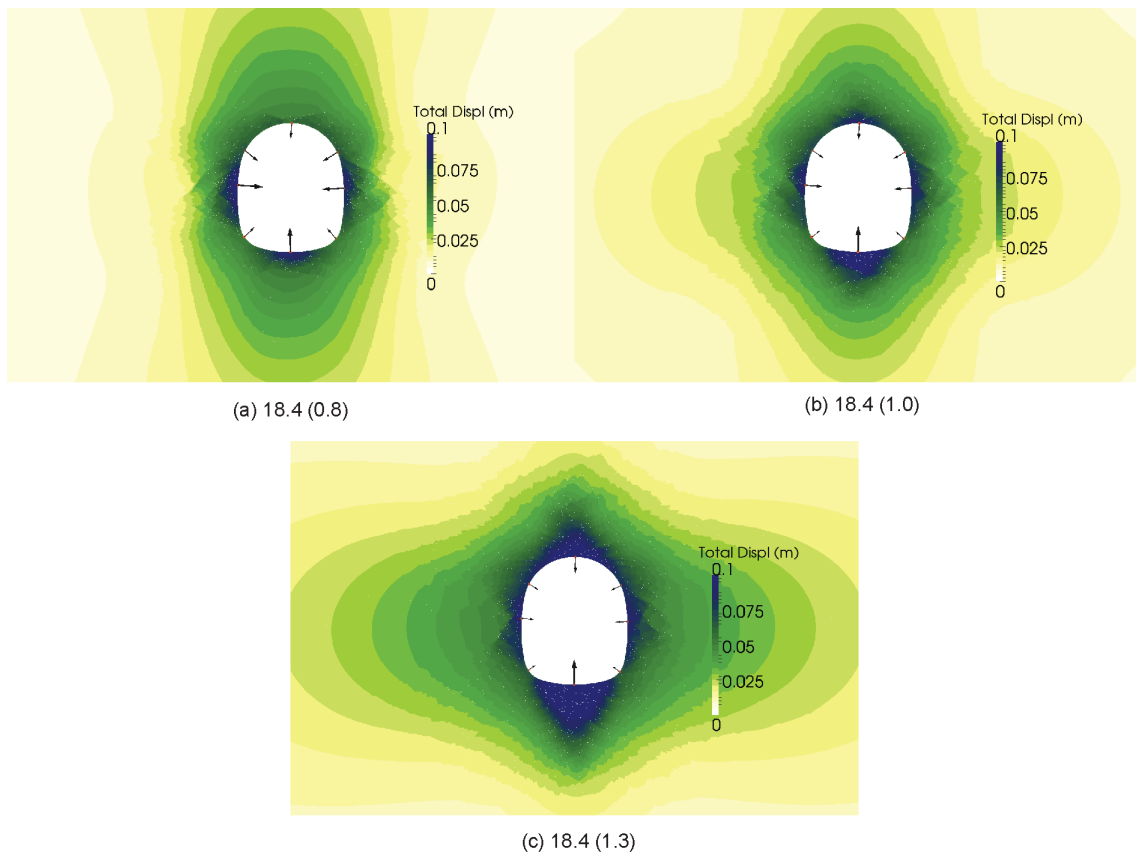


Fig. 7-3: Contour of displacement, δ , of the K09 model under different *in situ* stress conditions. The core softening ratio at the time of support installation is equal to 0.01. Rock strength parameters are "Opa x 2".

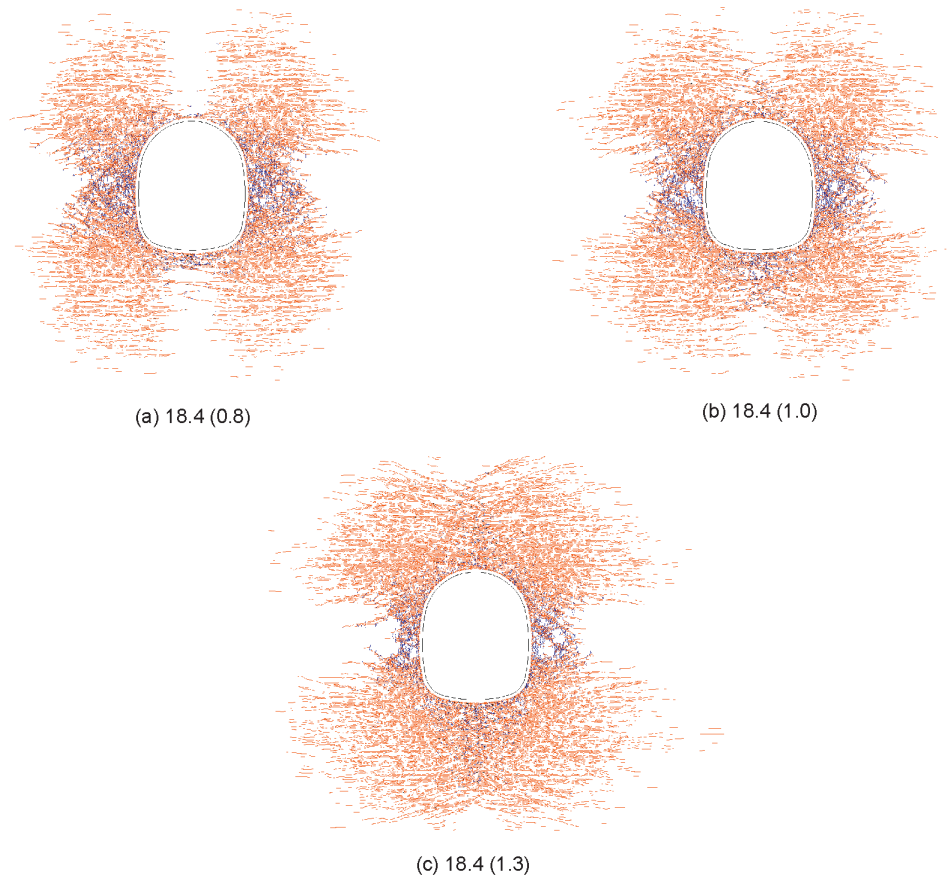


Fig. 7-4: Fracture patterns around the excavation of the K09 model under different *in situ* stress conditions. Tensile and shear failure are indicated in blue and orange, respectively. The core softening ratio at the time of support installation is equal to 0.01. Rock strength parameters are "Opa x 2".

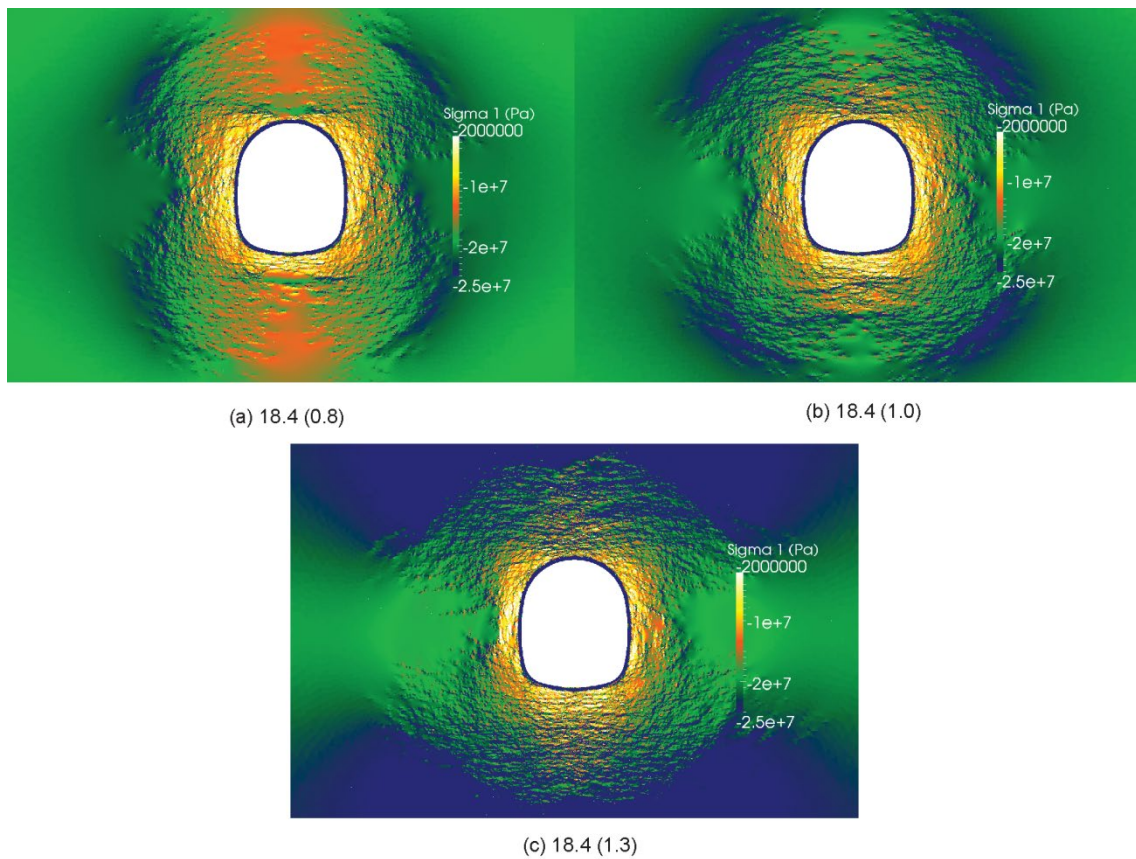


Fig. 7-5: Contours of maximum principal stress, σ_1 , of the K09 model under different *in situ* stress conditions. The core softening ratio at the time of support installation is equal to 0.01. Rock strength parameters are "Opa x 2".

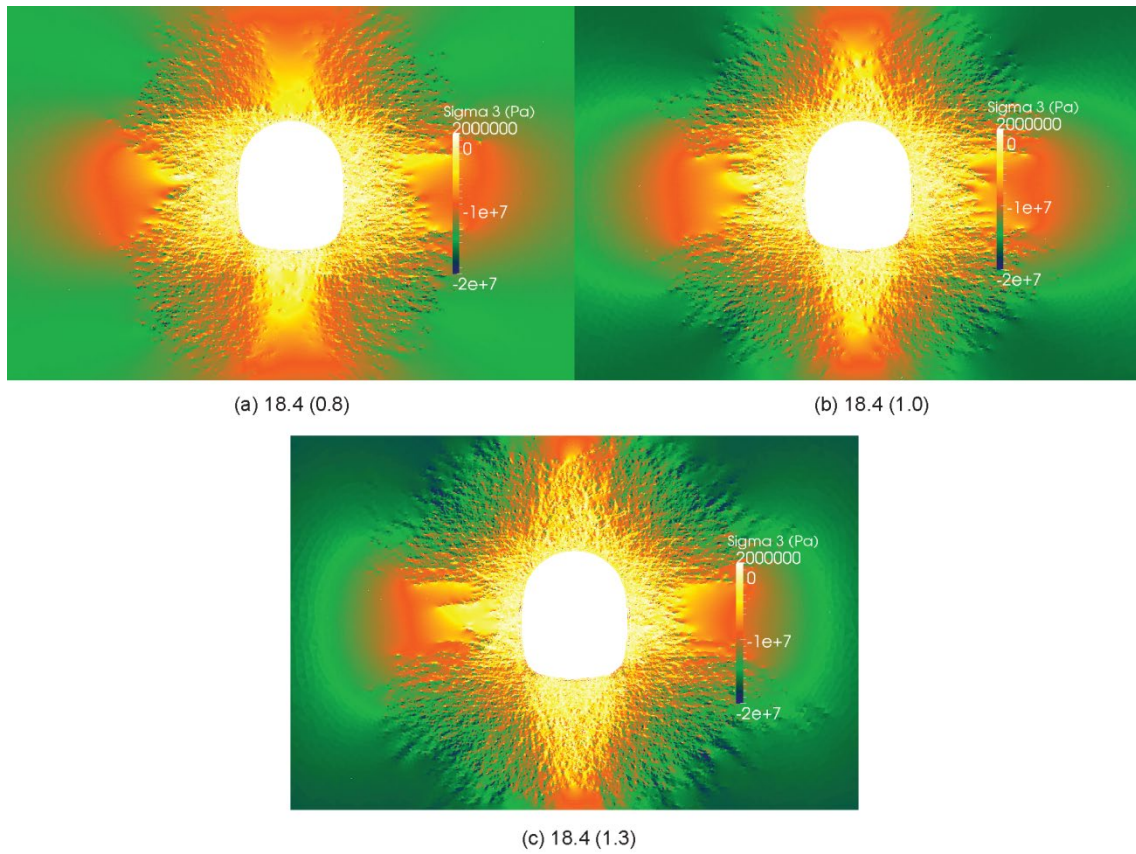


Fig. 7-6: Contours of minimum principal stress, σ_3 , of the K09 model under different *in situ* stress conditions. The core softening ratio at the time of support installation is equal to 0.01. Rock strength parameters are "Opa x 2".

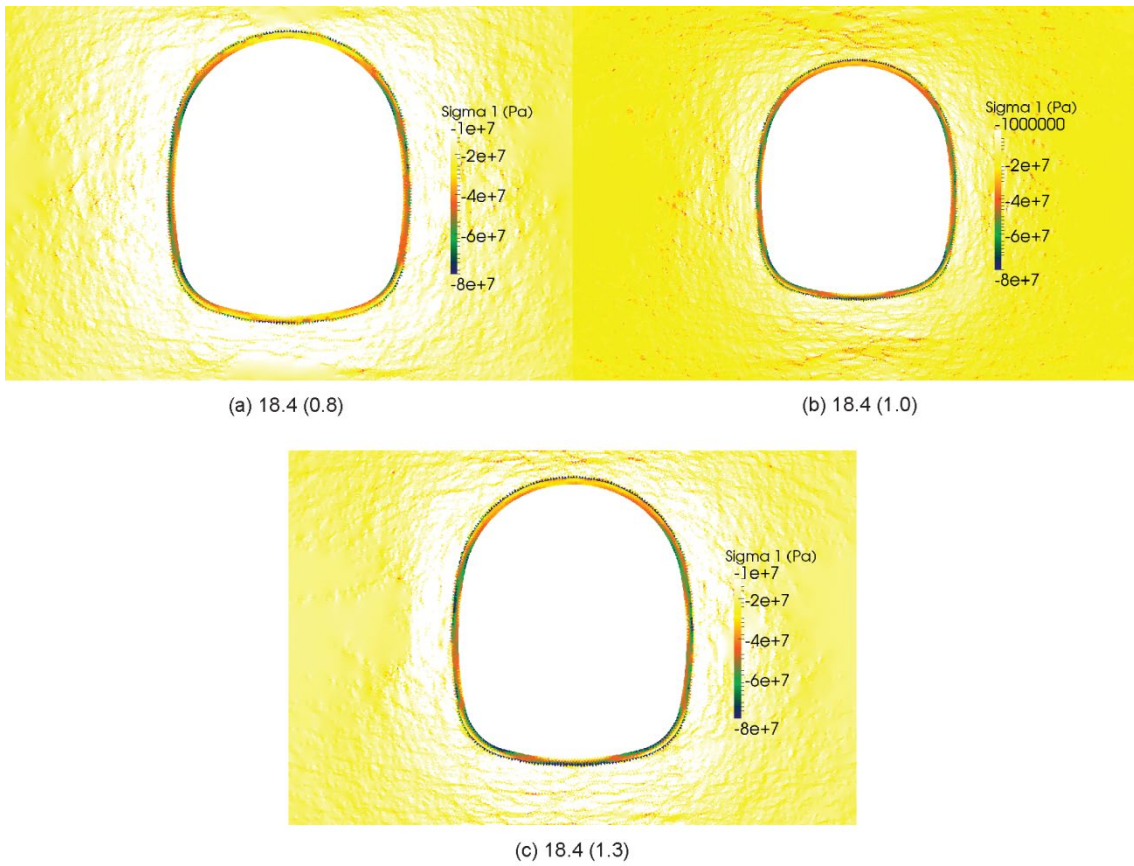


Fig. 7-7: Contours of maximum principal stress, σ_1 , in the support layer of the K09 model under different *in situ* stress conditions. The core softening ratio at the time of support installation is equal to 0.01. Rock strength parameters are "Opa x 2".

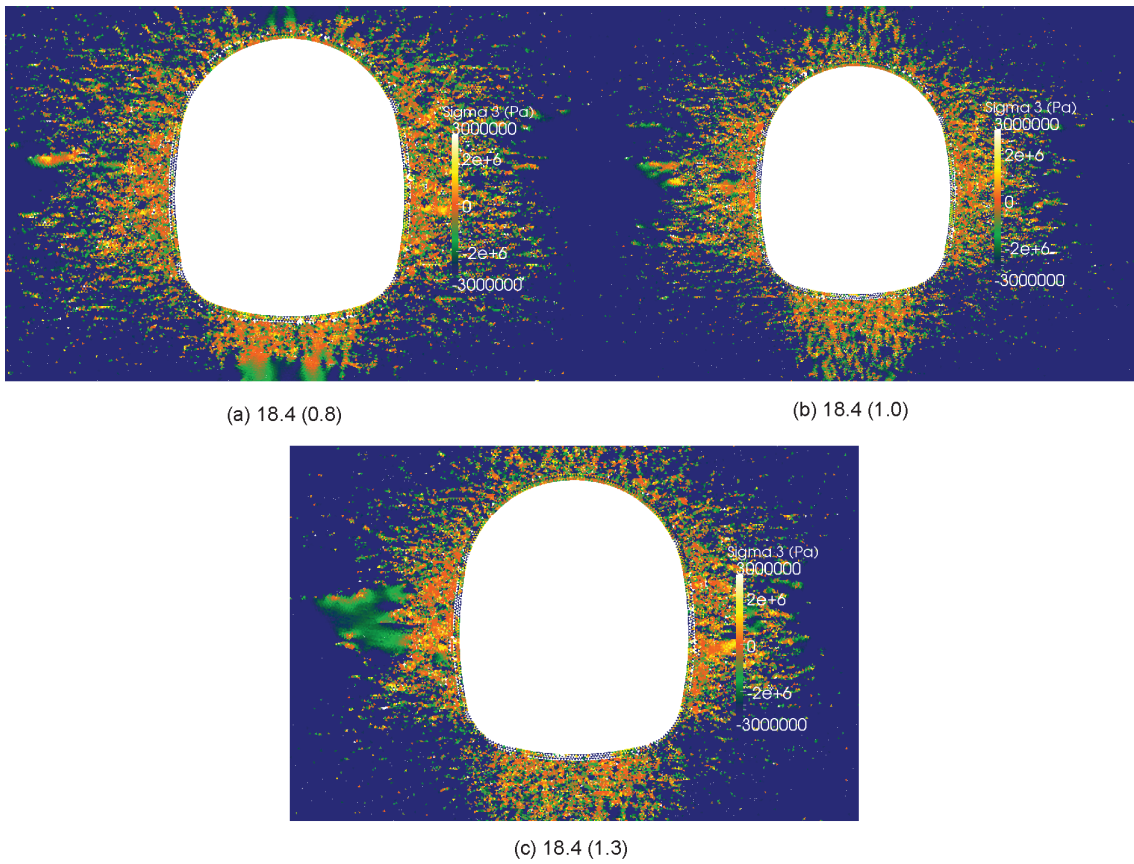


Fig. 7-8: Contours of minimum principal stress, σ_3 , inside the support layer of the K09 model under different *in situ* stress conditions. The core softening ratio at the time of support installation is equal to 0.01. Rock strength parameters are "Opa x 2".

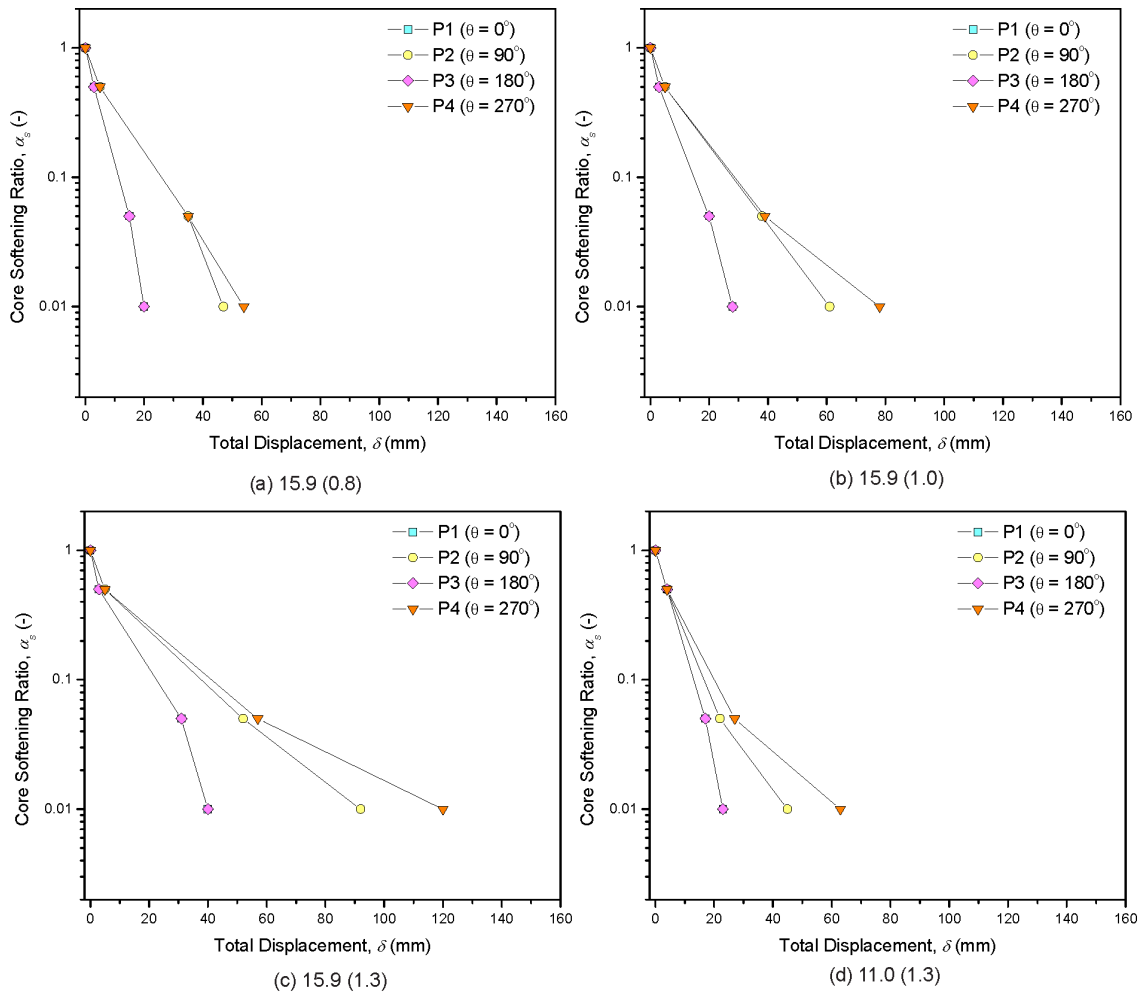


Fig. 7-9: Ground reactions curves of the K09 model under different *in situ* stress conditions. For each case, the *in situ* vertical stress, σ_v , is reported together with the stress ratio, K_0 , in brackets. Rock strength parameters are "Opa x 2". The exact location of points P1-P4 is reported in Fig. 5-2.

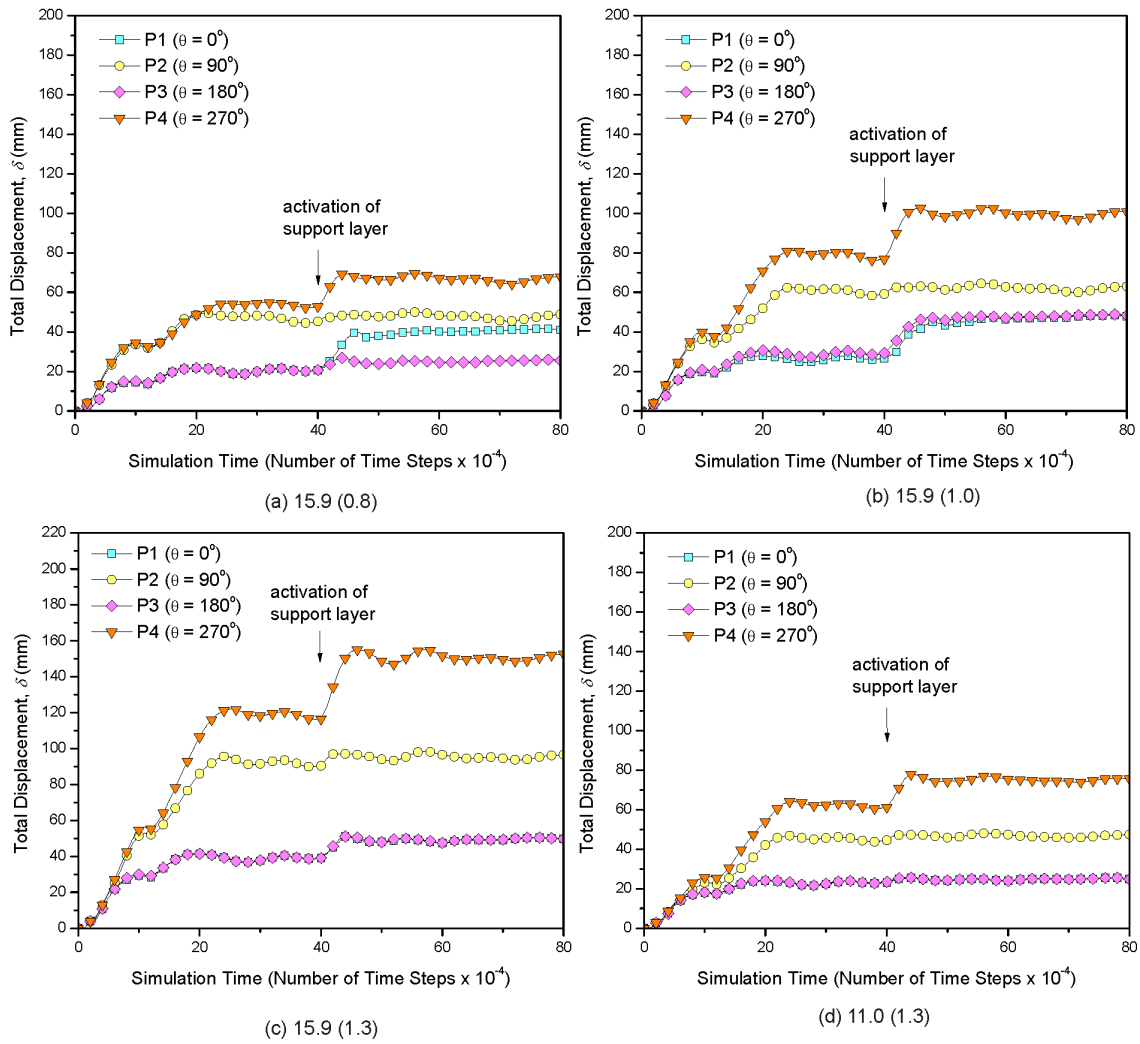


Fig. 7-10: Evolution of displacement, δ , around the excavation boundary of the K09 model under different in situ stress conditions. The core softening ratio at the time of support installation is equal to 0.01. Rock strength parameters are "Opa x 2". The exact location of points P1-P4 is reported in Fig. 5-2.

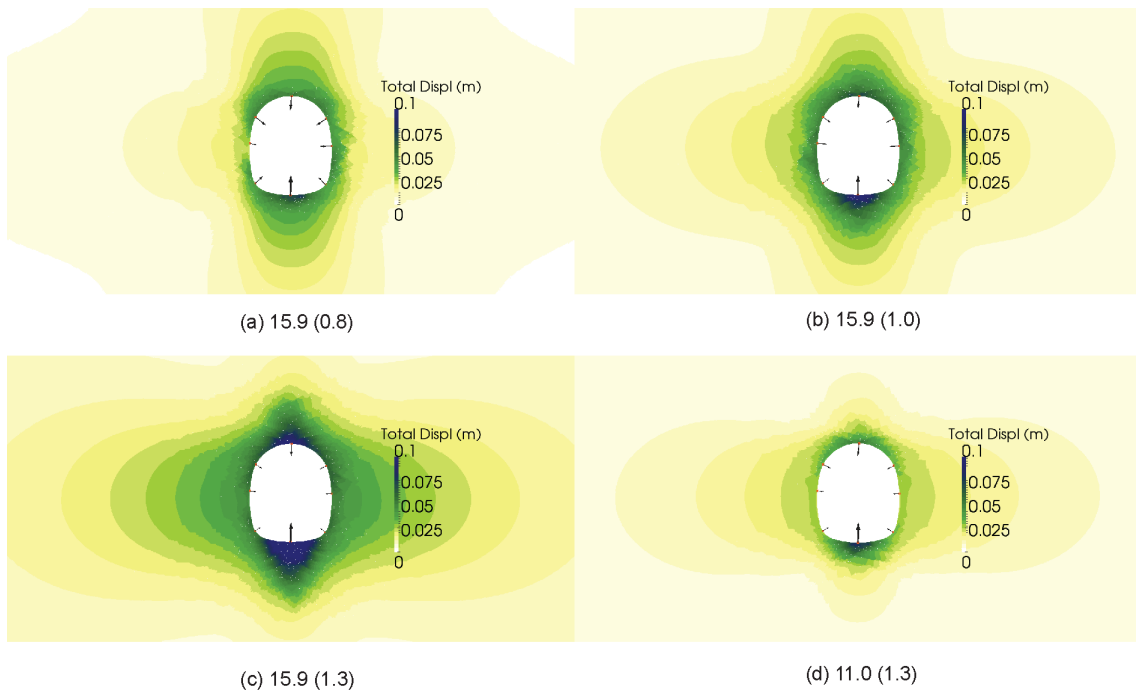


Fig. 7-11: Contours of displacement, δ , of the K09 model under different *in situ* stress conditions. The core softening ratio at the time of support installation is equal to 0.01. Rock strength parameters are "Opa x 2".

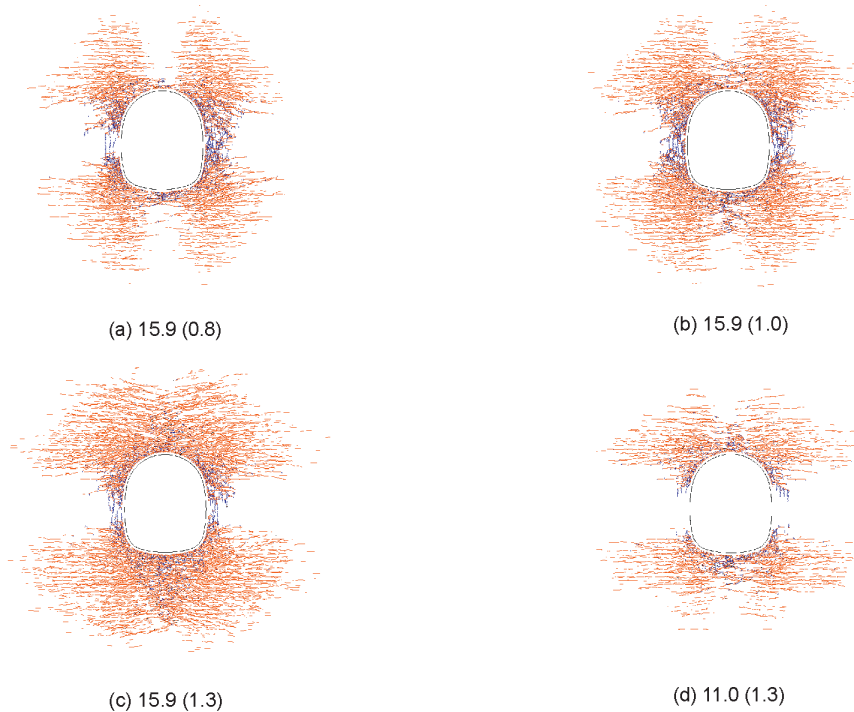


Fig. 7-12: Final fracture patterns around the excavation of the K09 model under different *in situ* stress conditions. Tensile and shear failure are indicated in blue and orange, respectively. The core softening ratio at the time of support installation is equal to 0.01. Rock strength parameters are "Opa x 2".

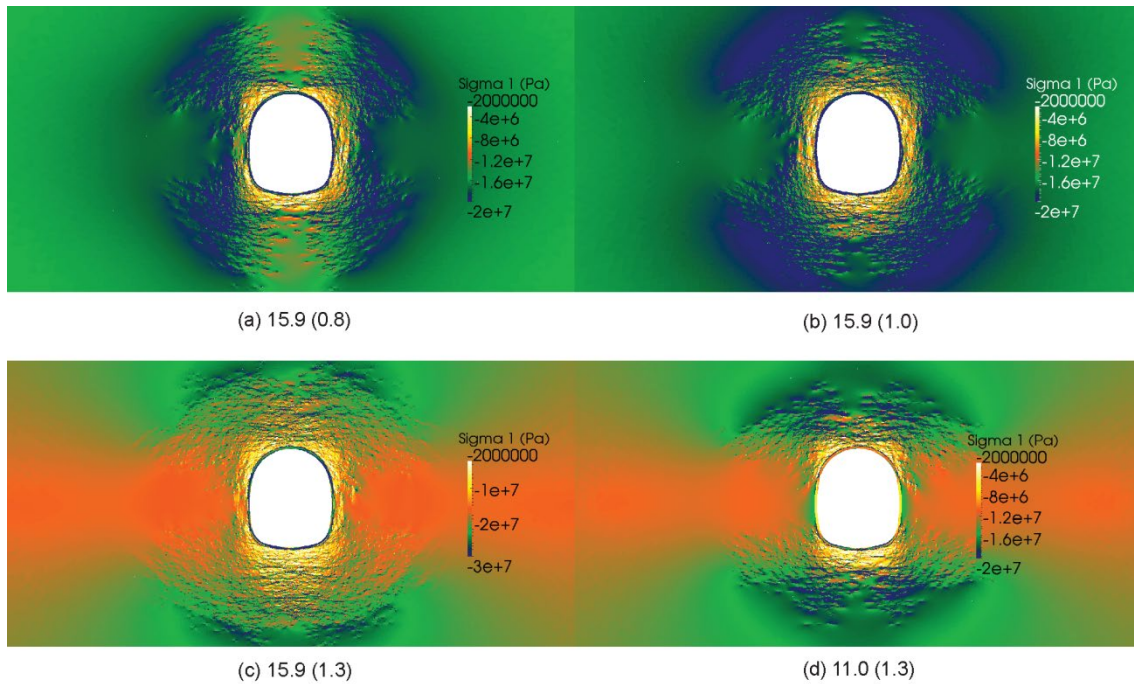


Fig. 7-13: Contours of maximum principal stress, σ_1 , of the K09 model under different *in situ* stress conditions. The core softening ratio at the time of support installation is equal to 0.01. Rock strength parameters are "Opa x 2".

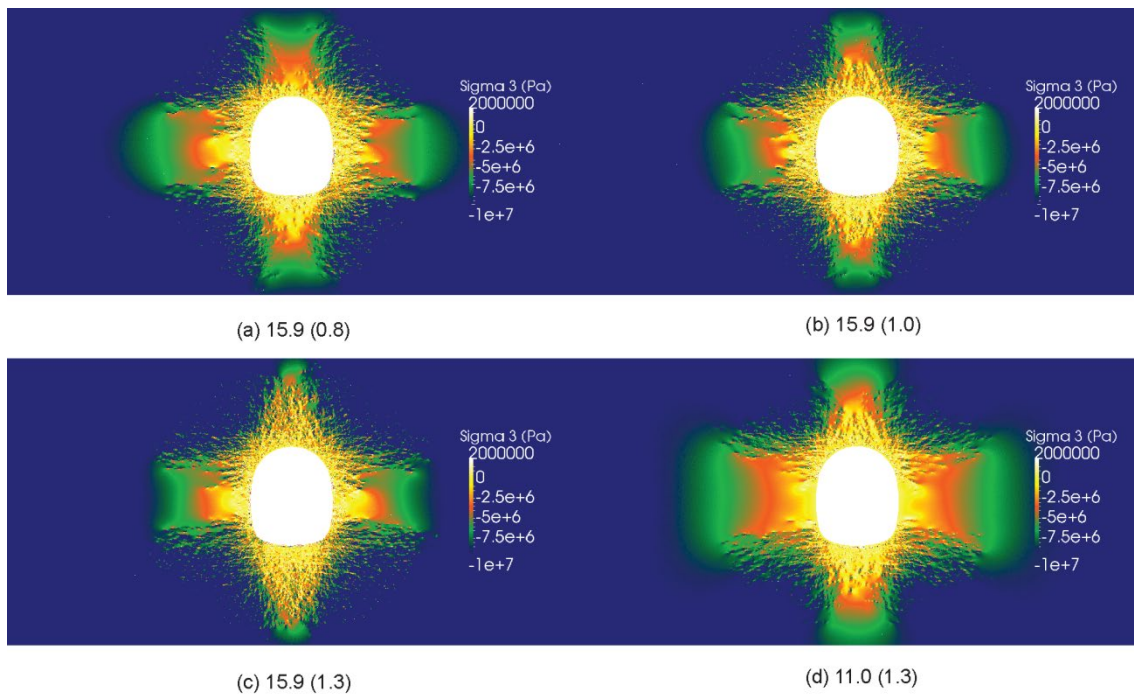


Fig. 7-14: Contour of minimum principal stress, σ_3 , of the K09 model under different *in situ* stress conditions. The core softening ratio at the time of support installation is equal to 0.01. Rock strength parameters are "Opa x 2".

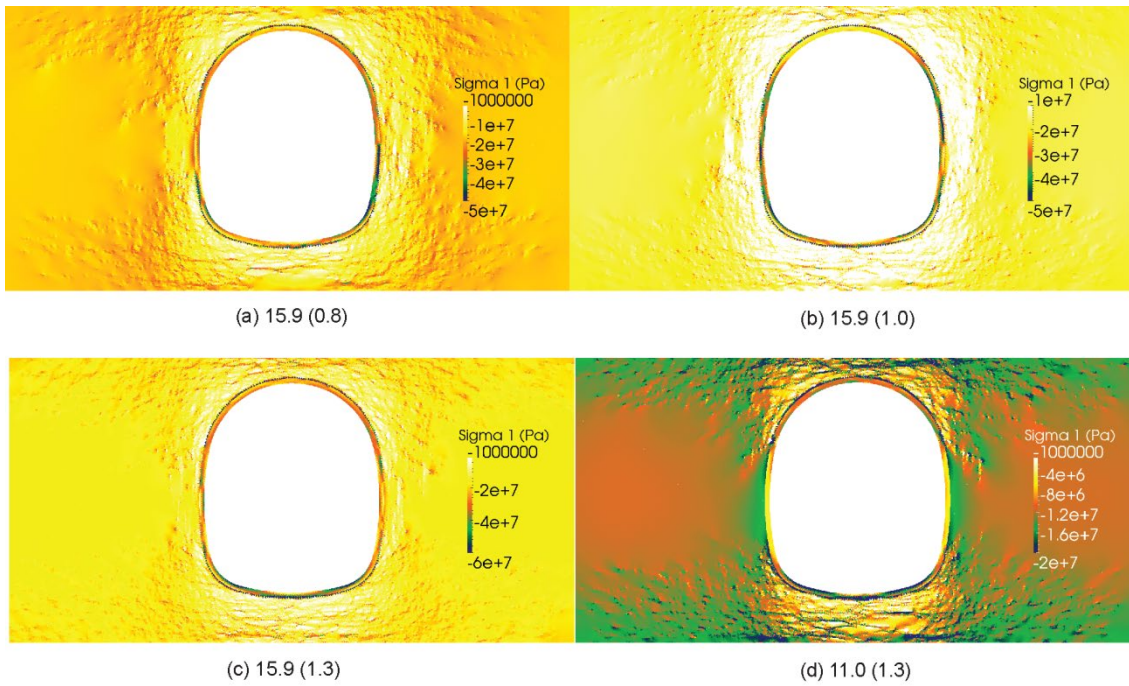


Fig. 7-15: Contours of maximum principal stress, σ_1 , in the support layer of the K09 model under different *in situ* stress conditions. The core softening ratio at the time of support installation is equal to 0.01. Rock strength parameters are "Opa x 2".

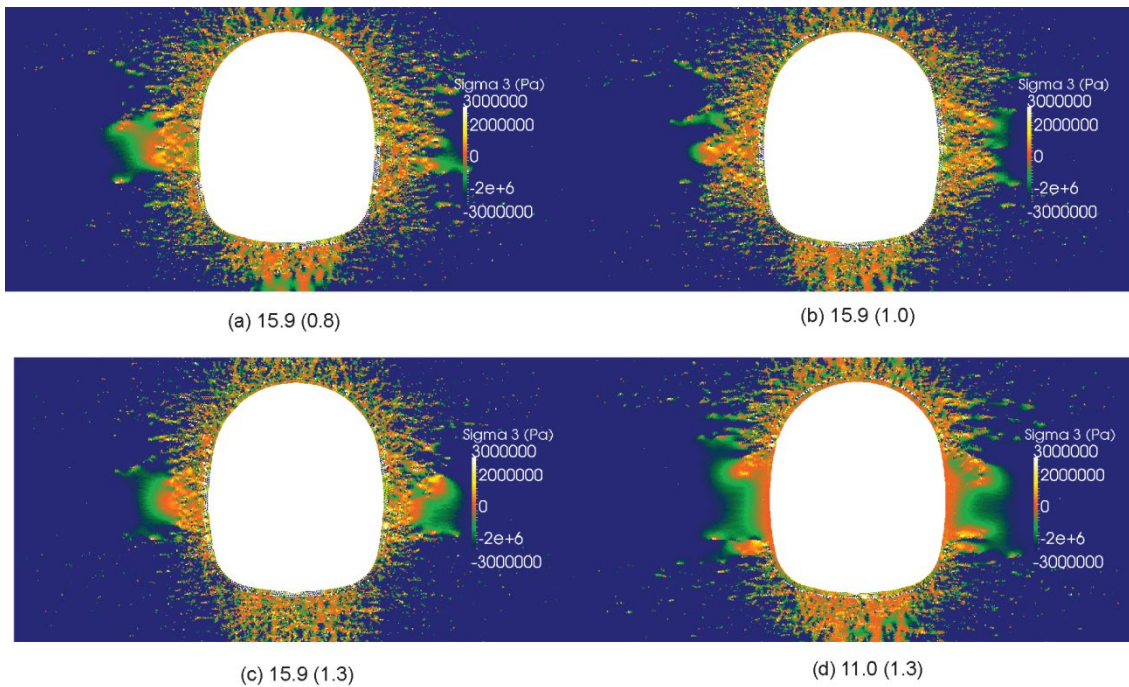


Fig. 7-16: Contours of minimum principal stress, σ_3 , in the support layer of the K09 model under different *in situ* stress conditions. The core softening ratio at the time of support installation is equal to 0.01. Rock strength parameters are "Opa x 2".

7.2 Analysis of sensitivity to the presence faults

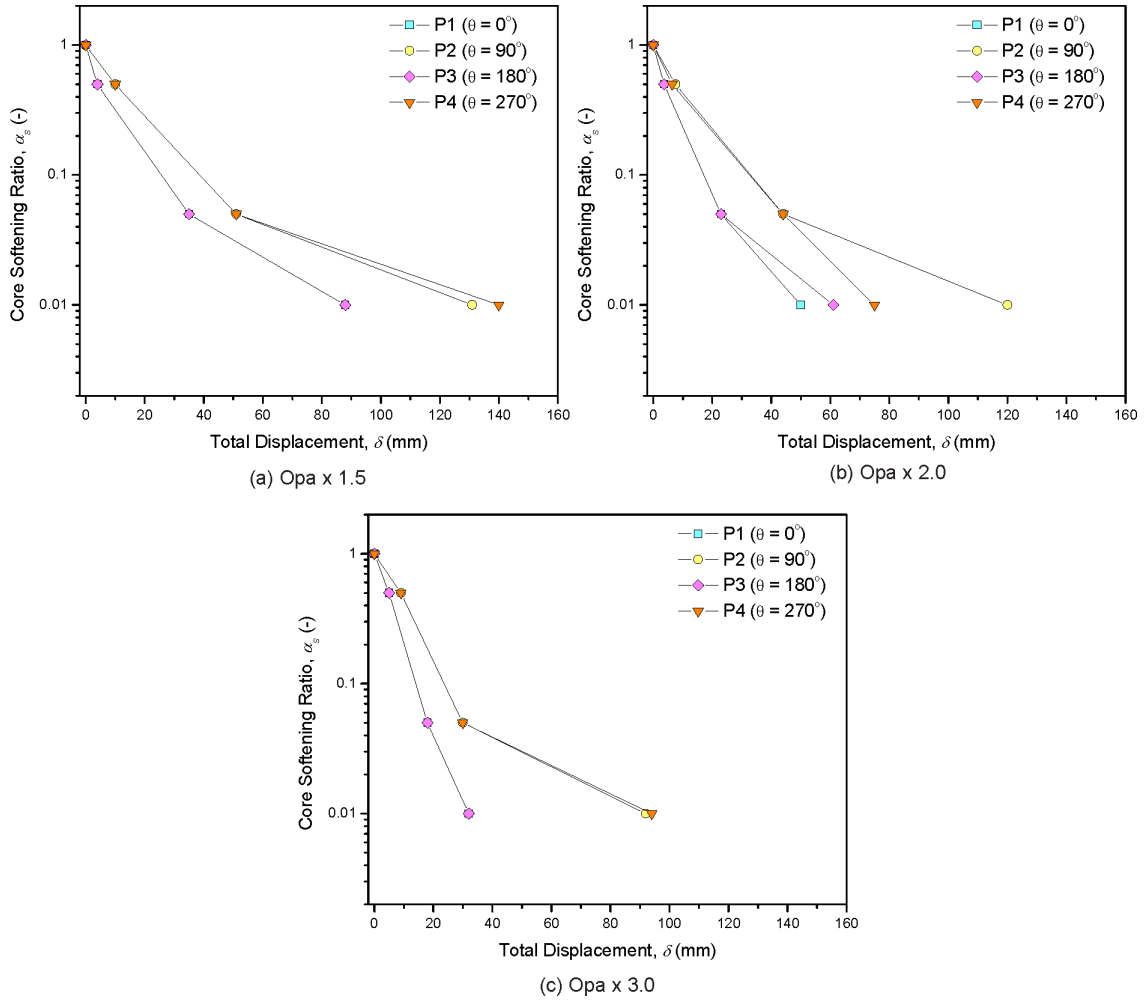


Fig. 7-17: Ground reactions of the K09 model with faults for different rock strength levels. The vertical *in situ* stress is equal to 18.4 MPa with a stress ratio $K_0 = 1.0$. The exact location of points P1-P4 is reported in Fig. 5-2.

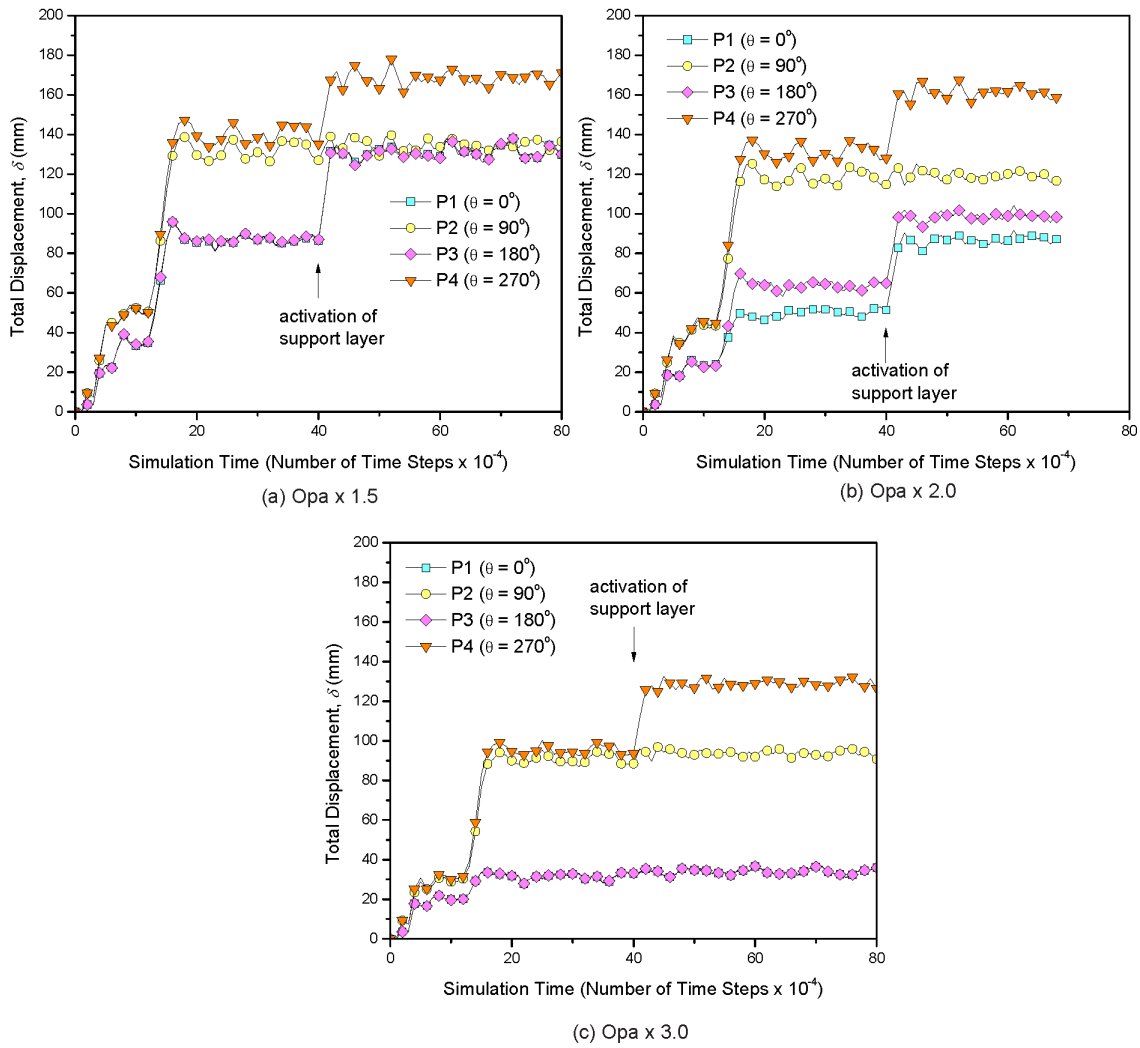


Fig. 7-18: Evolution of displacement, δ , around the excavation boundary of the K09 model with faults for different rock strength levels. The vertical *in situ* stress is equal to 18.4 MPa with a stress ratio $K_0 = 1.0$, while the core softening ratio at the time of support installation is equal to 0.01. The exact location of points P1-P4 is reported in Fig. 5-2.

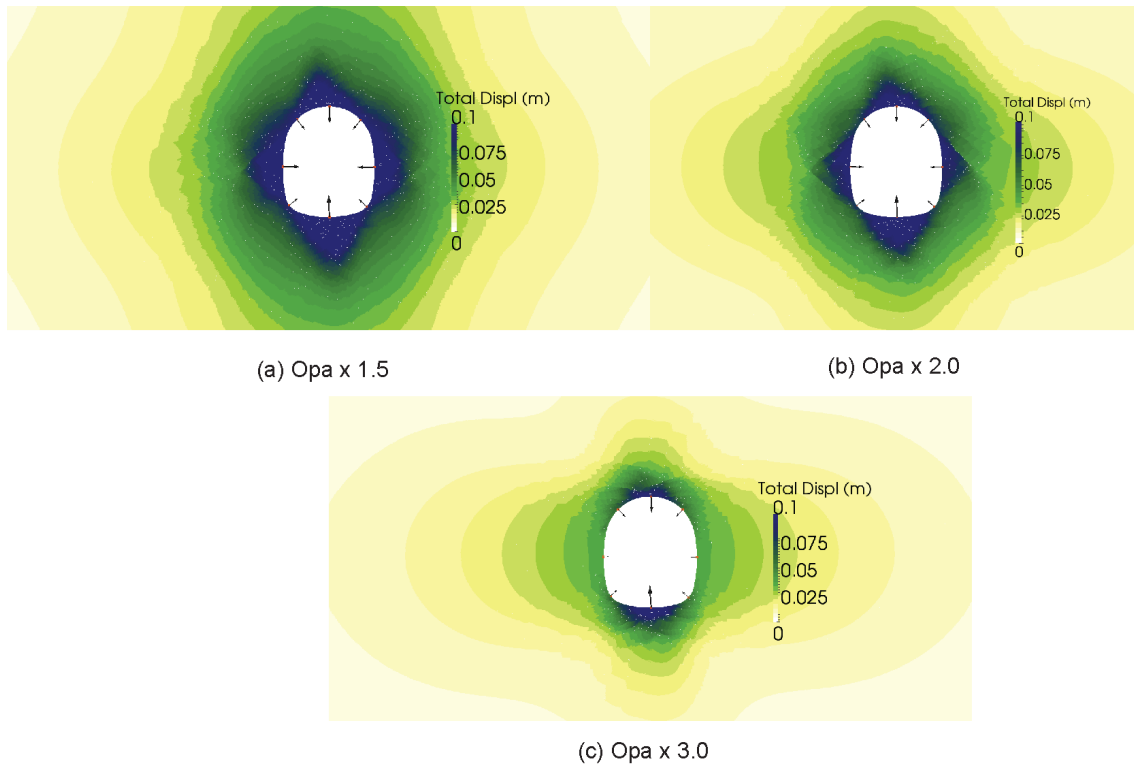


Fig. 7-19: Contour of displacement, δ , around the excavation of the K09 model with faults for different rock strength levels. The vertical *in situ* stress is equal to 18.4 MPa with a stress ratio $K_0 = 1.0$, while the core softening ratio at the time of support installation is equal to 0.01.

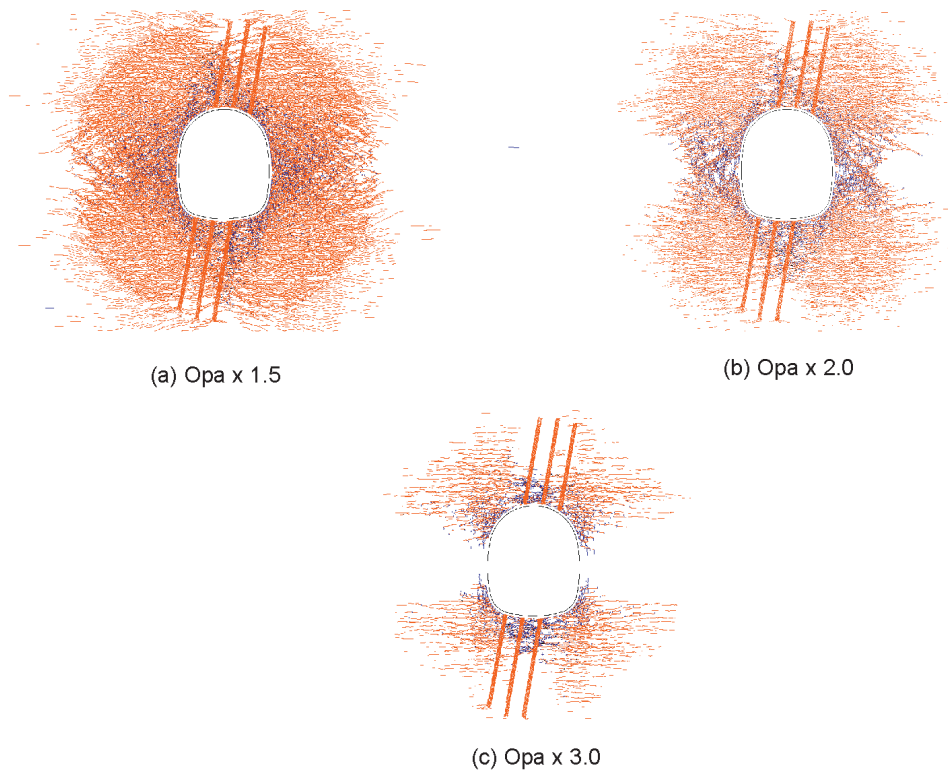


Fig. 7-20: Fracture patterns around the excavation of the K09 model with faults for different rock strength levels. Tensile and shear failure are indicated in blue and orange, respectively. The vertical *in situ* stress is equal to 18.4 MPa with a stress ratio $K_0 = 1.0$, while the core softening ratio at the time of support installation is equal to 0.01.

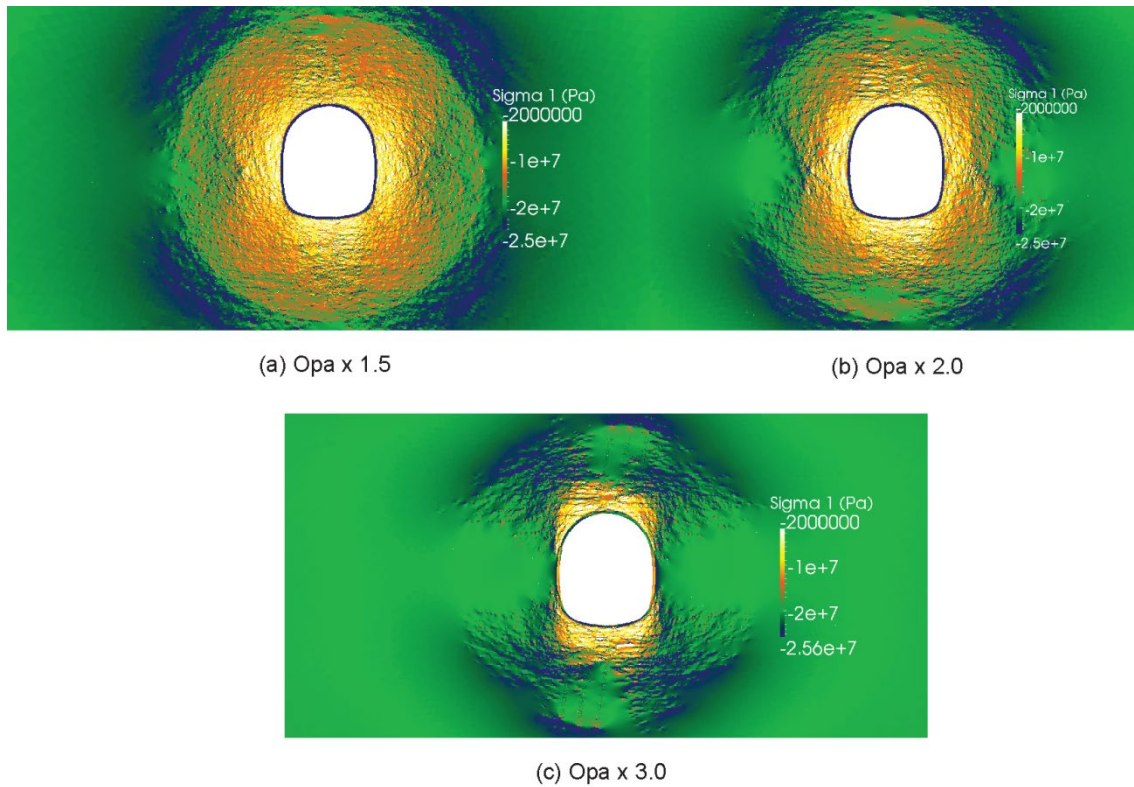


Fig. 7-21: Contour of maximum principal stress, σ_1 , around the excavation of the K09 model with faults for different rock strength levels. The vertical *in situ* stress is equal to 18.4 MPa with a stress ratio $K_0 = 1.0$, while the core softening ratio at the time of support installation is equal to 0.01.

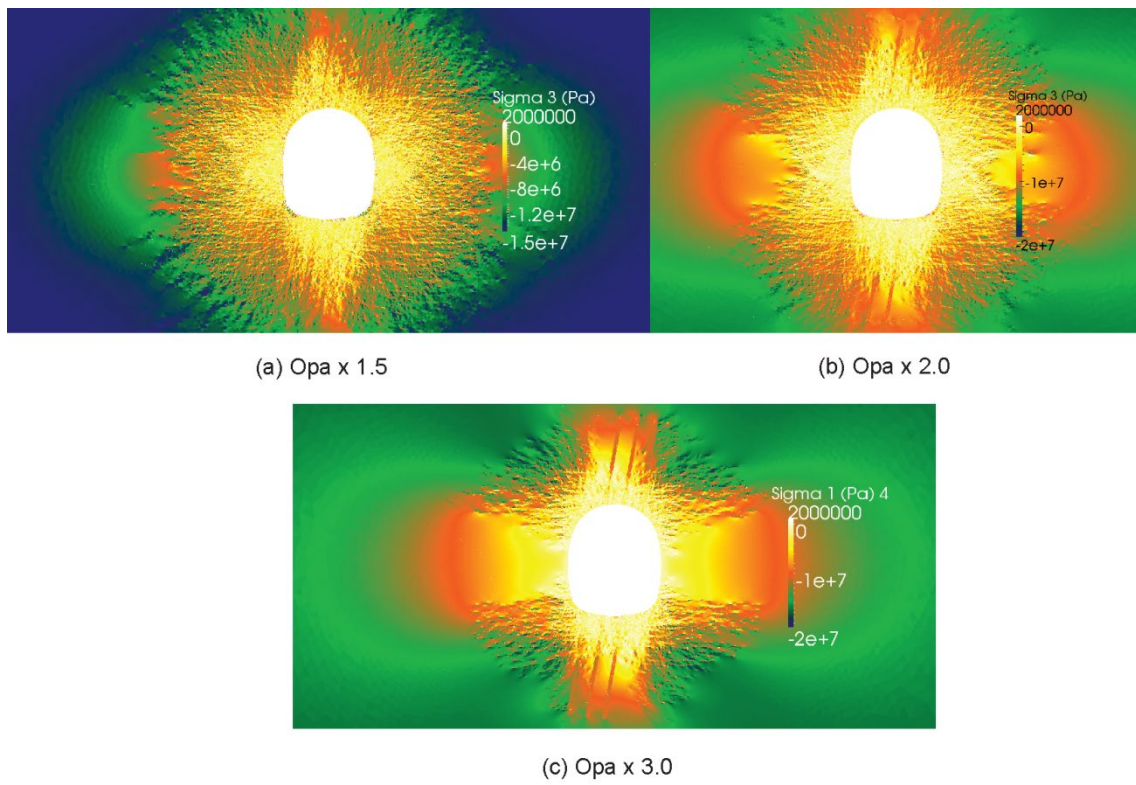


Fig. 7-22: Contour of minimum principal stress, σ_3 , around the excavation of the K09 model with faults for different rock strength levels. The vertical *in situ* stress is equal to 18.4 MPa with a stress ratio $K_0 = 1.0$, while the core softening ratio at the time of support installation is equal to 0.01.

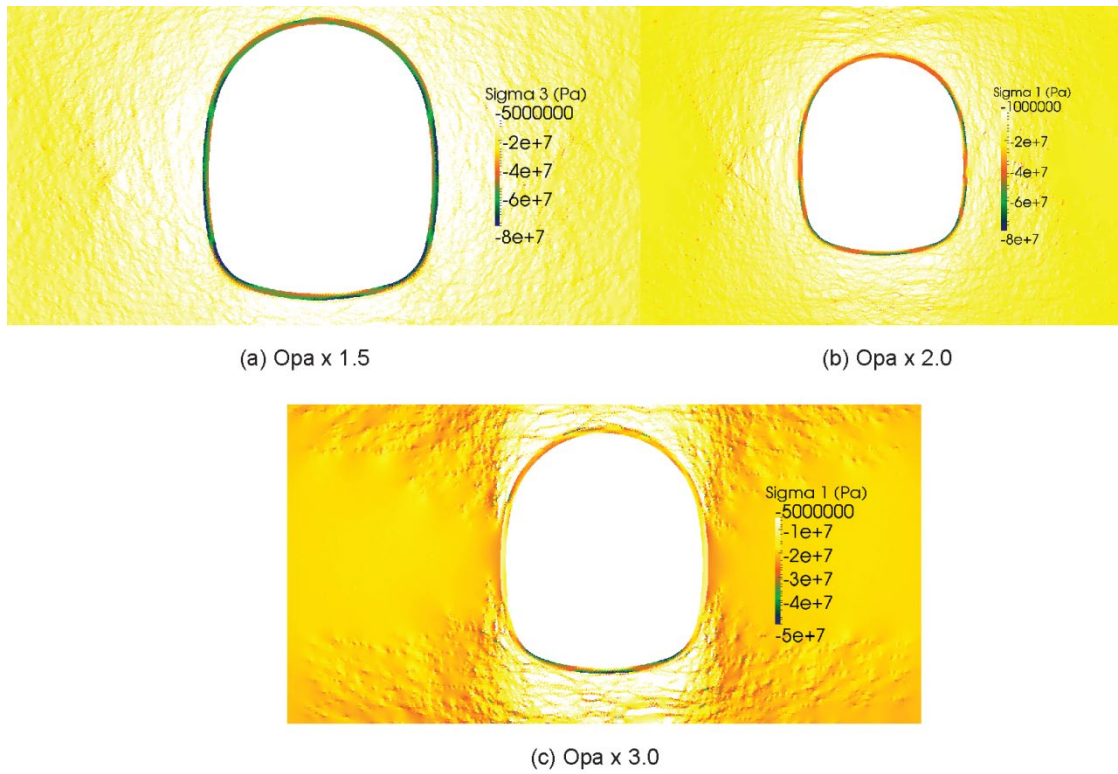


Fig. 7-23: Contour of maximum principal stress, σ_1 , inside the support layer of the K09 model with faults for different rock strength levels. The vertical *in situ* stress is equal to 18.4 MPa with a stress ratio $K_0 = 1.0$, while the core softening ratio at the time of support installation is equal to 0.01.

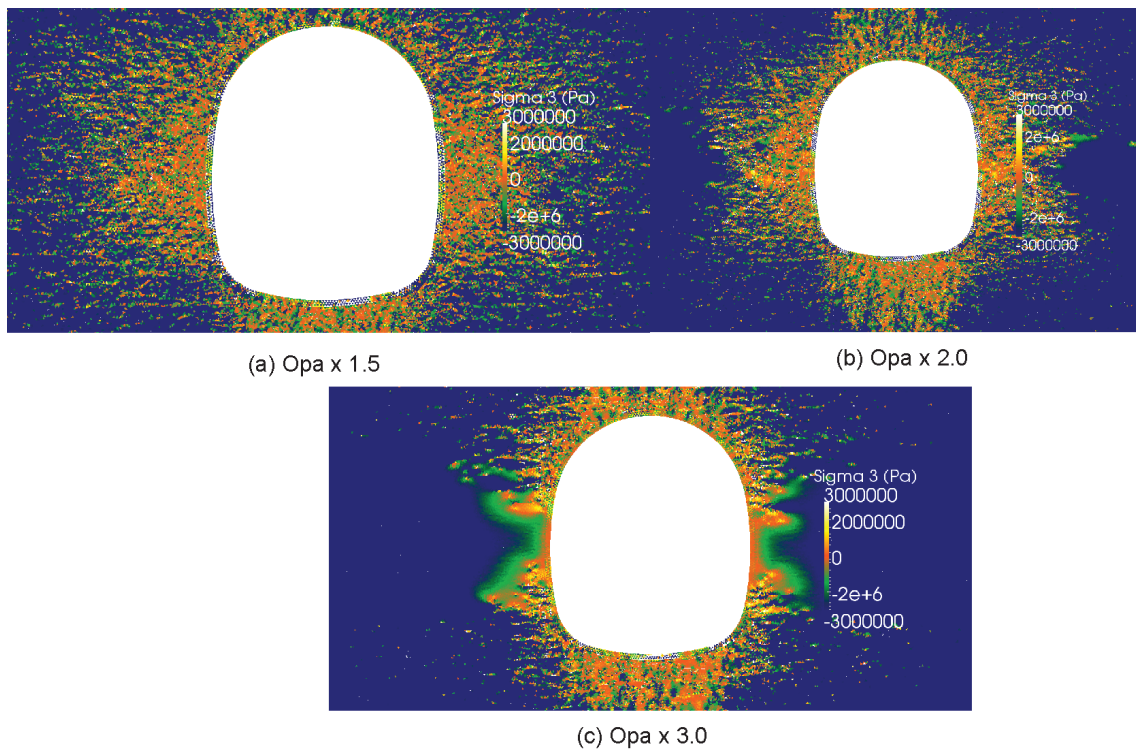


Fig. 7-24: Contour of minimum principal stress, σ_3 , inside the support layer of the K09 model with faults for different rock strength levels. The vertical *in situ* stress is equal to 18.4 MPa with a stress ratio $K_0 = 1.0$, while the core softening ratio at the time of support installation is equal to 0.01.

7.3 Analysis of sensitivity to strength parameters

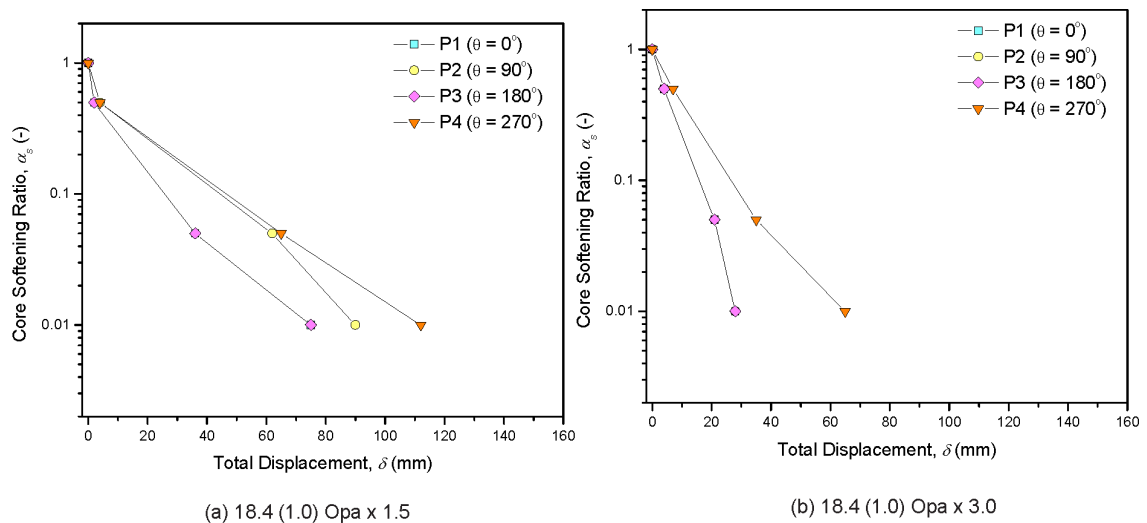


Fig. 7-25: Ground reactions of the K09 model for different rock strength levels. The vertical *in situ* stress is equal to 18.4 MPa with a stress ratio $K_0 = 1.0$. The exact location of points P1-P4 is reported in Fig. 5-2.

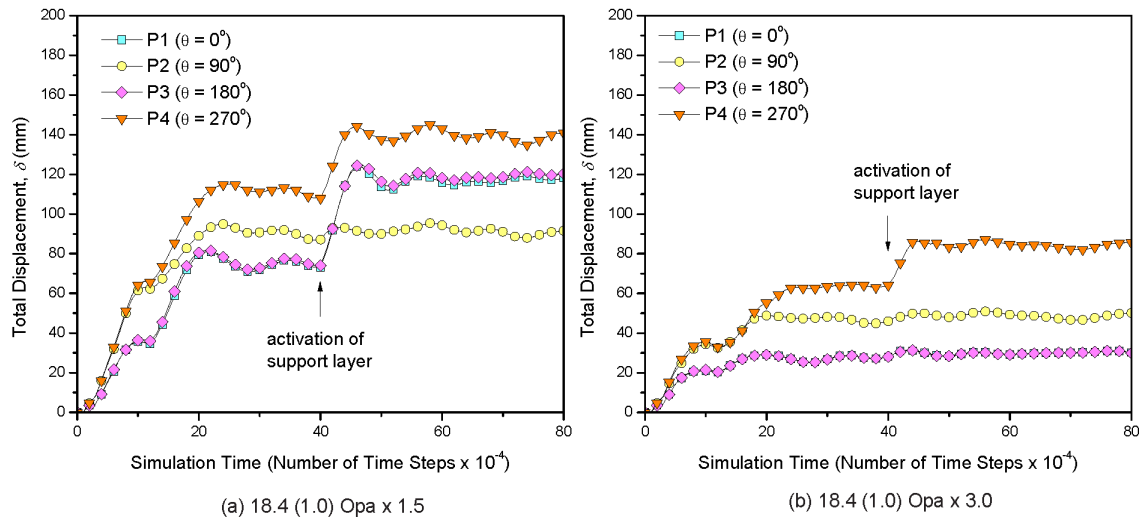


Fig. 7-26: Evolution of displacement, δ , around the excavation boundary of the K09 model for different rock strength levels. The vertical *in situ* stress is equal to 18.4 MPa with a stress ratio $K_0 = 1.0$, while the core softening ratio at the time of support installation is equal to 0.01. The exact location of points P1-P4 is reported in Fig. 5-2.

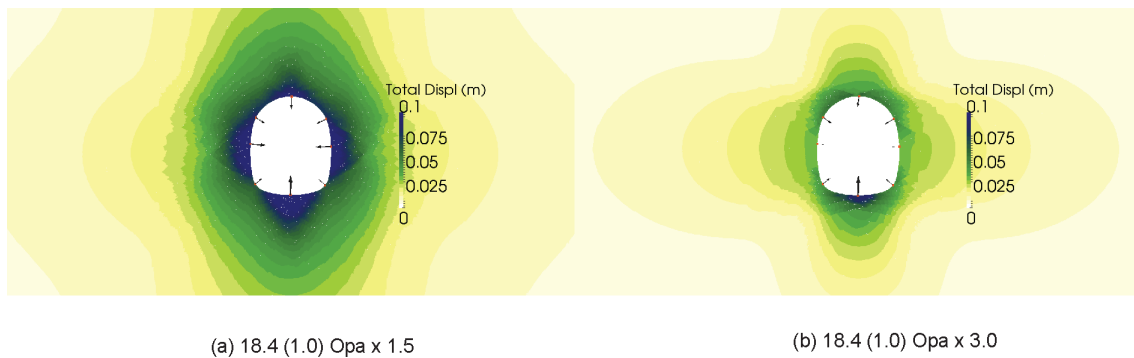


Fig. 7-27: Contours of displacement, δ , of the K09 model for different rock strength levels. The vertical *in situ* stress is equal to 18.4 MPa with a stress ratio $K_0 = 1.0$, while the core softening ratio at the time of support installation is equal to 0.01.

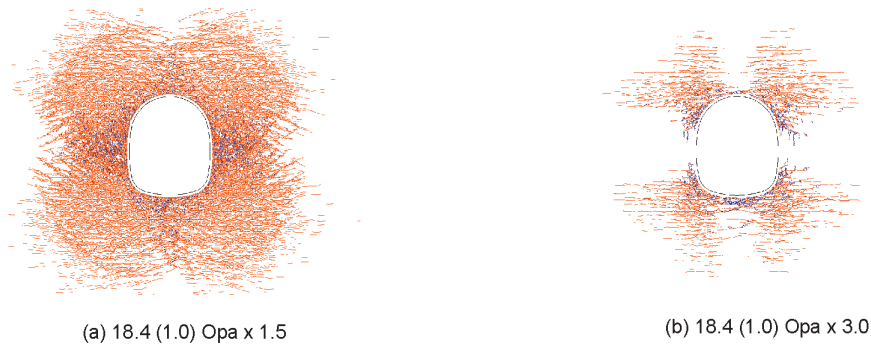


Fig. 7-28: Fracture patterns around the excavation of the K09 model for different rock strength levels. Tensile and shear failure are indicated in blue and orange, respectively. The vertical *in situ* stress is equal to 18.4 MPa with a stress ratio $K_0 = 1.0$, while the core softening ratio at the time of support installation is equal to 0.01.

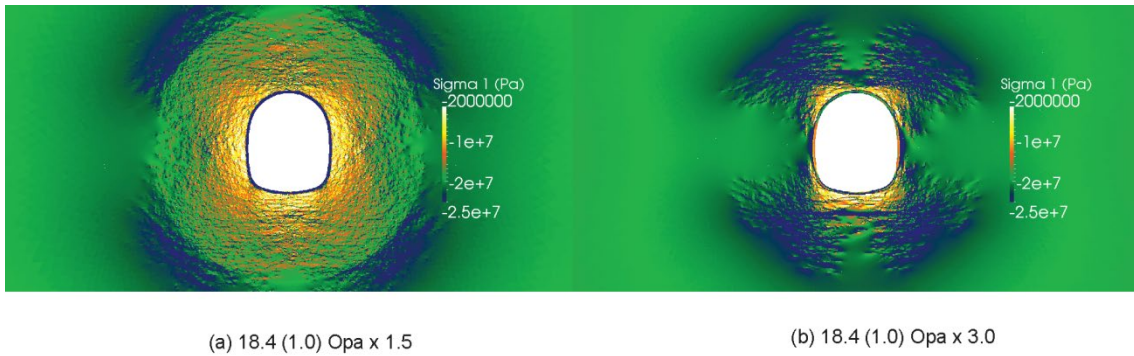


Fig. 7-29: Contours of maximum principal stress, σ_1 , of the K09 model for different rock strength levels. The vertical *in situ* stress is equal to 18.4 MPa with a stress ratio $K_0 = 1.0$, while the core softening ratio at the time of support installation is equal to 0.01.

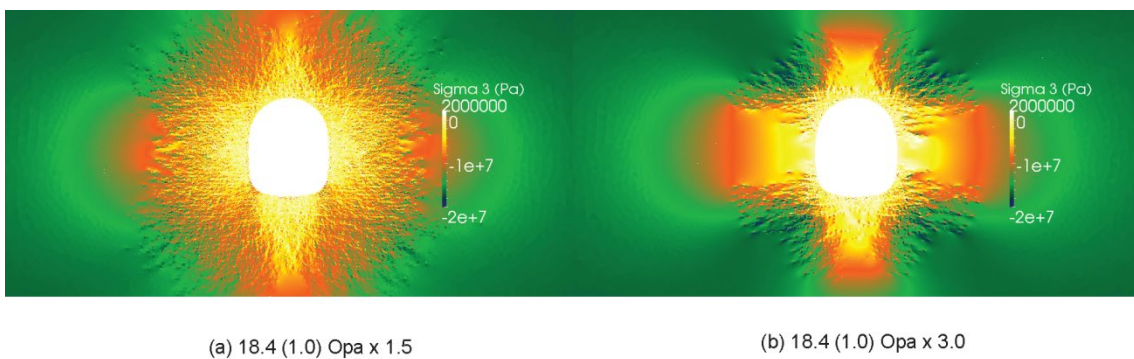


Fig. 7-30: Contours of minimum principal stress, σ_3 , of the K09 model for different rock strength levels. The vertical *in situ* stress is equal to 18.4 MPa with a stress ratio $K_0 = 1.0$, while the core softening ratio at the time of support installation is equal to 0.01.

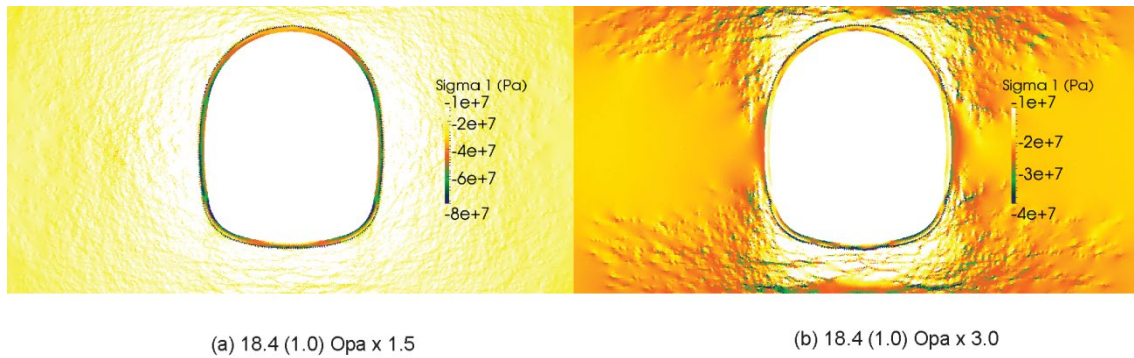


Fig. 7-31: Contours of maximum principal stress, σ_1 , in the support layer of the K09 model for different rock strength levels. The vertical *in situ* stress is equal to 18.4 MPa with a stress ratio $K_0 = 1.0$, while the core softening ratio at the time of support installation is equal to 0.01.

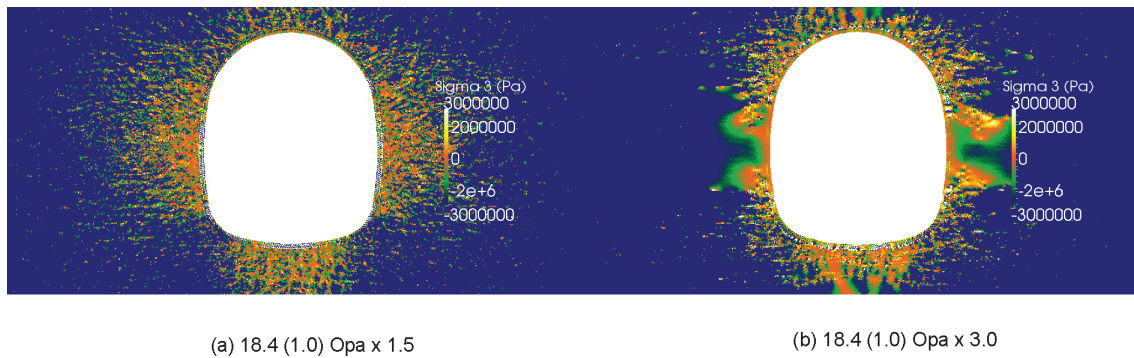


Fig. 7-32: Contours of minimum principal stress, σ_3 , in the support layer of the K09 model for different rock strength levels. The vertical *in situ* stress is equal to 18.4 MPa with a stress ratio $K_0 = 1.0$, while the core softening ratio at the time of support installation is equal to 0.01.

8 Results: EDZ simulations for shaft section

Tab. 8: Summary of shaft simulations.

Model	Section	In situ stress conditions	Strength properties	Elastic modulus of support	Faults	Core softening ratio at support installation	Reconsolidation pressure
Sensitivity to <i>in situ</i> stress conditions							
Shaft-1	Shaft	11.0, 1.5	OpaMax	32	N/A	0.01	N/A
Shaft-2	Shaft	15.9, 1.0	OpaMax	32	N/A	0.01	N/A
Shaft-3	Shaft	19.6, 0.8	OpaMax	32	N/A	0.01	N/A
Shaft-4	Shaft	19.6, 1.3	OpaMax	32	N/A	0.01	N/A
Sensitivity to strength parameters							
Shaft-5	Shaft	11.0, 1.5	OpaMax x 0.5	32	N/A	0.01	N/A
Shaft-6	Shaft	15.9, 1.0	OpaMax x 0.5	32	N/A	0.01	N/A
Shaft-7	Shaft	19.6, 0.8	OpaMax x 0.5	32	N/A	0.01	N/A
Shaft-8	Shaft	19.6, 1.3	OpaMax x 0.5	32	N/A	0.01	N/A
Shaft-9	Shaft	11.0, 1.5	OpaMax x 0.75	32	N/A	0.01	N/A
Shaft-10	Shaft	15.9, 1.0	OpaMax x 0.75	32	N/A	0.01	N/A
Shaft-11	Shaft	19.6, 0.8	OpaMax x 0.75	32	N/A	0.01	N/A
Shaft-12	Shaft	19.6, 1.3	OpaMax x 0.75	32	N/A	0.01	N/A

8.1 Analysis of sensitivity to *in situ* stress conditions

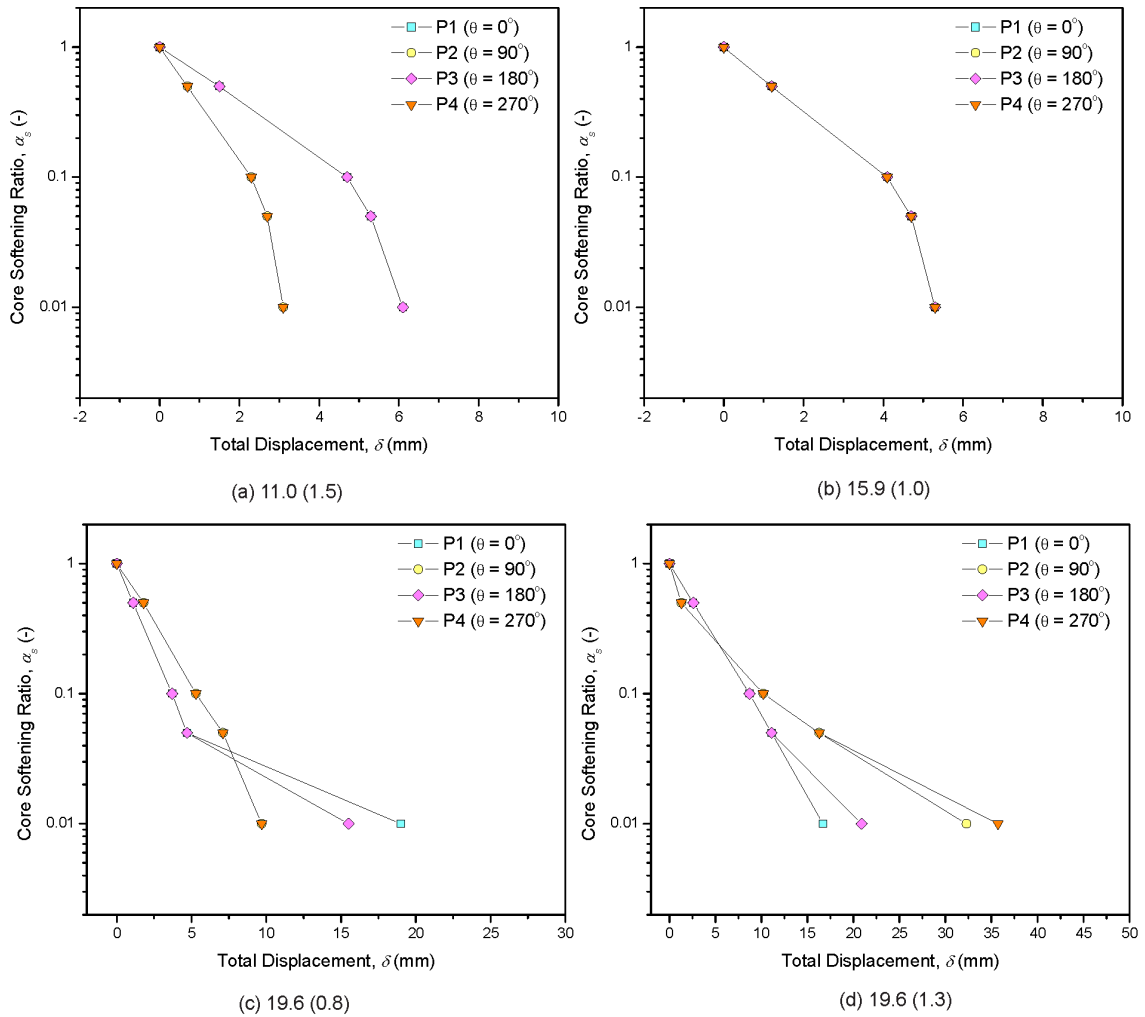


Fig. 8-1: Ground reactions of the shaft model under different *in situ* stress conditions. For each case, the *in situ* vertical stress, σ_v , is reported together with the stress ratio, K_0 , in brackets. Strength parameters are "OpaMax". The exact location of points P1-P4 is reported in Fig. 5-3.

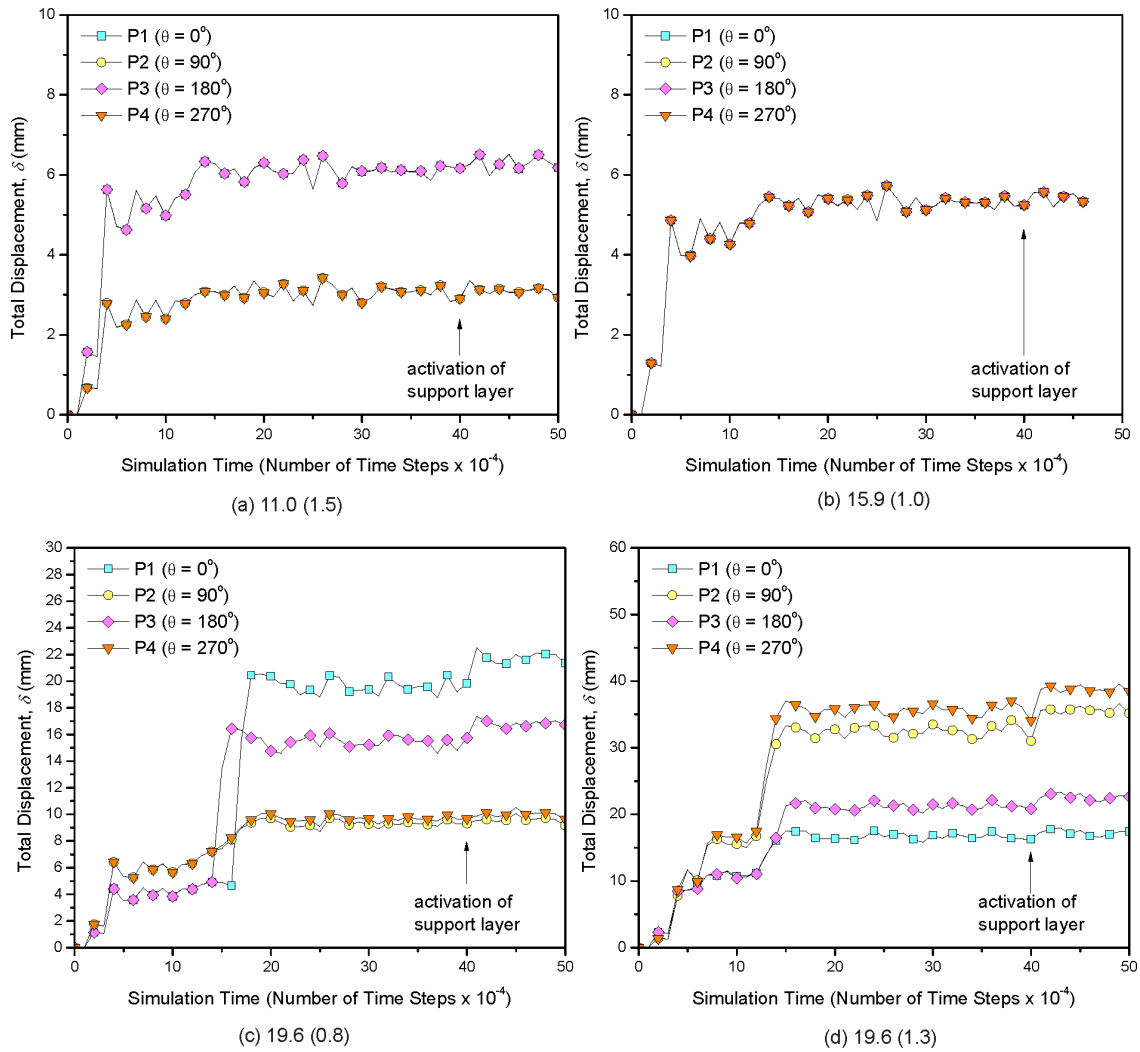


Fig. 8-2: Evolution of displacement, δ , around the excavation boundary of the shaft model under different *in situ* stress conditions. For each case, the *in situ* vertical stress, σ_v , is reported together with the stress ratio, K_0 , in brackets. Strength parameters are "OpaMax", while the core softening ratio at the time of support installation is equal to 0.01. The exact location of points P1-P4 is reported in Fig. 5-3.

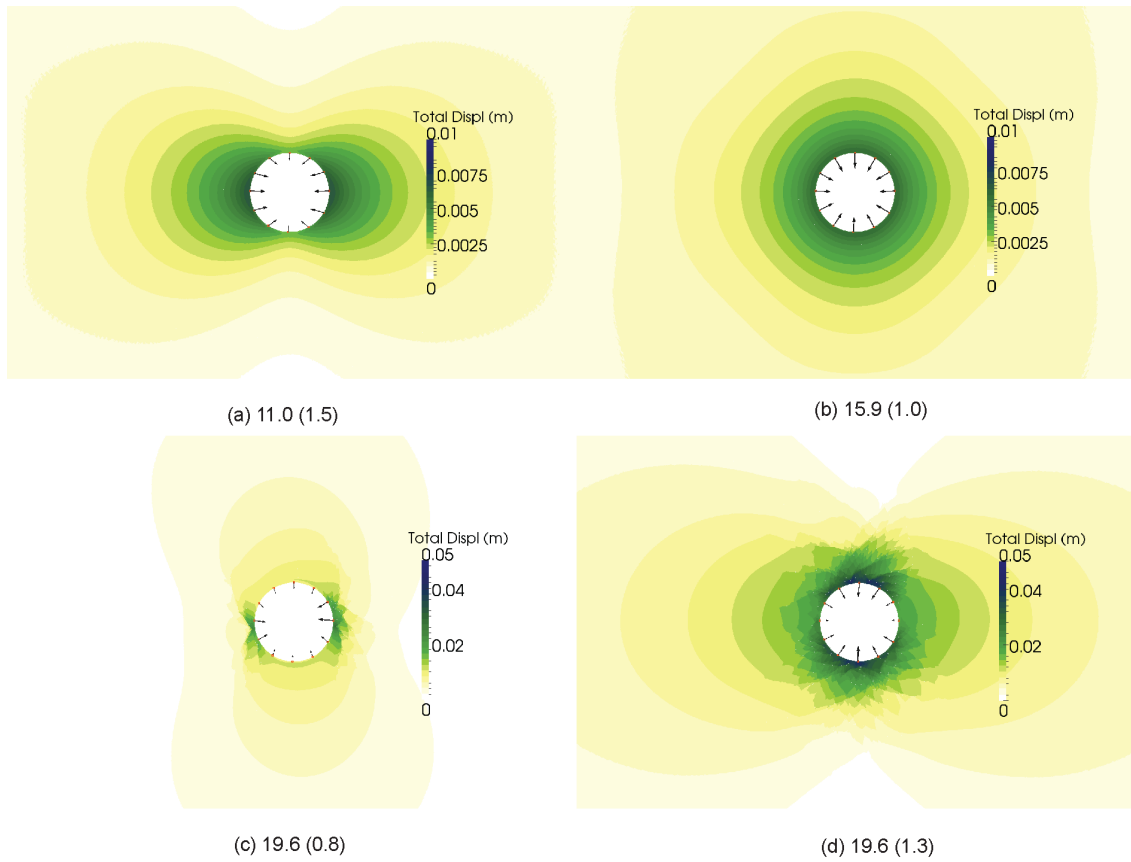


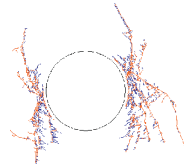
Fig. 8-3: Contours of displacement, δ , of the shaft model under different *in situ* stress conditions. For each case, the *in situ* vertical stress, σ_v , is reported together with the stress ratio, K_0 , in brackets. Strength parameters are "OpaMax", while the core softening ratio at the time of support installation is equal to 0.01.

no fracturing

no fracturing

(a) 11.0 (1.5)

(b) 15.9 (1.0)



(c) 19.6 (0.8)

(d) 19.6 (1.3)

Fig. 8-4: Fracture patterns around the excavation of the shaft model under different *in situ* stress conditions. Tensile and shear failure are indicated in blue and orange, respectively. For each case, the *in situ* vertical stress, σ_v , is reported together with the stress ratio, K_0 , in brackets. Strength parameters are "OpaMax", while the core softening ratio at the time of support installation is equal to 0.01.

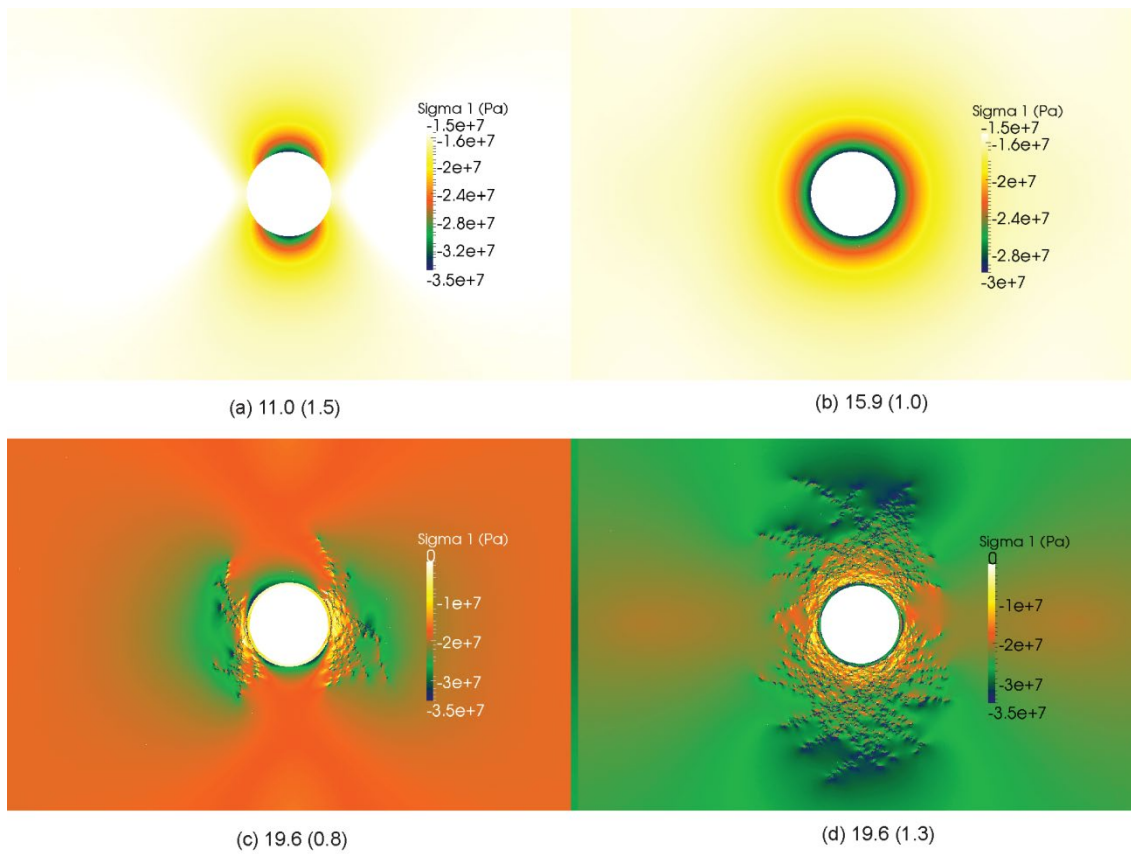


Fig. 8-5: Contours of maximum principal stress, σ_1 , of the shaft model under different *in situ* stress conditions. For each case, the *in situ* vertical stress, σ_v , is reported together with the stress ratio, K_0 , in brackets. Strength parameters are "OpaMax", while the core softening ratio at the time of support installation is equal to 0.01.

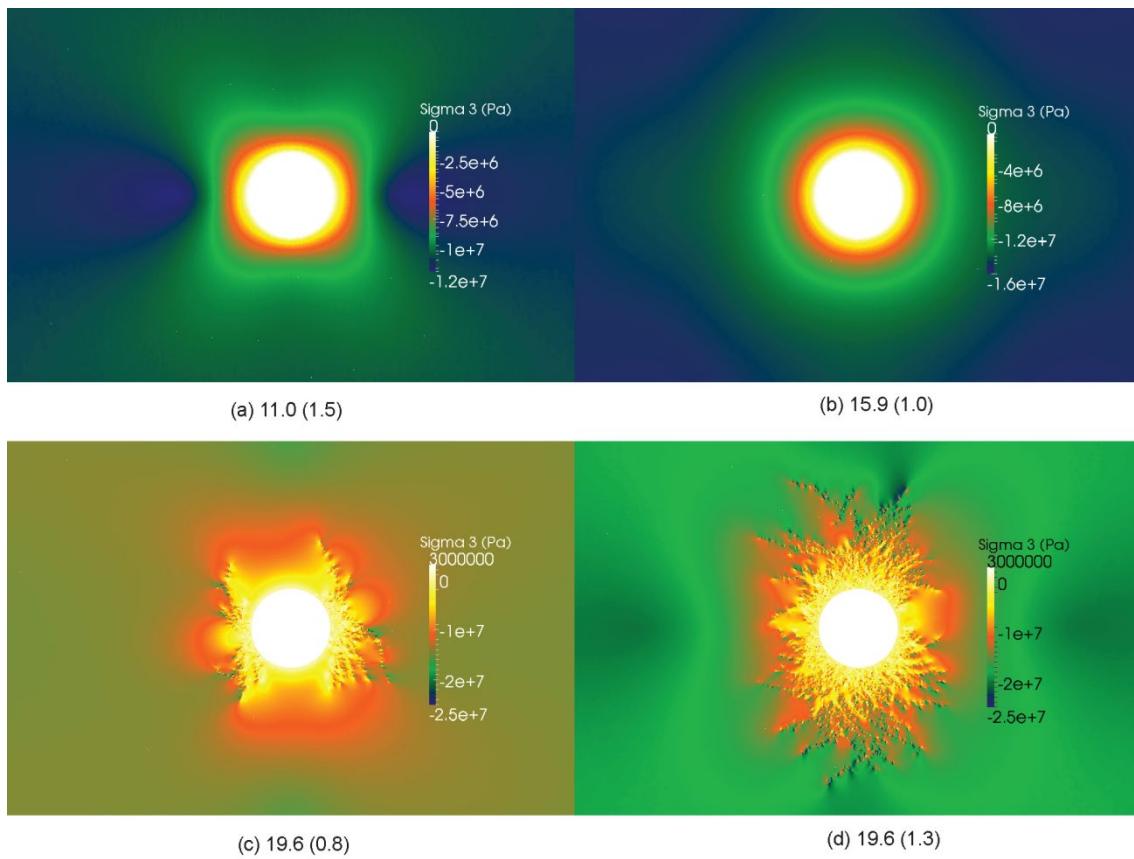


Fig. 8-6: Contours of minimum principal stress, σ_3 , of the shaft model under different *in situ* stress conditions. For each case, the *in situ* vertical stress, σ_v , is reported together with the stress ratio, K_0 , in brackets. Strength parameters are "OpaMax", while the core softening ratio at the time of support installation is equal to 0.01.

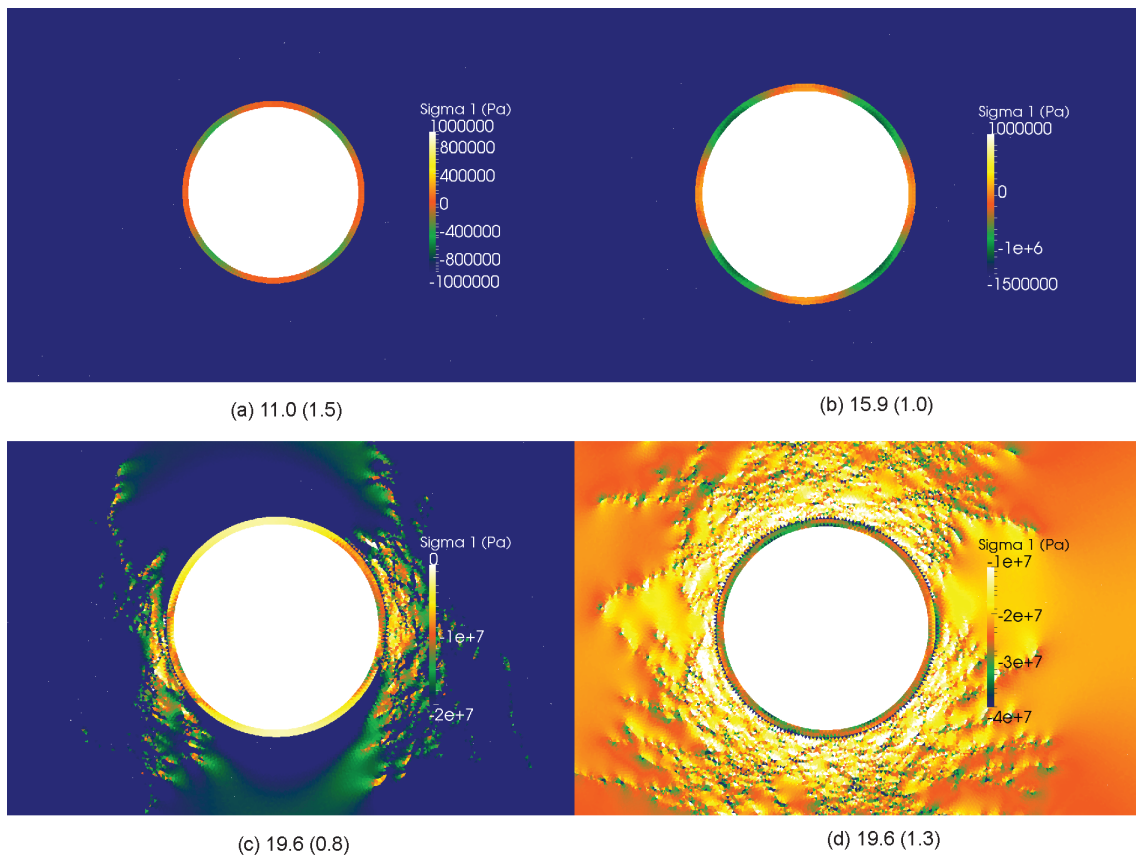


Fig. 8-7: Contours of maximum principal stress, σ_1 , in the support layer of the shaft model under different *in situ* stress conditions. For each case, the *in situ* vertical stress, σ_v , is reported together with the stress ratio, K_0 , in brackets. Strength parameters are "OpaMax", while the core softening ratio at the time of support installation is equal to 0.01.

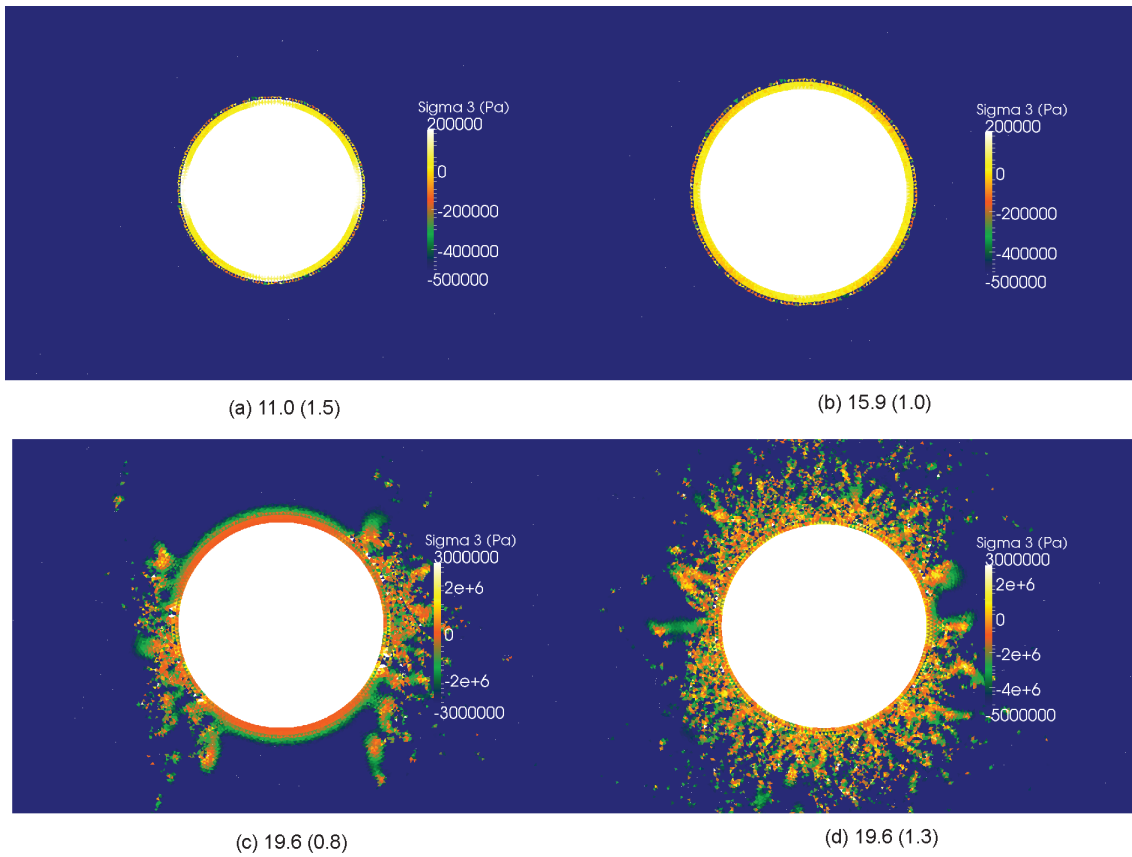


Fig. 8-8: Contours of minimum principal stress, σ_3 , in the support layer of the shaft model under different *in situ* stress conditions. For each case, the *in situ* vertical stress, σ_v , is reported together with the stress ratio, K_0 , in brackets. Strength parameters are "OpaMax", while the core softening ratio at the time of support installation is equal to 0.01.

8.2 Analysis of sensitivity to strength parameters

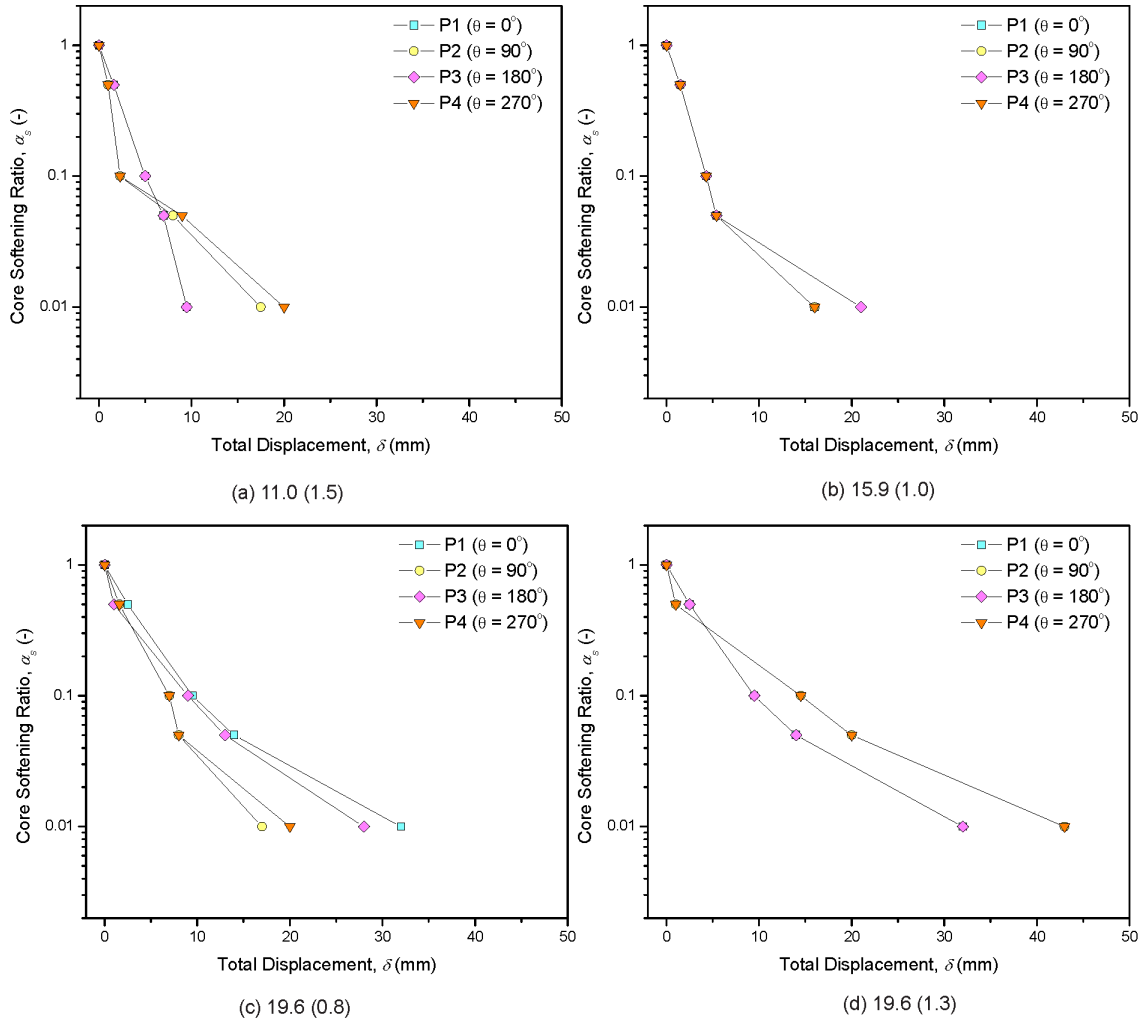


Fig. 8-9: Ground reactions of the shaft model under different *in situ* stress conditions. For each case, the *in situ* vertical stress, σ_v , is reported together with the stress ratio, K_0 , in brackets. Strength parameters are "OpaMax x 0.75". The exact location of points P1-P4 is reported in Fig. 5-3.

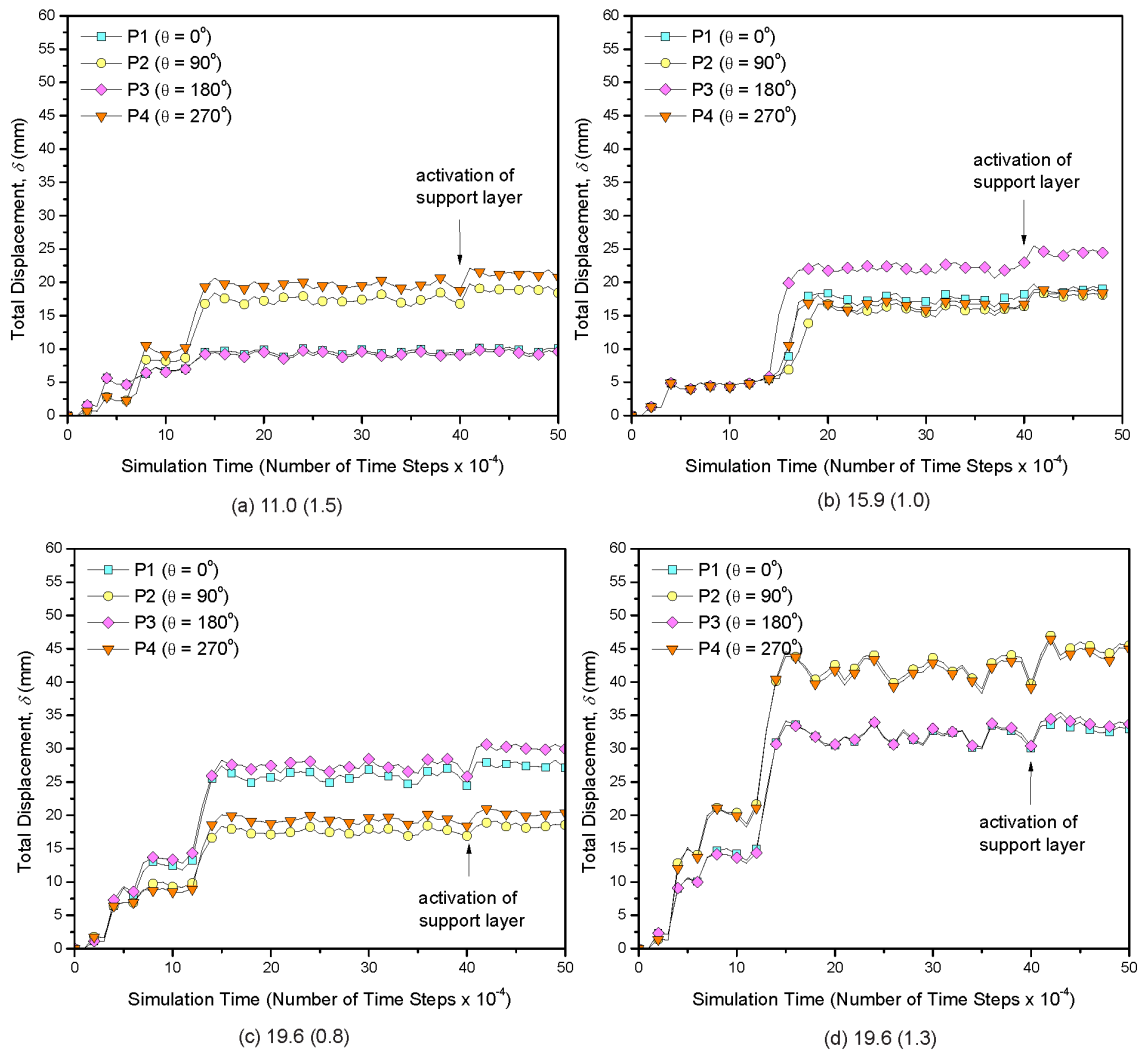


Fig. 8-10: Evolution of displacement, δ , around the excavation boundary of the shaft model under different *in situ* stress conditions. For each case, the *in situ* vertical stress, σ_v , is reported together with the stress ratio, K_0 , in brackets. Strength parameters are "OpaMax $\times 0.75$ ", while the core softening ratio at the time of support installation is equal to 0.01. The exact location of points P1-P4 is reported in Fig. 5-3.

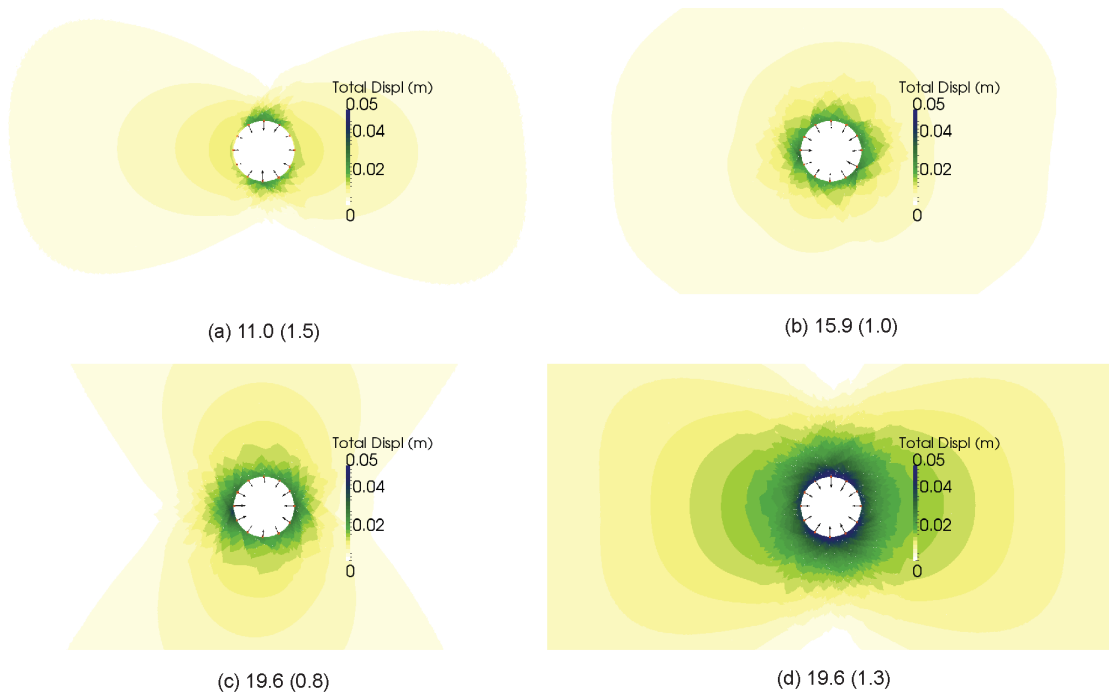


Fig. 8-11: Contours of displacement, δ , of the shaft model under different *in situ* stress conditions. For each case, the *in situ* vertical stress, σ_v , is reported together with the stress ratio, K_0 , in brackets. Strength parameters are "OpaMax x 0.75", while the core softening ratio at the time of support installation is equal to 0.01.

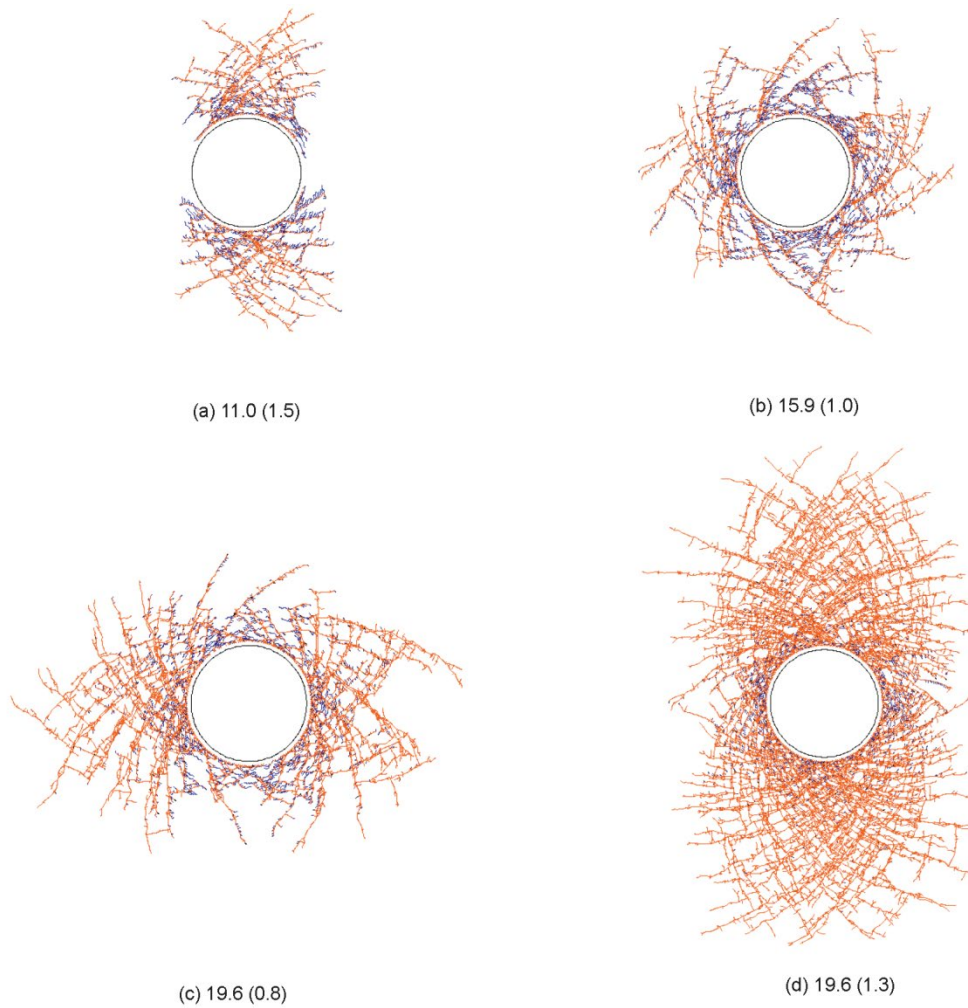


Fig. 8-12: Fracture patterns around the excavation of the shaft model under different *in situ* stress conditions. Tensile and shear failure are indicated in blue and orange, respectively. For each case, the *in situ* vertical stress, σ_v , is reported together with the stress ratio, K_0 , in brackets. Strength parameters are "OpaMax x 0.75", while the core softening ratio at the time of support installation is equal to 0.01.

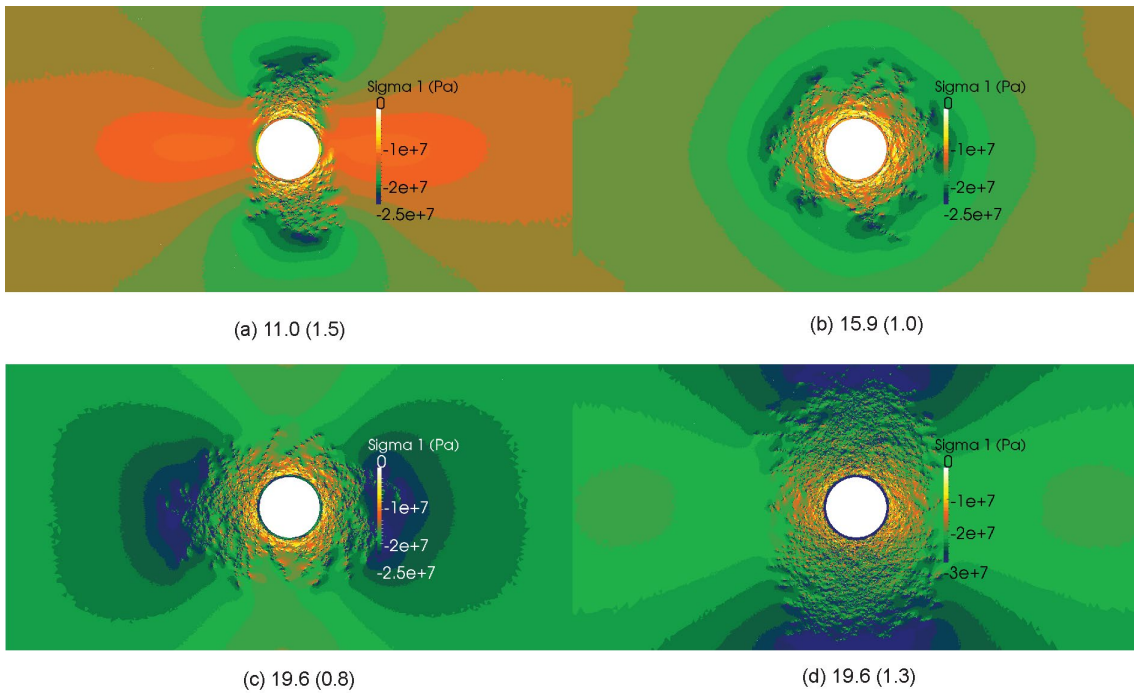


Fig. 8-13: Contours of maximum principal stress, σ_1 , of the shaft model under different *in situ* stress conditions. For each case, the *in situ* vertical stress, σ_v , is reported together with the stress ratio, K_0 , in brackets. Strength parameters are "OpaMax x 0.75", while the core softening ratio at the time of support installation is equal to 0.01.

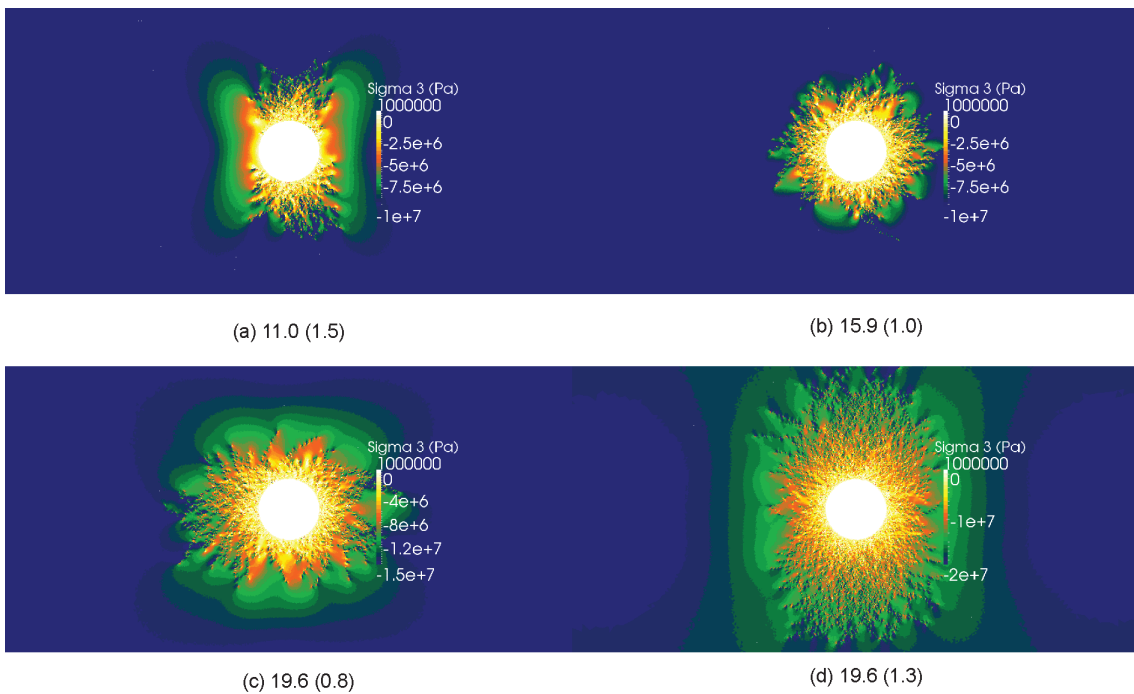


Fig. 8-14: Contours of minimum principal stress, σ_3 , of the shaft model under different *in situ* stress conditions. For each case, the *in situ* vertical stress, σ_v , is reported together with the stress ratio, K_0 , in brackets. Strength parameters are "OpaMax x 0.75", while the core softening ratio at the time of support installation is equal to 0.01.

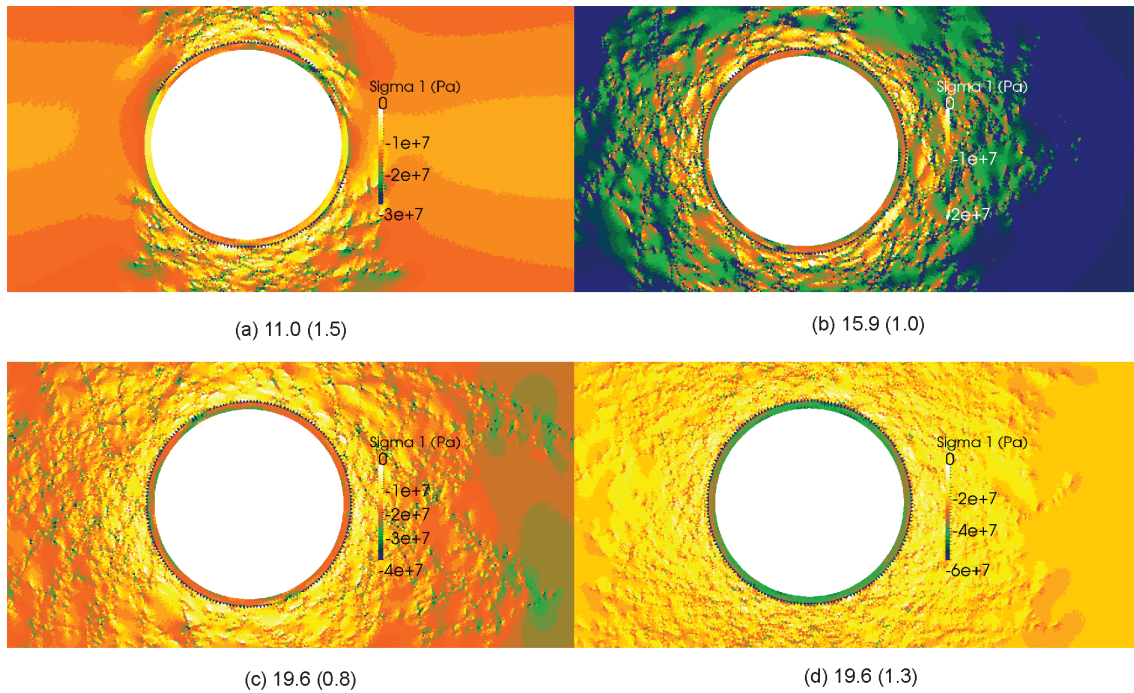


Fig. 8-15: Contours of maximum principal stress, σ_1 , in the support layer of the shaft model under different *in situ* stress conditions. For each case, the *in situ* vertical stress, σ_v , is reported together with the stress ratio, K_0 , in brackets. Strength parameters are "OpaMax x 0.75", while the core softening ratio at the time of support installation is equal to 0.01.

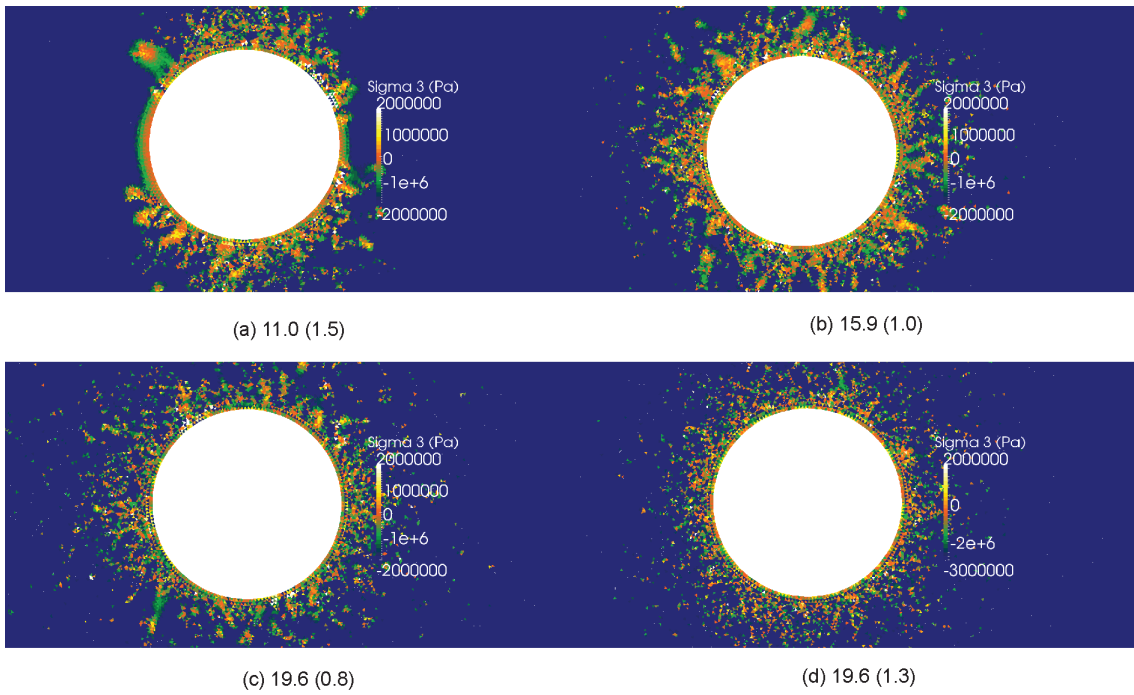


Fig. 8-16: Contours of minimum principal stress, σ_3 , in the support layer of the shaft model under different *in situ* stress conditions. For each case, the *in situ* vertical stress, σ_v , is reported together with the stress ratio, K_0 , in brackets. Strength parameters are "OpaMax x 0.75", while the core softening ratio at the time of support installation is equal to 0.01.

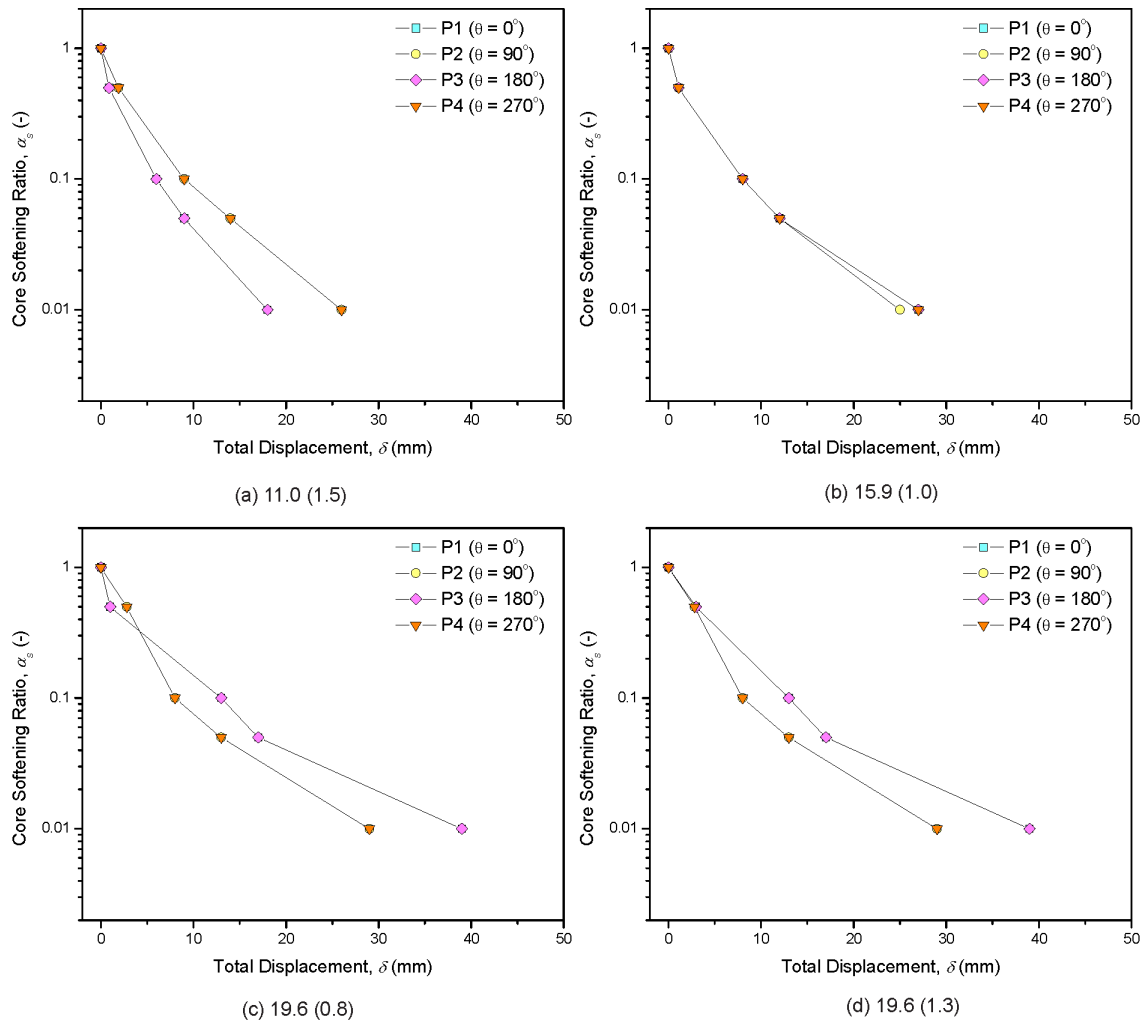


Fig. 8-17: Ground reactions of the shaft model under different *in situ* stress conditions. For each case, the *in situ* vertical stress, σ_v , is reported together with the stress ratio, K_0 , in brackets. Strength parameters are "OpaMax x 0.50". The exact location of points P1-P4 is reported in Fig. 5-3.

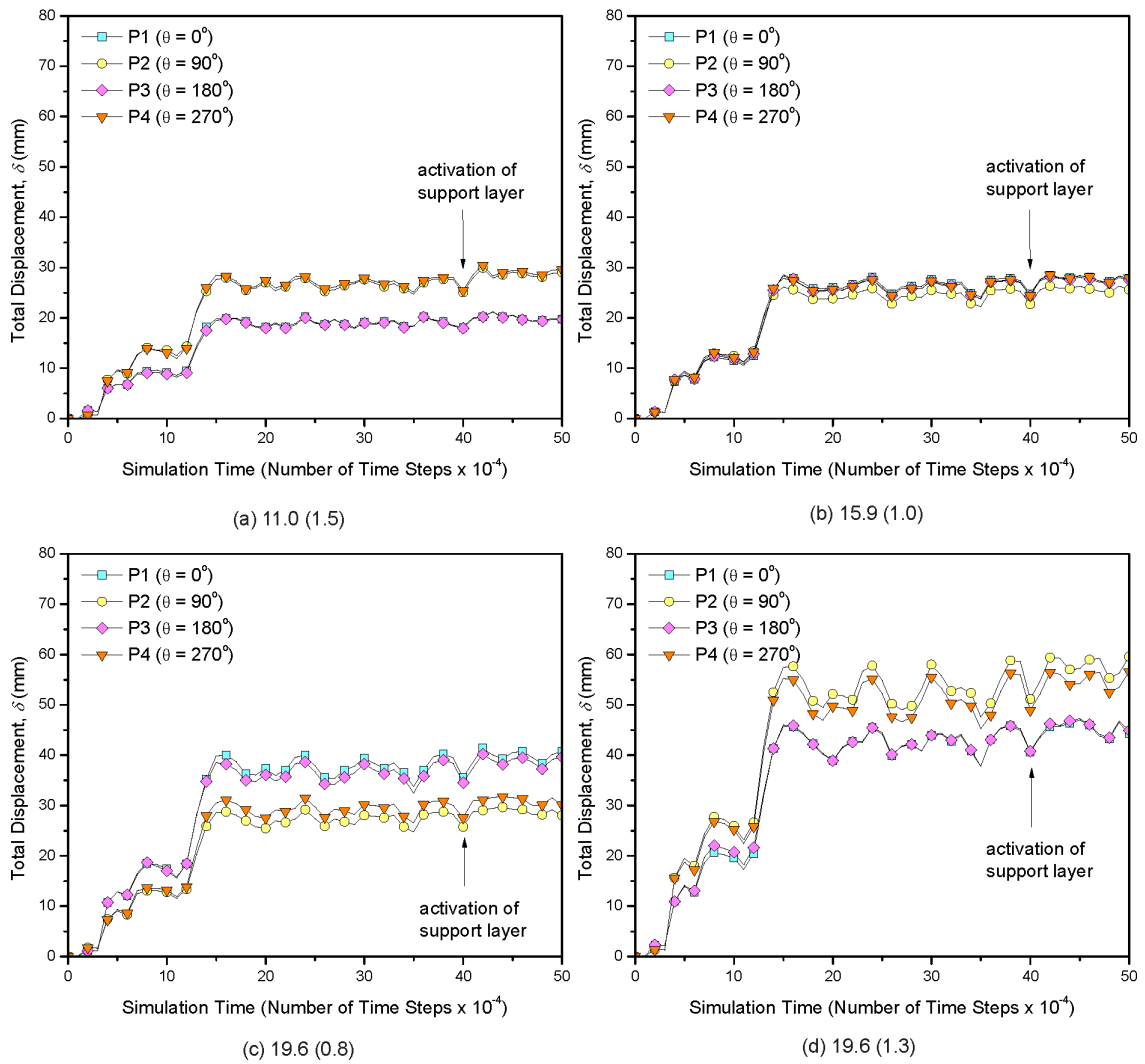


Fig. 8-18: Evolution of displacement, δ , around the excavation boundary of the shaft model under different *in situ* stress conditions. For each case, the *in situ* vertical stress, σ_v , is reported together with the stress ratio, K_0 , in brackets. Strength parameters are "OpaMax x 0.50", while the core softening ratio at the time of support installation is equal to 0.01. The exact location of points P1-P4 is reported in Fig. 5-3.

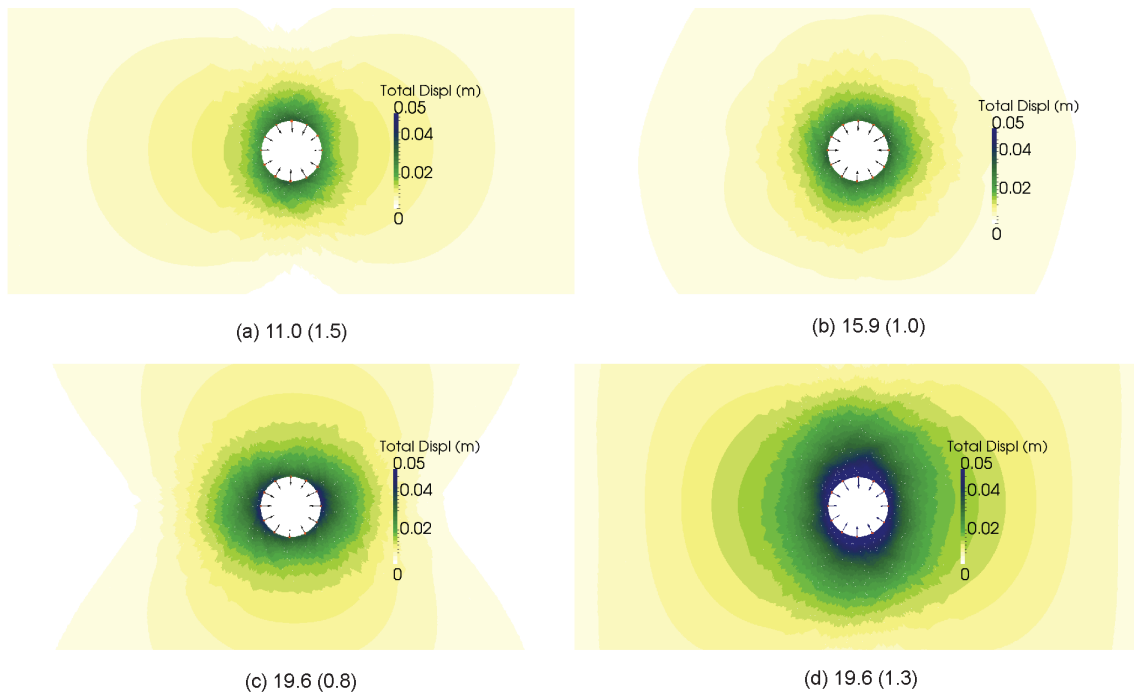


Fig. 8-19: Contours of displacement, δ , of the shaft model under different *in situ* stress conditions. For each case, the *in situ* vertical stress, σ_v , is reported together with the stress ratio, K_0 , in brackets. Strength parameters are "OpaMax x 0.50", while the core softening ratio at the time of support installation is equal to 0.01.

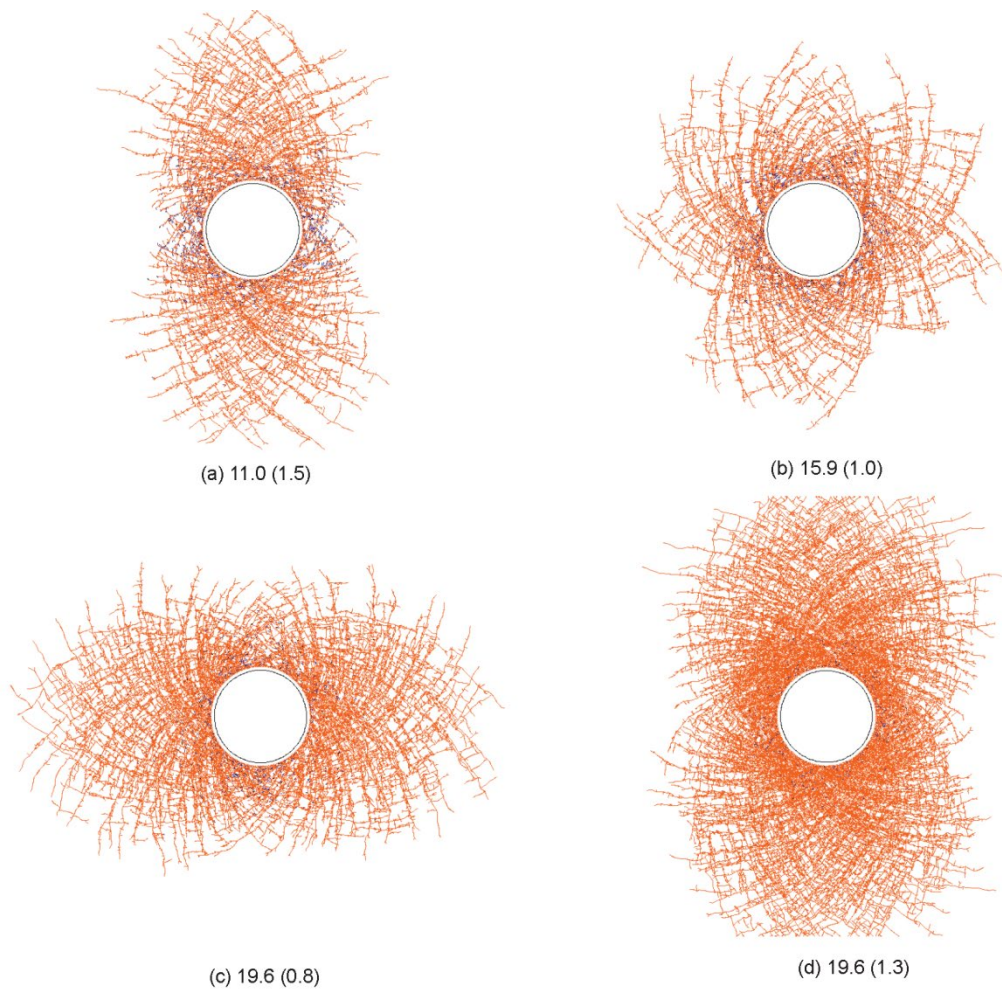


Fig. 8-20: Fracture patterns around the excavation of the shaft model under different *in situ* stress conditions. Tensile and shear failure are indicated in blue and orange, respectively. For each case, the *in situ* vertical stress, σ_v , is reported together with the stress ratio, K_0 , in brackets. Strength parameters are "OpaMax x 0.50", while the core softening ratio at the time of support installation is equal to 0.01.

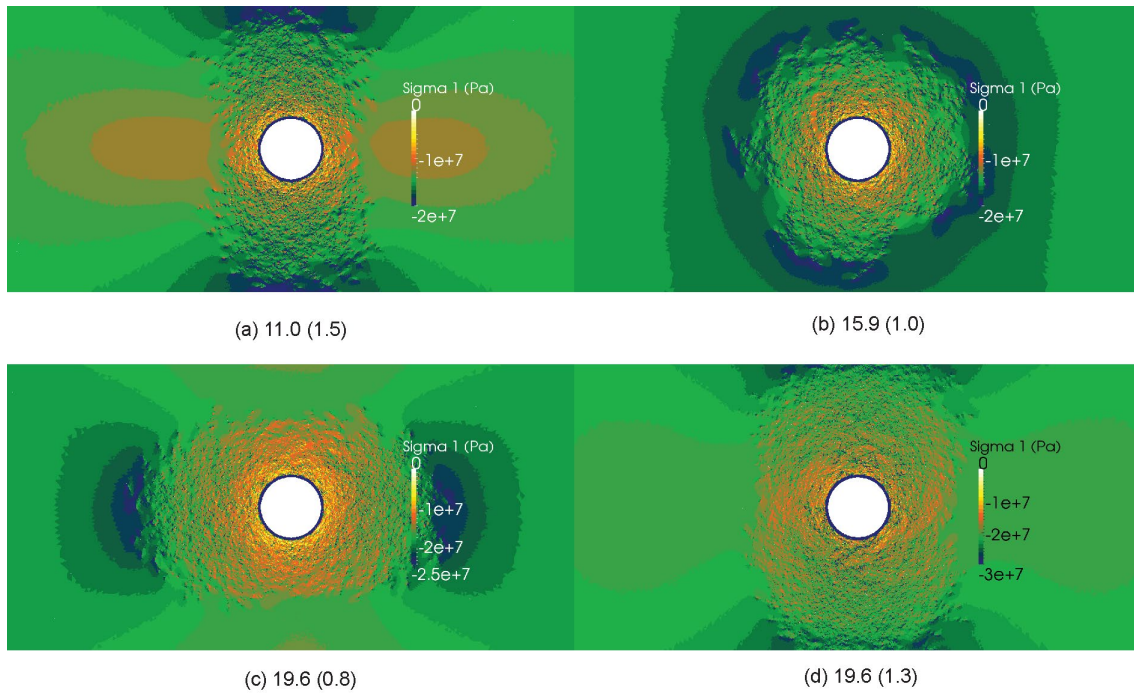


Fig. 8-21: Contours of maximum principal stress, σ_1 , of the shaft model under different *in situ* stress conditions. For each case, the *in situ* vertical stress, σ_v , is reported together with the stress ratio, K_0 , in brackets. Strength parameters are "OpaMax x 0.50", while the core softening ratio at the time of support installation is equal to 0.01.

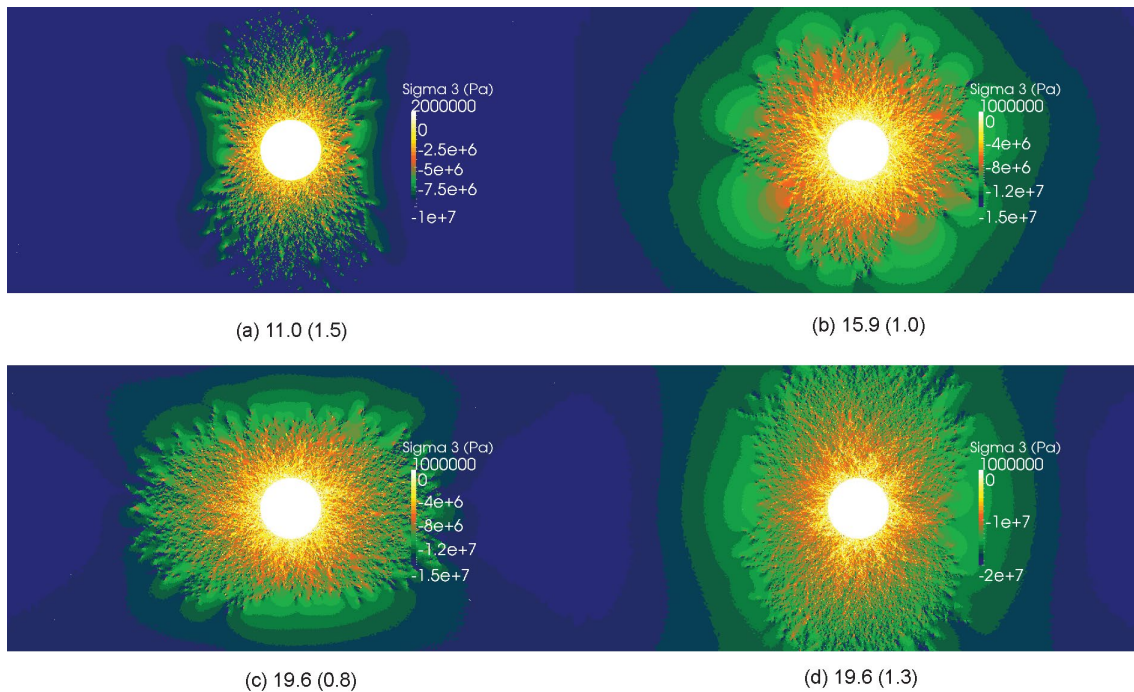


Fig. 8-22: Contours of minimum principal stress, σ_3 , of the shaft model under different *in situ* stress conditions. For each case, the *in situ* vertical stress, σ_v , is reported together with the stress ratio, K_0 , in brackets. Strength parameters are "OpaMax x 0.50", while the core softening ratio at the time of support installation is equal to 0.01.

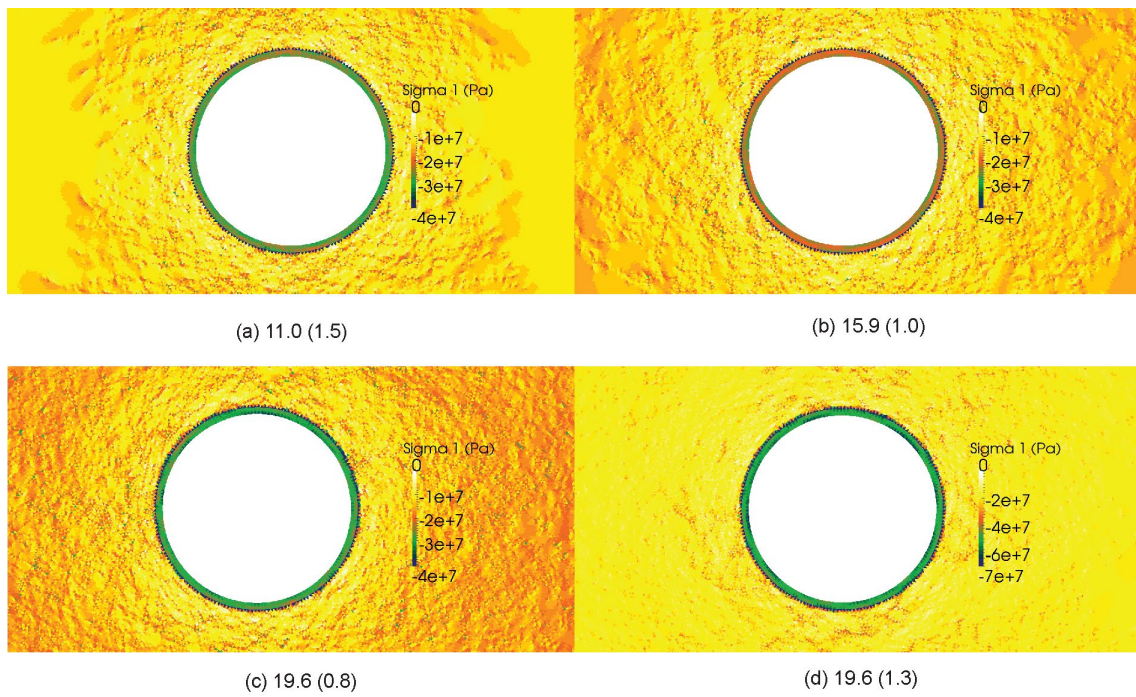


Fig. 8-23: Contours of maximum principal stress, σ_1 , in the support layer of the shaft model under different *in situ* stress conditions. For each case, the *in situ* vertical stress, σ_v , is reported together with the stress ratio, K_0 , in brackets. Strength parameters are "OpaMax x 0.50", while the core softening ratio at the time of support installation is equal to 0.01.

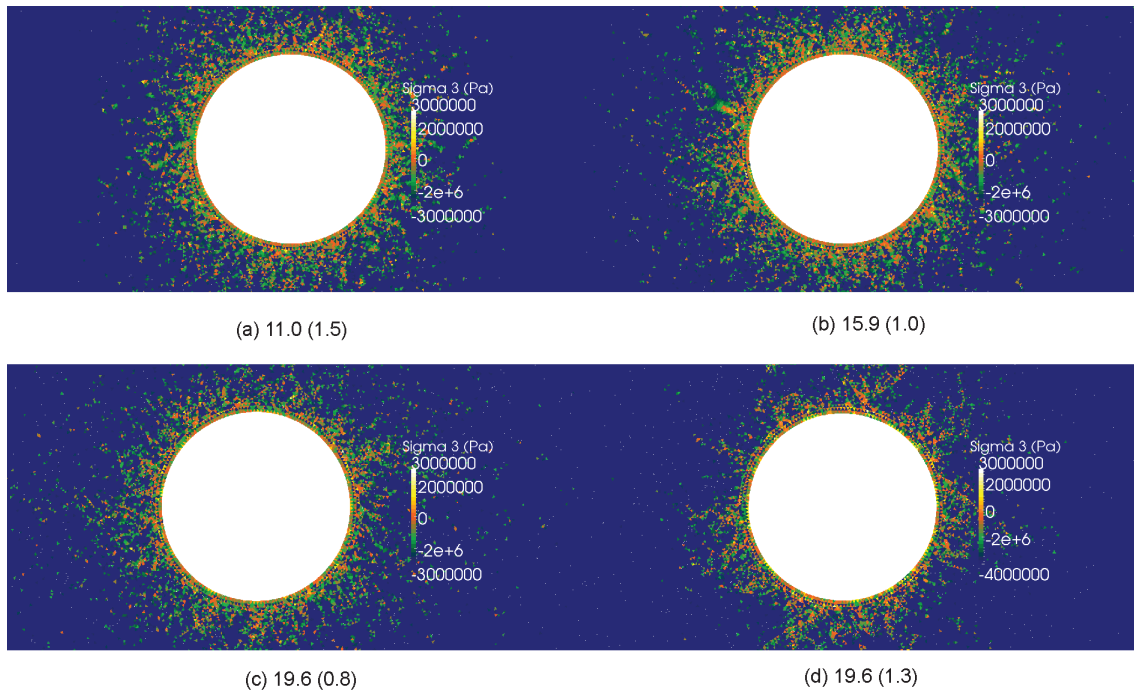


Fig. 8-24: Contours of minimum principal stress, σ_3 , in the support layer of the shaft model under different in situ stress conditions. For each case, the in situ vertical stress, σ_v , is reported together with the stress ratio, K_0 , in brackets. Strength parameters are "OpaMax x 0.50", while the core softening ratio at the time of support installation is equal to 0.01.

9 Results: simulation of EDZ reconsolidation

As summarized in Table 9, the reconsolidation of the EDZ was simulated for selected cases from the previous sensitivity analysis relative to both HAA (Section 9.1) and shaft model (Section 9.2).

Tab. 9: Summary of EDZ reconsolidation simulations.

Model	Section	In situ stress conditions	Strength properties	Elastic modulus of support	Faults	Core softening ratio at support installation	Recon-solidation pressure
HAA simulations							
HAA_Rec-01	HAA	19.6, 1.0	Opa x 2	32	N/A	0.01	10 MPa
HAA_Rec-02	HAA	15.9, 1.3	Opa x 2	32	N/A	0.01	10 MPa
HAA_Rec-03	HAA	19.6, 0.8	Opa x 2	32	N/A	0.01	10 MPa
HAA_Rec-04	HAA	19.6, 1.3	Opa x 2	32	N/A	0.01	10 MPa
HAA_Rec-05	HAA	15.9, 1.3	Opa x 3	32	N/A	0.008	10 MPa
HAA_Rec-06	HAA	15.9, 1.3	Opa x 1.5	3.2	N/A	0.008	10 MPa
HAA_Rec-07	HAA	15.9, 1.3	Opa x 2	3.2	N/A	0.008	10 MPa
HAA_Rec-08	HAA	15.9, 1.3	Opa x 3	3.2	N/A	0.008	10 MPa
Shaft simulations							
Shaft_Rec-01	Shaft	15.9, 1.0	OpaMax	32	N/A	0.01	10 MPa
Shaft_Rec-02	Shaft	19.6, 0.8	OpaMax	32	N/A	0.01	10 MPa
Shaft_Rec-03	Shaft	19.6, 1.3	OpaMax	32	N/A	0.01	10 MPa
Shaft_Rec-04	Shaft	11.0, 1.5	OpaMax x 0.75	32	N/A	0.01	10 MPa
Shaft_Rec-05	Shaft	15.9, 1.0	OpaMax x 0.75	32	N/A	0.01	10 MPa

In the following subsections, the simulation results are presented using time evolution of total fracture aperture and of total displacement, δ , of selected points located along the excavation boundary, contours of total displacements, δ , fracture patterns and contours of maximum and minimum principal stress, σ_1 and σ_3 , in the rock mass and the support layer.

9.1 SF/HLW emplacement tunnel

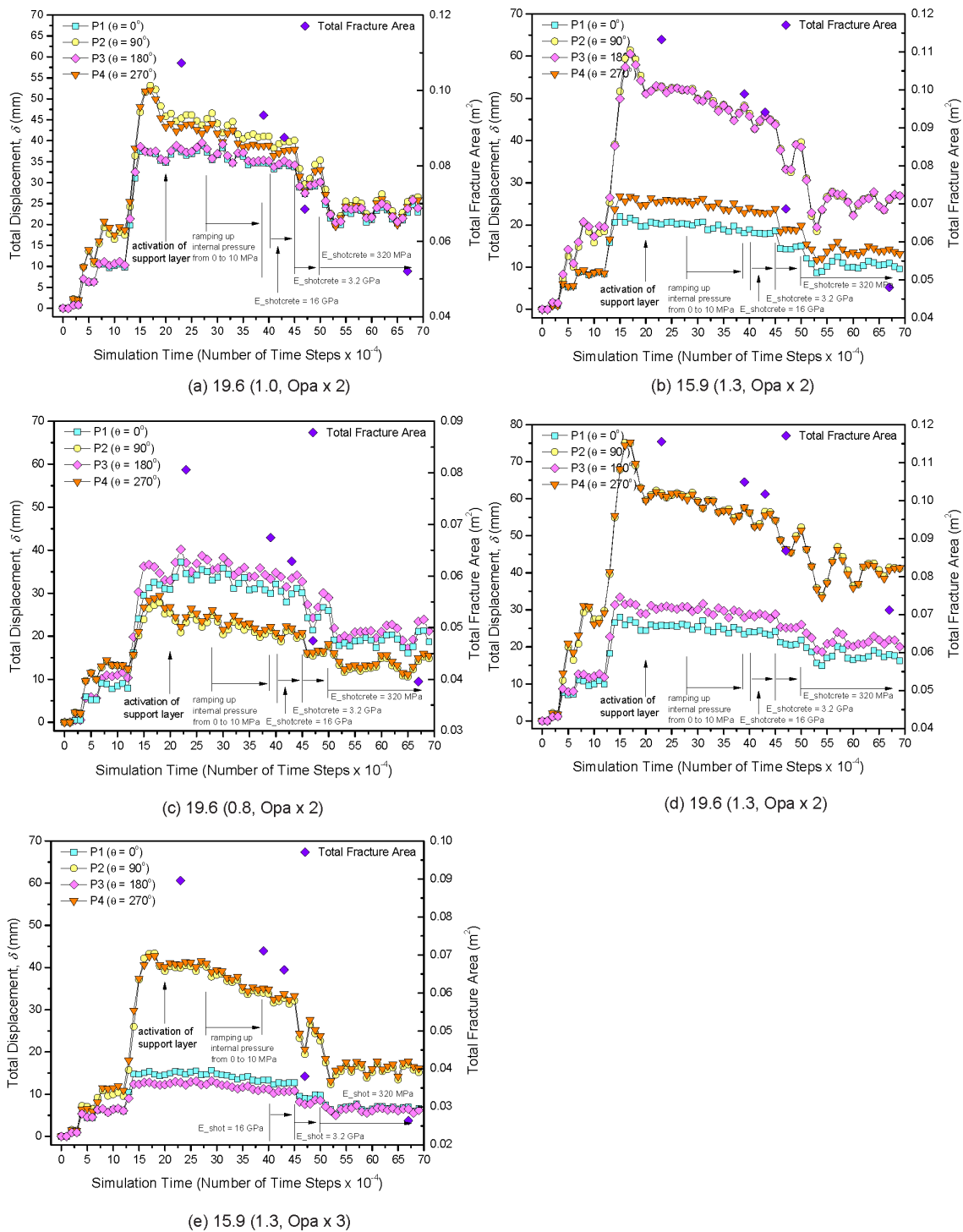


Fig. 9-1: Evolution of total fracture area and displacement, δ , around the excavation boundary of the HAA reconsolidation model under different in situ stress conditions and for varying strength parameters. For each case, the in situ vertical stress, σ_v , is reported together with the stress ratio, K_0 , and the strength parameters in brackets. The core softening ratio at the time of support installation is equal to 0.008. The exact location of points P1-P4 is reported in Fig. 5-1.

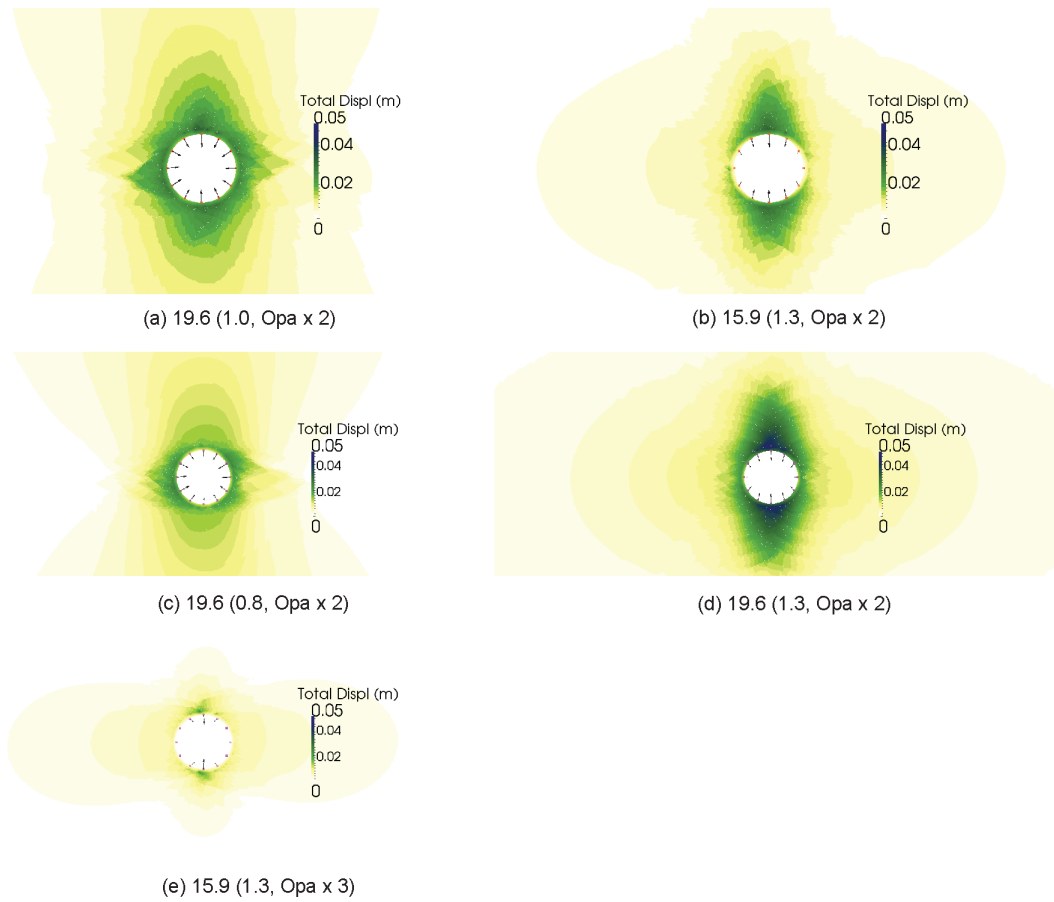


Fig. 9-2: Contours of displacement, δ , of the HAA reconsolidation model under different *in situ* stress conditions and for varying strength parameters. For each case, the *in situ* vertical stress, σ_v , is reported together with the stress ratio, K_0 , and the strength parameters in brackets. The core softening ratio at the time of support installation is equal to 0.008.

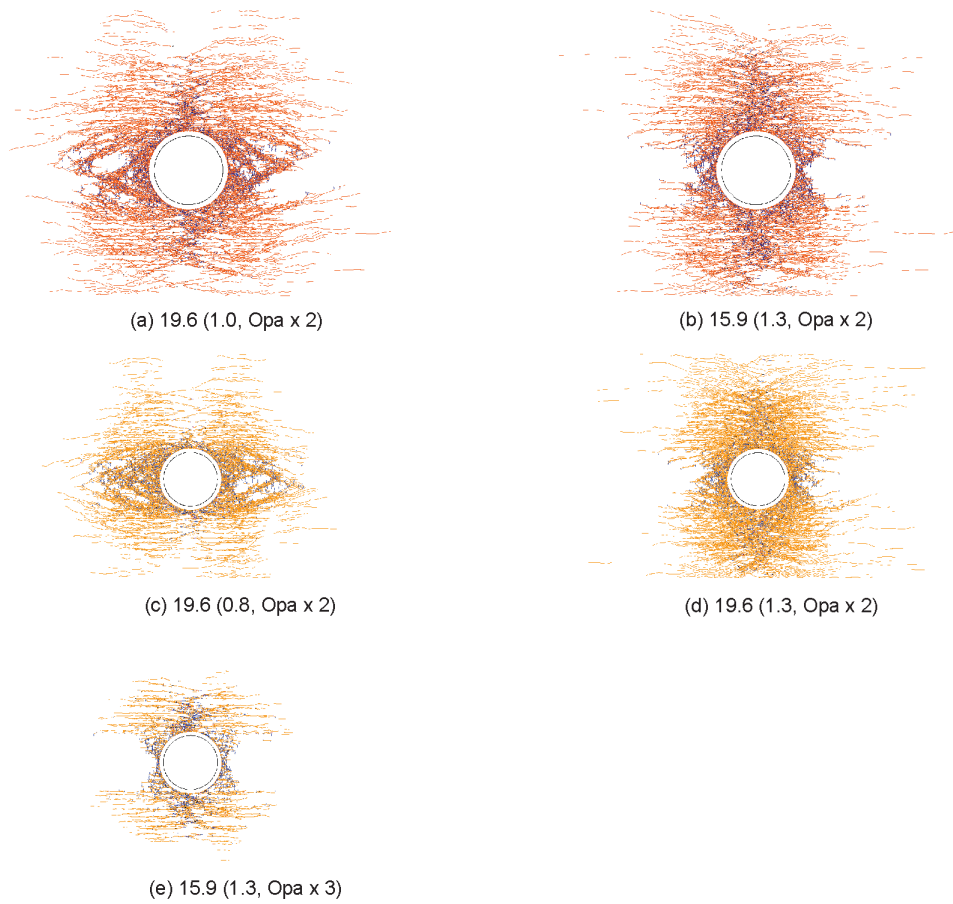


Fig. 9-3: Fracture patterns around the excavation of the HAA reconsolidation model under different *in situ* stress conditions and for varying strength parameters. Tensile and shear failure are indicated in blue and orange, respectively. For each case, the *in situ* vertical stress, σ_v , is reported together with the stress ratio, K_0 , and the strength parameters in brackets. The core softening ratio at the time of support installation is equal to 0.008.

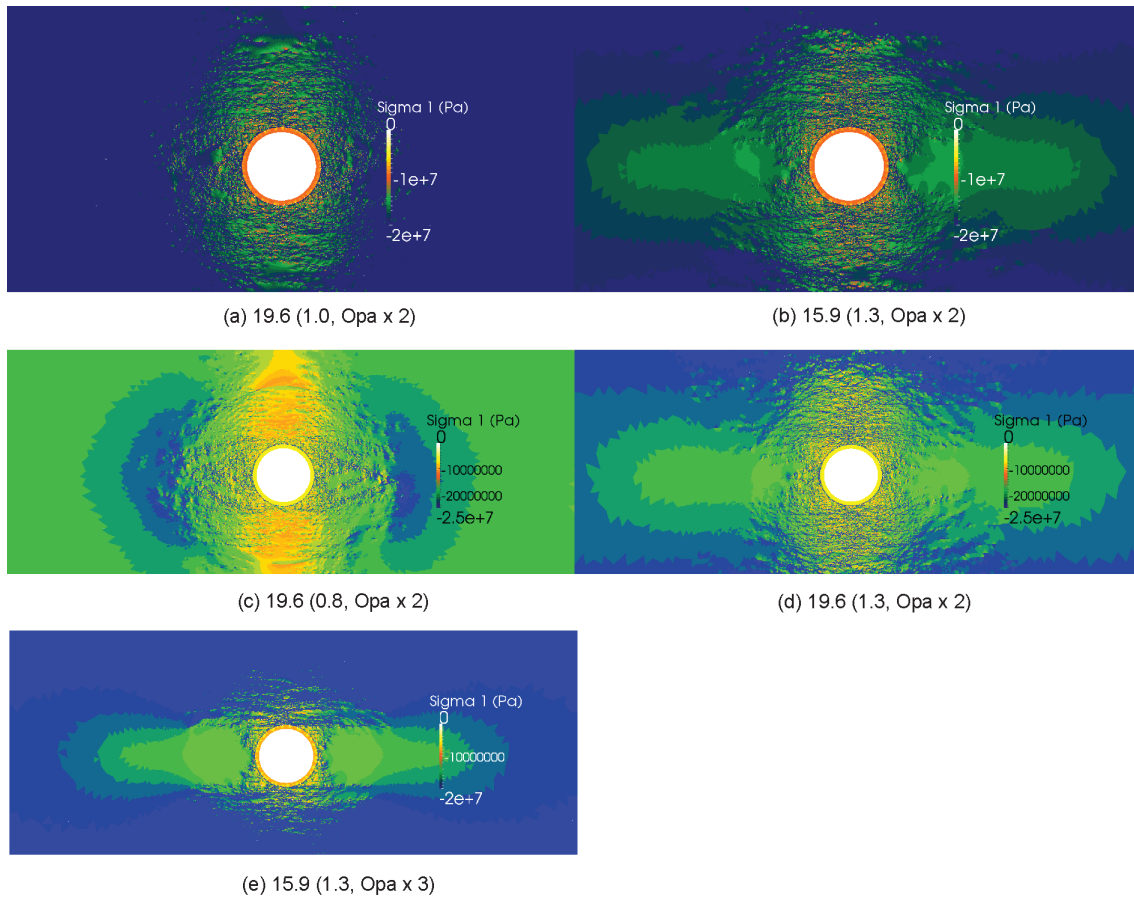


Fig. 9-4: Contours of maximum principal stress, σ_1 , of the HAA reconsolidation model under different *in situ* stress conditions and for varying strength parameters. For each case, the *in situ* vertical stress, σ_{v_0} , is reported together with the stress ratio, K_0 , and the strength parameters in brackets. The core softening ratio at the time of support installation is equal to 0.008.

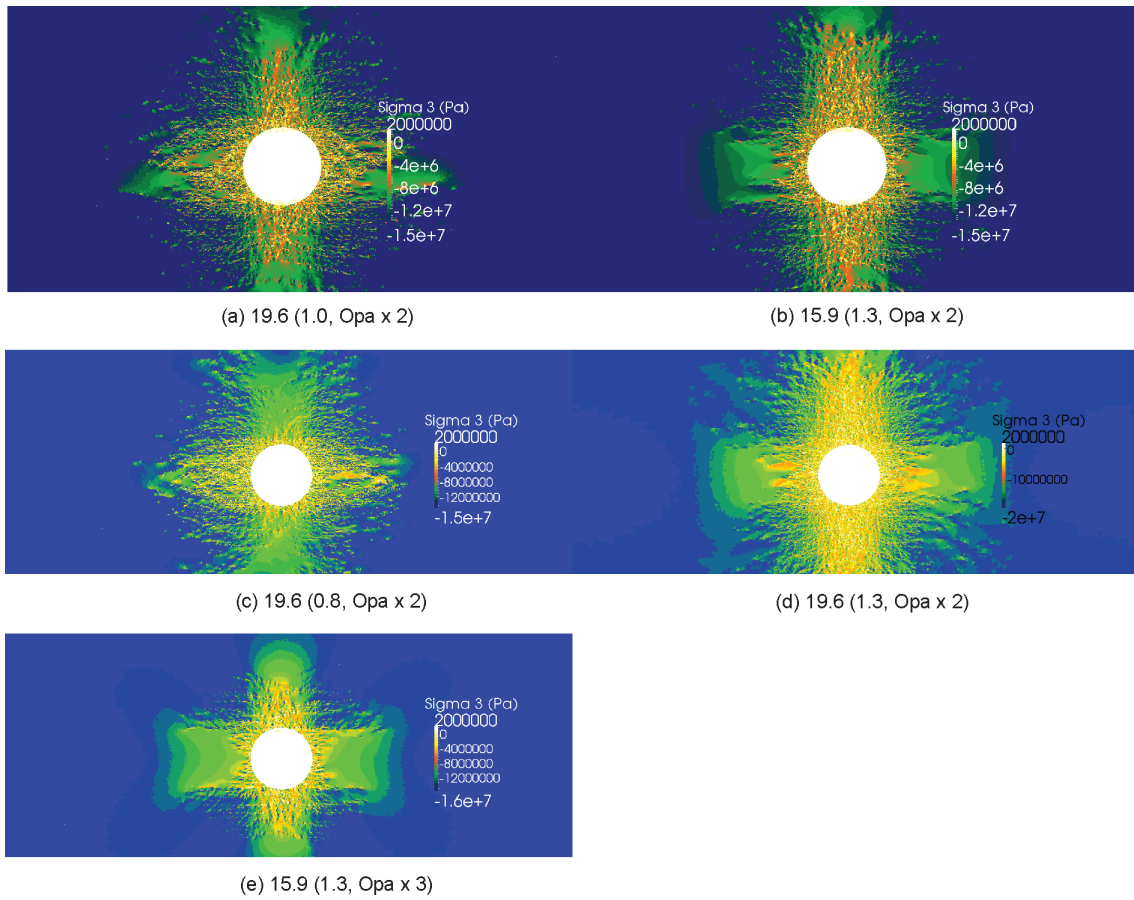


Fig. 9-5: Contours of minimum principal stress, σ_3 , of the HAA reconsolidation model under different *in situ* stress conditions and for varying strength parameters. For each case, the *in situ* vertical stress, σ_v , is reported together with the stress ratio, K_0 , and the strength parameters in brackets. The core softening ratio at the time of support installation is equal to 0.008.

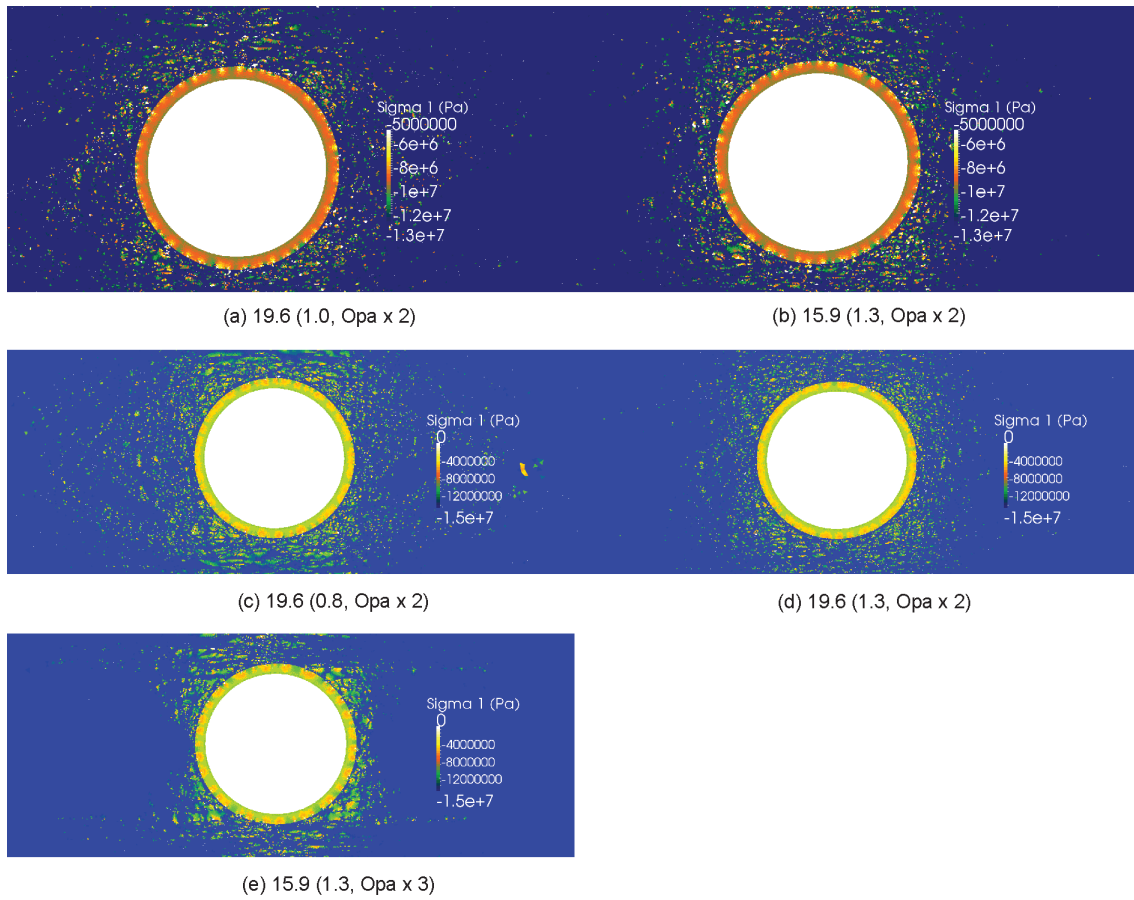


Fig. 9-6: Contours of maximum principal stress, σ_1 , in the support layer of the HAA reconsolidation model under different *in situ* stress conditions and for varying strength parameters. For each case, the *in situ* vertical stress, σ_v , is reported together with the stress ratio, K_0 , and the strength parameters in brackets. The core softening ratio at the time of support installation is equal to 0.008.

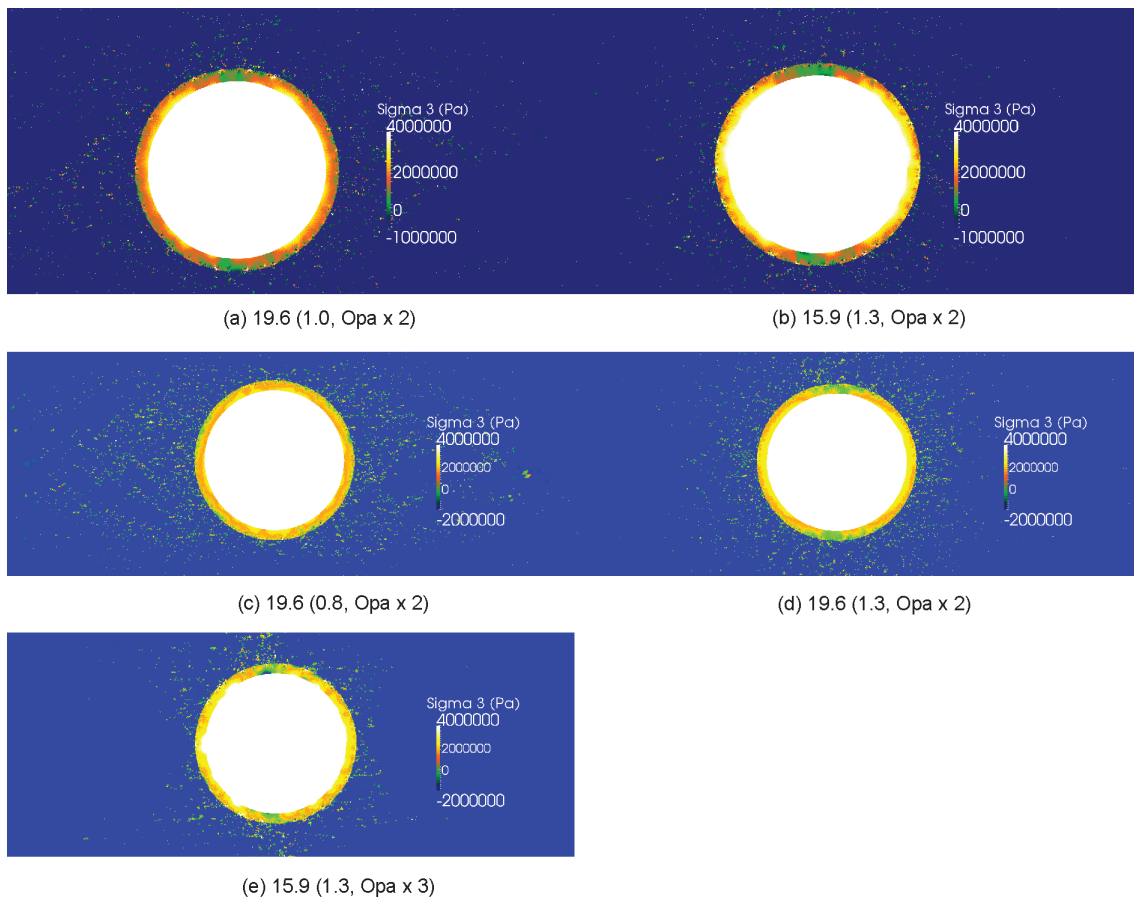


Fig. 9-7: Contours of minimum principal stress, σ_3 , in the support layer of the HAA reconsolidation model under different *in situ* stress conditions and for varying strength parameters. For each case, the *in situ* vertical stress, σ_v , is reported together with the stress ratio, K_0 , and the strength parameters in brackets. The core softening ratio at the time of support installation is equal to 0.008.

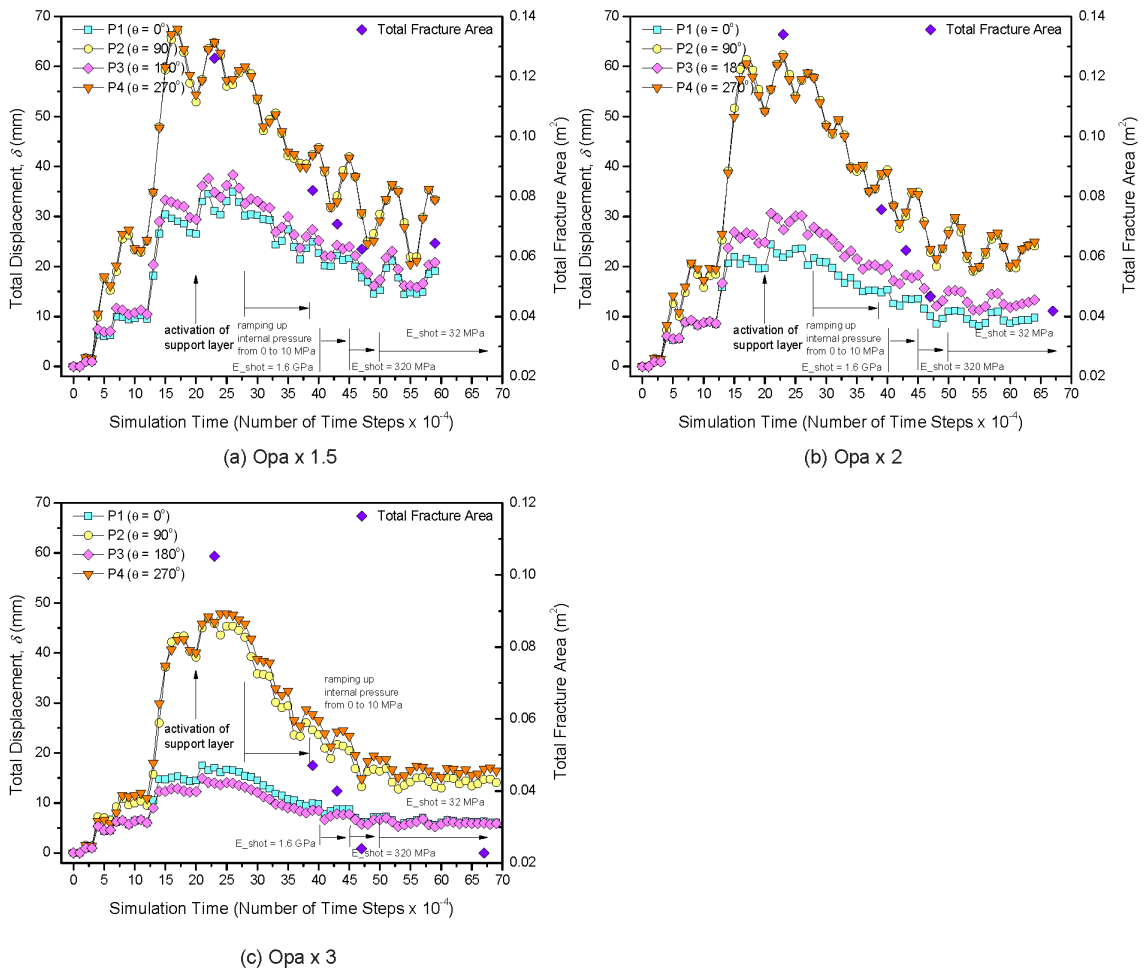


Fig. 9-8: Evolution of total fracture area and displacement, δ , around the excavation boundary of the HAA reconsolidation model for varying strength parameters. The vertical *in situ* stress is equal to 15.9 MPa with a stress ratio $K_0 = 1.3$, while the core softening ratio at the time of support installation is equal to 0.01. The initial Young's modulus of the support layer is equal to 3.2 GPa. The exact location of points P1-P4 is reported in Fig. 5-1.

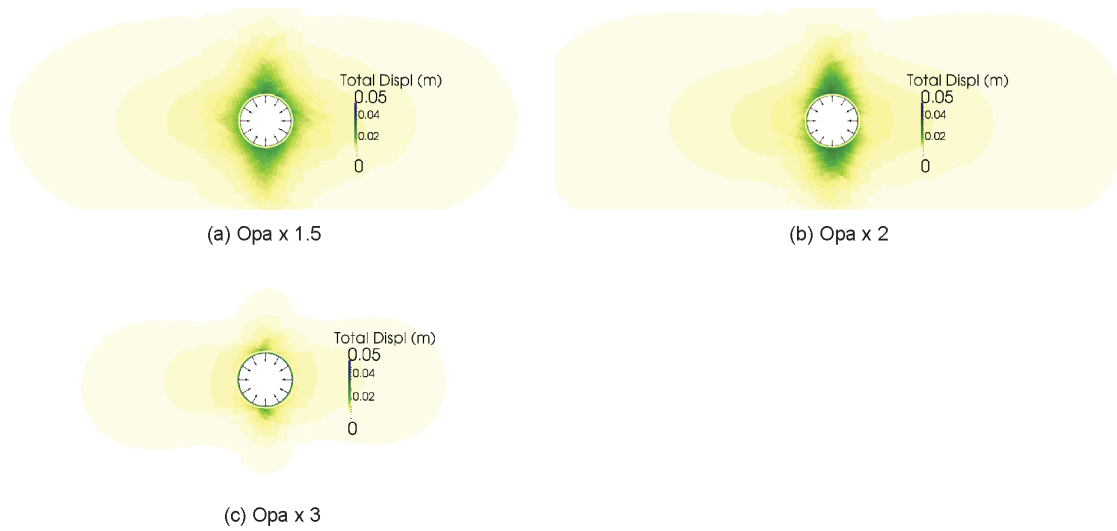


Fig. 9-9: Contours of displacement, δ , of the HAA reconsolidation model for varying strength parameters. The vertical *in situ* stress is equal to 15.9 MPa with a stress ratio $K_0 = 1.3$, while the core softening ratio at the time of support installation is equal to 0.01. The initial Young's modulus of the support layer is equal to 3.2 GPa.

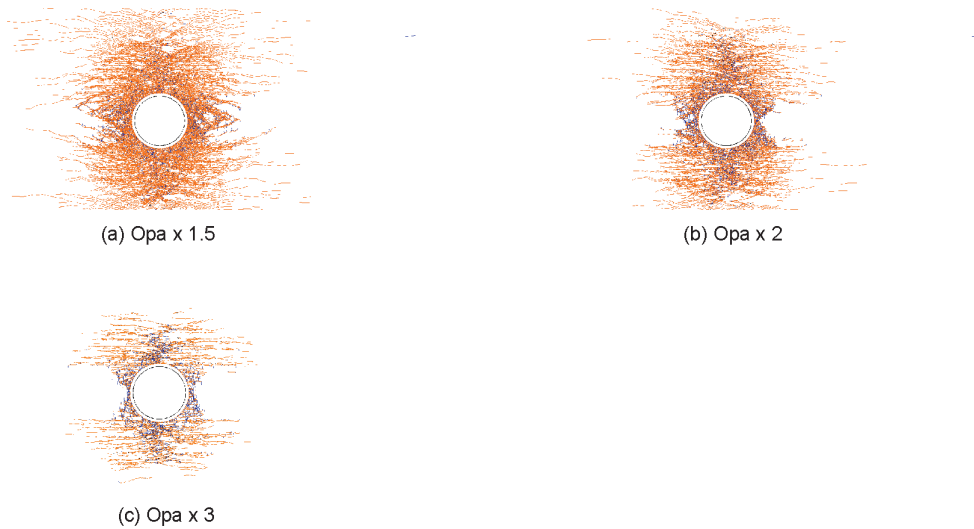


Fig. 9-10: Fracture patterns around the HAA reconsolidation model for varying strength parameters. Tensile and shear failure are indicated in blue and orange, respectively. The vertical *in situ* stress is equal to 15.9 MPa with a stress ratio $K_0 = 1.3$, while the core softening ratio at the time of support installation is equal to 0.01. The initial Young's modulus of the support layer is equal to 3.2 GPa.

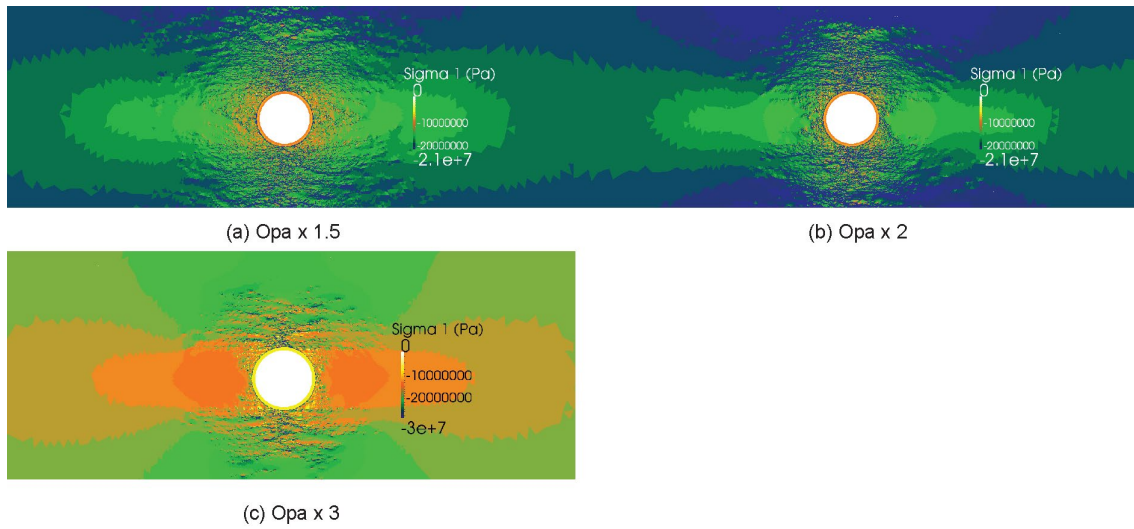


Fig. 9-11: Contours of maximum principal stress, σ_1 , of the HAA reconsolidation model for varying strength parameters. The vertical *in situ* stress is equal to 15.9 MPa with a stress ratio $K_0 = 1.3$, while the core softening ratio at the time of support installation is equal to 0.01. The initial Young's modulus of the support layer is equal to 3.2 GPa.

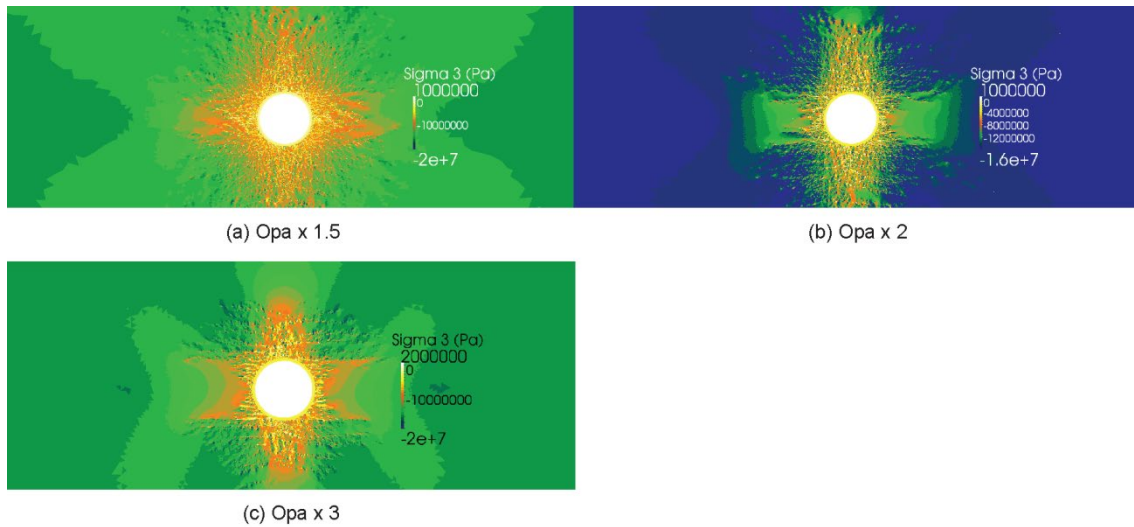


Fig. 9-12: Contours of minimum principal stress, σ_3 , of the HAA reconsolidation model for varying strength parameters. The vertical *in situ* stress is equal to 15.9 MPa with a stress ratio $K_0 = 1.3$, while the core softening ratio at the time of support installation is equal to 0.01. The initial Young's modulus of the support layer is equal to 3.2 GPa.

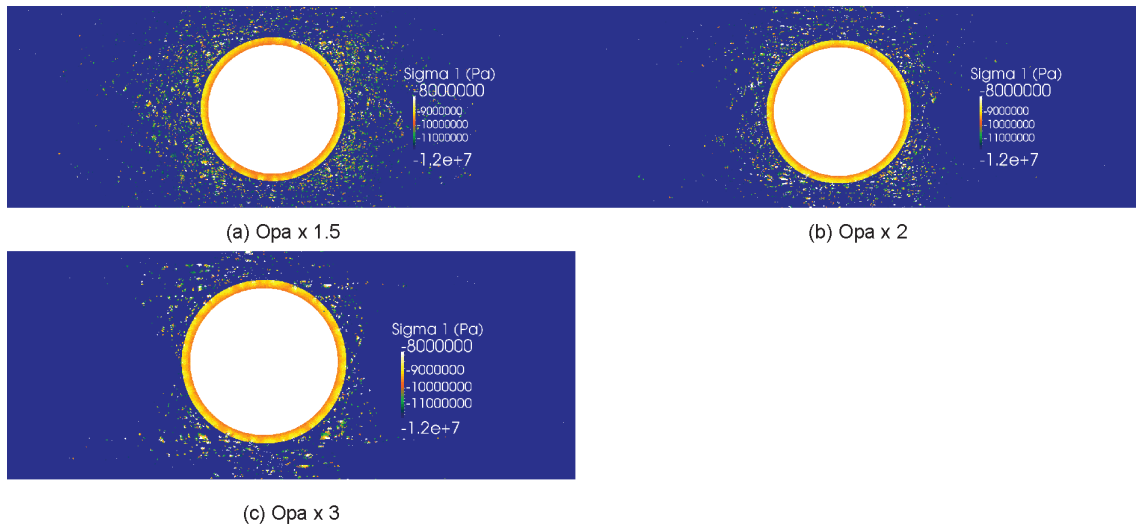


Fig. 9-13: Contours of maximum principal stress, σ_1 , in the support layer of the HAA reconsolidation model for varying strength parameters. The vertical *in situ* stress is equal to 15.9 MPa with a stress ratio $K_0 = 1.3$, while the core softening ratio at the time of support installation is equal to 0.01. The initial Young's modulus of the support layer is equal to 3.2 GPa.

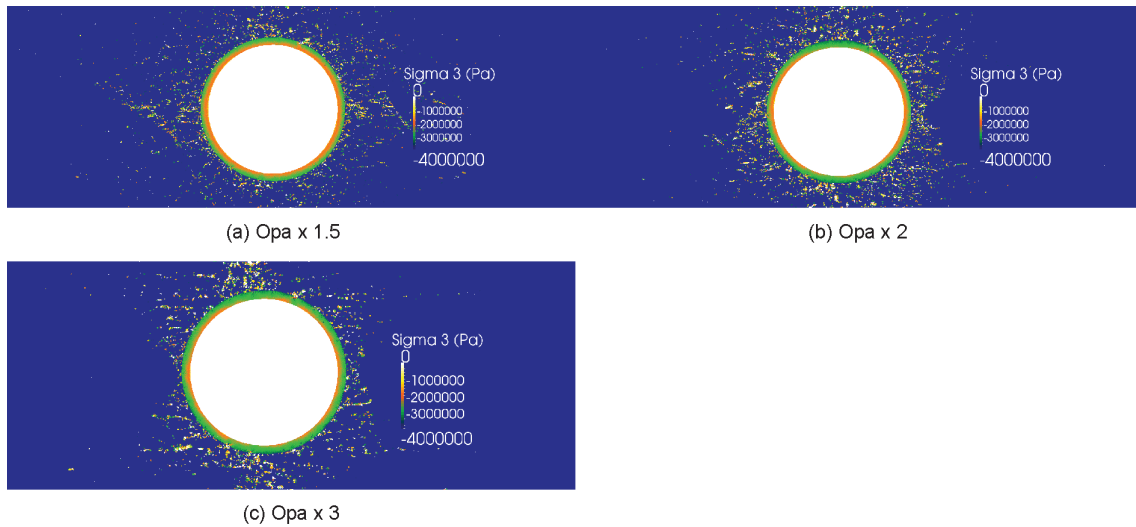


Fig. 9-14: Contours of minimum principal stress, σ_3 , in the support layer the HAA reconsolidation model for varying strength parameters. The vertical *in situ* stress is equal to 15.9 MPa with a stress ratio $K_0 = 1.3$, while the core softening ratio at the time of support installation is equal to 0.01. The initial Young's modulus of the support layer is equal to 3.2 GPa.

9.2 Shaft model

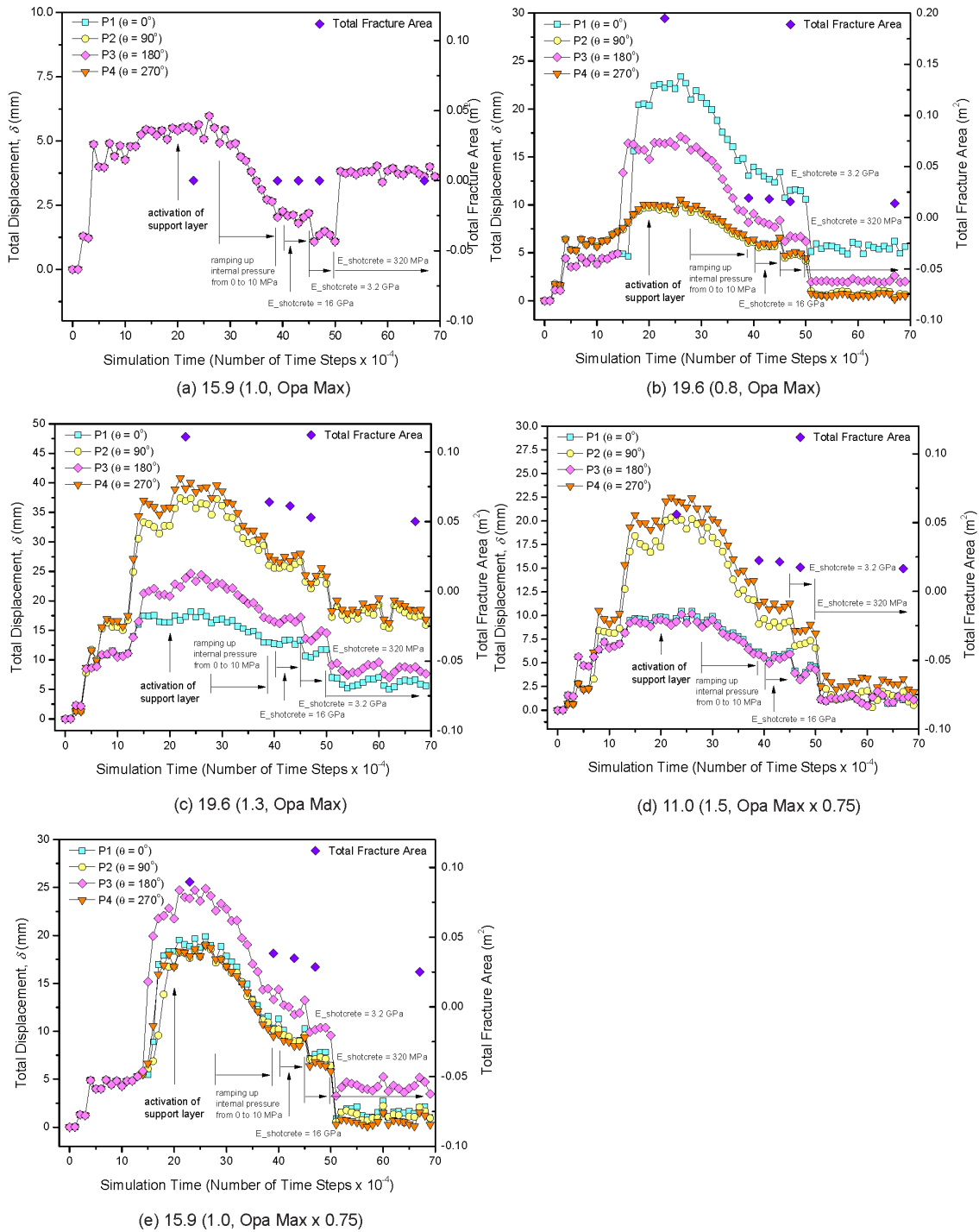


Fig. 9-15: Evolution of total fracture area and displacement, δ , around the excavation boundary of the shaft reconsolidation model under different *in situ* stress conditions and for varying strength parameters. For each case, the *in situ* vertical stress, σ_{v_s} , is reported together with the stress ratio, K_0 , and the strength parameters in brackets. The core softening ratio at the time of support installation is equal to 0.01. The exact location of points P1-P4 is reported in Fig.5-3.

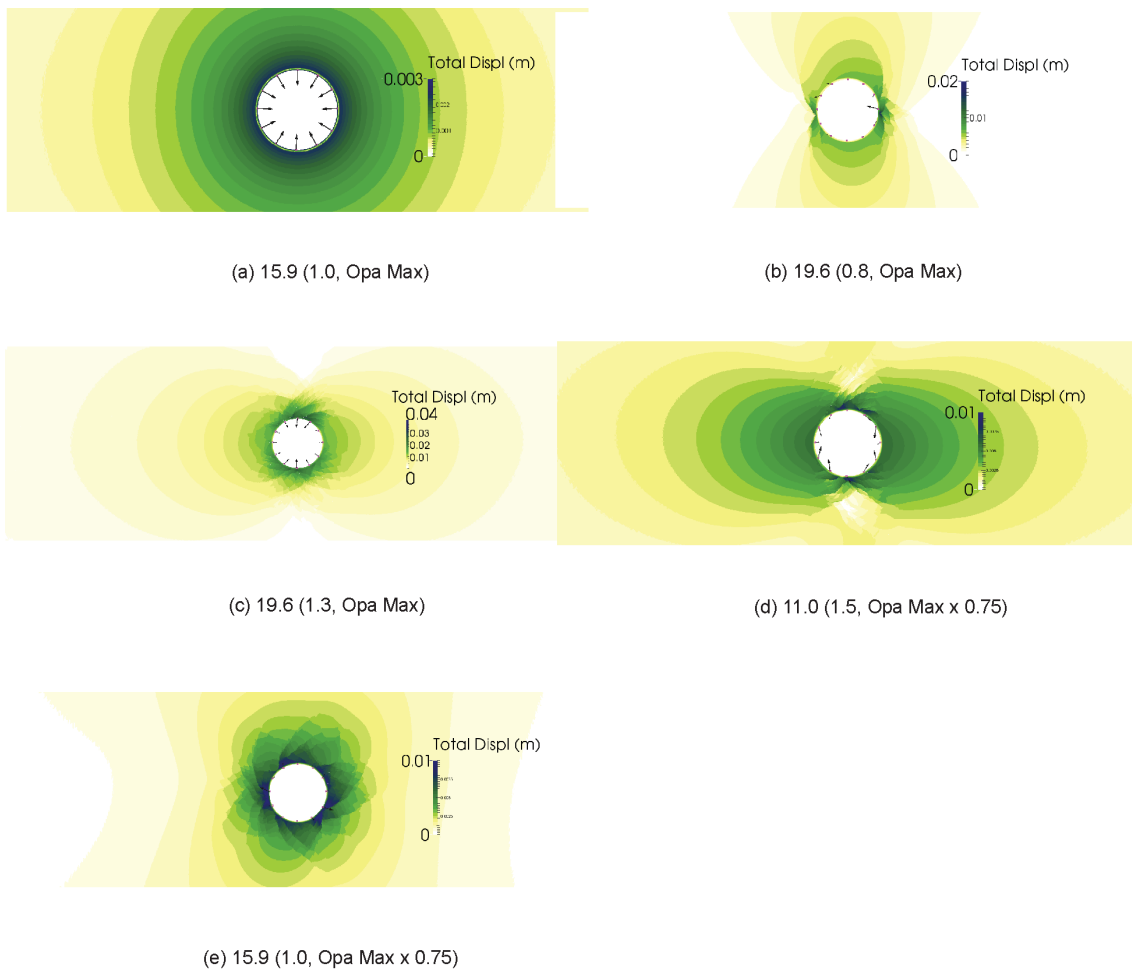


Fig. 9-16: Contours of displacement, δ , around the excavation boundary of the shaft reconsolidation model under different *in situ* stress conditions and for varying strength parameters. For each case, the *in situ* vertical stress, σ_v , is reported together with the stress ratio, K_0 , and the strength parameters in brackets. The core softening ratio at the time of support installation is equal to 0.01.

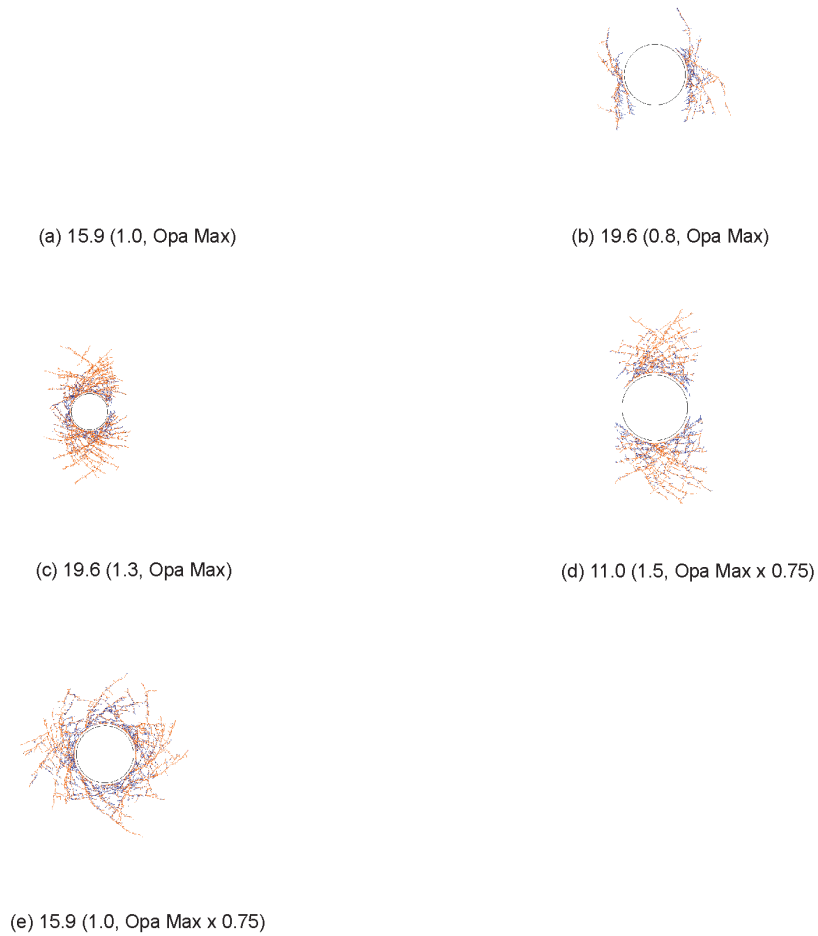


Fig. 9-17: Fracture patterns around the excavation of the shaft reconsolidation model under different *in situ* stress conditions and for varying strength parameters. Tensile and shear failure are indicated in blue and orange, respectively. For each case, the *in situ* vertical stress, σ_v , is reported together with the stress ratio, K_0 , and the strength parameters in brackets. The core softening ratio at the time of support installation is equal to 0.01. Note that no failure was observed in case (a).

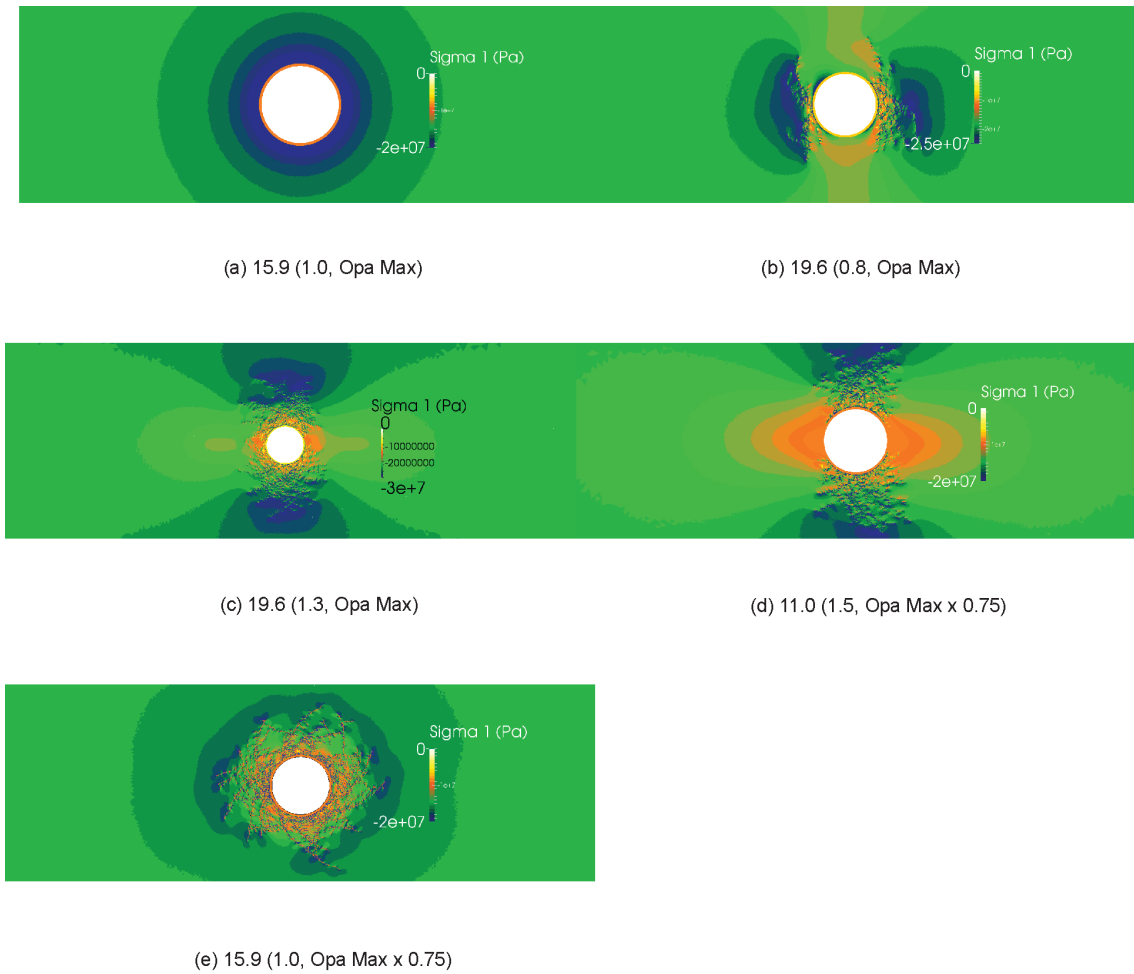


Fig. 9-18: Contours of maximum principal stress, σ_1 , of the shaft reconsolidation model under different *in situ* stress conditions and for varying strength parameters. For each case, the *in situ* vertical stress, σ_v , is reported together with the stress ratio, K_0 , and the strength parameters in brackets. The core softening ratio at the time of support installation is equal to 0.01.

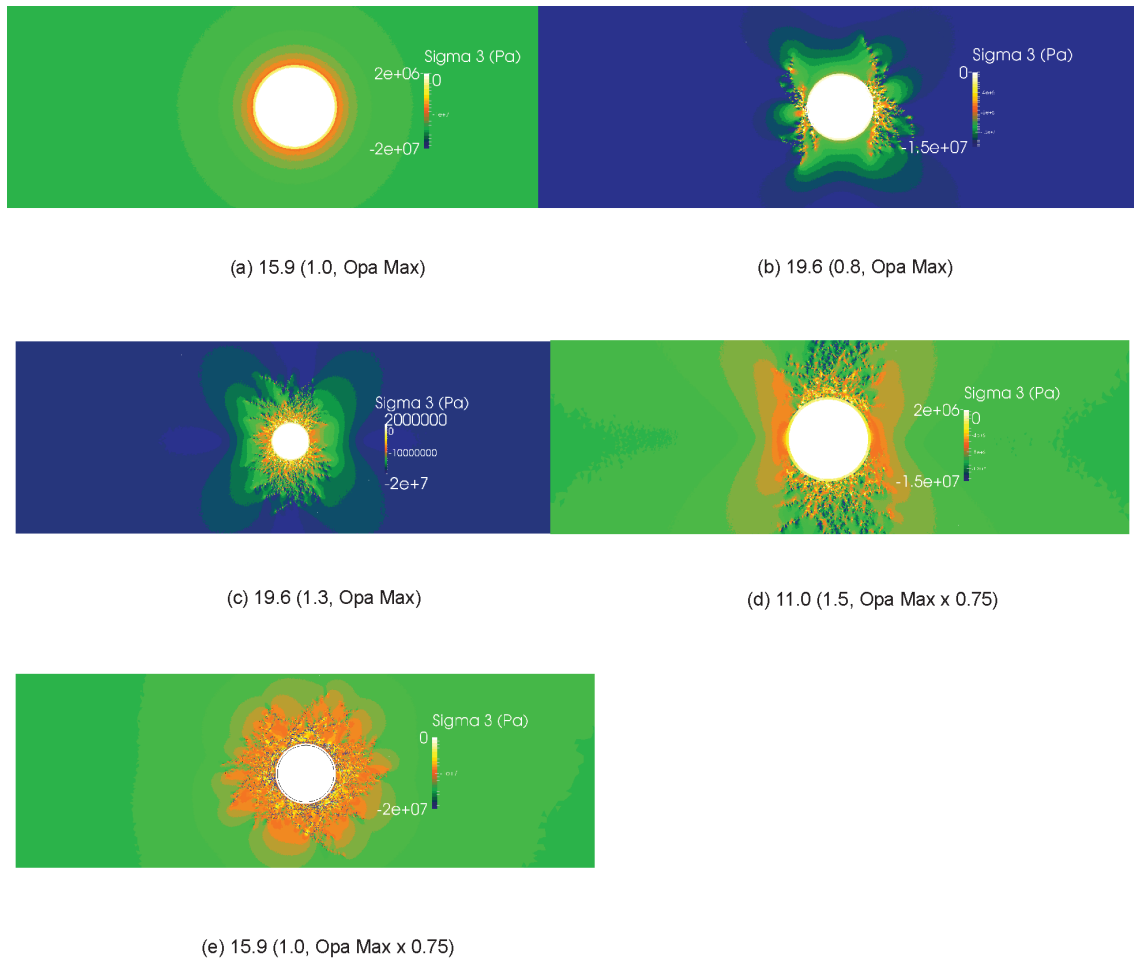


Fig. 9-19: Contours of minimum principal stress, σ_3 , of the shaft reconsolidation model under different *in situ* stress conditions and for varying strength parameters. For each case, the *in situ* vertical stress, σ_v , is reported together with the stress ratio, K_0 , and the strength parameters in brackets. The core softening ratio at the time of support installation is equal to 0.01.

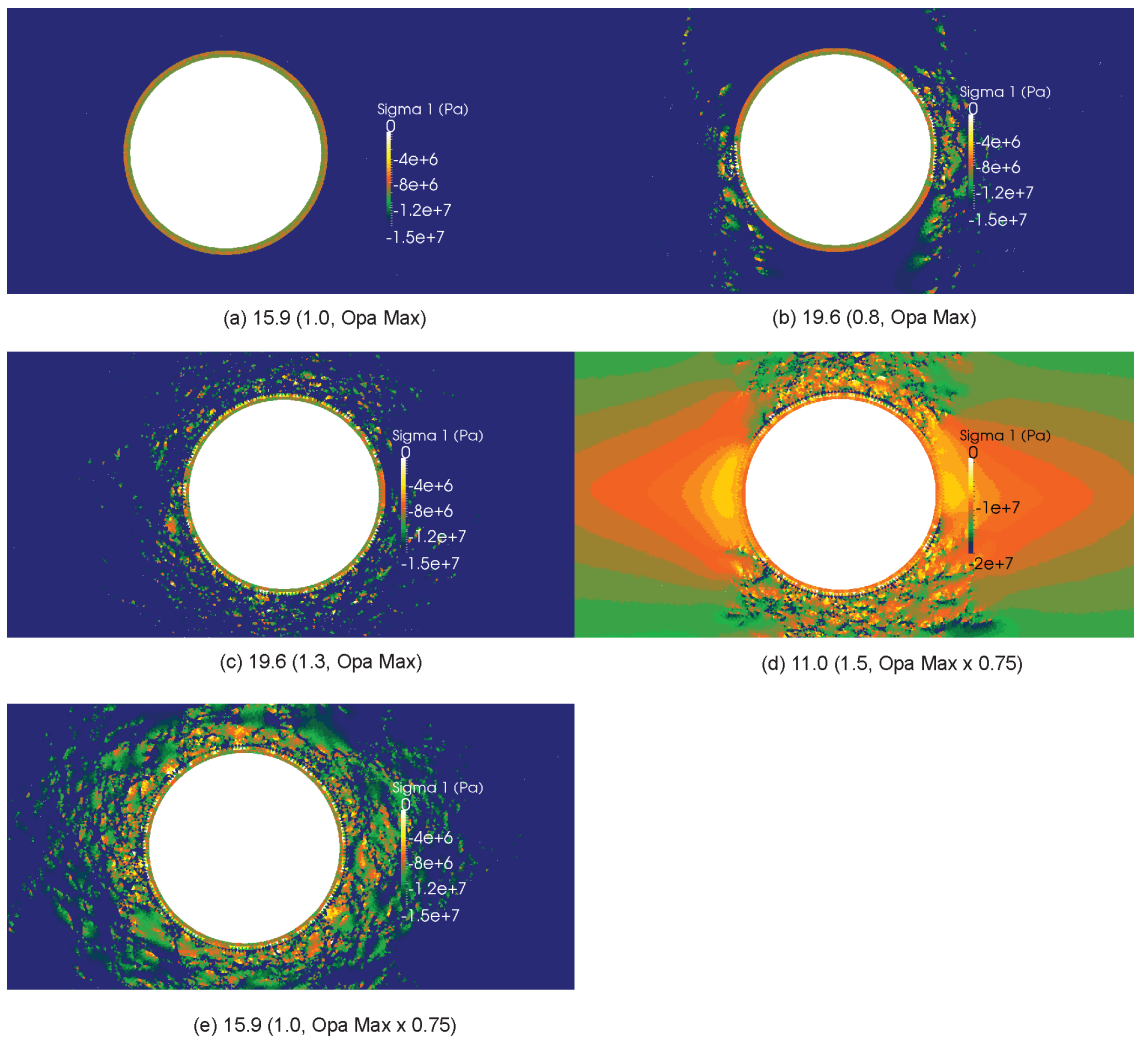


Fig. 9-20: Contours of maximum principal stress, σ_1 , in the support layer of the shaft reconsolidation model under different *in situ* stress conditions and for varying strength parameters. For each case, the *in situ* vertical stress, σ_v , is reported together with the stress ratio, K_0 , and the strength parameters in brackets. The core softening ratio at the time of support installation is equal to 0.01.

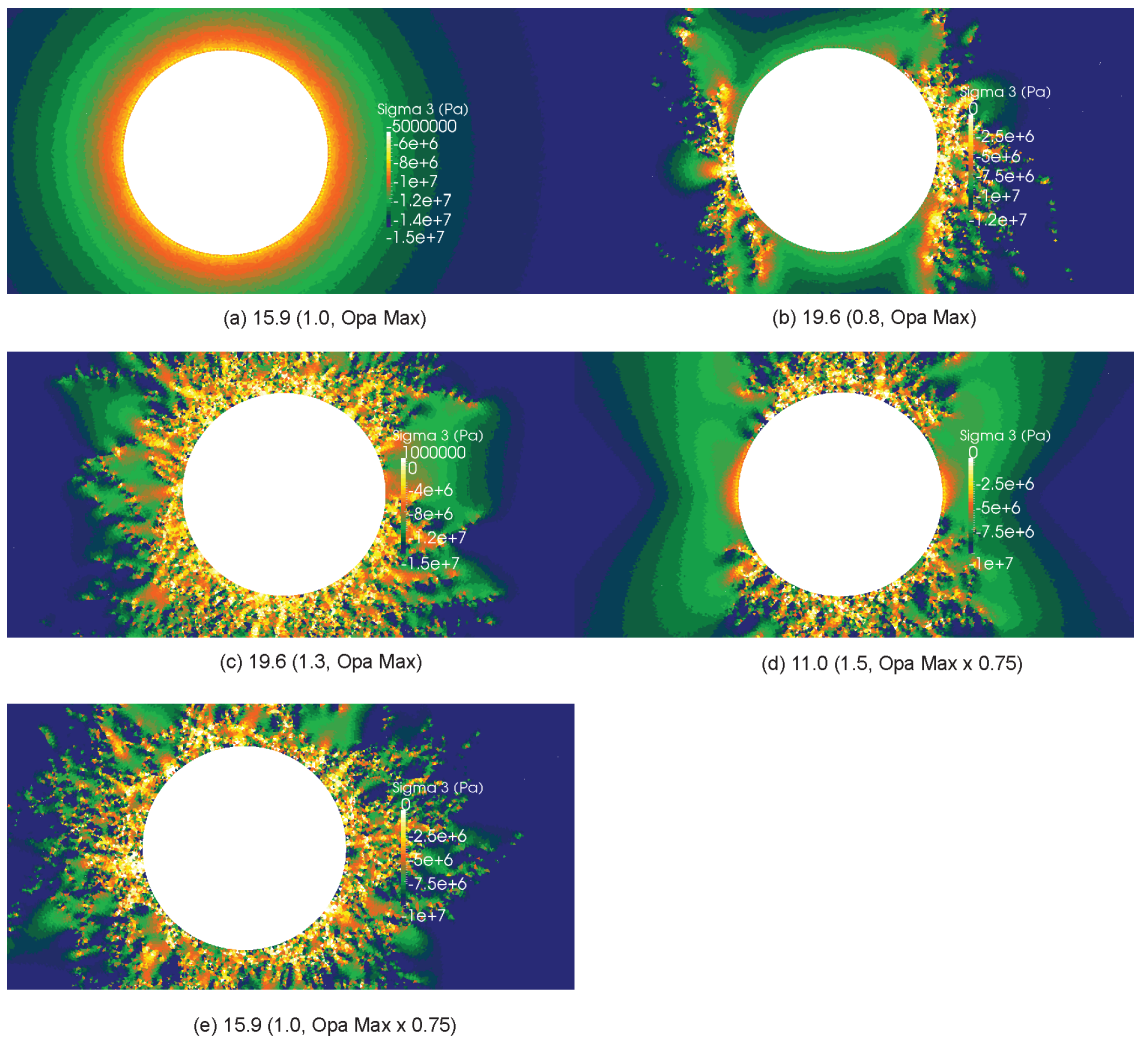


Fig. 9-21: Contours of minimum principal stress, σ_3 , in the support layer of the shaft reconsolidation model under different *in situ* stress conditions and for varying strength parameters. For each case, the *in situ* vertical stress, σ_v , is reported together with the stress ratio, K_0 , and the strength parameters in brackets. The core softening ratio at the time of support installation is equal to 0.01.

10 Discussion on the EDZ modeling results

10.1 SF/HLW emplacement tunnel simulations

For the sensitivity analysis of the SF/HLW model to the *in situ* stress state, the laboratory-calibrated strength parameters were increased by a factor of 2 (i.e., $\text{Opa} \times 2$ in Table 3). A preliminary analysis revealed that if the lab-scale calibrated parameters are used, the amount of fracturing is such that the model becomes numerically unstable and the simulations cannot be completed². For this specific model, this behaviour indicates the necessity of scaling the strength input parameters when increasing the element size from the millimeter (lab test models) to the centimeter (EDZ model). In this regard, a quantitative calibration study of the FE tunnel excavation (Geomechanica, 2013) showed that the lab-scale calibrated parameters had to be increased by approximately 2.75 times in order to correctly capture the rock mass deformation measured in the field. In the present study, the lack of *in situ* measurements to calibrate the field-scale FEMDEM model was addressed by running a sensitivity analysis over a wide range of input strength parameters (Table 3). The simulated ground reaction curves (Fig. 6-1) indicate, as expected, an increase of tunnel wall displacements for decreasing values of the core softening ratio. That is, as the stiffness of the core decreases, the convergence increase. For each step of the core modulus reduction sequence, the simulated displacement varies as function of the position along the tunnel perimeter (i.e., θ) and depends on the *in situ* stress anisotropy ratio, K_0 . Displacements of larger intensity are recorded for higher *in situ* stress magnitude. These curves were obtained from the graphs showing the evolution of displacement as function of time, as described in Section 5.3. In the numerical model, the evolution of displacement (Fig. 6-2) as a function of time tends to exhibit a polar symmetric deformation behaviour owing to the assumptions of homogeneous, transversely isotropic material and circular excavation shape. Simulated large deformations in the order of cm were a direct consequence of rock mass dilation induced by brittle fracturing. The stepped shape of these graphs is due to the procedure adopted for reducing the core modulus whereby a limited number steps was used. The anomalous displacements peaks (i.e., increases in total displacement immediately followed by a sharp decrease and then stabilization) are likely due to a dynamic rebound of the softened core upon reducing its elastic modulus. As a recommendation, a more gradual (e.g., linear instead of stepped) reduction of softening ratio should be implemented in the FEMDEM code. Upon installation of the stiff shotcrete liner (modulus = 32 GPa), negligible displacements were simulated. As depicted in Fig. 6-9, a total closure value of approximately 10 cm was obtained for a core softening ratio, α_s , equal to 0.008, 0.008 and 0.003 for vertical *in situ* stresses equal to 19.6 ($K_0 = 1.0$), 15.9 ($K_0 = 1.3$), and 15.9 ($K_0 = 1.0$). For all three cases, the maximum convergence is obtained along a vertical line passing through the tunnel center (i.e., $\theta = 90^\circ - 270^\circ$). The contours of total displacement (Fig. 6-3) clearly show that at a distance from the excavation, the rock mass behaves elastically and therefore small strains, induced by the stress redistribution around the damaged zone, are simulated. Due to the anisotropic rock mass response and anisotropic *in situ* stress field, this distance varies along the tunnel boundary. The fracture patterns (Fig. 6-4) are mainly characterized by shear mode of failure, with extent of the damaged zone that never extends more than two tunnel diameters from the excavation boundary. The intensity of fragmentation varies along the excavation boundary as function of the *in situ* stress rotation and is generally greater in the direction perpendicular to the maximum *in situ* stress. The contours of principal stress (Figs. 6-5 to 6-8) show that the redistribution of compressive stress in response to the tunnel excavation is influenced by the *in situ* stress anisotropy as well as the characteristic fracture pattern with bedding-parallel discontinuities and

² The scaling factor for strength parameters was introduced to avoid an unreasonably high fragmentation of the wallrock, which is not supported by in-situ observations. A comprehensive appraisal of the rationale for scaling strength parameters together with applications is given in Mahabadi (2012).

a heavily fractured zone around the tunnel. The extension of the EDZ due to bedding delamination is suppressed by the re-orientation of the maximum principal stress. In proximity to tunnel boundary, bedding plane slippage promotes a drastic reduction of confining stress with low to moderately negative values responsible for some extensional fracturing. The sensitivity analysis to the geomechanical properties (Fig. 6-16) shows that as the strength parameter are increased the simulated displacements decrease, with maximum values decreasing from 50 to approximately 5 mm. This behaviour is directly reflected in the EDZ extension (as indicated by the contours of displacement, fracture pattern and minimum principal stress) from about two tunnel diameters to less than about one tunnel radius. If the strength increases, fragmentation is replaced by the formation of distinct horizontal winged-shaped fractures that extend out from the tunnel haunch area together with extensional fractures in proximity of the excavation. The explicit incorporation of a three-fault system does not seem to sensibly influence the EDZ development and the tunnel deformational response. Conversely, a reduction of shotcrete stiffness (from 32 to 3.2 GPa), causes an average increase in the tunnel wall displacement between 2 and 7 mm.

10.2 L/ILW emplacement cavern simulations

The simulation of the I/LLW caverns (K09 models) indicates displacements of larger magnitude compared to the HAA tunnel model. Depending on the *in situ* stress state, displacements as high as 180 mm (i.e., 360 mm of total closure) were recorded. Unlike the case of the circular HAA model, the deformed excavation profile is no longer polar-symmetric. Higher stress concentrations are simulated in the flat floor (compared to the arched back) thus resulting in higher convergences. The sensitivity analysis to the geomechanical parameters indicates that in any case the fractured zone extends more than one time the height of the cavern from the excavation boundary. The presence of faults seems to have no noticeable effect on the model behaviour.

10.3 Shaft seal section simulations

Unlike the HAA and K09 models, the shaft seal section models used an isotropic material model, as the shaft is vertical and therefore perpendicular to the bedding plane strike. In this case, the EDZ network is characterized by a log-spiral type of shear fractures radiating from the tunnel boundary, resembling the characteristic lines that define the plastic zone around boreholes/tunnel in ductile materials. As expected, the damaged zone tends to develop from the boundary in the direction perpendicular to the maximum principal *in situ* stress.

10.4 EDZ reconsolidation simulations

In the EDZ recompaction models, the application of a reconsolidation pressure together with the long-term degradation of the shotcrete stiffness causes a partial reversal of displacements in the excavation walls (Fig. 9-1 and 9-7). This phenomenon is reflected in the total void area of the EDZ network, which experiences a total reduction ranging between 50 and 95% depending on the excavation type (BE/HLW emplacement rooms versus shaft) and *in situ* stress conditions. Although the application of the reconsolidation pressure changes the stress redistribution in the rock mass, it does not contribute to further rock mass fracturing.

11 Summary and conclusions

Executive summary

The EDZ around the backfilled underground structures of a geological repository represents a viable release path for dissolved and volatile radionuclides which has to be accounted for appropriately in the assessment of long-term safety. The efficiency of this release path depends on the characteristic features of the EDZ in terms of its geometry (shape, size) and the associated failure mechanisms (fracturing). The geomechanical simulations in this report provide a spectrum of discrete fracture networks of the EDZ around the disposal structures for a wide range of possible repository settings in the Opalinus Clay of the candidate siting regions in Northern Switzerland. Both repository types are considered in the sensitivity analyses, the L/ILW and the HLW repository.

Simulations were conducted for repository depths of 450m ($\sigma_v=11$ MPa), 650m ($\sigma_v=15.9$ MPa) and 800m ($\sigma_v=19.6$ MPa). Correspondingly, the assumed stress ratios σ_v / σ_h range between 0.8 and 1.3, covering the full spectrum of expected stress regimes in the siting regions of Northern Switzerland. Tunnel convergence was allowed to reach values of up to 4%, which exceeds the upper limit of tolerable deformation according to the agreed engineering requirements. The extreme cases with high convergence were aimed at exploring the upper bounds for the EDZ extent and fracture density to be expected in deep repository settings.

The report presents the modelling results, comprising the creation of the EDZ during the repository construction and its temporal evolution after backfilling of the underground structures. To this end, a hybrid finite-discrete element (FEMDEM) numerical code has been used. The fracture mechanics simulations were conducted on 2D cross sections for representative components of the geological repository, including SF/HLW tunnels, L/ILW caverns, and shaft seal sections. The sensitivity analyses included, in addition to the in situ stress conditions and repository depth, parameter variations of the geomechanical properties, rock mass fabric, and support stiffness.

The EDZ re-compaction process was numerically investigated for selected systems by applying a radial pressure on the liner, mimicking the swelling pressure of the bentonite up to 10 MPa. The modeling results are presented in terms of fracture patterns, principal stress components and displacements in the host rock, as well as total fracture area of the EDZ networks.

Concluding remarks

Based on the results obtained, the following general conclusions can be drawn:

- During the laboratory-scale calibration process, a good agreement of the simulated fracture patterns was reached for the modeled Brazilian tests and uniaxial compression tests. The emergent mechanical properties of the FEMDEM models are consistent with the geomechanical reference values of the Opalinus Clay, which are mainly based on the analysis of triaxial tests.
- Lab-calibrated input parameters were used as reference for the sensitivity analysis to the geomechanical properties in the EDZ simulations. The simulations indicated that the laboratory-calibrated strength parameters had to be increased typically by a factor 2 – 5 to avoid excessively large amount of fracturing, which is not consistent with in-situ observations in tunnels (e.g., Mont Terri).

- For the emplacement tunnel model, the time of support installation was initially adjusted to limit the total wall closure to < 0.10 m. Even though, this specification exceeds the limits of the general engineering requirements, it was selected for exploring the upper bounds of the EDZ extent.
- For the emplacement tunnel and cavern models, the simulation results indicate a strong influence of the rock mass layering on the EDZ network shape and extension as well as on the host rock deformational behaviour.
- For all simulations, the analysis of sensitivity to in situ stress conditions indicates a distinct influence of the stress magnitude and anisotropy on the EDZ network and associated stress and displacement distribution.
- The simulation of the EDZ reconsolidation highlights a distinct reduction of the total EDZ fracture area in response to the long-term bentonite swelling process and liner mechanical degradation.
- The final EDZ fracture geometries with the associated stress states produced in this study will be used as input for subsequent fluid model of the EDZ re-saturation process.

The sensitivity analysis provided for a variety of repository configurations valuable insight in the formation and evolution of the EDZ around underground structures. The following conclusions can be drawn with regard to the shape and extent of the EDZ around SF/HLW tunnels, L/ILW caverns, horizontal seal sections and vertical shafts:

- *SF/HLW emplacement tunnel*: the simulations were conducted for vertical stresses corresponding to burial depths between 450 and 800 m bg and for stress ratios between 0.8 and 1.3. The formation of the EDZ fracture pattern was controlled not only by the strength and stiffness of the Opalinus Clay but also by the overburden stress and by the stress ratio K_0 . Another important factor for the evolution of the EDZ is the tolerable tunnel convergence, closely linked to the design requirements for the liner. Notably, not a single simulation indicated an extension of the EDZ $>2\times$ tunnel diameter. Tensile features were largely restricted to a narrow zone around the tunnel wall (thickness of zone < 1 m). Re-compaction of the EDZ by the application of a radial stress of 10 MPa resulted in a significant reduction of the void volume of the EDZ fracture network by a factor of 2-3.
- *L/ILW emplacement cavern K9*: the simulations were conducted for vertical stresses corresponding to burial depths between 450 and 800 m bg. The EDZ fracture patterns of the cavern models were governed by the geomechanical properties of the Opalinus Clay but also by the stress ratio K_0 . The simulations with low rock strength (“OPA $\times 1.5$ ”) exhibit unrealistically high fracture densities. The implementation of a sub-vertical fracture zone, which intersects the cavern, did not change significantly the shape of the EDZ. The extension of the EDZ ranged between 1 and $2 \times$ tunnel diameter for the different sensitivity runs. A high density of tensile features was observed in a 1-2 m thick zone around the tunnel wall.
- *Shaft sections*: the simulations were conducted for vertical stresses corresponding to burial depths between 450 and 800 m bg and for stress ratios between 0.8 and 1.5. The rock strength was assumed isotropic in the horizontal plane (corresponding to the assumption of transverse isotropy of the Opalinus Clay). As a consequence the size of the EDZ is restricted and does not extend beyond $1 \times$ tunnel diameter.

12 References

- Alcolea, A., Kuhlmann, U., Lanyon, G.W., Marschall, P. (2014): Hydraulic conductance of the EDZ around underground structures of a geological repository for radioactive waste – A sensitivity study for the candidate host rocks in the proposed siting regions in Northern Switzerland. Nagra Arbeitsbericht NAB 13-94. Nagra, Wettingen, Switzerland.
- Bieniawski, Z.T., Hawkes, I. (1978): Suggested methods for determining tensile strength of rock materials. *International Journal of Rock Mechanics and Mining Sciences* 15, 99–103.
- Barenblatt, G.I. (1962): The mathematical theory of equilibrium cracks in brittle fracture. *Advances in Applied Mechanics* 7, 55–129.
- Dugdale, D.S. (1960): Yielding of steel sheets containing slits. *Journal of the Mechanics and Physics of Solids* 8, 100–104.
- Curran, J.H., Hammah, R.E., Yacoub, T.E. (2003): A two-dimensional approach for designing tunnel support in weak rock. In: *Proceedings of the 56th Canadian Geotechnical Conference*. Winnipeg, Canada.
- Geomechanica Inc. (2012): The excavation of a circular tunnel in a bedded argillaceous rock (Opalinus Clay): short-term rock mass response and numerical analysis using FEM/DEM. Mont Terri Technical Note 2012-06.
- Hillerborg, A., Modeer, M., Petersson, P.E. (1976): Analysis of crack formation and crack growth in concrete by means of fracture mechanics and finite elements. *Cement and Concrete Research* 1976;6(6):773–781.
- Jahns, E. (2010): RA experiment. Opalinus Clay rock characterization. Technical Note 2008-55rev. Mont Terri Project. St-Ursanne, Switzerland.
- Labuz, J., Shah, S., Dowding, C. (1987): The fracture process zone in granite: evidence and effect. *International Journal of Rock Mechanics and Mining Sciences & Geomechanics Abstracts* 1987;24(4):235–246.
- Lisjak, A., Grasselli, G., Vietor, T. (2013): Continuum-discontinuum analysis of failure mechanisms around unsupported circular excavations in anisotropic clay shales. *International Journal of Rock Mechanics and Mining Sciences* 2013; doi:10.1016/j.ijrmms.2013.10.006.
- Mahabadi, O.K. (2012): Investigating the influence of micro-scale heterogeneity and microstructure on the failure and mechanical behaviour of geomaterials. Ph.D. thesis; University of Toronto; Toronto, Canada; 2012.
- Mahabadi, O.K., Grasselli, G., Munjiza, A. Y-GUI (2010): A graphical user interface and pre-processor for the combined finite-discrete element code, Y2D, incorporating material inhomogeneity. *Computer and Geosciences* 2010;36(2):241–252.
- Mahabadi, O.K., Lisjak, A., Grasselli, G., Munjiza, A. Y-Geo (2012a): a new combined finite-discrete element numerical code for geomechanical applications. *International Journal of Geomechanics*;12(6):676–688.

- Munjiza, A. (2004): *The combined finite-discrete element method*. Chichester, West Sussex, England: John Wiley & Sons Ltd., 2004.
- Munjiza, A., Andrews, K.R.F. (2000): Discretised penalty function method in combined finite-discrete element analysis. *International Journal for Numerical Methods in Engineering* 2000;49(11):1495–1520.
- Munjiza, A., Andrews, K.R.F., White, J.K. (1999): Combined single and smeared crack model in combined finite-discrete element analysis. *International Journal for Numerical Methods in Engineering* 1999;44(1):41–57.
- Munjiza, A., Owen, D.R.J., Bicanic, N. (1995): A combined finite-discrete element method in transient dynamics of fracturing solids. *Engineering Computations* 1995;12(2):145–174.
- Nagra (2002): Projekt Opalinuston – Synthese der geowissenschaftlichen Untersuchungsergebnisse. Entsorgungsnachweis für abgebrannte Brennelemente, verglaste hochaktive sowie langlebige mittelaktive Abfälle. Nagra Technical Report NTB 02-03, Wetingen, Switzerland.
- Popp, T., Salzer, K., Minkley, W. (2008): Influence of bedding planes to EDZ-evolution and the coupled HM properties of Opalinus Clay. *Physics and Chemistry of the Earth, Parts A/B/C* 33, S374–S387. doi:10.1016/j.pce.2008.10.018.
- Potyondy, D.O., Cundall, P.A. (2004): A bonded-particle model for rock. *International Journal of Rock Mechanics and Mining Sciences* 2004;41(8):1329–1364.
- Swiss Federal Office of Energy (SFOE) 2008: Sectoral Plan for Deep Geological Repositories, Conceptual Part. Swiss Federal Office of Energy, Bern, Switzerland.
- Xu, X., Needleman, A. (1994): Numerical simulations of dynamic crack growth along an interface. *International Journal of Fracture* 1994;74(4): 289–324.

Appendix: File Identification Tables

All simulations presented in this report have been stored electronically in Nagra's data archive. The file IDs together with the link to the actual simulation cases are given in the appended Tables.

Table A1 reports the list of directories containing the files of the simulation cases reported in Tables 6, 7 and 8. Each folder contains the following file types:

- file_name.y: input file of the FEMDEM simulation
- Paraview output files:
 - *file_name.y_timestepnumber.vtp*: paraview output file at a given time step
 - *file_name.y_timestepnumber.vtp*: paraview output file at a given time step
 - *file_name.y_broken_joints_timestepnumber.vtp*:
paraview output file at a given time step
 - *file_name.y_yielded_joints_timestepnumber.vtp*:
paraview output file at a given time step
 - *file_name.y_principal_direction_timestepnumber.vtp*:
paraview output file at a given time step
- Other output files:
 - *Pi.csv*: *time-evolution of displacements along the excavation boundary*
- Folder containing the fracture aperture data:
 - *file_name.y_broken_joints_timestepnumber.vtp*:
paraview file containing the fracture output from the FEMDEM simulation
 - *file_name.y_timestepnumber.vtp*:
paraview file containing the stress and principal stress output from the FEMDEM simulation
 - *file_name.y_principal_direction_timestepnumber.vtp*:
paraview file containing the principal stress direction output from the FEMDEM simulation
 - *file_name.y_broken_joints_timestepnumber--c.csv*
 - *file_name.y_broken_joints_timestepnumber--p.csv*
 - *file_name_frac_data --c.csv*
 - *summary.txt*

Tab. A1: List of directories containing the output files of the simulation cases reported in Table 6, 7 and 8 (Sensitivity analysis).

Model ID	Directory	Size (GB)	Date
HAA-01	HAA/HAA-3m_20cm-Sv_19_6-Sh_15_7-MR_1-SC_32_01-Opa_x2-/	7.2	25/03/13
HAA-02	HAA/HAA-3m_20cm-Sv_19_6-Sh_19_6-MR_1-SC_32_01-Opa_x2-/	7.3	25/03/13
HAA-03	HAA/HAA-3m_20cm-Sv_19_6-Sh_25_5-MR_1-SC_32_01-Opa_x2-/	7.7	25/03/13
HAA-04	HAA/HAA-3m_20cm-Sv_19_6-Sh_15_7-MR_1-SC_32_05-Opa_x2-/	3.2	20/03/13
HAA-05	HAA/HAA-3m_20cm-Sv_19_6-Sh_19_6-MR_1-SC_32_05-Opa_x2-/	2.9	20/03/13
HAA-06	HAA/HAA-3m_20cm-Sv_19_6-Sh_25_5-MR_1-SC_32_05-Opa_x2-/	7.5	25/03/13
HAA-07	HAA/HAA-3m_20cm-Sv_19_6-Sh_19_6-MR_1-SC_32_008A-Opa_x2-/	6.6	25/04/13
HAA-08	HAA/HAA-3m_20cm-Sv_15_9-Sh_20_7-MR_1-SC_32_008A-Opa_x2-/	7.0	22/04/13
HAA-09	HAA/HAA-3m_20cm-Sv_15_9-Sh_15_9-MR_1-SC_32_003B-Opa_x2-/	8.2	03/05/13
HAA-10	HAA/HAA-3m_20cm-Sv_15_9-Sh_20_7-MR_1-SC_32_008A-Opa_x1_5-/	3.7	10/07/13
HAA-11	HAA/HAA-3m_20cm-Sv_15_9-Sh_20_7-MR_1-SC_32_008A-Opa_x3-/	7.4	24/05/13
HAA-12	HAA/HAA-3m_20cm-Sv_15_9-Sh_20_7-MR_1-SC_32_008A-Opa_x4-/	7.1	24/05/13
HAA-13	HAA/HAA-3m_20cm-Sv_15_9-Sh_20_7-MR_1-SC_32_008A-Opa_x5-/	7.0	24/05/13
HAA-14	HAA/HAA-3m_20cm-3F-80d-Sv_19_6-Sh_19_6-MR_1-SC_32_01-Opa_x2-/	4.7	05/04/13
HAA-15	HAA/HAA-3m_20cm-3F-80d-Sv_19_6-Sh_19_6-MR_1-SC_32_01-Opa_x1_5-/	10.8	23/06/13
HAA-16	HAA/HAA-3m_20cm-3F-80d-Sv_19_6-Sh_19_6-MR_1-SC_32_01-Opa_x3-/	8.5	22/05/13
HAA-17	HAA/HAA-3m_20cm-3F-80d-Sv_19_6-Sh_19_6-MR_1-SC_32_01-Opa_x4-/	8.0	22/05/13
HAA-18	HAA/HAA-3m_20cm-3F-80d-Sv_19_6-Sh_19_6-MR_1-SC_32_01-Opa_x5-/	7.9	22/05/13
HAA-19	HAA/HAA-3m_20cm-Sv_15_9-Sh_20_7-MR_1-SC_16_008A-Opa_x2-/	8.6	23/05/13
HAA-20	HAA/HAA-3m_20cm-Sv_15_9-Sh_20_7-MR_1-SC_3_2_008A-Opa_x2-/	8.6	23/05/13
HAA-21	HAA/HAA-3m_20cm-Sv_15_9-Sh_20_7-MR_1-SC_3_2_008A-Opa_x1_5-/	9.3	10/07/13
HAA-22	HAA/HAA-3m_20cm-Sv_15_9-Sh_20_7-MR_1-SC_3_2_008A-Opa_x3-/	8.0	24/05/13
HAA-23	HAA/HAA-3m_20cm-Sv_15_9-Sh_20_7-MR_1-SC_3_2_008A-Opa_x4-/	7.6	24/05/13
HAA-24	HAA/HAA-3m_20cm-Sv_15_9-Sh_20_7-MR_1-SC_3_2_008A-Opa_x5-/	7.5	24/05/13
K09-01	K09/K09-1-Sv_18_4-Sh_14_7-MR_1b-SC_32_01-Opa_x2-/	16.5	09/07/13
K09-02	K09/K09-1-Sv_18_4-Sh_18_4-MR_1b-SC_32_01-Opa_x2-/	16.5	10/07/13
K09-03	K09/K09-1-Sv_18_4-Sh_23_9-MR_1b-SC_32_01-Opa_x2-/	17.4	10/07/13
K09-04	K09/K09-1-Sv_15_9-Sh_12_9-MR_1b-SC_32_01-Opa_x2-/	16.3	04/09/13
K09-05	K09/K09-1-Sv_15_9-Sh_15_9-MR_1b-SC_32_01-Opa_x2-/	16.5	04/09/13
K09-06	K09/K09-1-Sv_15_9-Sh_20_7-MR_1b-SC_32_01-Opa_x2-/	17.0	04/09/13
K09-07	K09/K09-1-Sv_11_0-Sh_14_3-MR_1b-SC_32_01-Opa_x2-/	15.9	04/09/13
K09-08	K09/K09-1-Sv_18_4-Sh_18_4-MR_1b-SC_32_01-Opa_x1_5-/	18.8	03/09/13
K09-09	K09/K09-1-Sv_18_4-Sh_18_4-MR_1b-SC_32_01-Opa_x3-/	15.9	03/09/13
K09-10	K09/K09-1-3F_80d_2m-40cm-Sv_18_4-Sh_18_4-MR_1b-SC_32_01-Opa_x1_5-/	19.8	04/09/13
K09-11	K09/K09-1-3F_80d_2m-40cm-Sv_18_4-Sh_18_4-MR_1b-SC_32_01-Opa_x2-/	12.1	23/07/13
K09-12	K09/K09-1-3F_80d_2m-40cm-Sv_18_4-Sh_18_4-MR_1b-SC_32_01-Opa_x3-/	16.4	04/10/13
Shaft-01	Shaft/Shaft-Sv_11_0-Sh_16_5-MR_1b-SC_32_01-OpaMax-/	7.2	17/07/13
Shaft-02	Shaft/Shaft-Sv_15_9-Sh_15_9-MR_1b-SC_32_01-OpaMax-/	6.6	17/07/13
Shaft-03	Shaft/Shaft-Sv_19_6-Sh_15_7-MR_1b-SC_32_01-OpaMax-/	8.1	18/07/13
Shaft-04	Shaft/Shaft-Sv_19_6-Sh_25_5-MR_1b-SC_32_01-OpaMax-/	8.6	18/07/13
Shaft-05	Shaft/Shaft-Sv_11_0-Sh_16_5-MR_1b-SC_32_01-OpaMax_x0_5-/	9.1	20/09/13
Shaft-06	Shaft/Shaft-Sv_15_9-Sh_15_9-MR_1b-SC_32_01-OpaMax_x0_5-/	8.8	20/09/13
Shaft-07	Shaft/Shaft-Sv_19_6-Sh_15_7-MR_1b-SC_32_01-OpaMax_x0_5-/	9.4	20/09/13
Shaft-08	Shaft/Shaft-Sv_19_6-Sh_25_5-MR_1b-SC_32_01-OpaMax_x0_5-/	10.3	20/09/13
Shaft-09	Shaft/Shaft-Sv_11_0-Sh_16_5-MR_1b-SC_32_01-OpaMax_x0_75-/	7.5	12/09/13
Shaft-10	Shaft/Shaft-Sv_15_9-Sh_15_9-MR_1b-SC_32_01-OpaMax_x0_75-/	7.1	12/09/13
Shaft-11	Shaft/Shaft-Sv_19_6-Sh_15_7-MR_1b-SC_32_01-OpaMax_x0_75-/	7.5	12/09/13
Shaft-12	Shaft/Shaft-Sv_19_6-Sh_25_5-MR_1b-SC_32_01-OpaMax_x0_75-/	8.0	12/09/13

Tab. A2: List of directories containing the output files of the simulation cases reported in Table 9 (Reconsolidation study).

Model ID	Directory	Size	Date
HAA_Rec-01	HAA_Rec/HAA-3m_20cm-Sv_19_6-Sh_19_6-MR_1-SC_32_008A-Pi_10A-Opa_x2-	11.9	21/05/13
HAA_Rec-02	HAA_Rec/HAA-3m_20cm-Sv_15_9-Sh_20_7-MR_1-SC_32_008A-Pi_10A- Opa_x2-	12.3	14/09/13
HAA_Rec-03	HAA_Rec/HAA-3m_20cm-Sv_19_6-Sh_15_7-MR_1-SC_32_008A-Pi_10A- Opa_x2-	11.4	06/10/13
HAA_Rec-04	HAA_Rec/HAA-3m_20cm-Sv_19_6-Sh_25_5-MR_1-SC_32_008A-Pi_10A- Opa_x2-	12.0	06/10/13
HAA_Rec-05	HAA_Rec/HAA-3m_20cm-Sv_15_9-Sh_20_7-MR_1-SC_32_008A-Pi_10A- Opa_x3-	12.0	06/10/13
HAA_Rec-06	HAA_Rec/HAA-3m_20cm-Sv_15_9-Sh_20_7-MR_1-SC_3_2_008A-Pi_10A-Opa_x1_5-	10.9	29/10/13
HAA_Rec-07	HAA_Rec/HAA-3m_20cm-Sv_15_9-Sh_20_7-MR_1-SC_3_2_008A-Pi_10A- Opa_x2-	11.5	26/10/13
HAA_Rec-08	HAA_Rec/HAA-3m_20cm-Sv_15_9-Sh_20_7-MR_1-SC_3_2_008A-Pi_10A- Opa_x3-	10.5	26/10/13
Shaft_Rec-01	Shaft_Rec/Shaft-Sv_15_9-Sh_15_9-MR_1b-SC_32_01-Pi_10A-OpaMax-/	10.0	17/10/13
Shaft_Rec-02	Shaft_Rec/Shaft-Sv_15_9-Sh_19_6-MR_1b-SC_32_01-Pi_10A-OpaMax-/	10.1	17/10/13
Shaft_Rec-03	Shaft_Rec/Shaft-Sv_15_9-Sh_25_5-MR_1b-SC_32_01-Pi_10A-OpaMax-/	10.5	17/10/13
Shaft_Rec-04	Shaft_Rec/Shaft-Sv_11_0-Sh_16_5-MR_1b-SC_32_01-Pi_10A-OpaMax_x0_75-/	10.2	16/10/13
Shaft_Rec-05	Shaft_Rec/Shaft-Sv_15_9-Sh_15_9-MR_1b-SC_32_01-Pi_10A-OpaMax_x0_75-/	10.4	16/10/13